THIN FILM BATTERY/FUEL CELL POWER GENERATING SYSTEM

Final Report of the Continuation Contract (Tasks 1-4) for the Period April 1, 1978—March 31, 1980

June 30, 1980

Work Performed Under Contract No. AC02-76ET11305

Westinghouse Electric Corporation
Pittsburgh, Pennsylvania

DISCLAIMER

DISCLAIMER

Available from the National Technical Information Service, U. S. Department of Commerce, Springfield, Virginia 22161.

Price: Printed Copy A10
Microfiche A01

THIN FILM BATTERY/FUEL CELL POWER GENERATING SYSTEM

DOE/ET/11305-T7
Distribution Category UC-97d

Final Report of the Continuation Contract (Tasks 1-4)
Covering the Period
April 1, 1978 to March 31, 1980

W. Feduska, Project Manager
A. O. Isenberg, Technical Coordinator
J. E. Bauerle, E. F. Federmann, Y. Ichikawa,
R. J. Ruka, E. J. Vidt, S. A. Zeitman,
G. E. Zymboly, Contributors

Prepared for the United States Department of Energy
Under Continuation Contract No. DE-AC-0379ET11305
(Formerly Contract EY-76-03-1197)

by

Research and Development Center
WESTINGHOUSE ELECTRIC CORPORATION
Pittsburgh, Pennsylvania 15235

June 30, 1980

Westinghouse R&D Center
1310 Beulah Road
Pittsburgh, Pennsylvania 15235

FOREWORD

For the first year of the present two year continuation program (DOE Contract DE-AC-0379ET-11305) the Department of Energy Program Manager was Mr. R. F. Dudley, Jr. For the second year, the program was technically and financially managed at Argonne National Laboratories/DOE, under Dr. J. P. Ackerman, with Dr. A. V. Fraioli, as his Deputy Assistant Manager. Mr. O. S. Merrill of the Department of Energy was responsible for the administration of the program. Their assistance and guidance in program planning, program interaction and in direct contract-related matters is gratefully acknowledged.

PREFACE

For those who desire to learn about the objectives and results obtained during the first two-year contract period of this program, a Past Program Summary is given in Appendix A.

For purposes of providing background information to those readers who may be unfamiliar with the operation, design concept and some possible applications of the high-temperature, solid oxide electrolyte (HTSOE) fuel cell, Appendix B has been included in this report.

Acknowledgements

The following personnel made important contributions to results contained in this report:

1. D. F. Bradley - EVD fabrication, life testing, other outside processes
2. J. J. Duffala - Porous support tube development
3. W. D. Eagleson - Porous support tube development
4. G. M. Halgas - Porous support tube development
5. C. W. Hughes - SEM and EDAX analyses
6. R. C. Kuznicki - X-ray diffraction measurements
7. B. Lancaster - Sulfur tolerance estimation
8. R. W. Liebermann - Provided the computer program data thermodynamic calculations of sulfur tolerance of nickel, cobalt and lanthanum chromite
9. R. J. McKeever - Density measurements on lanthanum chromite films
10. J. N. Robinson (deceased) - Fuel electrode development
11. J. Rudolph - Elemental analysis of interconnection films
12. M. G. Stratis - Oxygen loss measurements on interconnection oxide films and doped indium oxide, and sulfur tolerance measurements
13. W. Summers (AES) - Cogeneration system analysis
14. G. G. Sweeney - DIMA analysis of interconnection layers
15. J. Valentich - Thermal expansion measurements of air electrode materials
16. A. L. Wolfe and G. Gidick - Analytical determination of magnesium and aluminum in lanthanum chromite interconnection films

TABLE OF CONTENTS

TABLE OF CONTENTS (CONT'D) PAGE(S)

TABLE OF CONTENTS (CONT'D) PAGE(S)

LIST OF ILLUSTRATIONS

LIST OF ILLUSTRATIONS (Cont'd)

LIST OF ILLUSTRATIONS (Cont'd)

LIST OF ILLUSTRATIONS (Cont'd)

LIST OF ILLUSTRATIONS (Cont'd)

LIST OF ILLUSTRATIONS (Cont'd)

LIST OF TABLES

ABSTRACT

Work on the modified lanthanum chromite interconnection (IC) proceeded in a number of areas. Toward determining the stability of the IC, oxygen ion transport mechanisms were evaluated, as well as IC stability under low oxygen partial pressures (10^{-6}t 10^{-18}atm). To produce long, continuous, 20 to 50 μm thick IC films on 0.3 m long porous support tubes, improvements were made in both the EVD apparatus and process.

The fuel electrode process was adapted to longer tubes and the sintering step was modified to prevent reduction of the zirconia and weakening of the porous support tubes.

Work on the air electrode current collector covered several areas. The high-temperature resistivity of doped indium oxide ($In_{1.96}Sn_{0.4}O_3$) was studied at various doping levels, as a function of oxygen partial pressure. The current collector has been improved, with respect to both lowering its resistivity and improving its air permeability. Also, other possible current collector formulations were investigated. Doped lanthanum manganite appears promising, as a possible replacement for doped indium oxide, based on initial fuel cell stack performance data.

Porous support tubes of calcia-stabilized zirconia were produced, up to 0.3 m long, for fuel cell stack fabrication. Here, also, improved equipment and processes were used to enhance the final tube quality.

A 20-cell stack has been successfully fabricated and a section of this stack is on life test. This stack met the initial milestone objectives (power and life goals) by delivering 10 watts of power, the target goal for coal-derived fuel. The stack is still undergoing life testing. Fifteen contiguous cells of this stack attained 700 h of stable life, delivering 0.73 $\overline{V}$/cell at 400 mA/cm^2 (program target: 0.66 $\overline{V}$/cell, 1000°C, H_2-3% H_2O inlet fuel, air oxidant). Seven cells of this stack are still stable after operating 4000 h of total test time, with about 2000 h under 85% fuel gas consumption condition, 150 mA/cm^2, at ~ 0.62 $\overline{V}$/cell.

During life testing to 4000 h (exceeding the second milestone), the stack has sustained 11 thermal cycles to date (1 h, RT to 1000°C; 3 h, 1000°C to RT, per cycle) without any apparent damage or loss in performance. Data have been obtained on the 15-cell stack with various fuel and oxidant conditions. With a simulated coal-derived fuel gas composition, corresponding to 85% fuel consumption of the inlet gas, 0.72 $\overline{V}$/cell was obtained at 100 mA/cm^2. Also, the stack has operated up to 800 mA/cm^2 (at $\sim$ 0.45 $\overline{V}$/cell) without any noticeable damage.

Fabrication of this stack included a processing procedure to enhance oxygen availability to the air electrode-interconnection interface. This resultant interface structure precludes oxygen depletion of the doped indium oxide, which can cause mechanical/electrical contact failure.

Measurement techniques have been refined on the fuel cell and its components. Realistic combination specimens, as fuel electrode-interconnection layers on a porous support tube, have been used to determine interconnection apparent resistivity at 1000°C. From polarization tests on fabricated fuel cell stacks, major electrical resistance contributors to the total cell resistance are the air electrode and the interconnection, with the latter being the largest contributor.

Measurements have been performed on realistic fuel electrode porous support tube samples by using the complex impedance measuring technique. Equivalent circuits have been defined for several samples.

A second 10-watt stack has been constructed and demonstrated stack reproducibility, partially fulfilling the final milestone objective of the program (reproducing ten 10-watt stacks).

The cost, design and benefit study to evaluate the nature and worth of an industrial cogeneration application of the HTSOE fuel cell is underway. Here, promising applications are now being considered, from which a single application has been selected as a basis for the study -- an integrated aluminum production facility.

Investigation of sulfur species and their effects on the HTSOE fuel cell stack performance and life is underway. Projected maximum tolerance levels for nickel-cermet is $\sim$ 70 ppm at 1000°C at a cell OCV of 0.7-0.8 V. For cobalt cermet fuel electrodes, the level increases to 200 ppm. Tests on modified lanthanum chromite indicate it will be more tolerant (5 to 6X) than nickel to sulfur in the fuel gas.

An experimental scheme was devised which can be utilized to evaluate gas diffusion coefficients at the fuel electrode in a fuel cell stack.

The HTSOE fuel cell stack was operated for a short time (a few hours) in the electrolyzer mode with H_2/H_2O and with CO/CO_2 mixtures. The stack demonstrated it could sustain reversible operation in this test at 1000°C without any harmful effects when returned to fuel cell operation.

1.0 General Conclusions

1. The electrochemical vapor deposition (EVD) process was improved, with regard to both equipment and process procedures, and now produces uniform ~40 μm thick layers of modified lanthanum chromite interconnection and yttria-stabilized zirconia solid electrolyte on long (30 cm), fuel cell stacks.

2. Considerable effort has been directed toward understanding the air electrode-interconnection interface behavior, through studies of $O^{=}$ transport and loss in the interconnection, as a function of temperature and oxygen partial pressure, with no adverse effects found with respect to property or compositional changes, at oxygen partial pressures from 10^{-7} to 10^{-17} atm at 1000°C. The interconnection film is stable, dense and of suitable electrical conductivity.

3. Nickel diffusion and subsequent reduction interaction with zirconia in the porous support tube has been suspected as a cause contributing to tube weakening and cracking, and the fuel electrode process was modified to eliminate this problem.

4. Air electrode resistance is being reduced by the use of a plasma spraying technique for oxides other than indium oxide. Here, lanthanum manganite is being used as an alternate air electrode current collector, rather than tin-doped indium oxide. Lower resistance in this component should improve the power capability of the stack. Meantime, work on sintered $In_{1.96}Sn_{.04}O_3$ air electrode current collector has reduced its resistivity and improved its air permeability.

5. A search for other, less expensive yet stable, air electrode materials was undertaken. Doped-lanthanum manganites appear promising.

6. Work on the porous support tube is leading to the preparation of more reactive calcia-stabilized zirconia batch materials which will allow porous tube fabrication at lower final sintering temperature.

7. In-house porous, calcia-stabilized zirconia support tubes, about 0.3 m long, are being fabricated with improved extrusion and sintering equipment and with improved processes, toward desired dimensional and physical properties.

8. The interface and air accessibility to the air electrode-interconnection interface has been improved by modified processing procedures.

9. Measurements on interconnection films, on a section of an actual, fabricated fuel cell stack specimen (less the air electrode) have shown improvement of the 1000°C resistivity from 30 Ωcm to 4.8 Ωcm (an acceptable level).

10. 20-cell stacks (Stacks #8 and Stack #9) have been successfully fabricated on a 0.3 m long porous support tube.

11. Stack #8 utilized component materials and processes, as developed for 5-cell stack #1 (which met the initial 2 year program goals), with improved air permeation in the interconnection area to avoid oxygen scavenging from the indium oxide air current collector via the interconnection (due to its slight oxygen permeation in the solid state).

12. Performance tests on the 20-cell stack demonstrated 10 watts maximum power, using carbon monoxide-hydrogen fuel and meeting the 10 watts power objective of the program.

    Life testing on 15 contiguous cells of Stack #8 proceeded to 1000 h at 1000°C, using H_2-3% H_2O inlet fuel, air oxidant, 400 mA/cm^2 with the stack delivering 0.73 to 0.70 $\overline{V}$/cell (0.66 $\overline{V}$ start was the program target, with less than 10% voltage degradation in 1000 hours).

13. At 2200 h, a seven-cell stack was delivering 0.72 $\bar{V}$/cell at 400 mA/cm^2, 1000°C, H + 3% H_2O fuel, air oxidant.

14. From 2200 to 4000 h the seven-cell stack operated under spent fuel condition (15% CO/H_2)-N_2 at 150 mA/cm^2 1000°C. Here it delivered a steady 0.63 $\bar{V}$/cell.

15. During the present 4000 h of testing to date, the seven-cell stack has undergone 11 fast thermal cycles (RT to 1000°C in 1 h; 1000°C to RT in 3 h, per cycle) without any apparent physical or performance degradation.

16. Initial tests were performed on 20 cells and, later, 15 cells of this stack, under various inlet fuel or oxygen conditions.

    a) H_2 + 3 v/o H_2O
    b) 33 v/o H_2 - 64 v/o CO - 3 v/o H_2O
    c) CO + 3 v/o H_2O
    d) (36 v/o H_2 - 64 v/o CO) as 11 v/o - 86 v/o N_2 - 3 v/o H_2O
    e) a) with 2.5-5 v/o O_2 in the inlet air
    f) 45/48 v/o H_2 - 3/20 v/o H_2O - N_2
    g) 5/10 v/o H_2 - 3/8 v/o H_2O - N_2
    h) 0/5 v/o H_2 - 3/8 v/o H_2O - N_2
    i) f) with 3/5 v/o O_2 in the inlet air
    j) g) with 4/5 v/o O_2 in the inlet air
    k) h) with 5 v/o O_2 in the inlet air

The general conclusions of these tests, having, rich-to-lean fuel inlet gas, normal-to-lean oxygen in the inlet air are:

- fuel can be consumed totally in a 15-cell stack by fuel flow adjustment
- a current density of 100 mA/cm^2 (min) can be expected with coal-derived fuel and 90% fuel consumption at 0.72 V (min)/cell under exit gas composition

- a high current density of 800 mA/cm^2 (min) can be sustained without noticeable damage to individual cells in short duration tests under the condition that sufficient fuel is available at the fuel electrode
- partial fuel depletion (90%) for the short time duration of this test condition was not harmful to the fuel cell stack.

17. Procedures have been developed and component and interfacial electrical resistance measurements have been made. Data correlate well with polarization data obtained by the current interruption technique, in a tested 5 cell stack.

18. By using complex impedance measurements (w/o DC bias current) an equivalent electrical circuit has been derived for the fuel electrode/electrolyte on the porous support tube. Here the Warburg impedance is associated with a diffusion-limited process, involving one of the electrode reactant species and a psuedocapacitance is believed due to an adsorption process (oxygen or hydrogen?) on one of the electrodes. The series resistance is believed related to ohmic resistance of the solid electrolyte and the lead wires.

19. A testing technique has been devised to measure effective diffusion coefficients of fuel and air gases through porous components of the fuel cell stack (fuel electrode and support tube).

20. The cost, design and benefit study to evaluate the nature and worth of an industrial cogeneration application of the HTSOE fuel cell is underway, with some initial system temperatures defined. Here, promising applications were considered, from which a single application, an integrated aluminum production facility, has been selected as a basis for the study.

21. The investigation of sulfur-species in simulated, coal-derived fuel is underway, with the high-temperature (1000°C) microweighing apparatus installed and operational. Initial work on the tolerance

of the HTSOE fuel cell stack to sulfur impurities in the fuel gas indicates that the least tolerant component will be the nickel of the fuel electrode, at ~70 ppm at 0.7-0.8 OCV at 1000°C. Tests on the IC material indicated that it will have more sulfur tolerance than the nickel fuel electrode. Cobalt fuel electrode tolerance is projected at 200 ppm in the fuel gas at 1000°C (0.7-0.8 OCV).

22. After 2000 h of life testing, the seven cell stack was successfully operated in the electrolysis mode at 1000°C, both with H_2/H_2O and CO/CO_2 mixtures. Current densities up to 500 mA/cm^2 were investigated. This test did not affect the stack performance, upon further testing of the stack (still continuing) in the fuel cell mode.

THIS PAGE

WAS INTENTIONALLY

LEFT BLANK

2.0 Program Summary

Highlights of progress, upon completion of the present, two-year continuation program, are now described.

1. A 20-cell stack was constructed, by using improved EVD process procedures and providing air permeability to the air electrode/IC interface, that demonstrated 13 watts of power. This test met the power objective of the program (10 watts required) -- Milestone ▽1.

2. Thirteen cells of Stack #8 operated at 400 mA/cm^2 for 1000 hours at 1000°C, with H_2-3% H_2O inlet fuel, air as the oxidant source, and delivered 0.71 $\overline{V}$/cell, exceeding the requirement of 0.66 $\overline{V}$ start, 0.60 $\overline{V}$ end of a 1000 h test for a single cell (Milestone ▽2) and a stack of, at least, 3 series connected cells (Milestone ▽3).

3. A second 20-cell stack (Stack #9) was fabricated and delivered 10 watts of power, meeting the minimum power requirement in a stack constructed to show reproducibility of power capability. Since 10 such stacks were to be built in the program, Milestone ▽4 was only partially achieved.

Additional stacks are presently being constructed which will be tested for performance and life capability, under a variety of test conditions, so that, in a follow-on program, confidence in reproducibility of stacks will increase.

THIS PAGE

WAS INTENTIONALLY

LEFT BLANK

3.0 INTRODUCTION

This report constitutes the Final Report, under DOE Continuation Contract No. DE-AC-0379ET11305. Presenting progress on work from April 1, 1978 through March 31, 1980, this report actually summarizes the level of technology attained on the HTSOE fuel cell, during the past 2 years of the present program for DOE, which has been conducted for the past 4 years.*

* Task 5, the Nature and Worth of an Industrial Cogeneration Application using the HTSOE Fuel Cell Generator, will be reported, as required by the contract, upon completion, on September 30, 1980.

THIS PAGE

WAS INTENTIONALLY

LEFT BLANK

4.0 THE PRESENT PROGRAM

The present two-year research program (DOE Continuation Contract DE-AC-0379ET11305, formerly DOE EY-76-C-03-1197), relating to the development of the high-temperature solid oxide electrolyte (HTSOE) fuel cell, has built upon the findings of the first two-year contract effort at Westinghouse.[1] Its purpose was to demonstrate extended performance and life stability of thin film, HTSOE fuel cell stacks. The fuel cell stack, a multiplicity of series-connected cells, constitutes the basic building block of this fuel cell system. These stacks have been constructed, using the component materials and their fabrication processes, developed in the past program, and those materials and processes that were further optimized during the first year of this program. Extended life has been demonstrated in single cells and small cell stacks, under some conditions anticipated in the operation of stacks in a total fuel cell system. A stack has been tested to determine power output capability and the effect of fuel/air conditions on performance. Also, the reproducibility of stacks, with respect to cell-to-cell and overall performance, has been demonstrated, in another 20-cell stack constructed and evaluated for that purpose.

Under the original continuation program, four milestones were to have been attained. For Milestone ∇ all the five fuel cell components -- porous support tube, fuel electrode, solid electrolyte, air electrode and the interconnection -- were to be specified and the fabrication sequencing and fabrication techniques were to have been established in a "bench mark" stack, delivering 10W of power. To attain

Milestone (2) at least a single cell, including an interconnection, was to have demonstrated a minimum of 1000 hours of life at 1000 C, under the following conditions:

- current density of 400 mA/cm^2
- voltage stability - no more than 10 percent degradation from an initial operating cell voltage of 0.66V, minimum, in H_2 +3% H_2O inlet fuel mixture.

Attainment of Milestone (2) was to show that the thin film, high-temperature fuel cell concept and design is viable and should show promise of further life improvement toward that required for applications as cited in Appendix B. Achieving Milestone (3) required that a small fuel cell stack, having at least 3 series-connected cells, demonstrate a minimum of 1000 hours of operation, under the same conditions as for Milestone (2). Milestone (4) required that additional stacks (10 was the original goal) be fabricated and tested, for a short time, to demonstrate reproducibility in materials fabrication and uniformity in cell and stack performance. The same test conditions, as described for the other milestones, were to be used to operate the 10W stacks.

In September 1979, two additional milestones were established for the program. Milestone (5) relates to a Design, Cost and Benefit Analysis of the HTSOE fuel cell in an industrial co-generation application. Milestone (6) is aimed at evaluating the effect of impurities in the fuel gas on the HTSOE fuel cell performance and life, as well as setting minimum tolerance levels for these impurities.

Therefore, the present program evaluated the components and verified the fabrication techniques developed to produce them. It established the ability of these components to operate properly in contact with each other in the thin film design under simulated service conditions. Also it determined the long-time stability characteristics both of the components and their interfaces and of a cell and cell stacks,

under simulated service conditions. Sufficient cell stacks were fabricated to verify their reproducibility, performance and life. With these objectives attained, the basic building block of the HTSOE fuel cell generator has been firmly established.

The study (Task 5) is still continuing (until the 9/30/80 target date for completion). It will identify an appropriate industrial cogeneration application and determine its potential economic value. Finally the effects of impurities, particularly, sulfur-bearing species, are being determined, as well as tolerance levels of these species. This impurity study (Task 6) will be completed by 6/30/80, the targeted date on the program.

Upon achievement of all 6 of the milestones of this program, by 9/30/80, the high-temperature, solid oxide fuel cell development program will have been advanced to the stage of generator system component design, stack bundle assembly and evaluation.

THIS PAGE

WAS INTENTIONALLY

LEFT BLANK

5.0 OVERALL TECHNICAL EFFORT

The overall technical effort, originally, was aimed at achieving four milestones in the two-year period of the contract. These included:

(1) Specifying all five fuel cell components, their fabrication sequencing and their fabrication techniques in a "bench mark" stack, delivering 10 watts of power;

(2) Demonstrating, at least in a single cell with an interconnection, a minimum of 1000 hours of life at 1000°C, under the conditions of 400 mA/cm^2, with no more than 10 percent voltage degradation from initial loaded voltage, using H_2/3% H_2O inlet fuel mixture;

(3) Demonstrating (2) in a fuel cell stack of at least 3 series connected cells;

(4) Fabricating and testing, for a sufficient time, 10 stacks to demonstrate reproducibility in materials fabrication and uniformity in cell and stack performance.

In September 1979, two additional milestones were added.

(5) Designing, costing and determining the economical and environmental worth of an HTSOE fuel cell system in an industrial co-generation application;

(6) Determining the effect(s) of fuel gas impurities to the operation of the HTSOE fuel cell system and establishing their safe tolerance levels.

5.1 TASK 1. DEVELOPMENT AND REFINEMENT OF FABRICATION PROCESSES

Work in this task includes:

1) fabrication of the cell interconnection by the electrochemical vapor deposition (EVD) process
2) definition of the fuel electrode stack process

3) definition of the air electrode stack process
4) porous support tube refinement
5) cell stack preparation.

5.1.1 Subtask A. Interconnection (IC) Fabrication

Work in this area dealt with improving the EVD reactor components to insure better halide delivery, thereby more uniform EVD film growth over the entire substrate.

Both electrolyte (yttria-stabilized zirconia) and interconnection (modified lanthanum chromite) materials are deposited as thin layers by EVD. Work in this area has dealt with the improvement of the existing EVD apparatus and with the investigation of deposition conditions for producing films of modified lanthanum chromite on stack tubes, carrying a minimum of twenty cells.

Modifications made to the vapor deposition apparatus have improved reliability and reproducibility in the deposited films. First, to allow accurate measurement of oxygen activity in the H_2/H_2O mixture that passes through the inside of the cell stack tube during the deposition process, an oxygen gauge was added. Hydrogen and oxygen are mixed at reduced pressure ($\sim$ 10 mm Hg) in the cold zone. Then this mixture is passed through an alumina wool plug, that is positioned inside a quartz tube, and heated to 800°C. The resulting H_2/H_2O mixture flows over a closed-end zirconia tube, serving as an oxygen sensor, and finally enters the EVD reactor. The oxygen sensor measures the oxygen activity and activates safety valves, when the oxygen activity increases over a set point (excess oxygen). This feature introduces increased reliability to the deposition process and eliminates the possibility of nickel electrode oxidation,* due to improper flow meter adjustment or line pressure fluctuations.

In addition, an all new gas valving system was installed on the EVD apparatus that reduces the possibility of leaks and increases

*Fuel electrode oxidation had been experienced on several occasions in past EVD runs, before the use of the oxygen gage.

reproducibility in deposited films. The new system, made entirely of glass and teflon tubing, minimizes the chances of leaks associated with corrosion, as can occur when standard fittings are used. The majority of connections are now ground glass joints. All carrier gases and non-corrosive gases have been "hard" plumbed and pressure tested for leaks.

A fail-safe system has also been installed on the vacuum system to protect stacks during the slow cool down period following the deposition experiments. The equipment is left unattended for extended periods, usually overnight, and, should there be a power failure, loss of the stack in process and damage to the vacuum pump would result. Solenoid valves have been installed that automatically close and prevent accumulation of explosive gas mixtures. Also, a latching relay circuit keeps the vacuum pump from restarting when power is restored. Should pump failure occur, the pump, as well as the reactor, are back filled with nitrogen and kept under a slight positive pressure to prevent diffusion of oxygen.

The halide delivery cartridges have evolved into a design that eliminates problems of previous designs and provides flexibility in the development of improved IC deposits. Prior cartridges were constructed from a solid block of high purity graphite. Holes were bored in the block for receiving the halide source. Thin wall sections between each chamber allowed cross contamination from one component to the next, due to graphite porosity, resulting in deposits whose composition could not be controlled effectively. This "solid block" cartridge also introduced a large heat sink into the hot zone of the furnace and produced undesirable temperature gradients.

To overcome these problems, single chambered cartridges were developed that hold only one halide source. These individual chambers can be bundled together in groups of 3 or 4, depending on the composition or type of deposit required. Figure 5.1 shows an individual chamber and a bundle of three. This design eliminates cross contamination, reduces the amount of unnecessary graphite in the hot zone, and provides flexibility in experimental design.

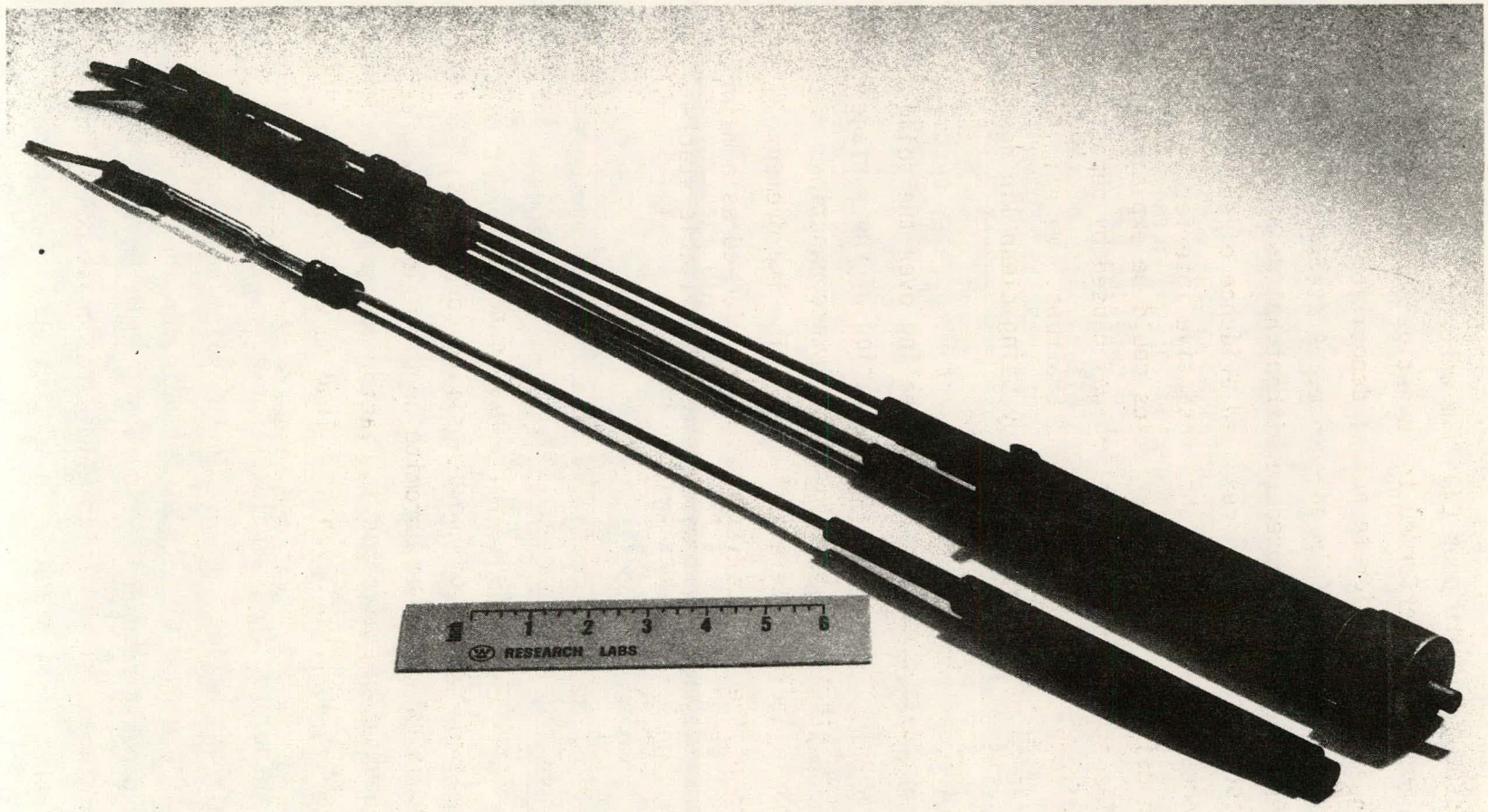

Fig. 5.1. Halide cartridge design for fabrication of interconnection material.

A problem associated with poor EVD film adherence caused concern and a number of experiments were performed to investigate possible causes. Contamination of stack surfaces, prior to actual deposition, was suspected and proved to be a deterent to good film adherence. A stack tube was exposed to the mounting and heat up procedure without halide introduction. After cool down, microscopic examination revealed evidence of surface contamination. Adherence problems and highly resistive interfacial layers that lead to undesirable IC characteristics could be explained by this contamination. The source of contamination was caused by deposits on reactor walls from the large number of preceding EVD runs. We eliminated predeposition contamination of substrate tubes by using clean linings for each deposition.

Improvement of IC-layer adherence and sealing over the solid electrolyte layers has been achieved by the elimination of the surface contamination. Also, the electrical properties of interconnection layers now approach that of bulk sintered material. The improvement of both characteristics of the IC deposits must be considered as a major break-through in the present program, toward achieving reliable stack-performance for 10 watt stacks.

Conclusions

Work in this area dealt with improvements in the EVD equipment and with the investigation of the deposition conditions, necessary to produce modified lanthanum chromite on 0.3 m long stack tubes. Improved instrumentation, advances in reactor design, and elimination of predeposition contamination have lead to well-adhering deposits with electrical properties that are adequate for successful stack operation.

5.1.2 Subtask B. Fuel Electrode Stack Process

Work in this area has involved extension and improvement of the fuel electrode technique, as applied to making stacks of series-connected fuel cells.

5.1.2.1 Fuel Electrode Sintering

Work in this area has resulted both in the extension and improvement of the fuel electrode fabrication technique to 20, and more, series-connected fuel cell stacks. These procedures have, essentially, been fixed, to consistently produce flawless Ni-ZrO_2 cermet fuel electrode structures.

The standard technique, by which the fuel electrodes are prepared, involves dipping of the porous support tube into a nickel oxide/zirconia slurry, then drying and sintering this coating in an oxygen-containing atmosphere and, finally, reducing the nickel oxide to nickel, which, with the zirconia, forms the final cermet structure.

As previously mentioned, fuel electrodes are prepared by dipping the porous support tube into a NiO-ZrO_2 slurry. During the dipping process the tube ends are closed to prevent coating of the inside tube wall. It has been found impractical to use this technique for tubes much longer than 0.2 m. During dipping, slurry liquid will penetrate through the porous tube wall and flow to the inside tube bottom. After removal of the tube from the slurry, this inside liquid washes the coated film from the outside. The longer the tubes, the higher will be the hydrostatic pressure during tube dipping, causing an exaggeration of this problem, and resulting in non-uniform coatings over longer tubes. Fuel electrode performance, therefore, would vary over the stack length because of this non-uniformity.

Dipping, however, is a fast coating method and results in obtaining fuel electrodes of superior smoothness and strength. Therefore, other methods have been rejected to coat long tubes. The search for new dipping methods resulted in the construction of a new holder for

porous tubes that is shown in Figure 5.2. An inflatable rubber sleeve (1) is held in position by a stainless tube (2) which has holes to allow the inflation of the rubber sleeve via a valve (3). This deflated assembly is introduced into the porous support tube (4) and the rubber sleeve is inflated, thereby allowing safe handling of tubes of any length. During dipping, liquid cannot accumulate on the inside of the tube and excellent and uniform coverage of long tubes with fuel electrode slurry is achieved. The coated tube is easily removed from the holder by pressure release and collapsing of the inflated rubber sleeve. This method of handling appears to be ideal for moving a large number of tubes from processing step to processing step, without danger of tube cracking.

The achievement of virtually-flawless surface conditions of the electrode has been accomplished through two preconditioning steps of the tube prior to slurry dipping. First, the tube surface is rubbed with the dipping slurry to fill any large defects and, secondly, through a precoating vacuum impregnation with the slurry carrier liquid. This eliminates trapped gases in the porous support tube and prevents the formation of holes in the electrode, due to gas bubble escape, after slurry coating.

A change also has been made in the reduction scheme of the sintered NiO/ZrO_2 layer to the Ni/ZrO_2 cermet electrode. Previously, this reduction took place with dry hydrogen/nitrogen mixtures. This caused porous support tubes to darken near the cermet electrode, a positive indication of oxygen deficiency of the stabilized tube material. Now, the nickel oxide reduction is accomplished by adding 30% water vapor to the N_2/H_2 mixtures. The same results can be obtained through the addition of CO_2, instead of water vapor. Porous support tubes do not darken under such conditions and the improved reduction scheme is partially responsible for a drastic reduction in the incidence rate of support tube fracture, during early stages of stack fabrication.

Dwg. 7684A31

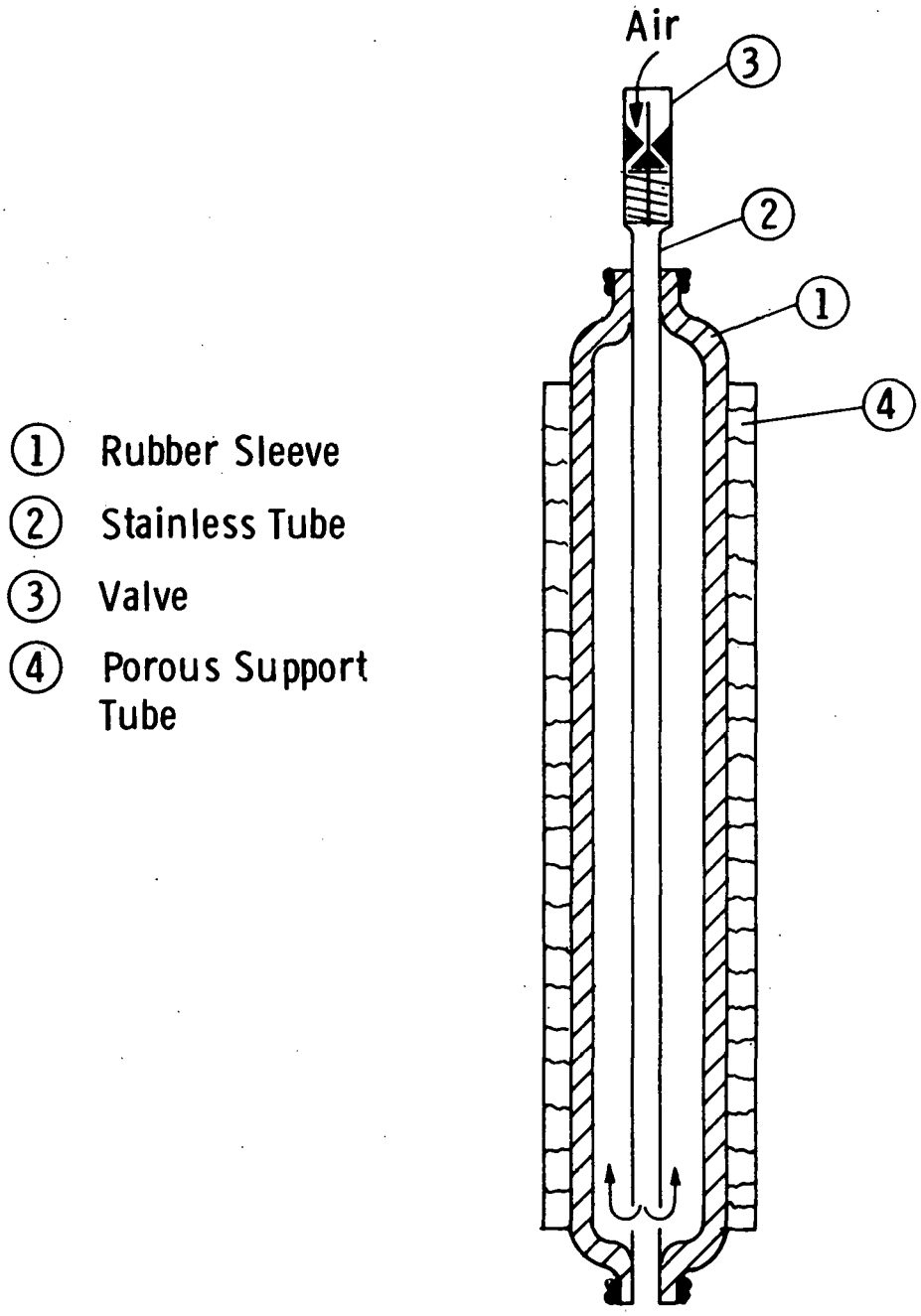

① Rubber Sleeve

② Stainless Tube

③ Valve

④ Porous Support Tube

Fig. 5. 2 — Holder for applying slurry coatings to porous tube surfaces

Conclusions

Long nickel-zirconia cermet electrodes can now be fabricated on 0.3 m long tube segments (or longer). The resulting electrodes consistently have high quality surfaces characteristics, uniform thickness and ceramic skeletons with good mechanical strength. Fuel electrode resistance values of below 0.1 Ω (ρ/δ) at room temperature, over 0.3 m long tube segments, have regularly been achieved. A new sintering procedure prevents darkening (reduction) of the porous support tube and reduces the incidence rate of tube cracking, during early stages of stack fabrication.

5.1.3 Subtask C. Air Electrode-Stack Process

Work in this area involved scale-up of the formulation and processes for fabrication of 20-cell stacks.

5.1.3.1 Indium Oxide Current Collector

Past work on the air electrode involved extension and improvement of the fabrication technique, as described in the final report of the past contract, to a stack of 20 series-connected fuel cells. Figure 5.3 shows the CVD reactor for applying the doped indium oxide current collector. This new reactor has a 40 cm long deposition zone, compared to only 25 cm in the previous reactor. It was not possible to obtain electrically uniform coatings at the ends of 25-cell stacks in the old reactor, due to reactant dilution effects at the end zones of the cross-flow reactor. However, the deposition conditions and basic constructional reactor characteristics have not been changed for the new reactor design.

Figure 5.4 shows the initial phase of contact deterioration of the In_2O_3 interconnection interface. The lighter colored, spotty areas in the IC region represent the optical effect of layer separation (electrical contact loss). Several methods have been investigated to alleviate this problem:

1) increasing collector porosity during CVD
2) applying microporous layers between the In_2O_3 CVD layer and the IC
3) plasma spraying In_2O_3 porous layers.

With regard to approach 1), the seeding of In_2O_3 grains onto the stack tube, before the CVD process, leads to nucleation centers for oxide growth during the deposition and creates porosity. The contact area of the large CVD crystals (~10 to 20 μm size) to the IC, however, is still too large and even these layers will flake and lose electrical contact.

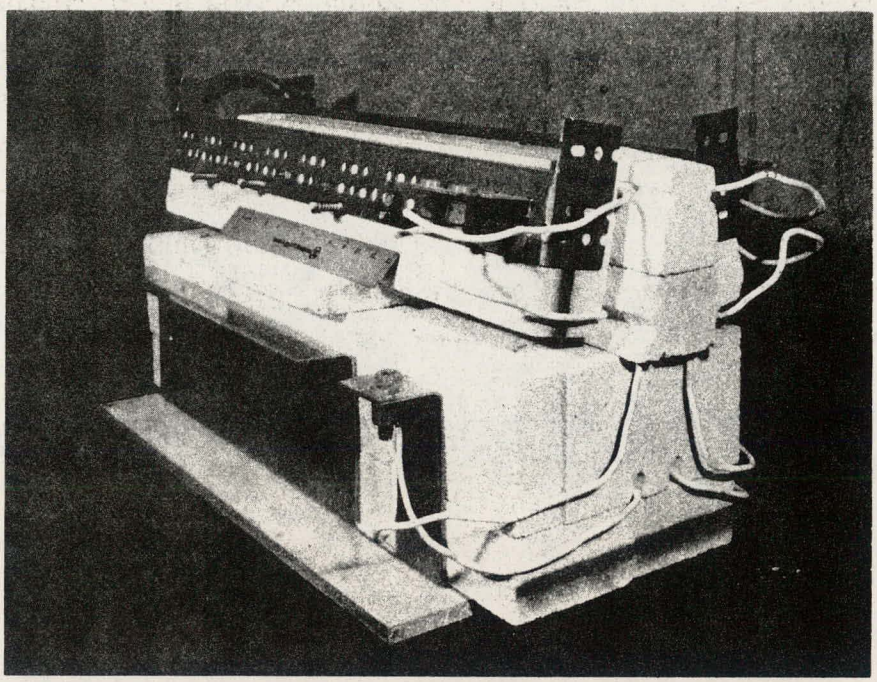

Fig. 5.3. New cross-flow CVD reactor for In_2O_3 current collector deposition.

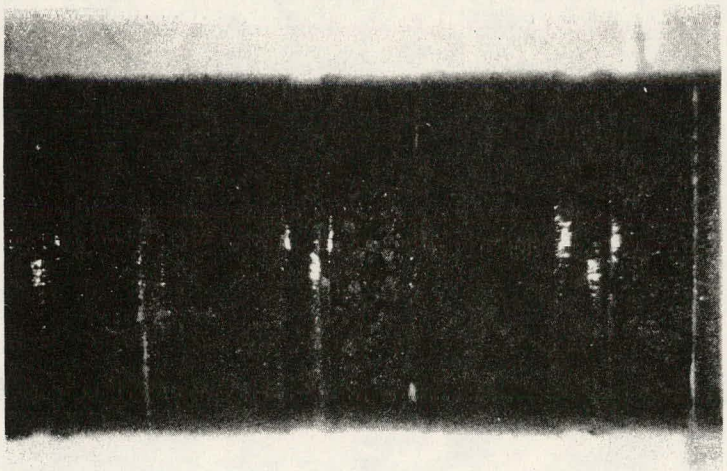

Fig. 5.4. Initial phase of contact loss of In_2O_3 to lanthanum chromite in the IC area.

Regarding approach 2), we applied thin metallic coatings of indium-tin alloy to the surface of the IC (by painting at 200°C). This alloy was oxidized at 1000°C in air. The resulting oxide layer was microporous. However, the lateral resistance of this coating was too high and an In_2O_3 CVD coating had to be applied over it. Due to rapid nucleation, this CVD coating grew as a porous layer over the microporous In_2O_3 film. Some samples had been obtained that showed stable electrical contact. However, severe problems were encountered in achieving uniformly painted metal layers. Variations of metal layer thickness in edge and corner areas led to flaking during the oxidation step. What proved to be possible on a flat-surfaced sample did not appear to be reliable in overlap areas (surface "steps" in the IC region) of stacks. It was concluded from this work, however, that the application of microporous oxide layers between the In_2O_3 collector and the IC could lead to stable mechanical and electrical contacts.

The objective of producing porous interfacial layers between the interconnection and In_2O_3 collector was then handled by structural modification of the interconnection, rather than modification of the In_2O_3 layer. The solution to this problem was found by depositing plasma-sprayed lanthanum chromite, in porous form, onto the EVD layer of the same material. By this technique the electrical contact to the In_2O_3-collector is now stable, because oxygen can diffuse through the porous interconnection layer to the critical interface, which eliminates the danger of flaking entirely.

With regard to approach 3), we experimented with plasma-spraying of In_2O_3 collectors, as a possible method for producing porous interfaces. However, this task was mainly directed to finding a possible replacement technique for CVD. Since plasma-spraying of other stack components was considered, it was logical to use this technique also for the air electrode. Plasma-spraying was done on preheated stack tubes, to minimize the danger of stack component fracture by thermal shocking. The preheat arrangement is shown in Figure 5.5. Indium oxide current collector layers on zirconia tubes have been produced in this fashion, yet no stack

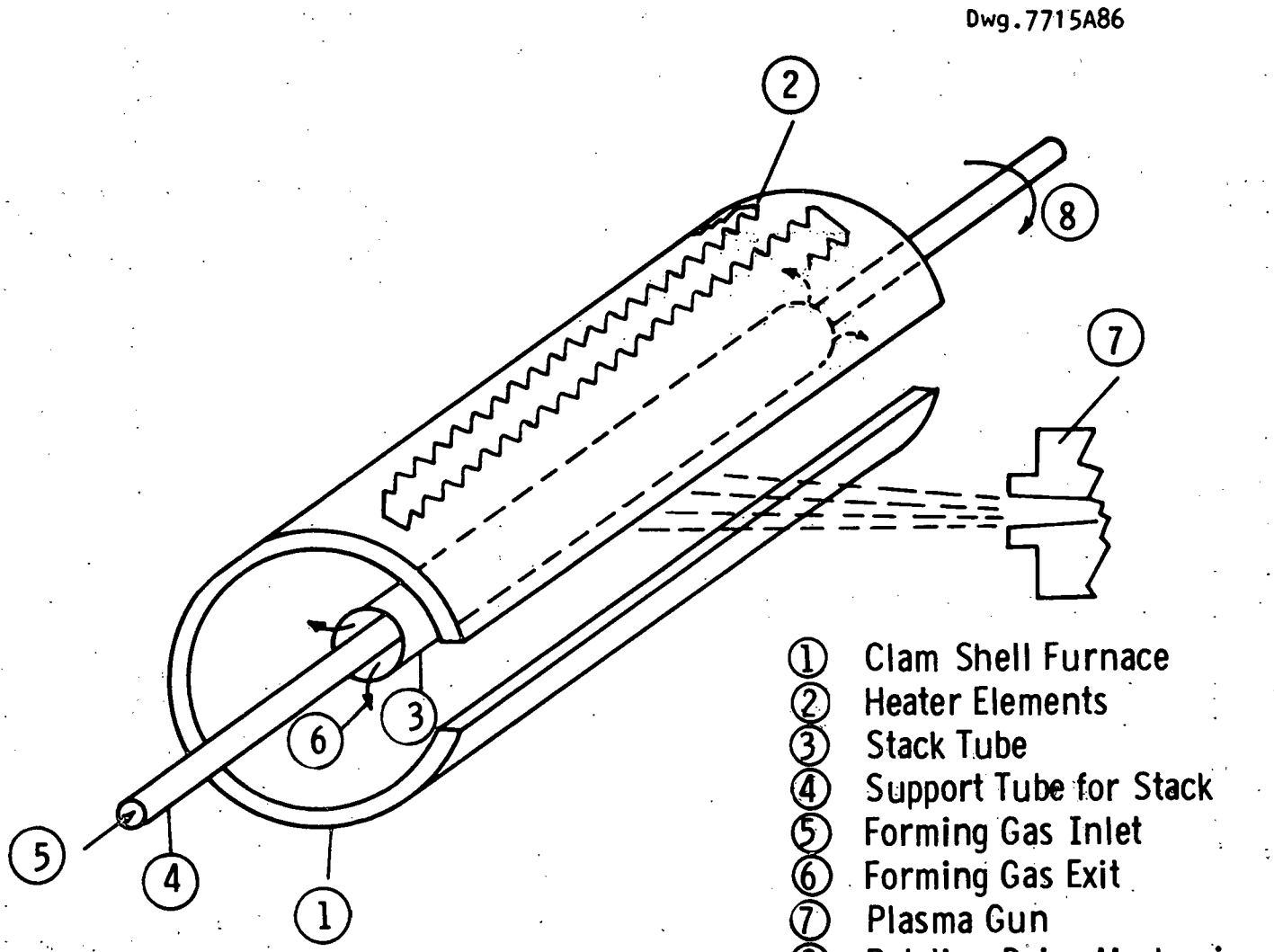

Fig. 5.5 – Preheat furnace for plasma spraying of stack components

has been tested with such collectors because they lacked sufficient collector conductance. This, however, is a question of layer thickness and plasma-sprayed collectors will be tested in the future.

5.1.3.2 Lanthanum Manganite Air Electrode Current Collector

As described in Section 5.1.3.1, we investigated methods of controlling indium oxide flaking from the interconnection material. Methods of increasing the porosity of indium oxide air electrode current collector did not result in improvements of electrical contact stability (see Section 5.1.3.1). This led us, alternatively, to the investigation of other oxides, that could be used as intermediate layers between the air electrode collector and the IC. The major problem arises when these layers are to be attached to the IC.

The first material that becomes apparent for this porous intermediate layer is the IC material itself, as discussed previously. Another possible material that has been used for air electrodes is strontium-doped, lanthanum manganite. We developed a sintering method that allows the bonding of these oxides to the solid electrolyte and the IC. The sintering is accomplished in a controlled atmosphere with the help of sintering aids. The sintering has to be accomplished below the melting point of nickel (1453°C).

We found in our tests that, by using lanthanum manganite, even as a current collector, and replacing the doped indium oxide altogether, a good stack performance could be obtained, when the current collector was impregnated with praseodymium oxide and/or cobalt-praesodymium oxide. The stack performance, as shown in Section 5.3.5. , was so stable and promising that further investigation of this mixed oxide and other modified manganites as air electrode materials will be tried. This formulation and processing technique could lead to a potentially less complicated and less expensive air electrode. As one can easily see (Section 5.3.6) the sensitivity to chemical reduction attack of such an air electrode is reduced. Furthermore, it is not prone to vaporization at temperature, as in the case of indium suboxide species that can be formed in the presence of fuel leaks.

The application of lanthanum manganite by plasma-spraying was also attempted, but stack performance was inferior, due to the dense structure of the applied layer. Modification of spraying parameters will be attempted in the future to increase the porosity of this potentially-useful air electrode candidate. Meanwhile the In_2O_3 air electrode current collector will continue to be the standard component of the fuel cell stack, since its performance characteristics are unsurpassed by any other oxide.

5.1.4 Subtask D. Porous Support Tube Refinement

Porous support tube work concentrated on improving materials preparation, as well as improving extrusion and sintering steps.

Identification of fabrication techniques for porous support tubes that will withstand the processing sequences of the fuel cell stack was the major goal of this task. Several improvements have been achieved in the quality of the porous support tubes fabricated during this period. The support tubes have smoother surfaces, higher strength and more uniform porosity over longer sections (>0.4 m). Strength of the porous support tubes now exceed 10,000 psi in flexural strength, versus earlier results of 5000-7000 psi.

5.1.4.1 Support Tube Experiments

Support tube fabrication experiments have involved both the evaluation of starting materials, from which calcia-stabilized zirconia was formulated, and the development of processing procedures, to effectively control the physical properties of the extruded support tubes. A special, high-temperature, gas-fired furnace was designed and constructed to fire long tubes (~0.45 m), at temperatures high enough (>1850°C) to sinter the porous support tubes. Special refractory shapes and materials were engineered to support the tubes during the firing process and to assist in the maintenance of the furnace. Figure 5.6 shows the furnace arrangement and Figure 5.7 shows a schematic cross section to indicate the hanging arrangement for tubes.

5.1.4.1.1 Powder Preparation

Calcia-stabilized zirconia $(ZrO_2)_{0.85}(CaO)_{0.15}$ raw material batches were prepared by reacting monoclinic zirconia powder (SC-grade, Magnesium Elektron, Inc.) and calcium carbonate (reagent grade, Fisher Scientific Co.) following an improved process flow diagram of powder preparation for the porous support tube. Batches prepared by this process produced stable, reproducible and contamination-free starting material for the tube extrusion process.

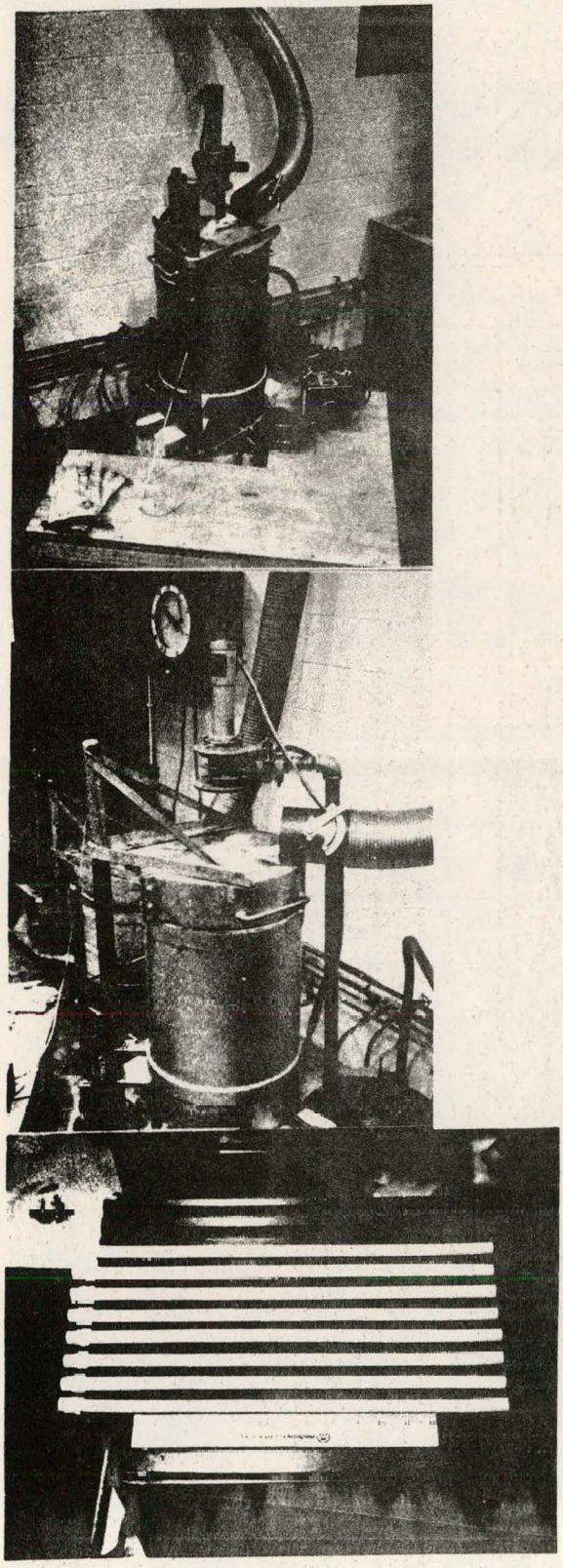

Overall View of the High-Temperature Gas Kiln with New Working Platform

Furnace Operating at 1950°C

Example of Support Tubes after Firing Run

Fig. 5.6. Sintering furnace and sintered support tubes.

Dwg. 2618C92

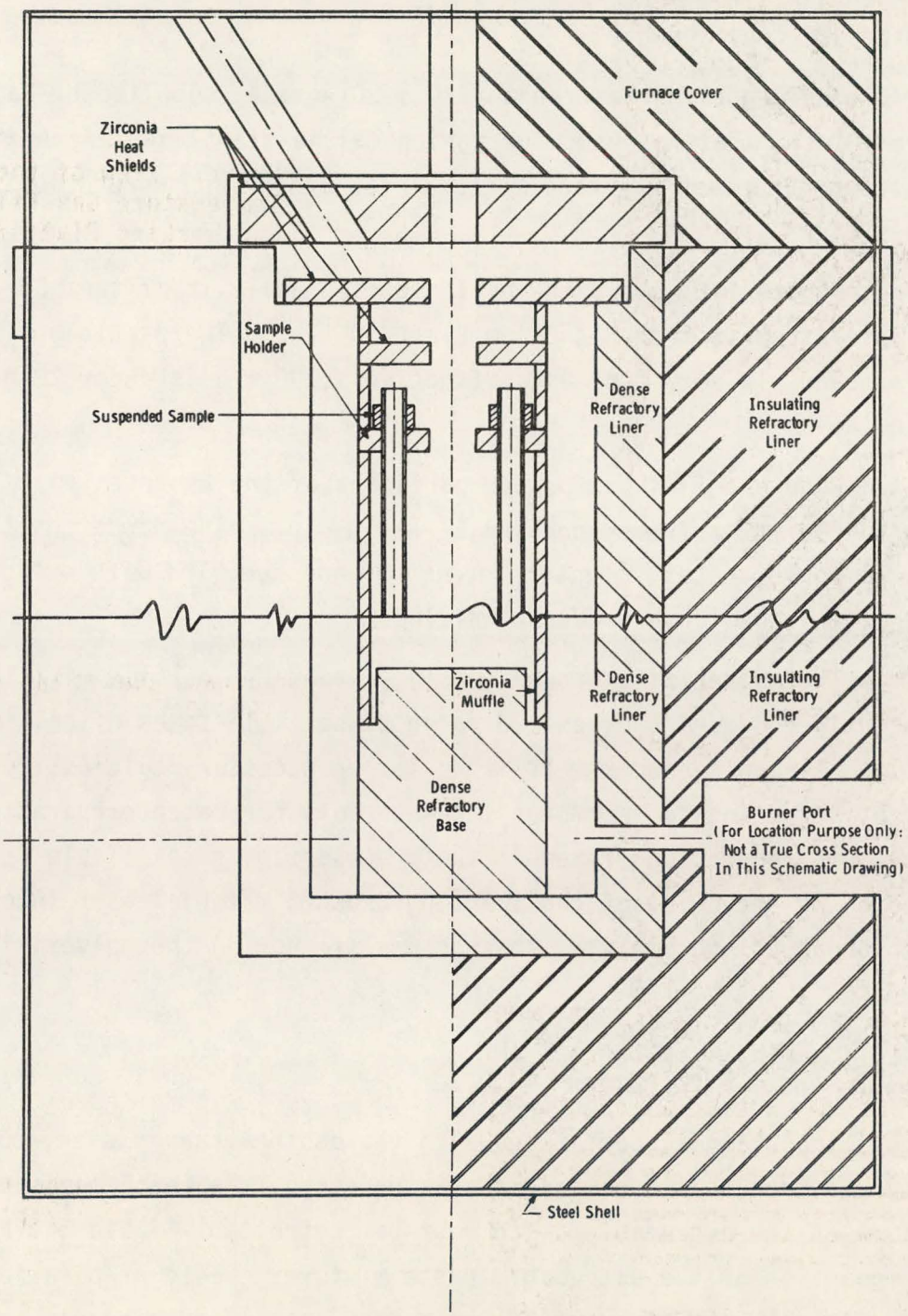

Fig. 5.7 – Schematic of samples during firing in high temperature gas kiln

Table 5.1 shows the improved, porous support tube process flow sheet which eliminated four (4) processing steps, as compared to an earlier process, thus saving time in the preparation of the calcia-stabilized zirconia powder.

The monoclinic zirconia (ZrO_2) SCX-grade, supplied by Magnesium Elektron, Inc., that was used for making calcia-stabilized zirconia tubes, proved to be the best starting material for achieving reproducibility of tubes.

Figure 5.8 shows the particle size analysis of the SCX grade monoclinic zirconia from Magnesium Elektron, Inc. The particle size of this powder is very fine and, effectively, 98 w/o is under 20 micron in size.

Figure 5.9 shows powder particles of the as-received SCX-grade, monoclinic zirconia from Magnesium Elektron, Inc. The powder particles appear as agglomerates, clustered together and speckled with a light dust of the finer sub-micron powder particles.

The pulverizing process, using a tungsten carbide mill, has consistently produced the desired range of particle sizes of calcia-stabilized zirconia powder. It is no longer necessary to classify the powder by screening to recombine the materials for batch preparation. The screening operation listed in the process flow sheet (Table 5.1) only refers to the recycling of the starting crushed material back into the mill to break up agglomerates that accumulate during the pulverizing process.

5.1.4.1.2 Paste Preparation

To obtain support tubes with the desired shape, size, pore structure, strength and surface characteristics, the homogeneous plastic structure of the extrudable paste must be controlled. Table 5.2 shows the composition of the extrudable paste mixture. Paste preparation started with the dry blending of the calcia-stabilized zirconia powder with the starch binder and the water reducing agent in powder form.

Table 5.1

Porous Support Tube Development Process Flow Sheet

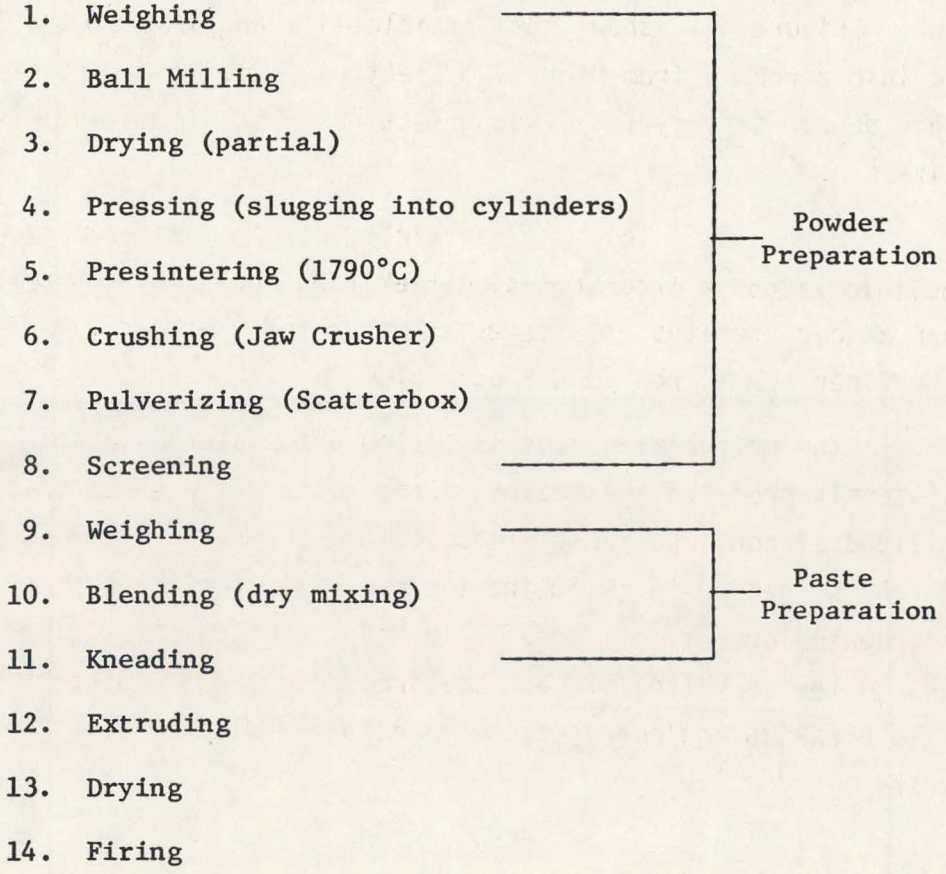

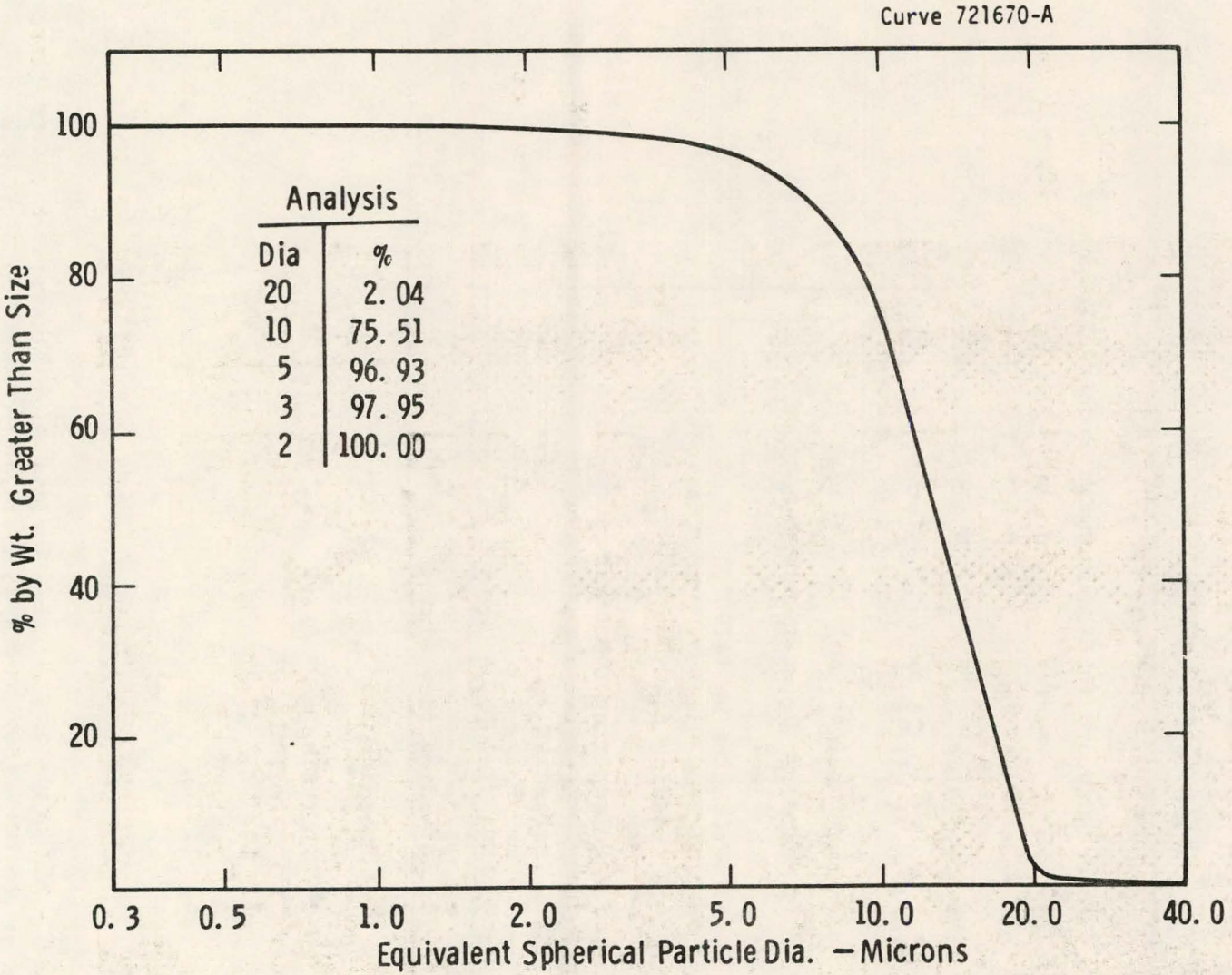

Fig. 5.8 — MSA sedimentation particle size analysis of SCX - oxide (ZrO_2)

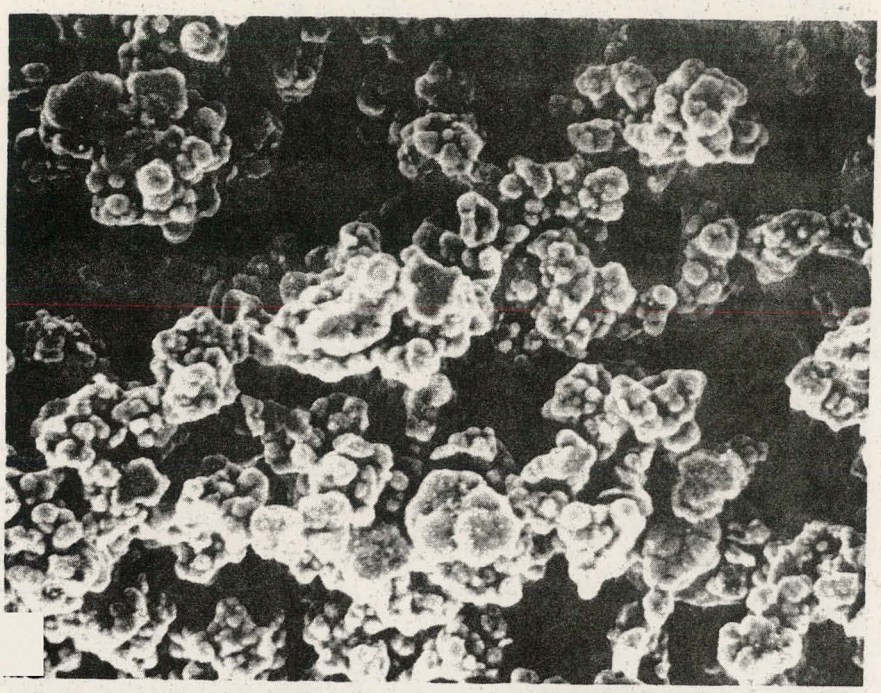

1000X

10μ = 1 cm

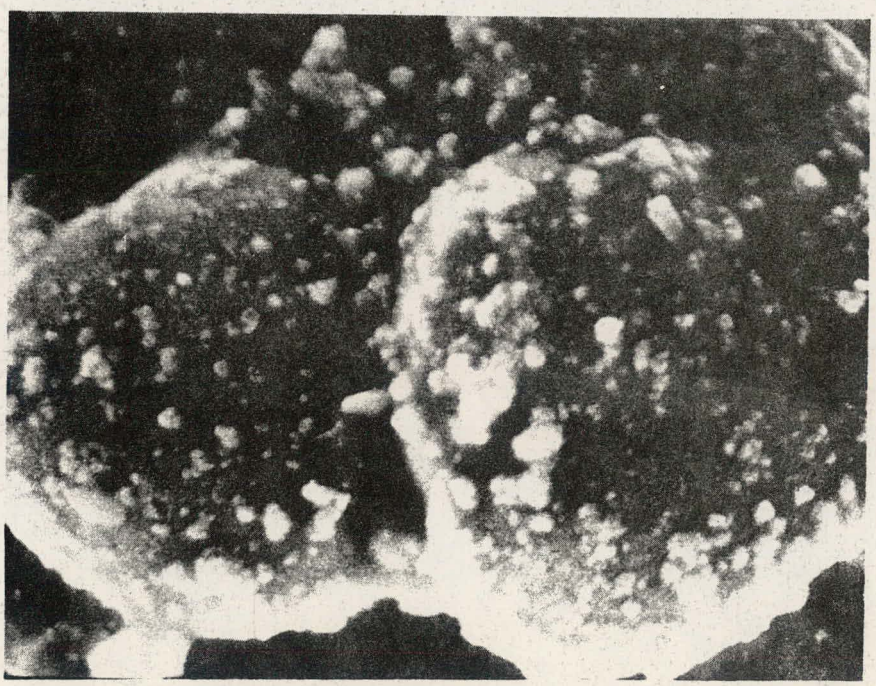

10,000X

1μ = 1 cm

Figure 5.9 - SCX grade monoclinic ZrO_2 powder of Magnesium Elektron, Inc. Primary ZrO_2 powder used in the formulation of calcia stabilized zirconia.

Table 5.2

Composition of the Mixture for Extruding Porous Support Tubes

Materials	Wt %
zirconia powder $(ZrO_2)_{.85}(CaO)_{.15}$	85.4
cellulose	0.8
organic binder:	
corn starch	3.2
PVA	2.0
dispersant:	
Lomar PWA	0.6
water	8.0
	100.0

After the dry blending process, the blended powder and the solution of PVA is mixed in the kneading machine until the material exhibits the proper plastic condition (~20 minutes mixing time).

The extrudable mix is stored in a plastic bag and extruded, as soon as possible, to minimize moisture loss that affects the plastic property of the batch material.

5.1.4.1.3 Firing

Porous support tubes were fired in the propane/oxygen furnace, using various combinations of available muffle sizes and reflective coatings on the furnace liner surfaces. The best combination appears to be a thick wall muffle, made by pressing (1.3 cm thick wall), with a reflective coating on the furnace liner made with zirconia fibers. Muffles, utilizing cast crucibles with thin walls (~0.6 cm thick wall), were serviceable for only one complete firing schedule.

5.1.4.1.4 Results and Discussion

After the development of an extrudable mix, refinement efforts were concentrated on improving the firing process to attain stronger tubes. Strength determinations, by flexure tests, indicated stronger support tubes than the earlier group of fabricated tubes. The flexural strength of the tubes are now in the 10,000 psi range. Tensile strengths of a small sample lot did not show any major increase and these results should not be interpreted as conclusive.

Table 5.3 shows a comparison of the flexural strength and tensile strength data of a twice-fired sample and a current processed tube, labeled as a strong tube. The tensile strength of the two samples are not in agreement, nor in agreement with the level of the flexural strength. It is a well-known fact[2] that values of tensile strength should agree more closely with those of flexural strength and improved tension testing techniques should be developed to achieve reproducible test data.

Table 5.3

Physical Properties of Support Tube Samples
From Firings Nos. 11 and 29

Sample	Apparent Density g/cc	Apparent Porosity (%)	Flexural Strength (psi)	Tensile Strength (psi)
11A*	3.69	20.7	10,200	4480
29F	3.70	23.9	9,520	2450

*Sample 11A was fired twice. The second firing positioned the tube top side down in the furnace.

The flexural strengths of the porous support tubes shown in Table 5.4 are greater than 10,000 psi, mainly due to the use of a new thick wall muffle and support system during firing, since the firing temperature of 1910°C for four hours was well within the average time-temperature schedule established for most of the tube firings. This experimental firing also proved that the collar supports for the hang-firing of the tubes are strong enough to fire tubes as long as four feet. An experiment to fire "weighted" tubes was performed, in anticipation of firing longer tubes that may be required in the future, for improving firing efficiency and economic considerations.

To date only surface and bulk characteristics of the porous support tubes have been observed microscopically and at low magnification. Recent examination of surfaces and fractures of the porous tubes have revealed the texture of grain surface boundaries, where grains have fused together in the polycrystalline matrix. Figure 5.10 shows the texture of the outside surface of a porous support tube with details of the grains bonded together after fusing. A fractured surface of the porous support tube with details of the fused polycrystalline grains is shown in Figure 5.11.

Figures 5.12 and 5.13 compare the fractured surfaces exposed on the samples that were tested for strength by flexing, as well as by tension. Sample 29F, tested in tension, appears to have less fused area or bonds as compared to sample 11A, which was fired twice. This may be one of the reasons for low strength of 29F and the scatter in the test data.

In the flexure test only the extreme outer fibers on one side of the specimen undergoes maximum tensile stress decreasing to zero at the neutral plane. On the other side of this neutral plane the compressive stress balances the tensile stress and provides a non-uniform tensile stress field. Figure 5.14 shows exposed, failed surfaces, subjected to the tensile and compressive stress field, during the flexure test. Surfaces depicting the area of a compressive stress field show loose polycrystalline grains of the support tube wall that were, apparently, crushed during testing.

Table 5.4

Physical Properties of Porous Support Tubes from Firing No. 30

Sample	Apparent Density (g/cc)	Specific Gravity	Apparent Porosity (%)	Flexural Strength (psi)
A*	3.69	4.78	22.8	10,770
B**	3.67	4.64	21.5	11,322

Note: Average of four determinations taken on four specimens from the 0.5 m length of tube.

*Sample weighted to simulate 0.9 m long tube during firing.

**Sample weighted to simulate 1.2 m long tube during firing.

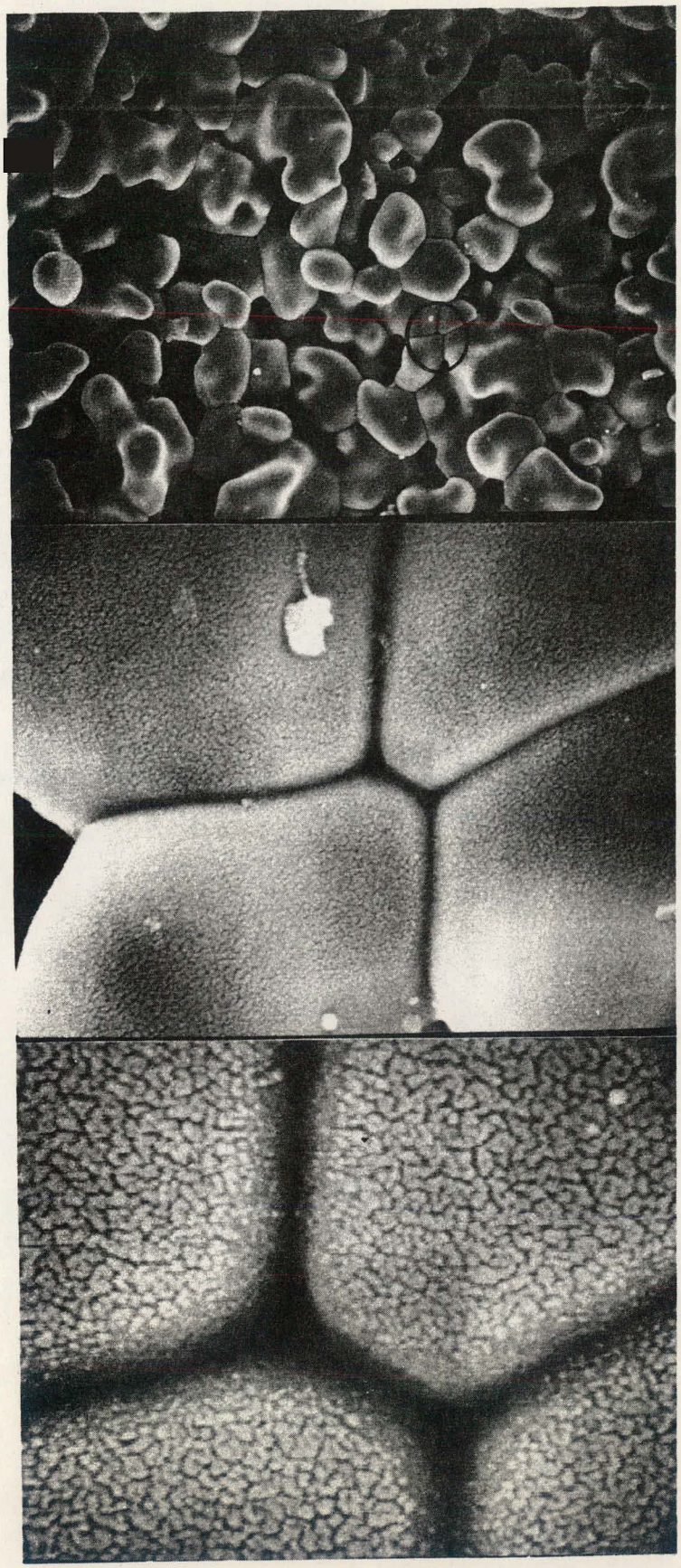

900X

11μ = 1 cm

9000X

1.1μ = 1 cm

27,000X

.375μ = 1 cm

Figure 5.10 - Surface texture of the polycrystalline calcia-stabilized zirconia porous support tube, showing grains bonded together on the outside surface (Sample 27E).

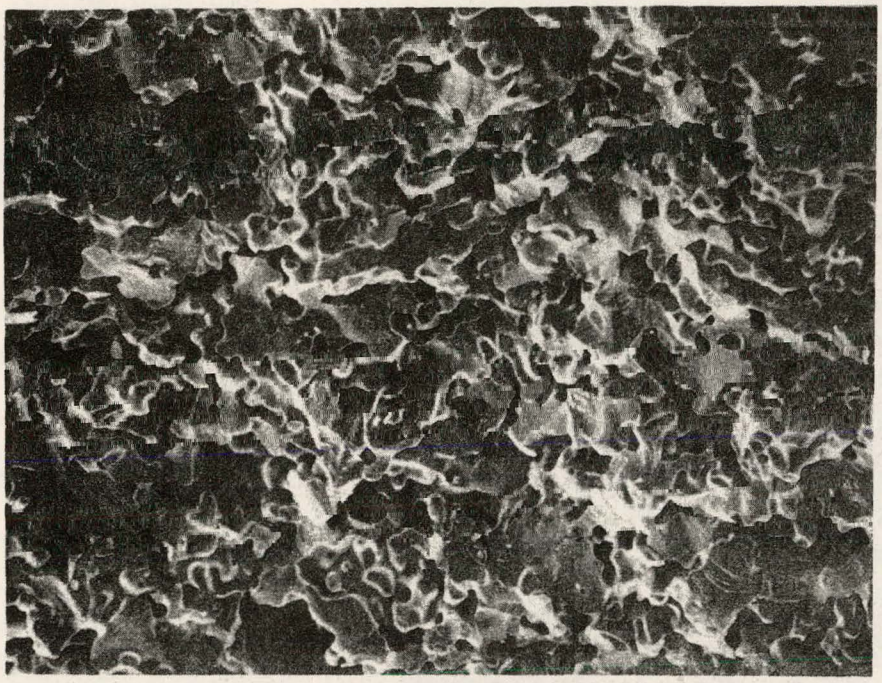

200X

50μ = 1 cm

500X

20μ = 1 cm

Figure 5.11 - Fractured surface of support tube, showing fused polycrystalline grains of calcia-stabilized zirconia (Sample 22B).

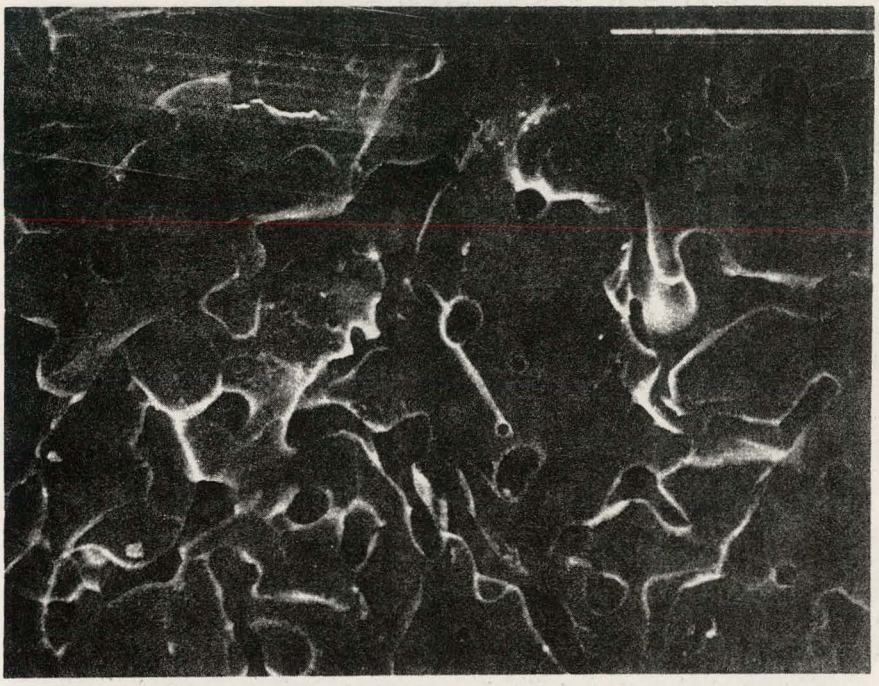

1000X

10μ = 1 cm

Surface exposed in tensile test

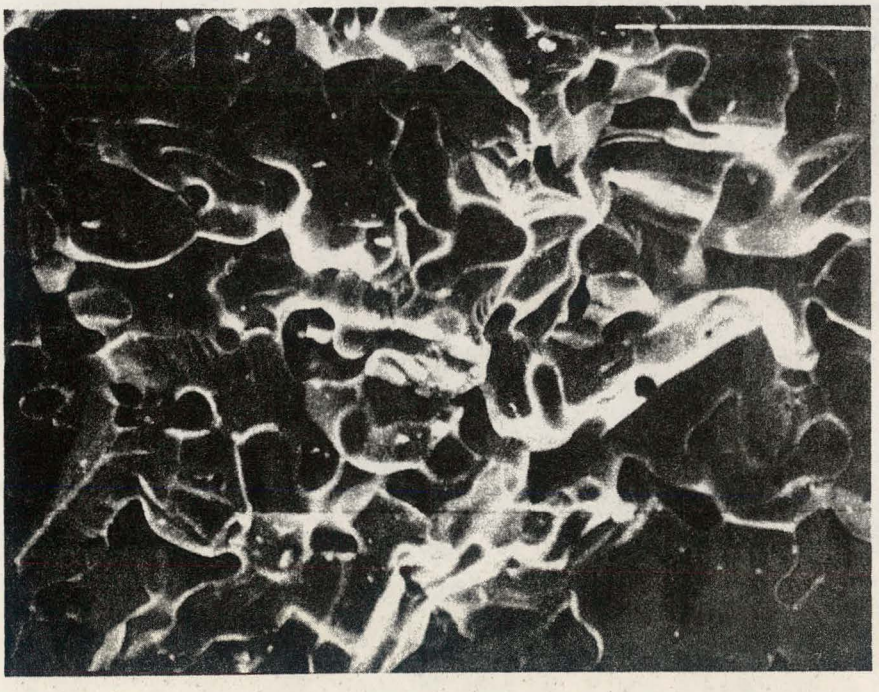

1000X

10μ = 1 cm

Surface exposed in flexure test

Figure 5.12 - Cross sections of sample 11A, tested for tensile and flexural strength. (Surfaces shown are those produced by fracture during test.)

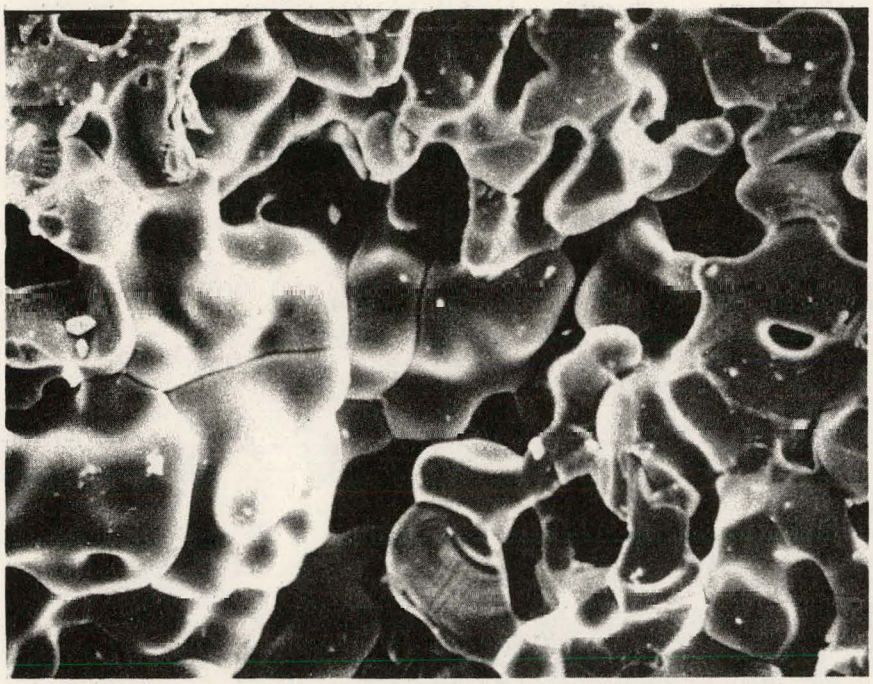

1000X

10μ = 1 cm

Surface exposed in tensile test

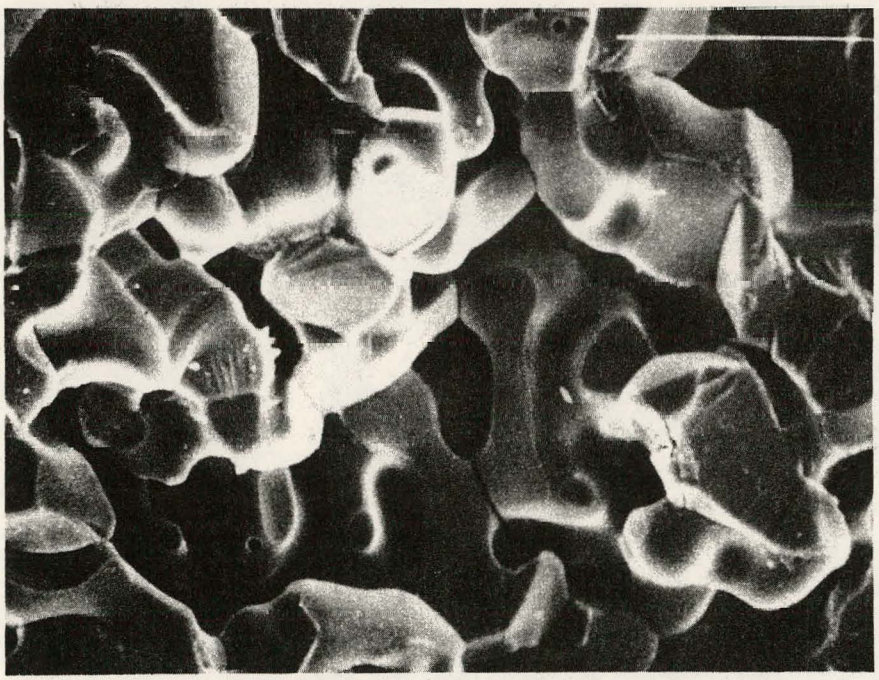

1000X

10μ = 1 cm

Surface exposed in flexure test

Figure 5.13 - Cross sections of sample 29F tested for tensile and flexural strength. (Surfaces shown are those produced by fracture during test.)

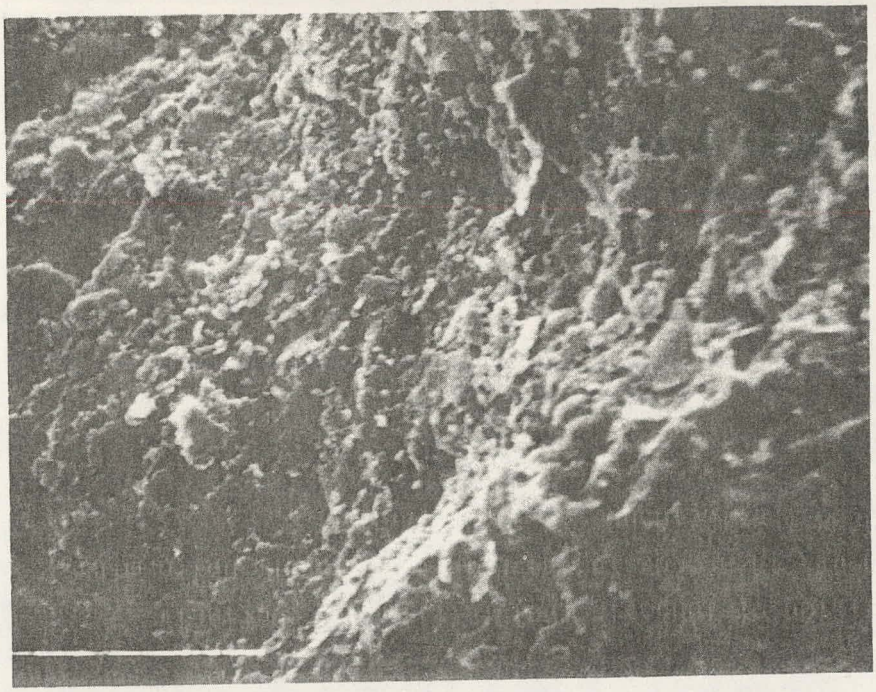

1000X

10μ = 1 cm

Exposed surface of failure in compressive stress field

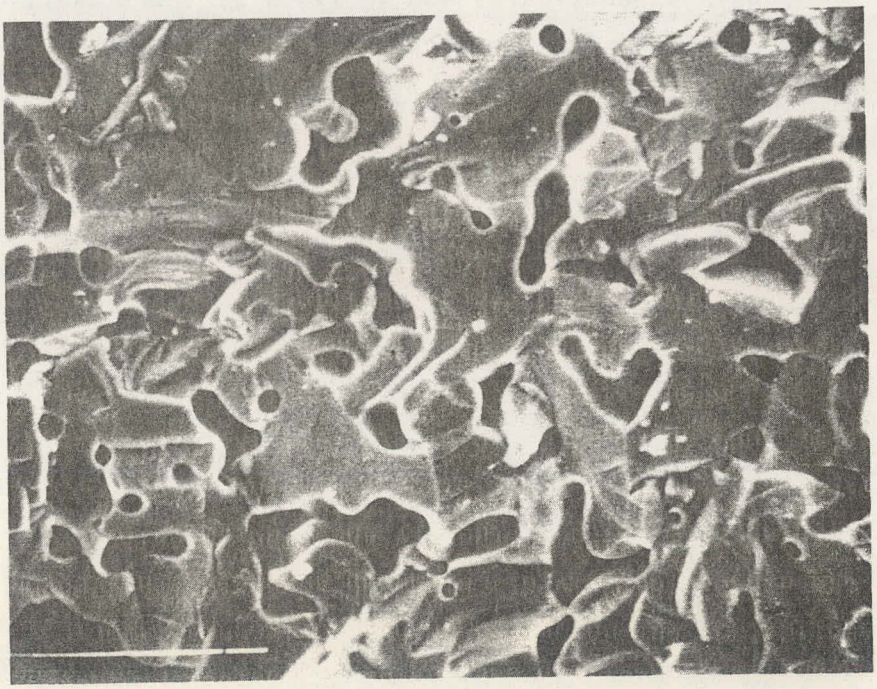

1000X

10μ = 1 cm

Exposed surface of failure in tensile stress field

Figure 5.14 - Cross sections of flexural strength breaks of sample 11A.

Linear regression analyses were run on previously reported data to investigate the correlation of grouped data on the fired properties of the porous support tubes.

Figure 5.15 shows the linear regression analysis of the apparent porosity versus bulk density from the data reported in Table 4 of the Sixth Quarterly Report. This relationship shows good correlation.

Figure 5.16 shows flexural strength versus bulk density of grouped data based on Table 2 of the Seventh Quarterly Report. The regression analysis shows good relationship exists between flexural strength and bulk density.

The relationship of flexural strength and bulk density based on grouped data from Table 4 of the Sixth Quarterly Report as shown in Figure 5.17 did not have as good a correlation as compared to Figure 5.16.

Figure 5.18 shows a linear regression analysis of the flexural strength versus apparent porosity with low correlation. The grouped data from Table 4 of the Sixth Quarterly Report was used for the calculations.

The grouped data, which represent the range of firing conditions, are from samples fired in four different batches.

5.1.4.1.5 Future Work

Future tube fabrication will be improved by a better die assembly mouthpiece, larger die-containment, etc, as well as through the availability of improved furnace installations. Future tube analyses will include improved pore and surface analyses, as well as improved techniques for tensile strength measurements.

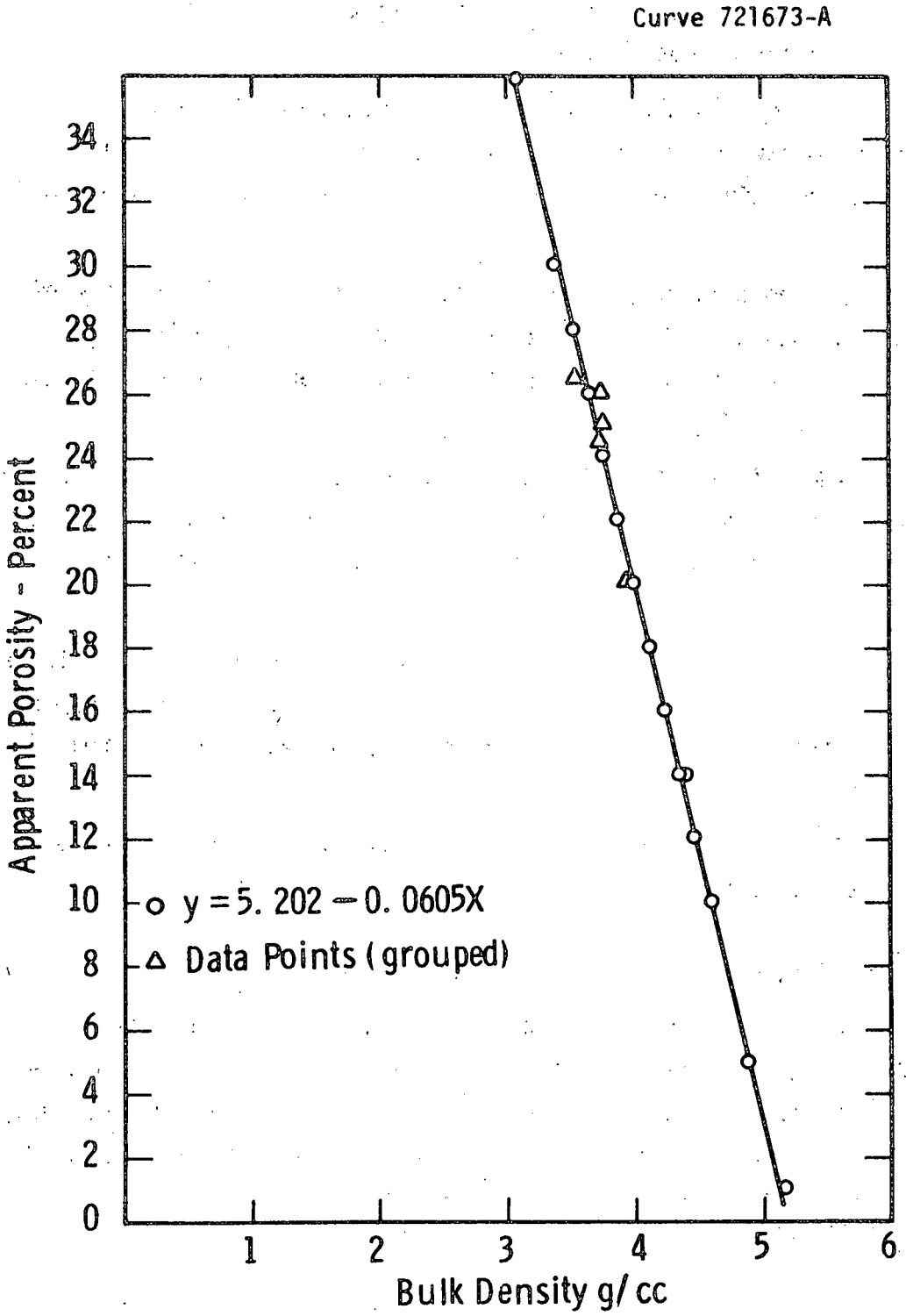

Fig. 5.15 — Apparent porosity vs bulk density of porous support tubes.

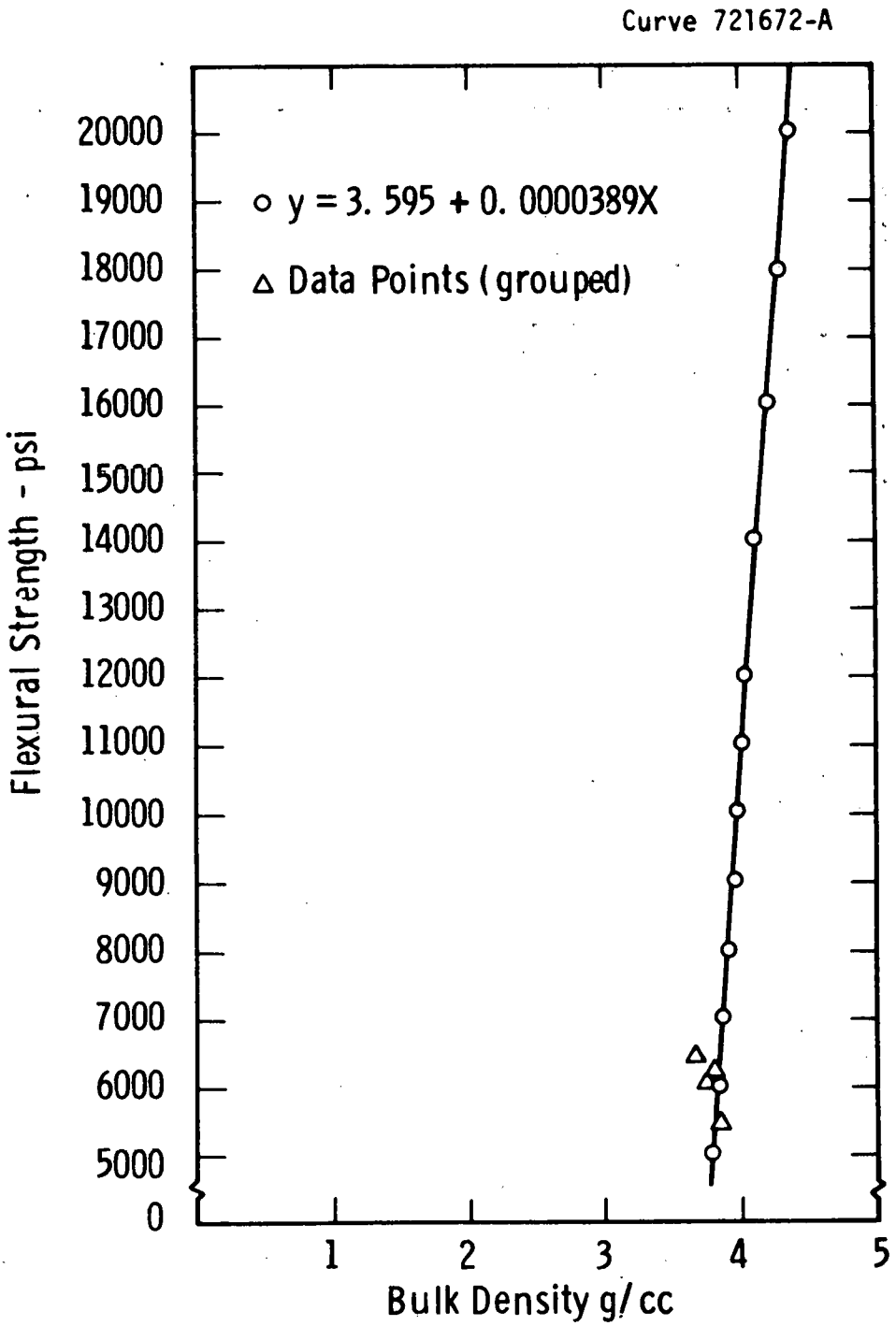

Fig. 5.16 — Flexural strength vs bulk density of porous support tubes

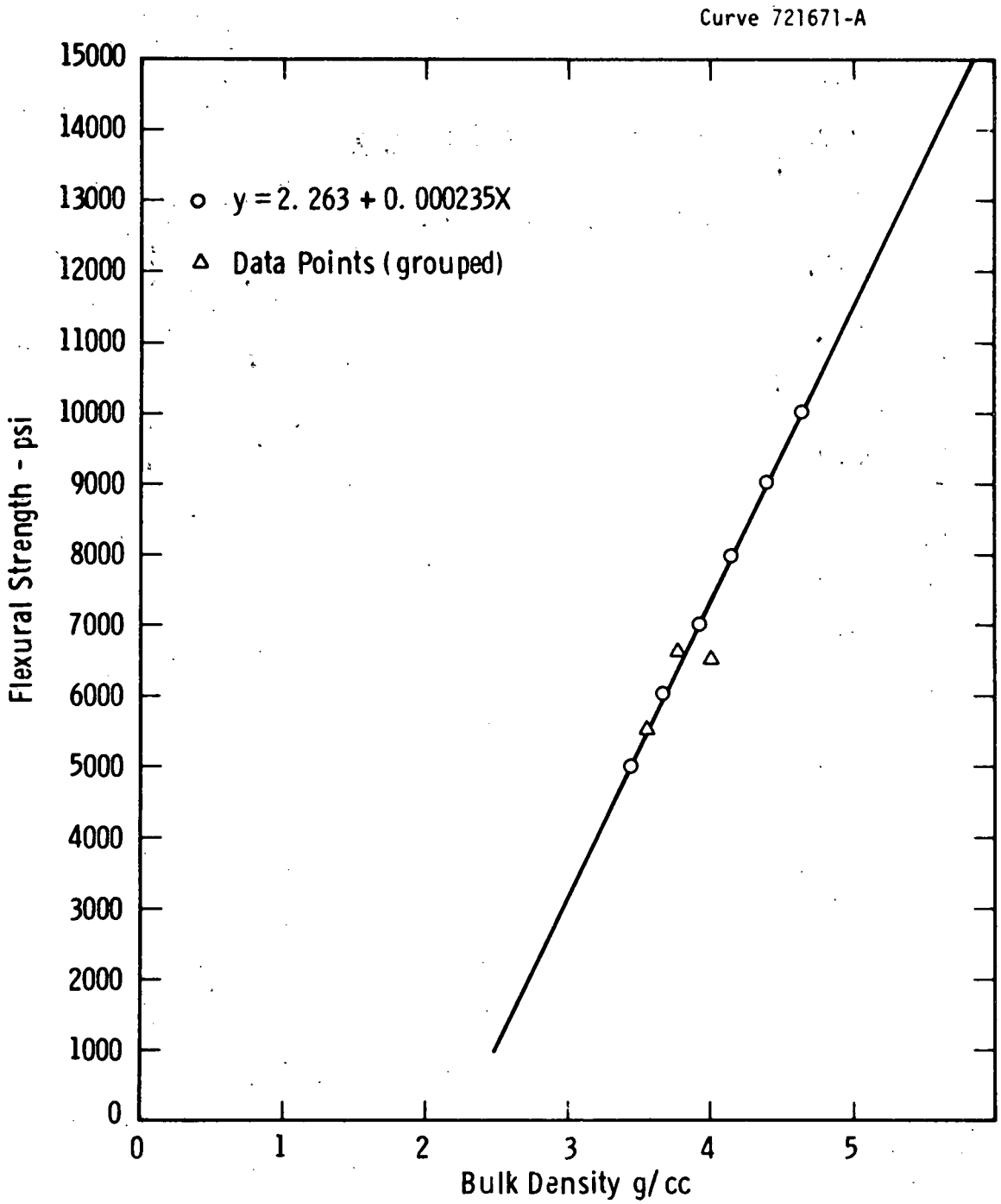

Fig. 5.17 — Flexural strength vs bulk density of porous support tubes.

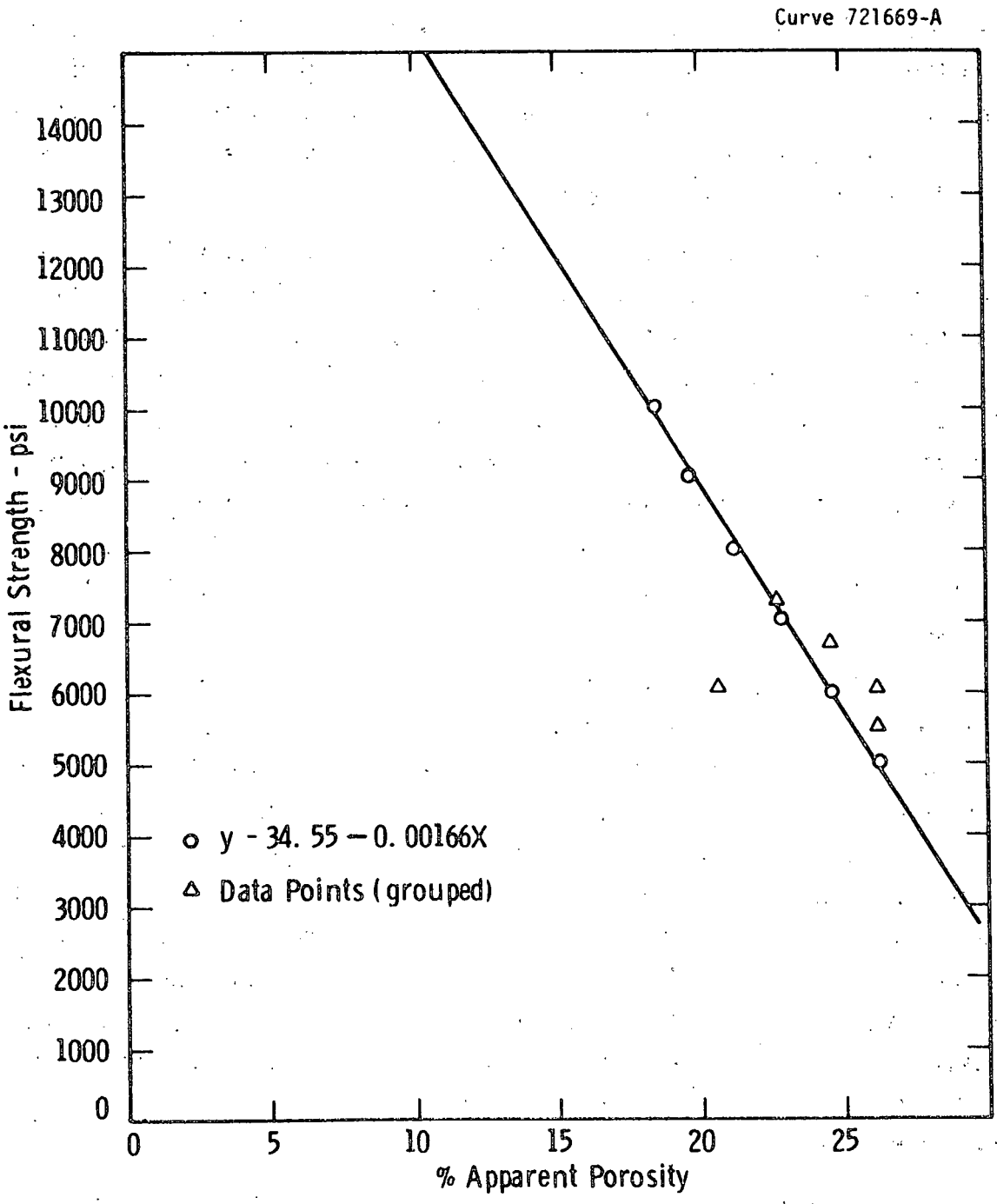

Fig. 5.18— Flexural strength vs apparent porosity of porous support tubes.

5.1.5 Electrolyte Fabrication by EVD

The formation of thin layers of yttria-stabilized zirconia has been achieved with great reliability with many fuel cell stacks and substrates of varying length, up to 0.3 m and longer, using the EVD process. This process has been constantly reevaluated and, concurrently, changes have been made to improve film characteristics and reduce the incidence of support tube cracking.

Previously, we reported that support tube fracturing became apparent during, or subsequent to, the deposition of zirconia electrolyte. Corrosive attack and destabilization of support tube material (calcia leaching) was suspected. Tube fracture was also investigated, as related to fuel electrode fabrication, due to nickel-induced zirconia reduction. We are still not able to clearly attribute tube cracking to a single other cause. Also, we have found that reducing the electrolyte deposition temperature, by as much as 150°C (from 1250 to 1100°C) greatly reduced the severity of tube failure. This again suggests that the EVD conditions are, possibly, too harsh at higher temperatures.

Recently, we developed a stack processing scheme that considers all known aspects that can relate to tube cracking. In this scheme we reduce fuel electrodes after sintering in wet hydrogen (30% H_2O) at 1300°C. This leaves the support tube unreduced. Secondly, we start the electrolyte deposition at a low temperature (1100°C) until pores are closed and no further halide or HCL attack on the support tube is possible. Also, during this initial start-up period, a small amount of calcium chloride is introduced to help prevent calcia leaching (calcium chloride is thermodynamically more stable than CaO which is the stabilizing agent of the zirconia support). Subsequently, after initial film growth, the deposition temperature is raised to 1250°C to increase the growth rate.

Adherence of the electrolyte film has also been improved by preventing any pre-deposition contamination, as discussed in connection with interconnection fabrication.

In addition, a new approach has been taken for applying a porous electrolyte layer (which becomes incorporated into the air electrode) to the dense electrolyte. Before, a granular zirconia layer was applied to the fuel electrode that was incorporated by the growing electrolyte into a dense structure. By discontinuing the EVD process early enough, a consolidated, but uncovered granular zirconia layer, was left on top of the dense electrolyte. Although adequate, this porous layer had some disadvantages (missing tortuosity and fine porosity) because it was exposed to a two-hour deposition. Therefore, we investigated another method. Here, a dense electrolyte layer was deposited first, then the porous zirconia layer was applied and fixed to the dense electrolyte layer by a short deposition run of only one-half hour. Although this approach requires an additional processing step, much better control over air electrode quality can be achieved, by optimizing the porous substructure of the air electrode. The improved porous electrolyte structure, that becomes a part of the composite oxide air electrode, results in air electrodes that exhibit adequate performance.

Conclusions

The deposition of long electrolyte films is routinely achieved. Improvements in processing have increased film uniformity, adherence, and reduced the incidence of tube cracking.

5.1.6 Subtask E. Cell Stack

The intention of this subtask was to define and reduce to practice all the materials and fabrication procedures, needed to produce fuel cell stacks that could meet the targeted performance goals of the program. As a result of the efforts over the past 4 years, these materials and processes, leading to stacks that met the program objectives, have been defined, and are listed in Table 5.5. This listing does not rule out improvements of materials and processes that can lead to enhanced stack performance in the future.

Table 5.5

HTSOE Fuel Cell Stack
State of Technology of Materials and Processes

Component	Material	Fabrication Process
fuel electrode	nickel-zirconia cermet	slurry coat/sinter
solid electrolyte	yttria-stabilized zirconia	electrochemical vapor deposition (EVD)
air electrode	tin-doped indium oxide current collector over porous zirconia, perovskite coated	combination of EVD (ZrO_2), CVD or plasma spray (In_2O_3) and impregnation
interconnection	magnesium-aluminum doped lanthanum chromite	EVD
support tube	calcia-stabilized zirconia	extrusion/sintering

5.2 Task 2. Life Testing of Cell Components and Stacks

To enable life testing of cell components, unit cells, and cell stacks, a life test facility had to be installed. The facility had to meet the following requirements:

1) be able to accept several multicell stacks
2) have a completely fail-safe gas supply system
3) have the ability to monitor several tests simultaneously and collect data automatically
4) operate reliably for extended periods with a minimum of attention.

During the first year of this continuation program, such a facility was designed and constructed in the laboratory.

5.2.1 Test Facility Design

The fuel cell test facility was designed to test up to 5 multi-cell stacks, simultaneously, and to provide fail-safe, dependable operation, while requiring a minimum of attention. Furnace elements were specified to operate several hundred degrees below their design temperature, to extend their life and thereby, reduce their maintenance. The furnace temperature controllers are of the power proportioning type, supplying only the current necessary to maintain the set temperature. Thermocouple break protection, which prevents overheating, should a thermocouple fail, also extends furnace element life and increases reliability.

Figure 5.19 is a schematic diagram of the gas supply system. Backup supplies have been provided to assure fail-safe operation and stack protection during power failures, or loss of house-supplied gases. Under normal operation, hydrogen, nitrogen and air are obtained "in-house." Should line pressure be lost, a pressure switch activates an electrical solenoid valve to permit backup cylinders to continue to supply the required gases. During power failures, a three-way solenoid valve fails closed, cutting off all combustible gases, and allowing a low-combustible

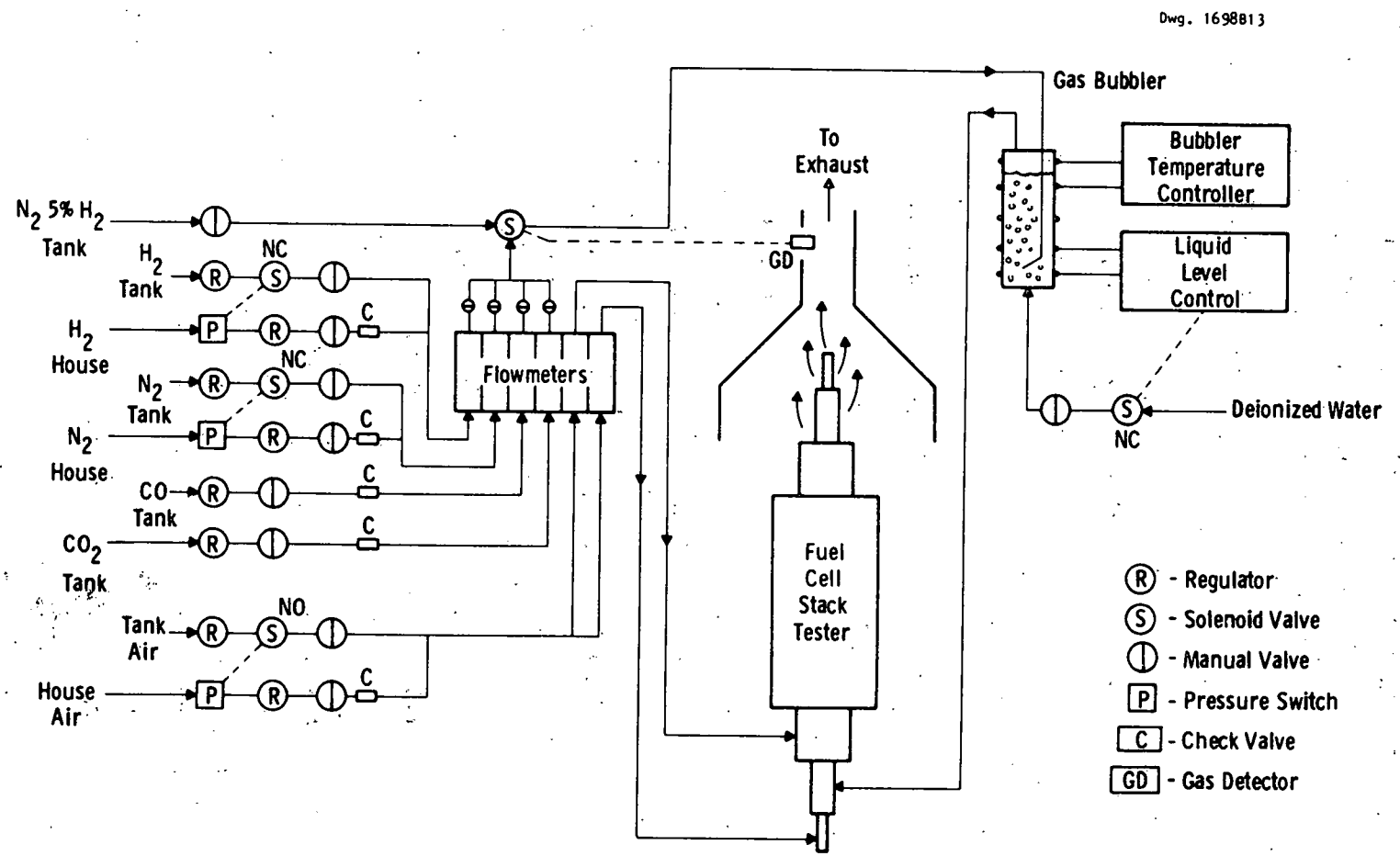

Fig. 5.19—Schematic diagram of fail-safe gas plumbing system for test facility

nitrogen/5 percent hydrogen gas mixture to be supplied. This gas prevents the formation of explosive mixtures at low temperatures, until alarm systems are reset and normal operation is restored. This same three-way valve is also wired to a combustible gas detector. The detector mounted in the canopy hood ducting, monitors the exiting gases. As a preset percentage of the lower explosive level is approached, an audible alarm is sounded. If the situation is not corrected and gases continue to accumulate, the detector activates the three-way valve, stopping the flow of all combustible gases, and introduces the safe forming gas atmosphere, until the system is manually reset. Air, supplied by house compressors, and also lost during power failures, is protected by a fail-open solenoid valve. Again, backup air is supplied from cylinders until power is restored and normal, automatic operation is resumed.

The electrical testing of the stacks is accomplished through the use of a specially designed and constructed test unit. The test unit includes the oscilloscope sync and monitor inputs, as well as a high speed, transistorized switch for increased accuracy in measuring ohmic stack losses and slow polarization losses by the current interruption technique. Also included in the panel is the stack load device. Previously the stack current density was adjusted through the use of a resistor bank. The new device accomplishes this by utilizing the stack as a power source and stabilizing the current at a preset level. The device will maintain this current until the stack voltage drops below a preset adjustable limit. At the limit the instrument cuts off the load and the stack can return to open circuit voltage. To return the stack to load conditions, the instrument must be manually reset. This feature prevents damage that would occur if, for example, a continuous load was applied to a stack that was cooling due to a furnace failure.

The actual fuel cell stack can be wired into the system in any number of ways. One possible arrangement, shown in Figure 5.20 would have the cells wired in groups of 5. An individual cell could be left at

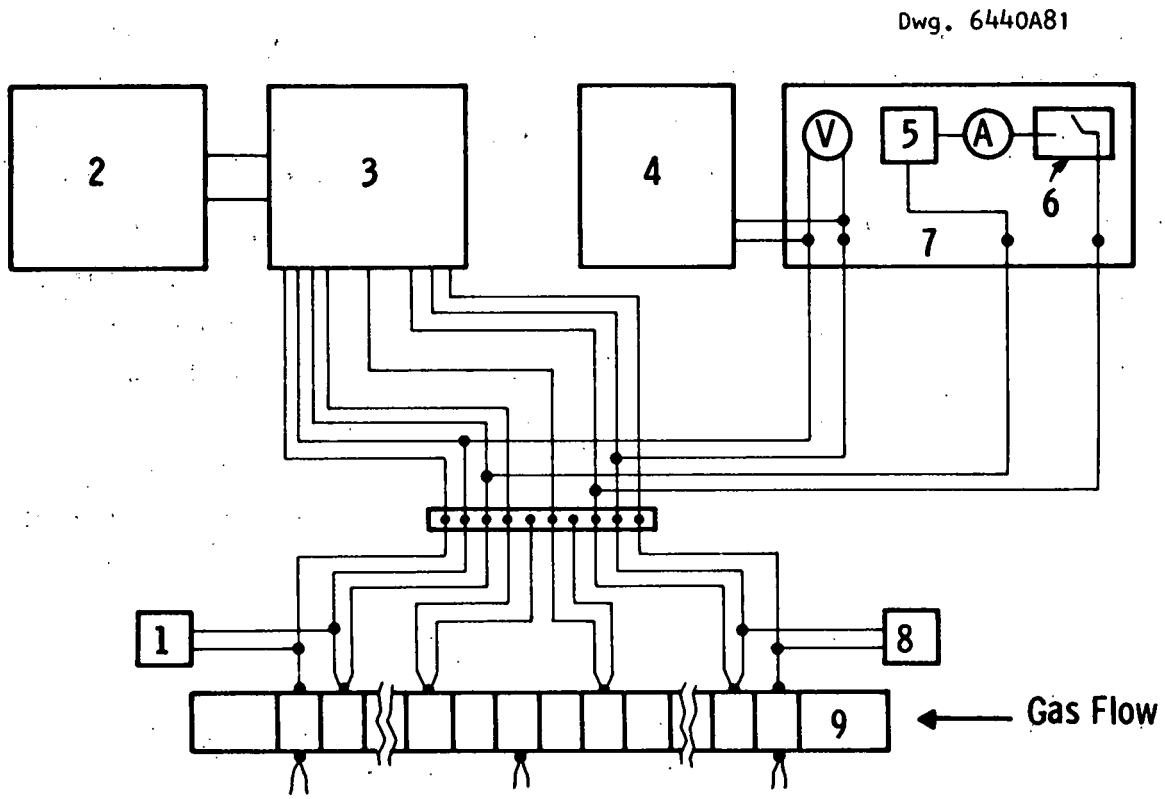

1 - Exit Gas Oxygen Gauge
2 - Magnetic Tape Recorder
3 - Data Acquisition System
4 - Oscilloscope
5 - Electronic Load Device
6 - Transistor Switch
7 - Test Station Panel
8 - Entrance Gas Oxygen Gauge
9 - Fuel Cell Stack

Fig. 5.20 —Wiring diagram for a fuel cell stack

each end of the stack and be used as an oxygen gauge to measure oxygen activity of the fuel. This would establish the maximum achievable cell stack voltage obtainable from the entering gas mixture and measure the change in the exiting fuel composition, as the fuel is depleted during stack operation. Thermocouples, placed along the length of the stack, are used for monitoring and controlling furnace temperature. Continuous monitoring and data collection is accomplished through the use of a Fluke model 2240B Data Logger. A patch panel, located at each test station, is wired into the 150 channel data logger and provides each station with 30 channels of input. Patch cords, wired to a terminal strip on the stack to be tested, can be plugged into the panel to relay the information to the data logger. Each channel on the data logger can be programmed, individually, to record temperatures from three types of thermocouples, or voltage up to 40 volts. All information from the stack on test is scanned continuously and, at predetermined times, printed on a paper tape, and, ultimately, stored on magnetic tape. This system is also an important part of the fail-safe operation. Each channel or function monitored can have a high or low limit set point. The instrument continually scans and compares measured values to the set limits. Should either be exceeded, the time and values are recorded and an output is triggered that can be used to sound an audible alarm, open or close valves, or shut off furnaces.

The completed life test facility is shown in Fig. 5.21. The five test furnaces (1) can be seen on the left beneath the canopy hood (2). At the end of the bench is a white cabinet (3) which contains the combustible gas cylinders. This cabinet is ducted into the canopy hood and all exhaust is monitored by the explosive gas mixture alarm system (4). The instrument cabinets on the right contain the furnace heating controls (5), the tester panels (6), and the data acquisition system (7). All wiring is carried from the test stations to the instrument cabinets via the overhead ducting (8).

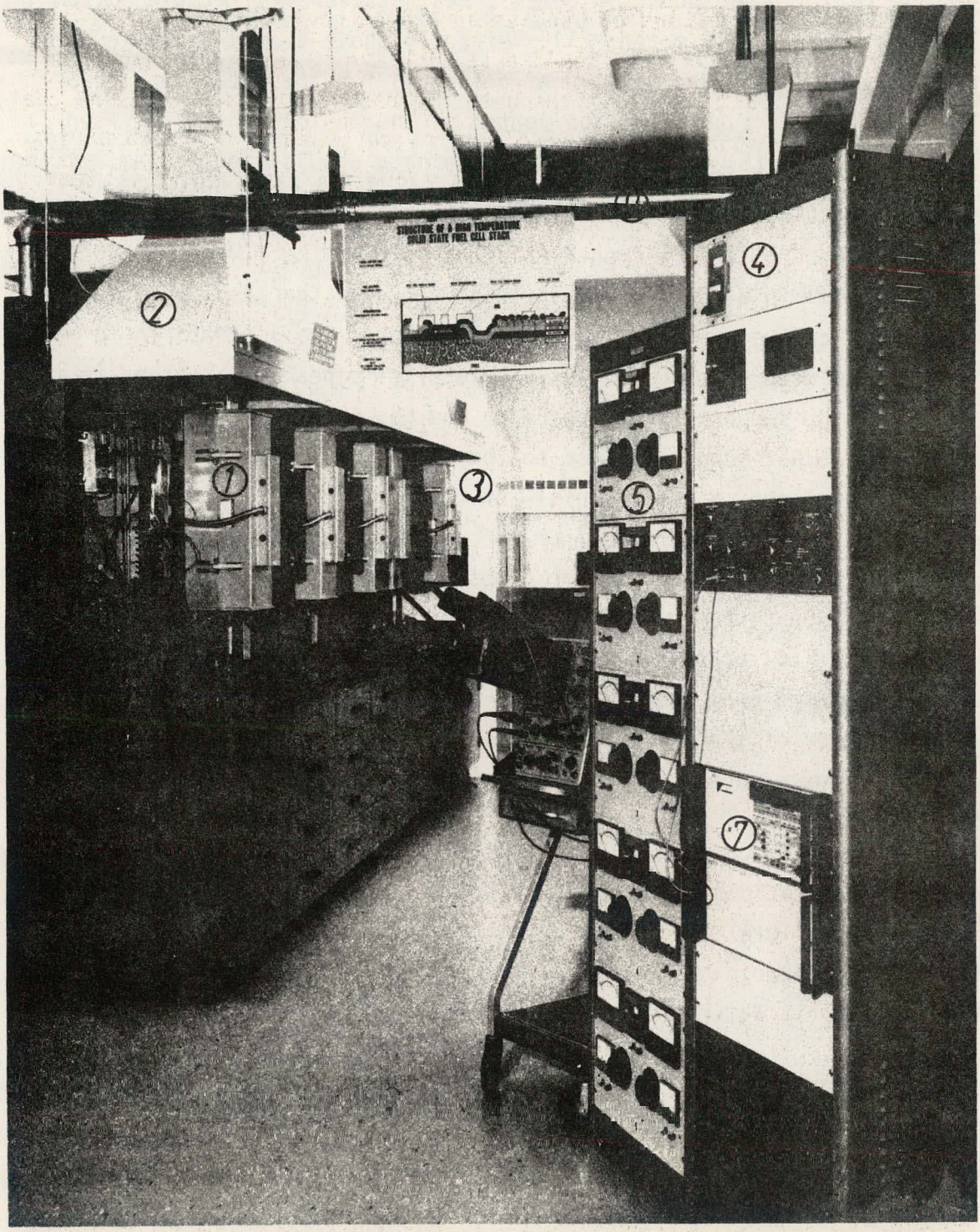

Fig. 5.21. General view of 5-station HTSOE fuel cell life test facility (left) and control and data acquisition system (right).

Fig. 5.22 shows, in detail, test station #1. At the bottom left are the gas flow meters (1). Directly above them are the temperature controller (2) and level controller (3) for the water bubbler (4) located to their right. At the center of the photograph can be seen the patch panel (5) that is wired to the data acquisition system. It's into these panels that all stacks must be wired.

Fig. 5.23 is a frontal view of four of the five test stations and Fig. 5.24 is a rear view. In this rear view the gas supply regulators (1) can be seen at the far left center. Gas is supplied to each set of flow meters through the seven parallel pipes (2) attached to the bottom of the support frame. Beneath the gas lines is the electrical conduit (3) that supplies power to the water bubbler temperature and level controllers, and also to all of the gas solenoid valves. All instrument wiring is carried from the patch panels (4) via conduit to the larger (5) of the two square ducts near the top of the photo. The wiring is then routed overhead to the data acquisition system. The smaller duct (6) carries power to the furnaces from the control panels and is isolated from the instrument wiring to prevent interferences. At the center of the photo, near the top of the support frame, is the deionized water supply (7) for the bubblers. A small flow of water is continually supplied and allowed to overflow to maintain a constant level. Water is carried from this reservoir via plastic tubing to each of the five stations. This water supply system is so designed that, if there is a failure in both the automatic level controller and its corresponding solenoid valve, the water bubbler will not overfill. This design prevents water from ever being injected into a hot fuel cell stack.

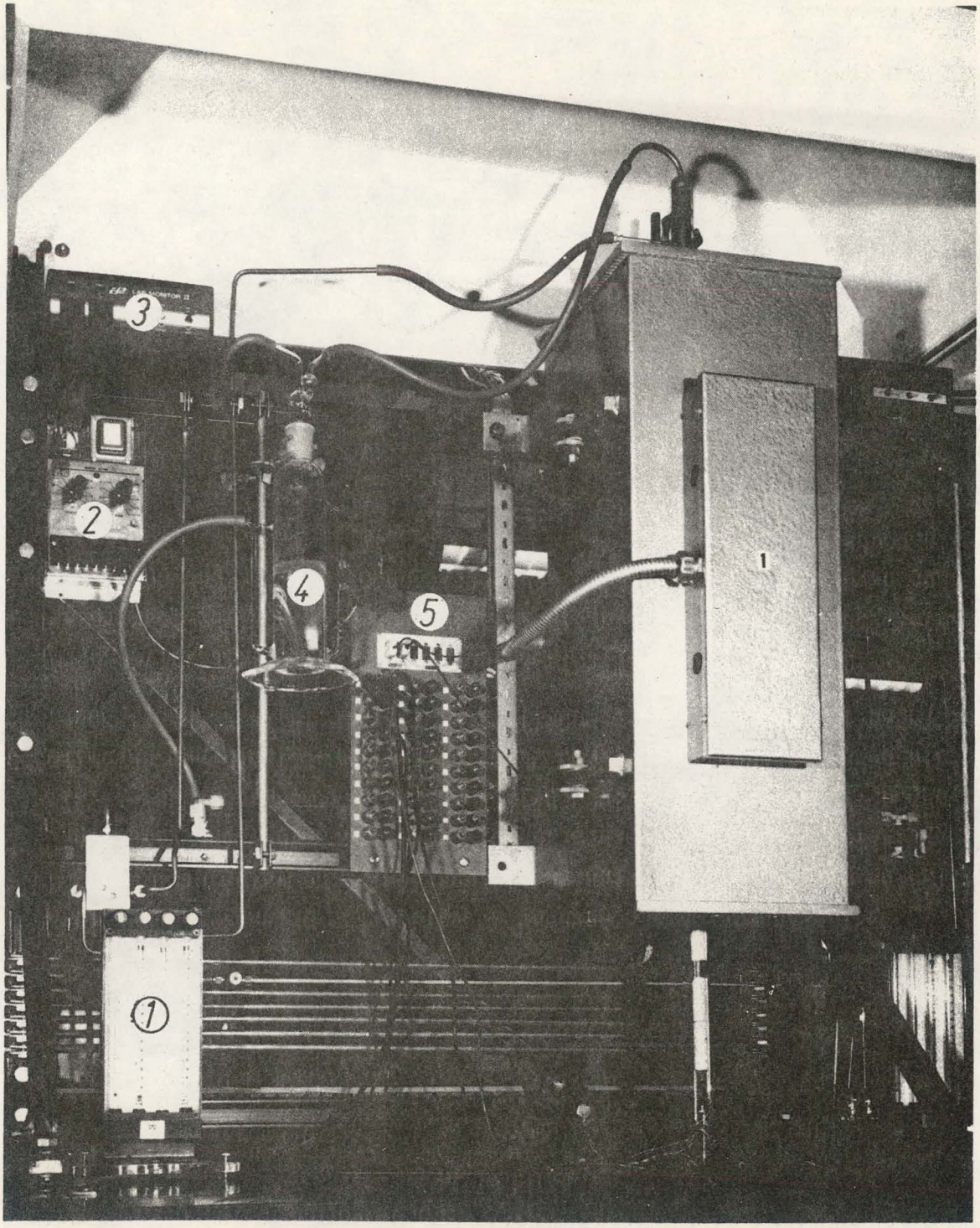

Fig. 5.22. Detailed view of HTSOE fuel cell test station #1 showing furnace. Flow meters (1), water bubbler (4), bubbler temperature (3) and level (2) controls and patch panel (5).

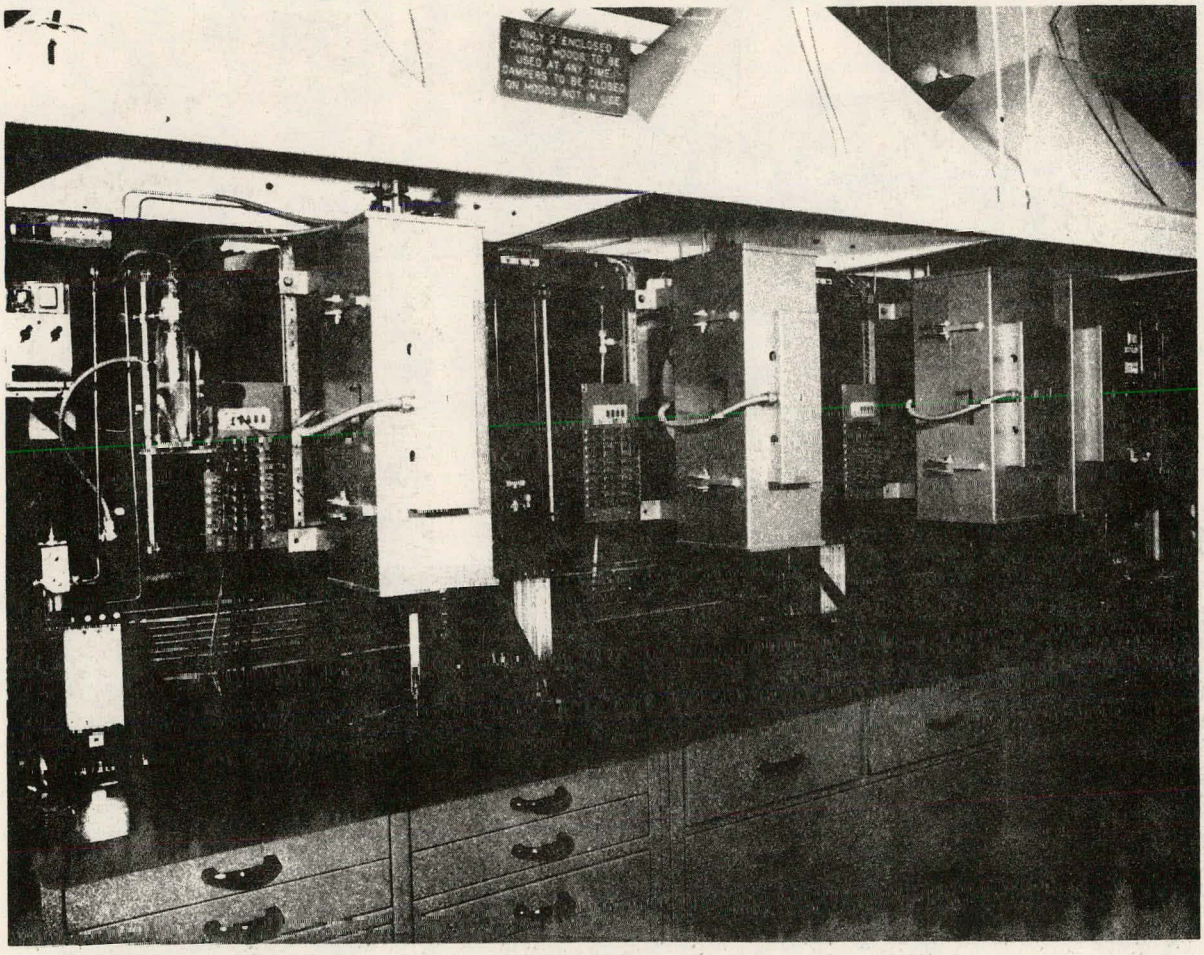

Fig. 5.23. A front view showing four of the five HTSOE fuel cell test stations.

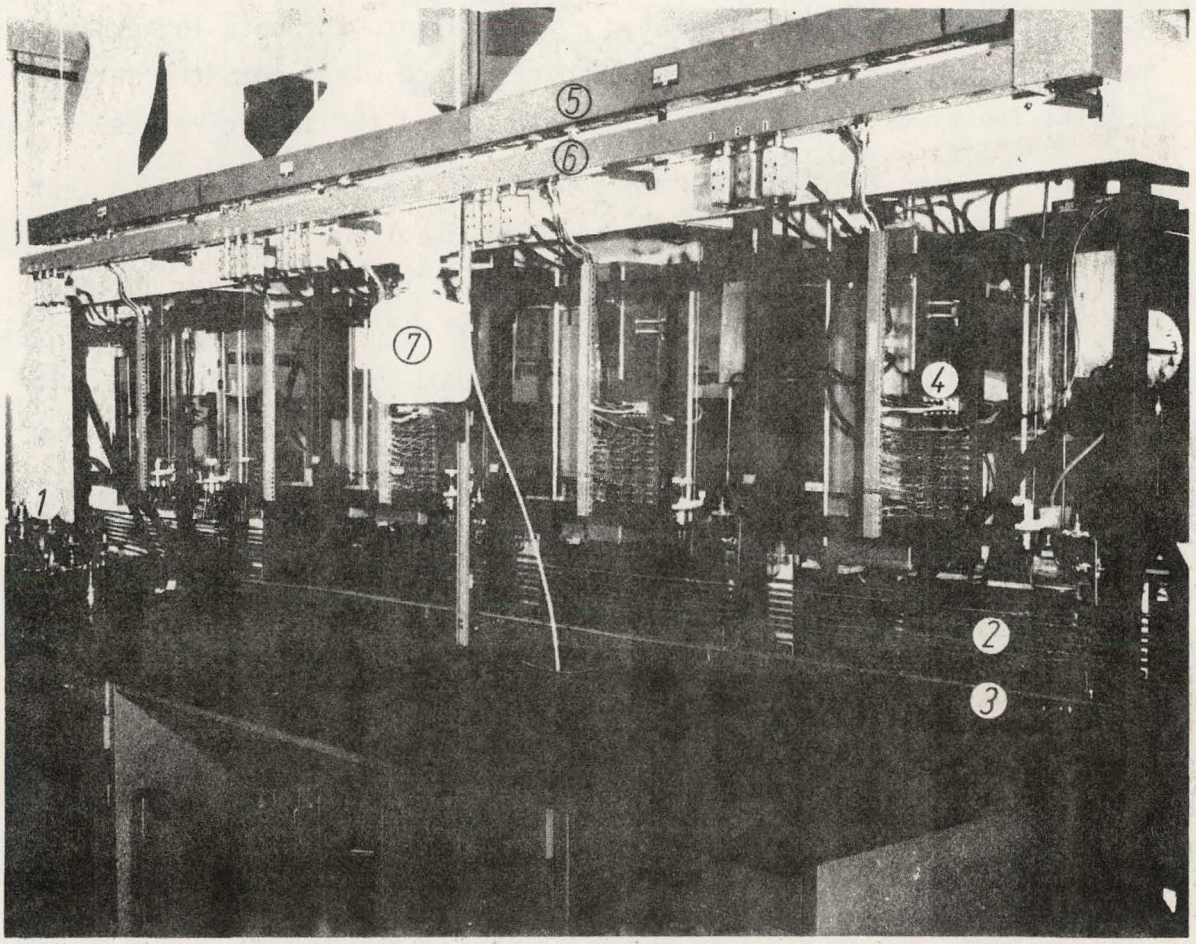

Fig. 5.24. A rear view showing details of gas supply lines (2), wiring conduits (3) and water supply system (7).

Summary

The five station fuel cell life test facility is operational under fail-safe conditions. All gas supplies, both primary and backup, that were plumbed in, had been leaked checked, and tested for fail-safe operation. Furnace heating controls were calibrated and tested. Installation, calibration, and testing of the explosive gas alarm system was completed and the alarm system was wired into the data logger for monitoring. All test station patch panels were wired into the data acquisition system and are programmed to record the proper values.

During the past two years the facility has been used to test a number of fuel cell stacks and, currently, a life test is being conducted at one of the stations. The system is functioning, as designed, and has provided protection for the stacks during several power failures and loss of house supplied gases for over 8000 hours of operation. The facility can be upgraded and modified to provide for operation under various fuel conditions, including contaminated fuel.

5.2.2 Subtask A. Interconnection Testing in a Dual Atmosphere

The goal of this task was life and life performance predictions of the interconnection, while in contact with the air and fuel electrodes, as required in the fabricated fuel cell stack.

5.2.2.1 Oxygen Diffusion Phenomena at 1000°C in a Bulk Lanthanum Chromite Resistivity Specimen

In earlier work (July 1977 through January 1978) on thin, sputtered films of $La_{0.95}Mg_{0.05}Al_{0.75}Cr_{0.25}O_3$, it was found that the equilibrium values of resistance in either air or hydrogen-water atmospheres were reached within an hour at 1000°C. It was decided to examine the resistance behavior of a bulk specimen of this same composition in air and hydrogen-water atmospheres, to see whether or not the oxygen permeation behavior would be greatly different.

The specimen employed was a 2mm x 2mm x 14mm bar, cut from a much larger sample of hot-pressed $La_{0.95}Mg_{0.05}Al_{0.75}Cr_{0.25}O_3$, prepared by a homogeneous chemical reaction. (Similar material has been employed in the microbalance oxygen weight change studies that have been reported.) Platinum electrodes, 4 microns thick, were deposited on the bar by RF sputtering. A two-terminal resistance technique was employed, since the correction for leads was, at most, 1-1/2 percent of the specimen resistance. The specimen was held at 1000°C in either air or hydrogen-water ($pO_2 = 5 \times 10^{-16}$ atm) and, periodically, the temperature was varied over a wide range below 1000°C, in order to determine its resistance-temperature dependence.

The results shown in Figure 5.25 were at first found puzzling. Equilibration with hydrogen-water appeared to occur quite rapidly (even overnight at 600°C was sufficient), indicated by the attainment of a stable, temperature-reversible resistivity curve, having a high activation energy. This would be similar to the resistivity behavior obtained with thin film specimens in a hydrogen-water atmosphere.

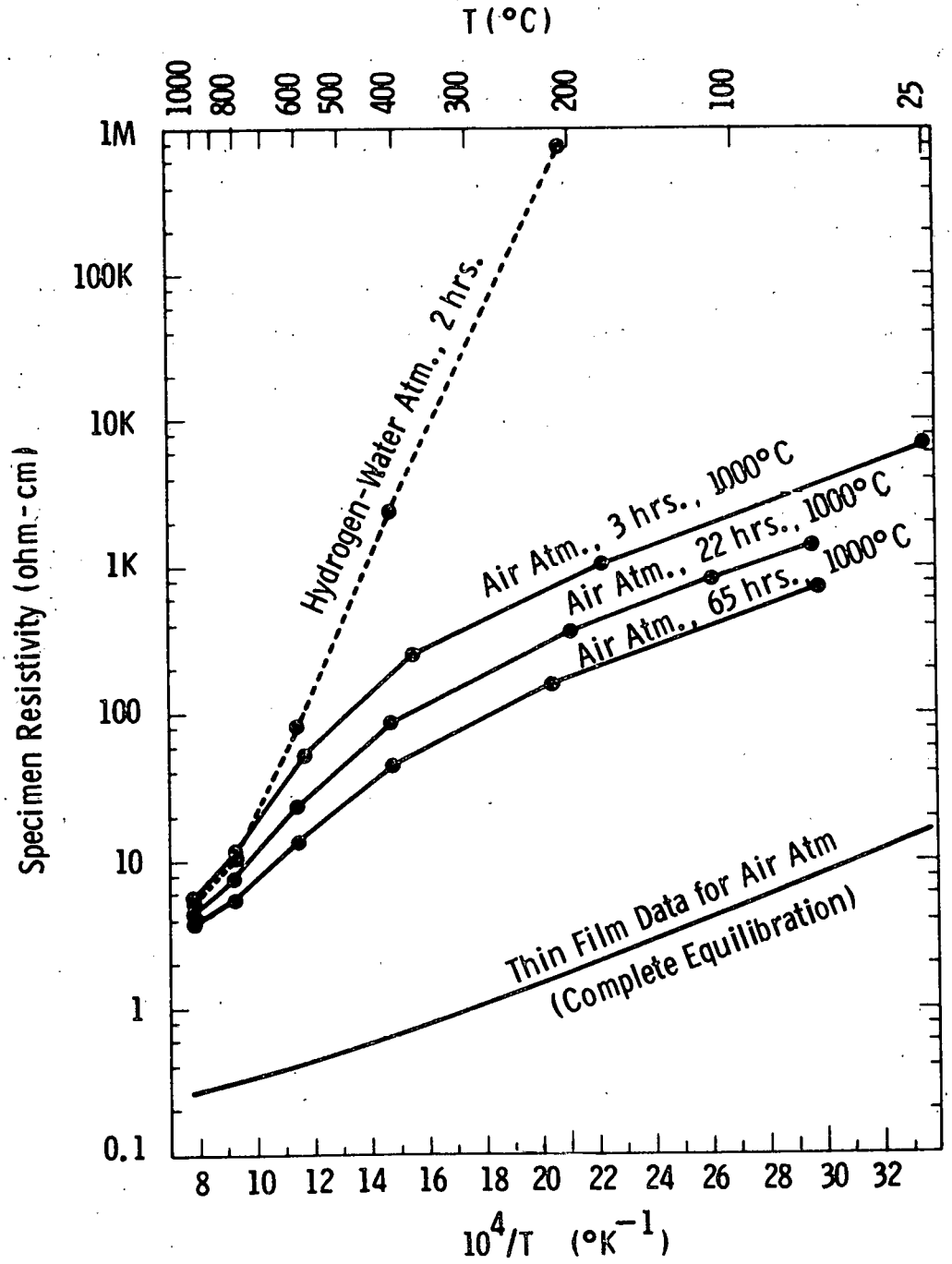

Fig. 525– Resistivity data for a bulk specimen of $La_{0.95}Mg_{0.05}Al_{0.75}Cr_{0.25}O_3$, showing the effect of progressive oxygen diffusion into its surface

In air, however, the "reversible" curve very slowly shifted to lower values, depending on the amount of annealing time at 1000°C. Initially the resistivity in air at 1000°C was 5.6 ohm-cm. After 110 hours of annealing it had decreased to only 3.5 ohm-cm. This is an order of magnitude higher than that obtained for thin sputtered films of this same material.

The results shown in Figure 5.25 are understandable if one assumes that only a thin outer layer of the specimen has equilibrated with the air atmosphere for the times considered here. The specimen would then consist of the low resistivity outer layer in parallel with the higher resistivity core. At temperatures below 400°C the core contribution would be negligible; consequently, the apparent resistivity would exhibit a temperature dependence, similar to that of a completely equilibrated specimen, but would be considerably higher in absolute value, since only a thin surface layer of the specimen would conduct effectively.

On the basis of this model one can estimate the equilibration layer thicknesses for the various 1000°C equilibration times from the resistivity data at 200°C. Also, from diffusion theory one would predict that

$$(\Delta X)^2 \cong 4\,Dt \qquad (1)$$

where ΔX is the layer thickness, D is the diffusion coefficient for oxygen (1000°C) in the lanthanum chromite, and t is the 1000°C equilibration time. Consequently, it is possible to obtain estimates of D from the data. Values for thicknesses and diffusion coefficient appear in Table 5.6 below:

Table 5.6 ESTIMATION OF OXYGEN DIFFUSION COEFFICIENT FROM THE LAYER THICKNESS OF $La_{0.95}Mg_{0.05}Al_{0.75}Cr_{0.25}O_3$

t(hrs)	$\Delta X(\mu m)$	$D(cm^2/sec)$
3	1.0	2.3×10^{-13}
22	2.2	1.5×10^{-13}
65	4.5	2.2×10^{-13}

The approximate constancy of values for D lends support to a diffusion mechanism for surface equilibration. The value of D, $\sim 2 \times 10^{-13}$ cm^2/sec, is surprisingly small; however, the value for oxygen diffusion in NiO at 1000°C is about this same magnitude.[3] It should be noted that a sputtered 3 μm thick film of lanthanum chromite was found in earlier work to equilibrate with air in less than 1 hour.

One might consider this to contradict the results given here. However, the extremely fine grain size in such a film might lead to a higher oxygen diffusion rate, via penetration of and irrigation from the grain boundaries.

5.2.3 Subtask B. Fuel Electrode-Interconnection Interaction

The purpose of this task was to study and understand occurrences at the fuel electrode-interconnection interface at high temperatures.

5.2.3.1 Resistivity of Interconnection Films on Stacks Prepared by Improved Techniques

Early EVD-deposited interconnection films (specifically, magnesium-doped lanthanum chromite) exhibited high apparent resistivities. Deviations from ideal film composition, occurring mainly during the start-up of each deposition, were found to be the source of this problem. Continued improvements in the EVD process have greatly reduced these deviations, resulting in a dramatic lowering the apparent resistivities for interconnection films. In addition, advancements have been made in the resistivity measurement techniques -- the values reported here were measured on a segment of fuel cell, rather than on a specially prepared film of interconnection material.

5.2.3.1.1 Preparation of the Specimen for Resistivity Measurement

The overall specimen, pictured in Figure 5.26, was a cell segment taken from a partially-completed fuel cell stack (air electrode absent). At one end of the cell where the interconnection film was exposed, three 5 μm thick platinum electrodes, 1.6 mm x 1.6 mm, were applied. The structure in this region contained the porous support tube, the nickel-cermet fuel electrode, the interconnection film and the platinum surface electrodes. Each surface electrode was contacted by a two-terminal probe; consequently, four-terminal measurements between the various electrodes yielded the interconnection film resistance beneath each surface electrode. A hydrogen-water atmosphere was employed at temperatures ranging from 400 to 1000 C.

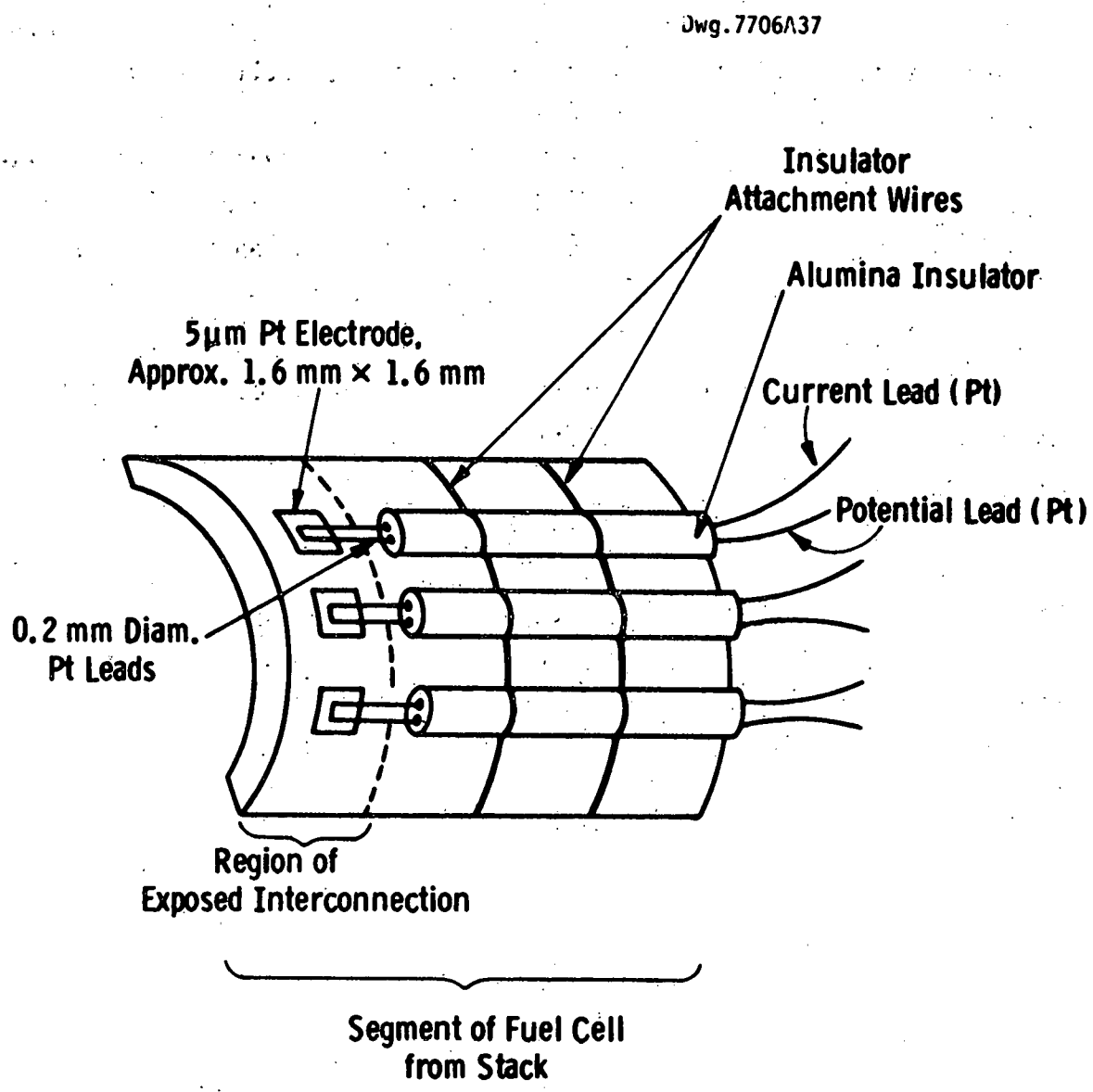

Fig. 5.26 – Sketch of electrode arrangement for measuring effective interconnection resistivity on a segment of fuel cell. (Air Electrode is Absent on Exposed Interconnection for this Measurement.)

5.2.3.1.2 Results and Discussion

A summary of resistivity data is presented in the graph of Figure 5.27. The highest resistivity line represents the previous best (lowest) values obtained for EVD-deposited interconnection films. The intermediate solid line* refers to the interconnection film which was prepared by EVD, using the Grafoil protective sleeve technique (discussed elsewhere in this report). The lower (dashed) line represents "ideally-low" resistivity values for magnesium-doped lanthanum chromite, measured on a film deposited by RF sputtering onto an alumina substrate (see Annual Report, March 31, 1978, p. 123).

It is seen that improvements in EVD techniques have lowered the 1000°C resistivity value for interconnection films from 30 ohm-cm to 4.8 ohm-cm, which compares very favorably with the "ideal" value of 3.3 ohm-cm obtained for the special RF sputtered film of magnesium-doped lanthanum chromite. The pronounced curvature (concave) in the log ρ vs 1/T plot for our present specimen could be explained by a film doping level variation with time during the EVD process. Measurements on additional specimens should clarify this matter and also provide information on possible variations in doping from cell-to-cell, along the length of the stack.

*Resistivities were averaged for two electrodes which were in close agreement; the third electrode gave anomalously high resistivities (factor of 3) for unknown reasons.

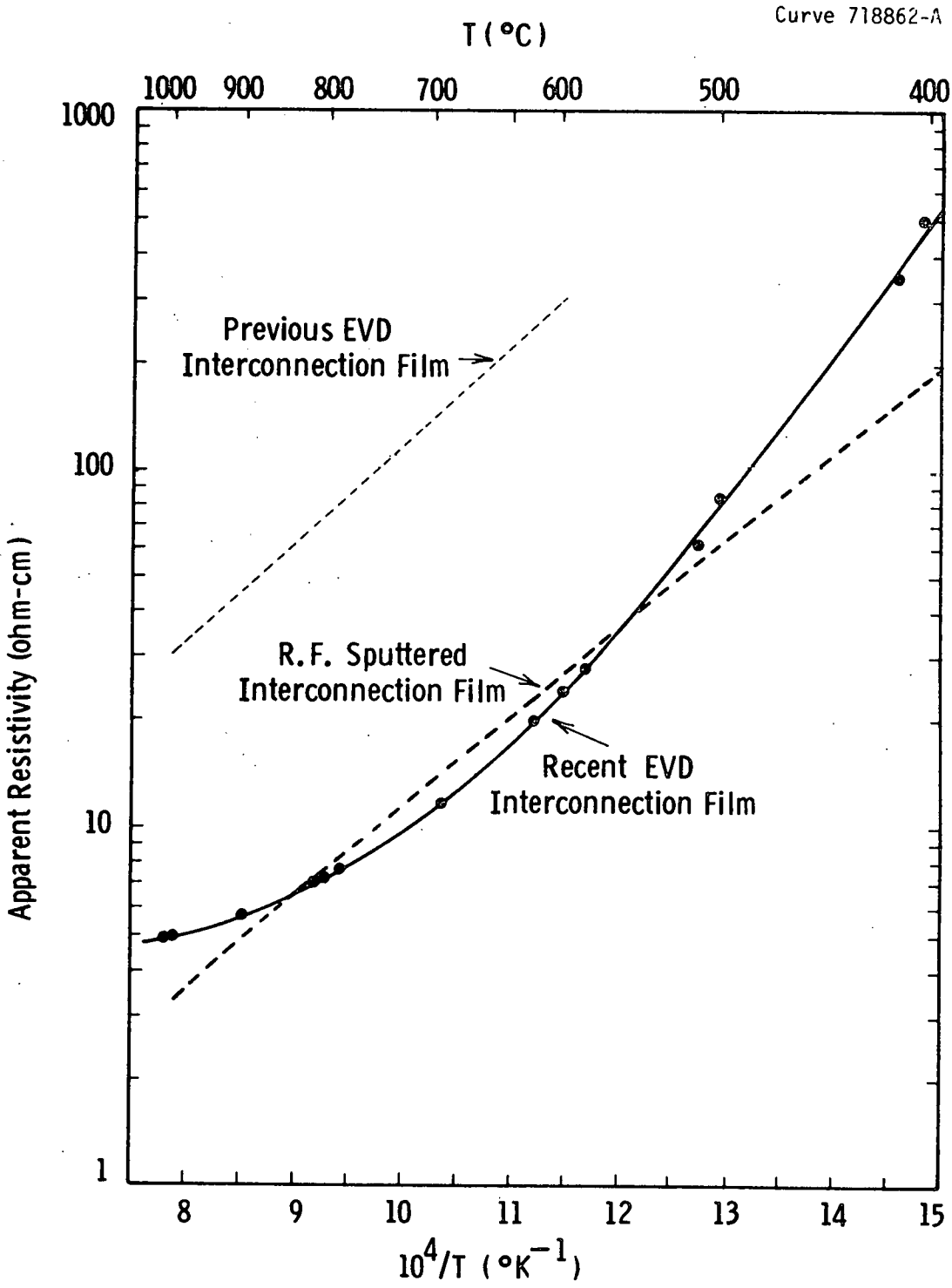

Fig. 5.27 – Apparent resistivity vs. temperature for an EVD-deposited interconnection film, measured on a segment of fuel cell. Dashed lines are for comparison specimens (see text)

5.2.4 Subtask C. Air Electrode - Interconnection Interaction

Our present program has been aimed at improving stack performance on 20-cell stacks, using the modified lanthanum chromite interconnection material.

5.2.4.1 Oxygen Loss From Lanthanum Chromite Interconnection and Indium Oxide -- General Considerations

The previous DOE program[1] on the HTSOE fuel cell resulted in the identification, fabrication, and testing of a five-cell stack, containing a new interconnection material, lanthanum chromite, doped with magnesia and alumina. The present program set goals of improved stack performance and life on longer stacks, having this cell interconnection material.

From the earlier work it was recognized that a major improvement in stack performance could be attained by reducing ohmic resistance losses in the interconnection section, particularly, at the lanthanum chromite/air electrode interface, where flaking of the indium oxide (the air electrode current collector) had occurred during the first 100 hours of operation of small stacks. One of the prime goals of the present program has been to eliminate this effect, which we attributed to a very low rate of permeation of oxygen through the indium oxide layer, as compared to that through the lanthanum chromite interconnection. This imbalance of oxygen permeation in these layers can result in extraction of oxygen from the indium oxide at the interface with lanthanum chromite, resulting in the formation of volatile In_2O, In and SnO species at the interface. A small hydrogen permeation effect might also occur with similar, potentially destructive, effects at the interface, by reduction of the oxide and formation of H_2O vapor pockets.

Therefore, work on the air electrode/interconnection problem was focused on means of improving oxygen permeation through the indium oxide, examining conditions determining oxygen permeation through

lanthanum chromite and investigating possibilities for substituting other conducting oxides, either directly for the air electrode or as intermediate layers between the indium oxide current collector and the lanthanum chromite interconnection.

In exploring these major areas eight different experimental studies were made:

1) use of a mechanically-porous layer of lanthanum chromite (magnesium- or strontium-doped) between the indium oxide and the interconnection (This method proved successful in a stack which has been under test for more than 3000 hours.)

2) use of alternate doping agents and different amounts of tin doping to increase oxygen permeability in indium oxide

3) use of alternate air electrode materials which could improve access of oxygen to the interconnection interface and perhaps reduce materials cost of the air electrode

4) use of low melting (e.g., 1000°C) second phase additives to bond air electrode powder particles to each other and the interconnection interface (to provide an air electrode with improved permeability for air)

5) alternate methods for improving mechanical porosity of air electrodes formed by chemical vapor deposition

6) study of electrical resistivity and oxygen content of doped indium oxides as a function of oxygen partial pressure

7) study of oxygen composition changes in lanthanum chromite, as related to the degree of doping, the oxygen partial pressure and the temperature. (This affects the oxygen permeability of the interconnection.)

8) chemical stoichiometry and stability of EVD films of lanthanum chromite, as compared with the corresponding, thermodynamically-stable bulk form of the oxide.

In the following sections, those areas that were extensively investigated, with respect to improving the air electrode-interconnection interface stability, are described.

5.2.4.2 Alternate Doping Agents for Indium Oxide

Indium oxide, containing two to four atomic percent tin, is the major chemical component of the air electrode of the HTSOE fuel cell. A 20 to 40 micron thick layer of magnesium-doped lanthanum chromite is sandwiched between an extension of both the indium oxide and the nickel fuel electrode layers to provide a series, electrical connection between adjacent cells of the fuel cell stack. A physical barrier, preventing direct reaction of the fuel with oxygen (from air) at the cathode, is also maintained by the interconnection. Of these three layers comprising the electrical junction, the lanthanum chromite is (ideally) non-permeable to oxygen, while the indium oxide and nickel layers are actually physically porous.

In reality, however, a small solid state permeability to oxygen exists, via vacant oxygen sites in the crystalline lattice of the lanthanum chromite. This permeability is accentuated at low oxygen partial pressures and in the presence of the magnesium-doping component that is used to enhance the electronic conductivity. Actually, this permeability by solid state diffusion is small and should present no problem, unless oxygen access to the interface through the indium oxide

layer is restricted. In this restricted case indium oxide itself becomes a parasitic source of part of the oxygen that diffuses through the lanthanum chromite to the fuel side of the interconnection. In this situation it is possible, due to the oxygen depletion, to form volatile In, In_2O and SnO species, which may result in separation and spalling of the indium oxide layer. If some hydrogen could permeate the lanthanum chromite, a similar problem would arise with the additional formation of H_2O vapor pockets. Sufficient physical porosity of the indium oxide would obviate either difficulty. Therefore, we examined methods to increase the physical porosity, as well as the solid state permeability to oxygen of the indium oxide.

Our data show that indium oxide, in which about two atomic percent of the indium is replaced by tin, loses a small quantity of oxygen when the oxygen partial pressure is reduced. The effect is reversible for equilibration times of a few hours and oxygen pressures of 10^{-4} atm, and higher. At low pressures (e.g., 1^{-12} atm) irreversible losses were observed in controlled atmosphere microweighing experiments. Thermodynamic data of others[4] suggest that the irreversible losses may be due to vaporization of In_2O, SnO, and In, in particular, depending on the oxygen partial pressure and temperature involved.

Figure 5.28 shows a comparison of the oxygen loss from $In_{1.84}Sn_{.16}O_{3\pm x}$, $In_{1.96}Sn_{.04}O_{3+x}$ and pure In_2O_3. It is seen that the oxygen loss is greater at the higher doping level but not proportional to the tin content. In contrast to the doped specimens, oxygen loss from the pure indium oxide is negligible below 10^{-2} atmospheres. This behavior suggests that perhaps "interstitial" oxygen, or metal ions, are involved. The explanation is plausible from a consideration of the crystal structure, which is C-type rare earth. This can be considered as a distortion of the fluorite structure in which oxygen ions are arranged in simple cubic packing with alternate "interstitial" positions filled with cations. There is also an ordered removal of two of every eight oxygen ions in the simple cubic packing of the oxygen ions of the crystal. Thus one-fourth of the potential oxygen sites, and one-half of the sites coordinated to eight oxygen ions, which are potential metal ion sites, are available as "interstitial" sites.

Curve 721869-B

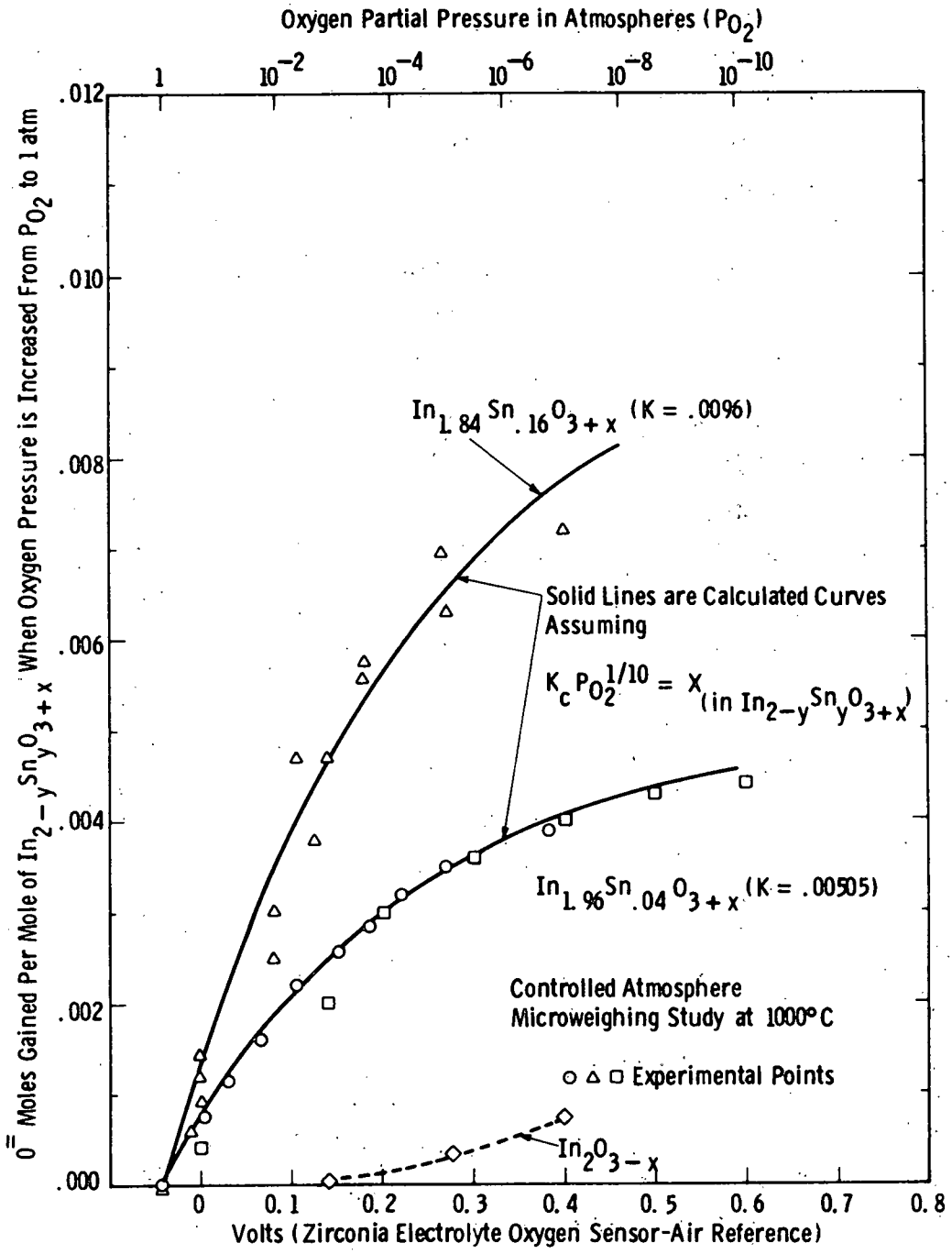

Fig. 5.28—Change in oxygen content of $In_{2-y}Sn_yO_{3+x}$ when oxygen pressure changes

In our studies we have also examined the effect on the oxygen content of indium oxide of additions of other dopants, including zirconium, titanium, niobium and tantalum. It is assumed that tin enters the lattice, at least partially, as a nominal Sn^{4+} species. This would suggest that other species, such as Zr^{4+}, Ti^{4+}, Nb^{5+}, Ta^{5+} may also dope indium oxide in a similar manner. Figures 5.29 and 5.30 are plots analogous to Figure 5.28 which show that for $In_{1.96}Zr_{.04}O_{3\pm x}$ and $In_{1.98}Ta_{.02}O_{3\pm x}$, the oxygen loss dependence on oxygen partial pressure is similar in nature and magnitude to that of the tin-doped system.

As with pure and tin-doped indium oxides, exposure to very low oxygen partial pressures, such as 10^{-14} atmospheres (provided by a water/hydrogen mixture), resulted in irreversible weight losses. No irreversible weight losses were observed in our experiments in atmospheres containing one to 100 percent oxygen. This behavior is anticipated from thermodynamic considerations. However, the oxygen loss dependence on oxygen partial pressure is not suggested by a simple mechanism. The oxygen loss dependence on oxygen pressure is very small. In the case of $In_{1.96}Sn_{.04}O_{3\pm x}$ this is approximated, as indicated in Figure 5.28. by the relation:

$$KP_{O_2}^{1/10} = x \qquad (1)$$

where x represents the "excess" oxygen ($O^{=}$) in the crystal lattice. We assume, in analogy to the $Y_{2-x}Zr_xO_{3+x/2}$ system, which has the same C-type rare earth crystal structure, that doping by a higher valence ion, Zr^{4+} in the latter case and Sn^{4+} in the indium oxide case, results in excess oxygen in the crystal. This excess is, presumably, located in large "oxygen size" vacant sites in this type of crystal structure. No simple model explains the pressure dependence indicated by Eq. 1.

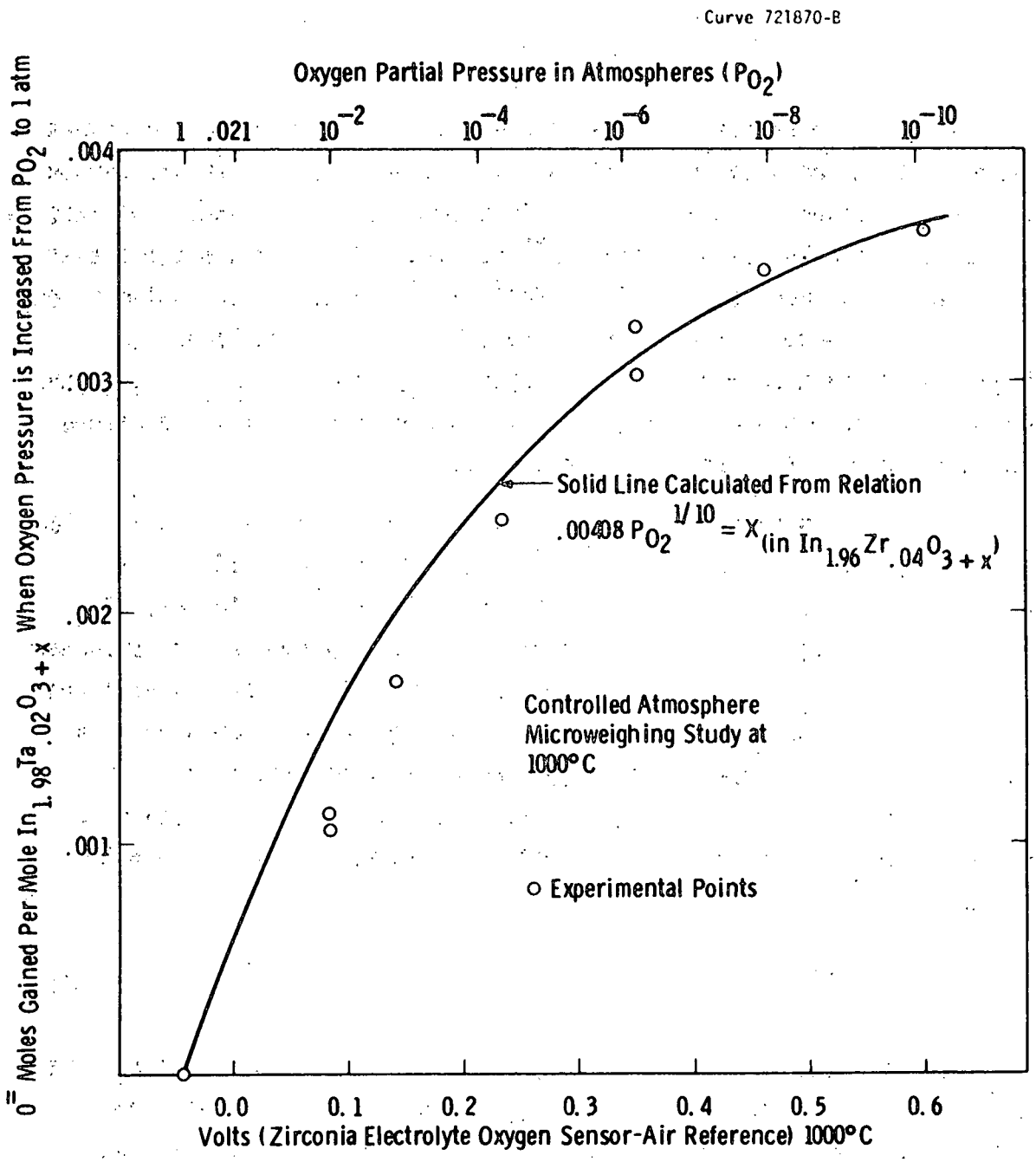

Fig. 5.29— Change in oxygen content of $In_{1.95}Zr_{.04}O_{3+x}$ when oxygen pressure changes

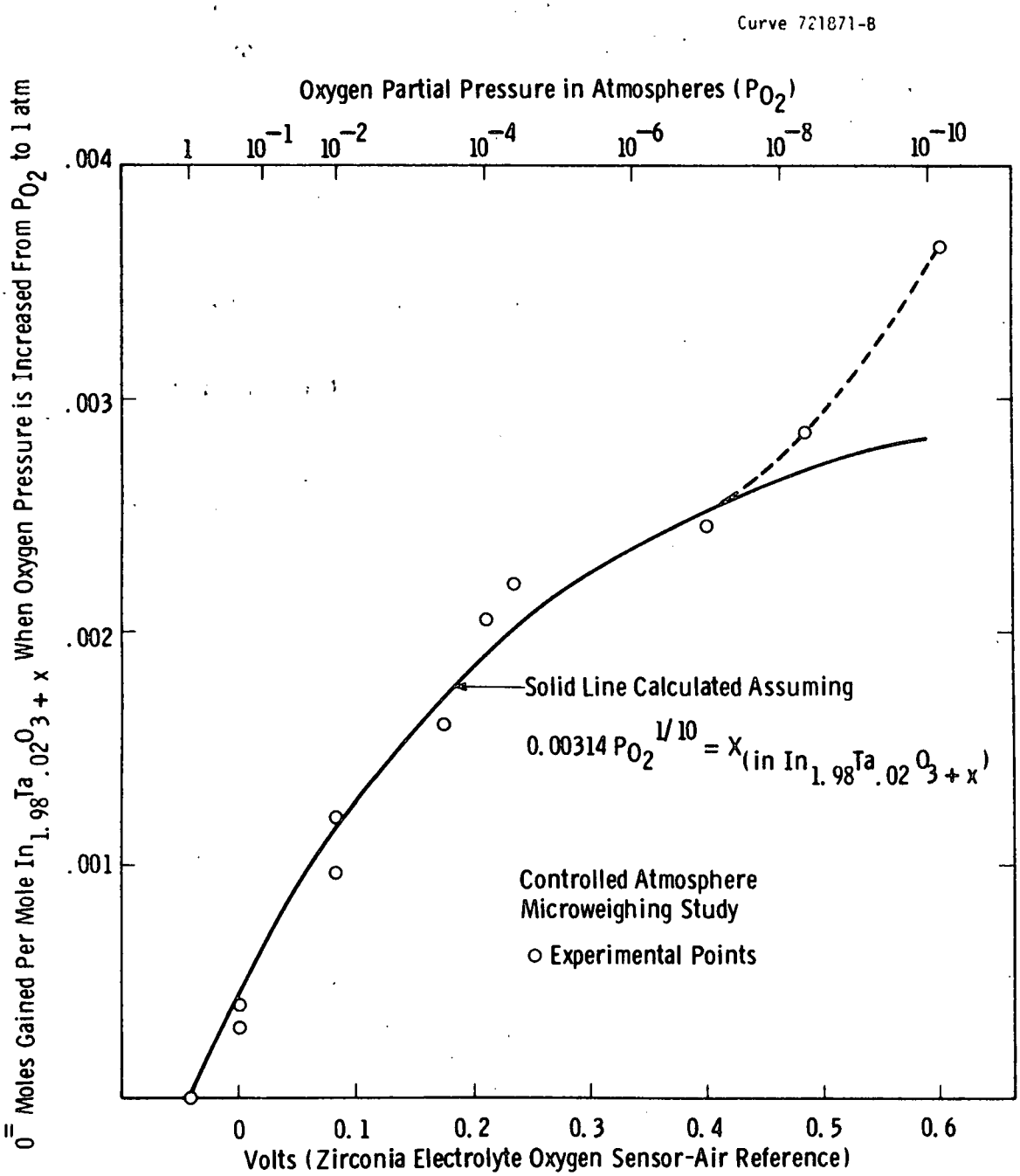

Fig. 5.30 – Change in oxygen content of $In_{1.98}Ta_{.02}O_{3+x}$ when oxygen pressure changes

It could perhaps result from inactivation of the four nearest vacant "oxygen size" sites to an excess oxygen ion, which is separated from these sites in each instance by an intervening metal ion. This could be written:

$$1/2\ O_2 + 5\ \square_{n.v.a.} \rightleftarrows \square_{n.v} + 4\ \square_{n.v.i.} \qquad (2)$$

where $\square_{n.v.a.}$ represents 5 normally vacant accessible sites for excess oxygen and $\square_{n.v.i.}$ represents normally vacant inaccessible sites for excess oxygen, due to occupation of the near neighbor "normally vacant" site by an excess oxygen. By another interpretation, any metal ion in this C-type rare earth crystal structure (which normally has six nearest oxygen neighbors) can have 7 but not 8 nearest neighbors of oxygen when excess oxygen is present, thus rendering four sites unavailable for reaction in the equilibrium between indium oxide (tin-doped) and oxygen. These four sites are coordinated crystallographically through a metal ion intermediate to the excess oxygen ion. The equilibrium constant for the reaction would then be:

$$P_{O_2}^{1/2} K' = \frac{(\square_{n.v.})(\square_{n.v.i.})^4}{(\square_{n.v.a.})^5} \qquad (3)$$

A major objection to this formulation is the consideration of the inaccessible sites as separate entities. However, the presence of metallic-like conductivity with modestly-large mobilities for an oxide conductor could, perhaps, be responsible for such an apparent effect. If we let x equal the excess oxygen, then $4x = \square_{n.v.i.}$, and, for x is small, $\square_{n.v.a.}$ is approximately constant and we may write:

$$K P_{O_2}^{1/10} = x \qquad (4)$$

In Figures 5.28, 5.29, and 5.30 we plot, vs P_{O_2}, the experimental oxygen gain of the sample resulting from an increase in oxygen pressure from P_{O_2} to one atmosphere. K in Eq. 4 represents the excess oxygen, x, per mole, e.g., of $In_{2-y}Sn_yO_{3+x}$ at one atmosphere oxygen pressure. Although Eq. 4 is not easily explained, it nevertheless gives a "reasonable" agreement with the data on $In_{1.96}Sn_{.04}O_{3+x}$, as seen in Figure 5.28.

Electrical conductivity studies by others[5,6] suggest that the major effect of doping indium oxide with higher valence ions of tin, zirconium, etc., is to produce electronic charge carriers. In addition the number of electronic charge carriers increases as the oxygen pressure is decreased. This effect is discussed in Section 5.2.4.5.2.

Overall, the data suggest that no large improvement in oxygen permeation of indium oxide is likely, due to simple doping by different chemical species other than tin.

5.2.4.3 Alternate Air Electrodes

In addition to indium oxide air electrodes prepared by CVD (chemical vapor deposition), highly porous sintered layers of tin-doped indium oxide were made for use as the air electrode current collector. These studies suggest that sintered layers of tin-doped indium oxide can be produced with the desired, more-porous structure than by the chemical vapor deposited layers alone, but with a higher, though adequate, electrical resistance. Figure 5.31 shows the temperature dependence of the resistance of a 0.022 cm sintered layer of this type. Such layers are continuous, adherent to the zirconia or lanthanum chromite, and as indicated in the figure, can be produced with an ohmic resistance in air at 1000°C which is lower than the projected requirement of 0.4 ohm per square for the air electrode.

For operating conditions of the fuel cell (1000°C in air), tin-doped indium oxide, with the approximate composition $In_{1.96}Sn_{0.04}O_3$, has the highest electrical conductivity of any oxide. It has previously been prepared by the CVD technique to give a bulk resistivity as low as about

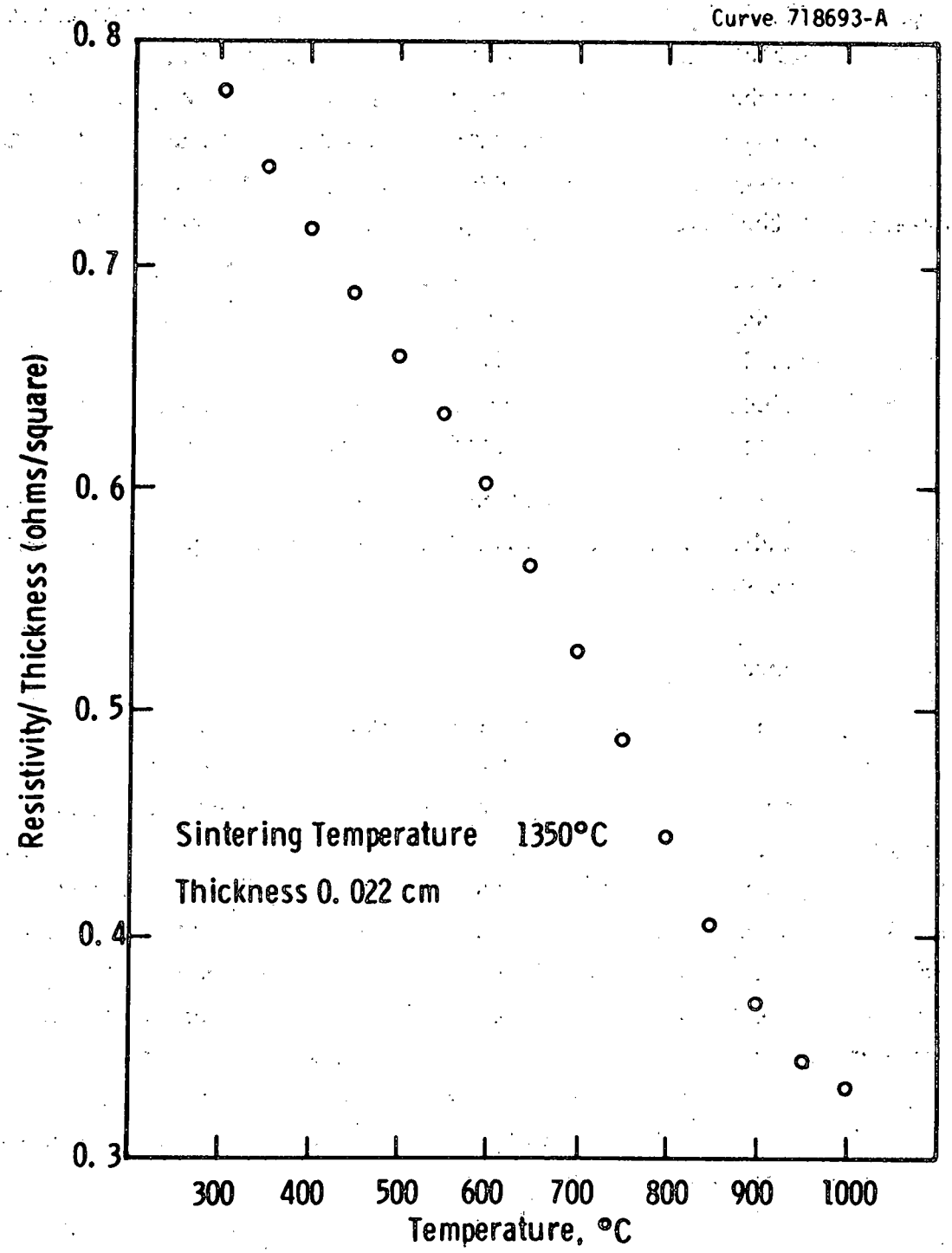

Fig. 5.31 – Sintered $In_{1.96}Sn_{0.04}O_3$ air electrode. Dependence of resistivity/ thickness parameter on temperature

5×10^{-4} ohm-cm at 1000°C in air. However, a bulk resistivity as high as 5×10^{-3} ohm-cm can, in principle, be tolerated, which makes the porous sintered indium oxide preparation described, as well as a few other oxides, potential candidates as air electrodes, provided thermal expansion characteristics are suitable. A number of differently doped indium oxide compositions, such as the more heavily doped $In_{1.84}Sn_{0.16}O_3$, compositions doped with other species, such as $In_{1.98}Ta_{0.02}O_3$, and multiply-doped compositions, such as $In_{1.94}Sn_{0.04}Nb_{0.02}O_3$, are in this class.

In addition, a variety of perovskite-structured manganites are viable candidates. For example, $Ca_{0.5}La_{0.5}MnO_3$ has both the (bulk) electrical conduction and thermal expansion characteristics which suggest its use as an air electrode. A comparison of this material, with strontium substituted lanthanum manganites, is made in Figure 5.32, which shows that the calcium-substituted composition has the highest conductivity.

Two techniques are being studied to apply $Ca_{0.5}La_{0.5}MnO_3$ to a fuel cell stack: (1) sintered powder layers, and (2) plasma jet spraying. In technique (1) an aqueous slurry of the powder, mixed with a liquid sintering agent, is dried in air and sintered at temperatures up to 1350°C. The resulting layer is highly porous (e.g., 20%-30% of theoretical density) and has an electrical resistance suitable for use as an intermediate air electrode layer but about four times higher (1.6 ohms per square) than required for it to be the sole air electrode component. In technique (2), plasma jet spraying, a free flowing powder is injected through a hot plasma and the hot, usually molten, particles impact on the preheated, rotating tube, which has all but the air electrode component already fabricated on it. This technique produces denser, though still porous electrodes. Manganites of both calcium and strontium have been applied by this technique, but, thus far, performance of cell stacks with these materials is well below that presently attainable with indium oxide electrodes prepared by the CVD method. It is also possible to prepare indium oxide electrodes by this method, but such electrodes have not yet been tested.

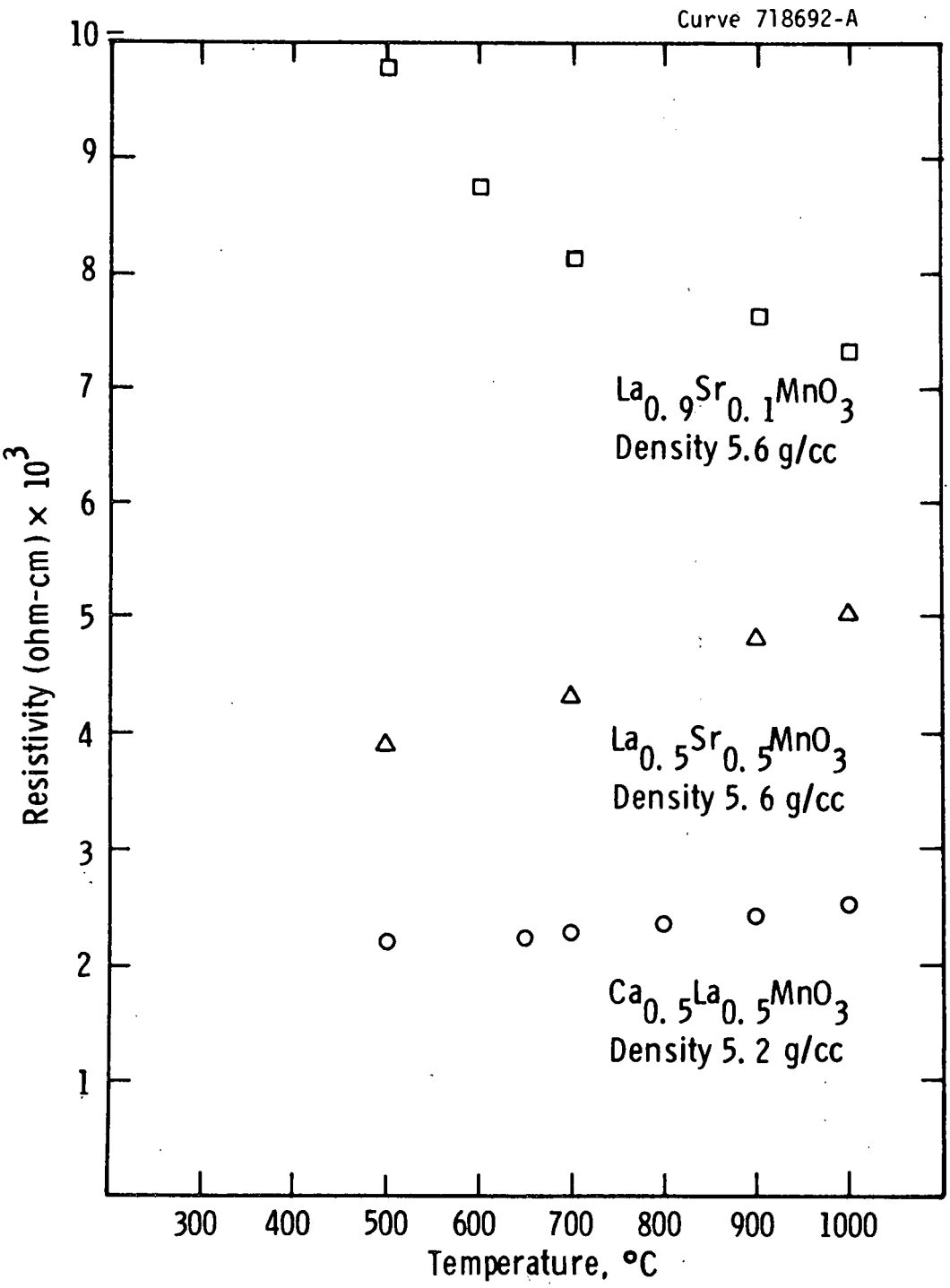

Fig. 5.32— Resistivity of lanthanum manganite with strontium and calcium substituitions

Alternative methods for applying indium oxide and substitute oxides, in particular the lanthanum manganites, though potentially useful, will require further development, before they can replace the currently-used indium oxide air electrode, prepared by the CVD method.

5.2.4.4 Oxygen Loss from Lanthanum Chromite Interconnection

To assist in obtaining a better understanding of the lanthanum chromite/air electrode interface interaction, a study was conducted on the oxygen loss from lanthanum chromite at elevated temperatures.

In its pure form, lanthanum chromite has a very low diffusion coefficient for oxygen. It apparently also has a low oxygen vacancy content, which changes less than one part in ten thousand for samples pretreated at 1700°C and then heated at 1000°C over a pressure range from 0.21 to 10^{-16} atm of oxygen, as indicated by our high temperature microweighing experiments.

If we add magnesium (or other alkaline earth ion) to increase the electrical conductivity of lanthanum chromite, a different behavior occurs. Near operating temperatures of the fuel cell (1000°C), the oxygen content of the doped lanthanum chromite changes, from essentially the theoretical maximum in air to a small deficit at low oxygen partial pressures. According to H. Anderson,[7] and in agreement with our earlier assumptions; the maximum loss from the magnesium-doped compositions approximates one mole of oxygen per two moles Mg (as Mg^{2+}) in solid solution. Figure 5.33 is an example of the oxygen deficiency as a function of oxygen partial pressure at 1000°C, as analyzed by the high-temperature microweighing technique described in a previous report.[1] The oxygen loss decreases as the magnesium doping decreases. In practice this suggests that insufficient access of oxygen to the lanthanum chromite interface with indium oxide can result in a deficit of oxygen, in lanthanum chromite, which implies the presence of oxygen vacancies. These vacancies act as diffusion carriers to transfer oxygen from that interface to the fuel electrode. If the effective (thermodynamic) oxygen partial pressure at the interface is too low, volatile indium suboxide can form, damaging intimate electrical contact between the lanthanum chromite and indium oxide layers and resulting in increased fuel cell stack resistance.

Curve 721872-B

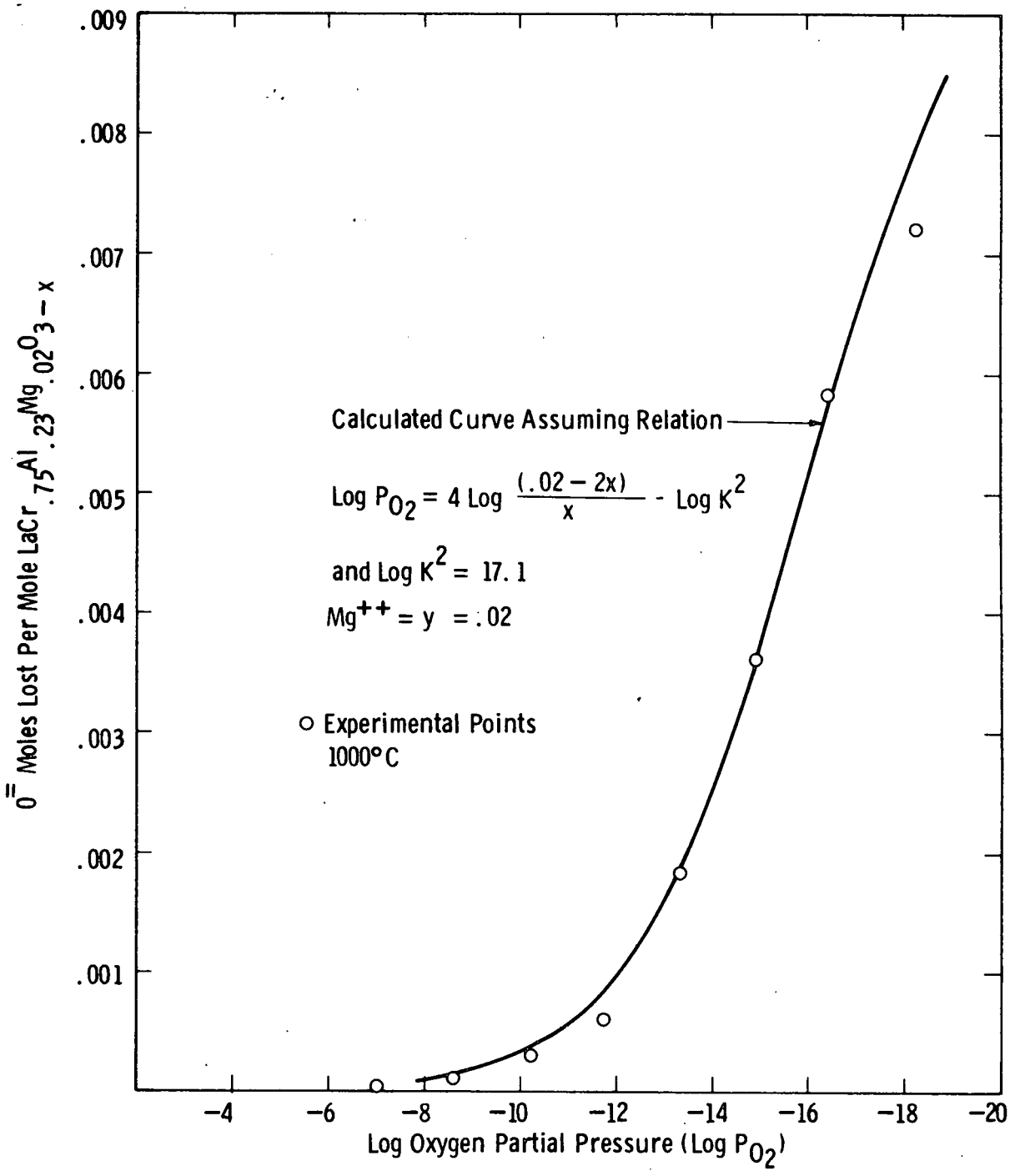

Fig. 5.33 – Oxygen loss from $LaCr_{.75}Al_{.23}Mg_{.02}O_{3-x}$ vs. P_{O_2}

Since the oxygen vacancy content is related both to the oxygen permeability and the electrical conductivity of the lanthanum chromite, we are interested in any factors which affect this property. Two additional factors, which might change the oxygen vacancy content of lanthanum chromite, are: (1) preparation method and (2) non-stoichiometry in occupation of the A and B sites by the metal ions of lanthanum, chromium, and magnesium in the ABO_3, perovskite structure. Work of Anderson[8] suggests that either a stable or metastable lanthanum chromite with $A \neq B$ may exist. If this can indeed occur, an oxygen loss, due to metal ion vacancy "doping," similar in nature to that of magnesium ion doping of lanthanum chromite, may be possible. The analogous reactions for magnesium ion and "chromium vacancy" doping are:

(a) $$LaCr^{3+}_{1-2x}Cr^{4+}_{x}Mg^{2+}_{x}O_3 \rightleftharpoons LaCr^{3+}_{1-2x+2y}Cr^{4+}_{x-2y}Mg^{2+}_{x}O_{3-y}\square^{o}_{y} + \frac{y}{2}O_2$$

(b) $$LaCr^{3+}_{1-4x}Cr^{4+}_{3x}\square^{Cr}_{x}O_3 \rightleftharpoons LaCr^{3+}_{1-4x+2y}Cr^{4+}_{3x-2y}\square^{Cr}_{x}O_{3-y}\square^{o}_{y} + \frac{y}{2}O_2$$

Air Atmosphere Fuel Atmosphere

where $\square^{Cr}$ is a chromium vacancy and $\square^{o}$ is an oxygen vacancy in the perovskite crystal lattice.

To examine this possibility, we obtained three samples of lanthanum chromite with different La/Cr ratios. They had the nominal compositions: (1) $LaCrO_3$ (stoichiometric), (2) $La_{1.03}CrO_{3.045}$, and (3) $LaCr_{1.03}O_{3.045}$. These were prepared for us by H. Anderson, by chemical interaction and oxidation steps, all occurring below 800°C. Under these conditions metastable solid solutions may occur. To examine this possibility, we examined each material in the high-temperature microweighing apparatus in the following forms: (1) as-received powder annealed for 63 hours at 1000 C in air, (2) pressed powder, heat treated at 1650°C for 17 hours in nitrogen, then annealed at 1000°C in air for 7 days. The powder samples of treatment (1) all showed a significant

oxygen loss at reduced oxygen partial pressures from 1 atmosphere to 10^{-6} atmospheres oxygen. However, after the high-temperature treatment (2), all samples showed losses of less than one part of ten thousand of the total oxygen content over the same pressure range. Figure 5.34 illustrates this behavior for the nominal composition $LaCr_{1.03}O_{3+y}$. A reasonable interpretation of these results is that: (1) surface desorption is responsible for most of the oxygen loss from the fine powder sample between 1 to 10^{-7} atm oxygen; (2) that oxygen loss to form oxygen vacancies at pressures below 10^{-7} atm is largely due to the metastable presence of metal ion vacancies, as suggested by the previous equation (b); and (3) cation vacancies are eliminated by appropriate heat treatment, creating nearly stoichiometric $LaCrO_3$ composition.

An oxygen loss attributable to surface was also seen in a similar powder preparation of $LaMg_{.02}Cr_{.75}Al_{.23}O_{3\pm x}$. This is illustrated in Figure 5.35. High-temperature heat treatment again eliminated the oxygen loss (below about 10^{-7} atmospheres) attributable to "surface adsorption." Figure 5.35 shows the normal behavior of a thermodynamically stable bulk sample of magnesium-doped lanthanum chromite.

We now compare these data with the analogous oxygen loss behavior of an actual lanthanum chromite interconnection film, prepared by the EVD method and stripped from the fuel cell stack. These data are shown in Figure 5.36. This data are consistent with that expected for a thermodynamically stable oxide bulk sample. Chemical analysis of this film by atomic absorption showed the composition to be $LaCr_{.965}Mg_{.035}O_3$. The film showed the expected orthorhombic crystal symmetry by x-ray diffraction, and a high density (99% of theoretical).

Electrical conductivity measurements on such films show factors of six to ten drop in conductivity as the oxygen partial pressure changes from that in air to 10^{-16} atmospheres (water/hydrogen mixtures). Suitable resistance values (i.e., less than ten ohm-cm) are maintained over this range nevertheless.

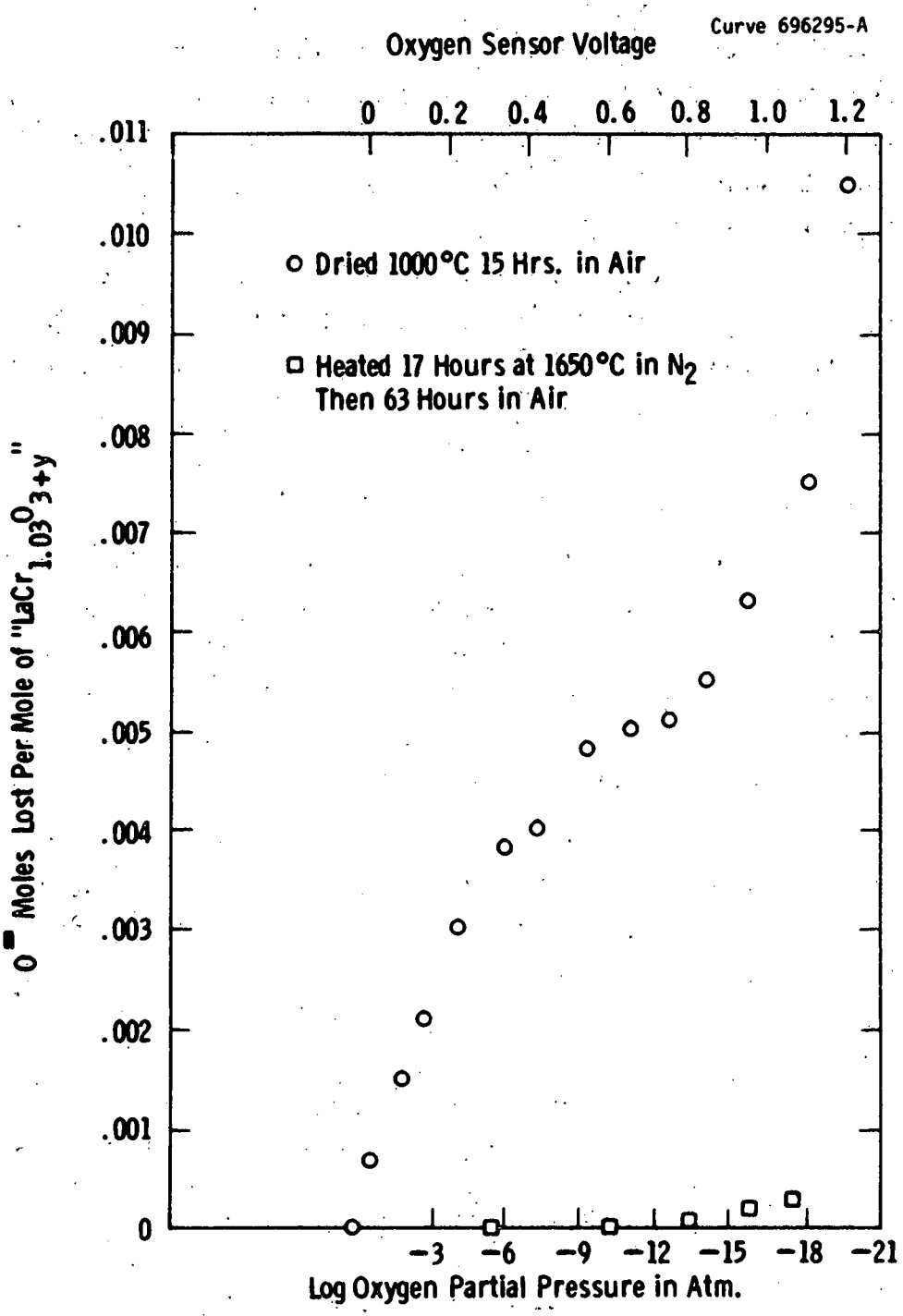

Fig. 5.34—Effect of heat treatment on oxygen loss from "$LaCr_{1.03}O_{3+y}$" at 1000°C

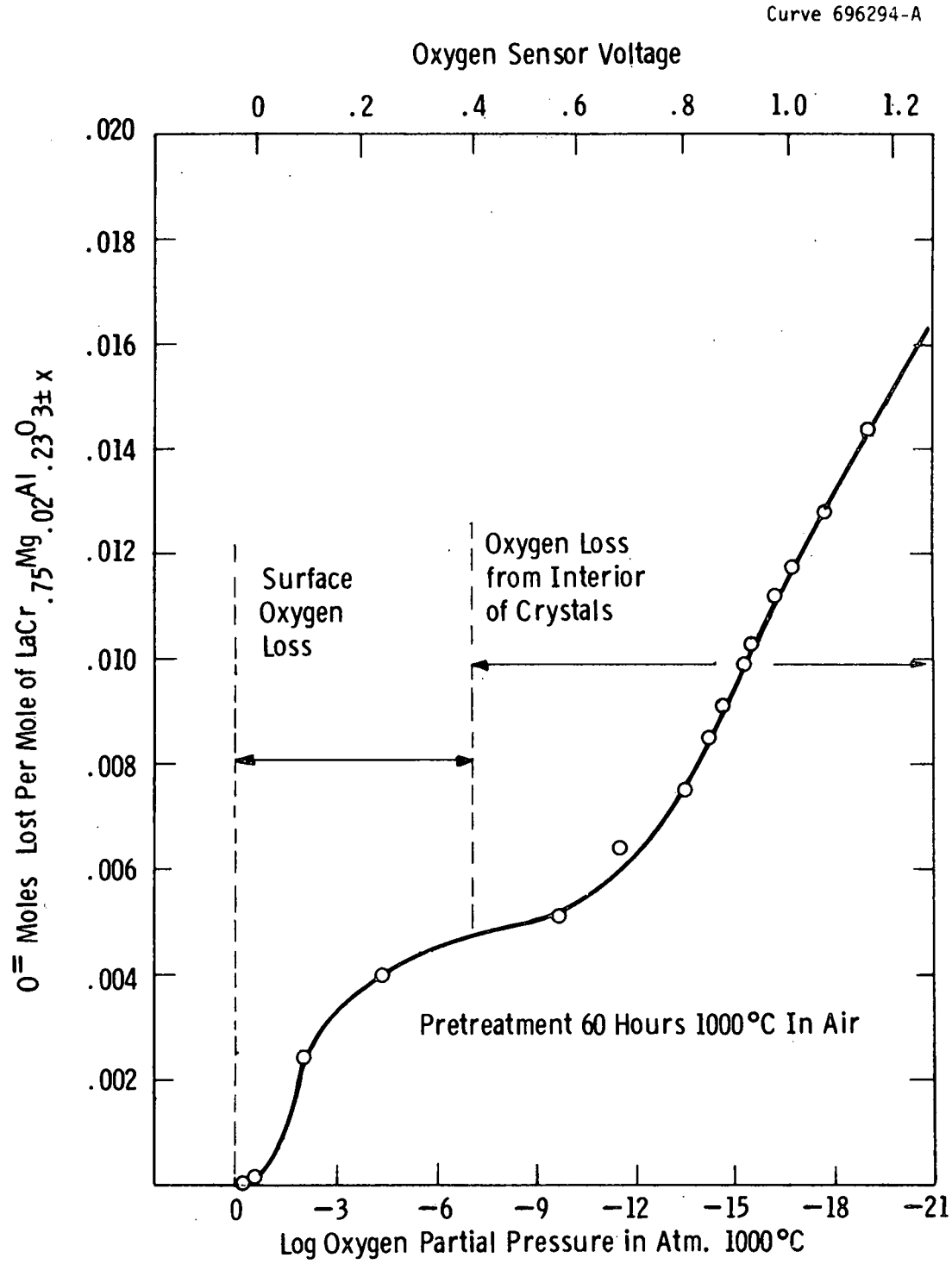

Fig. 5.35—Oxygen loss from $LaMg_{.02}Cr_{.75}Al_{.23}O_{3\pm x}$ powder at different oxygen partial pressures at 1000°C

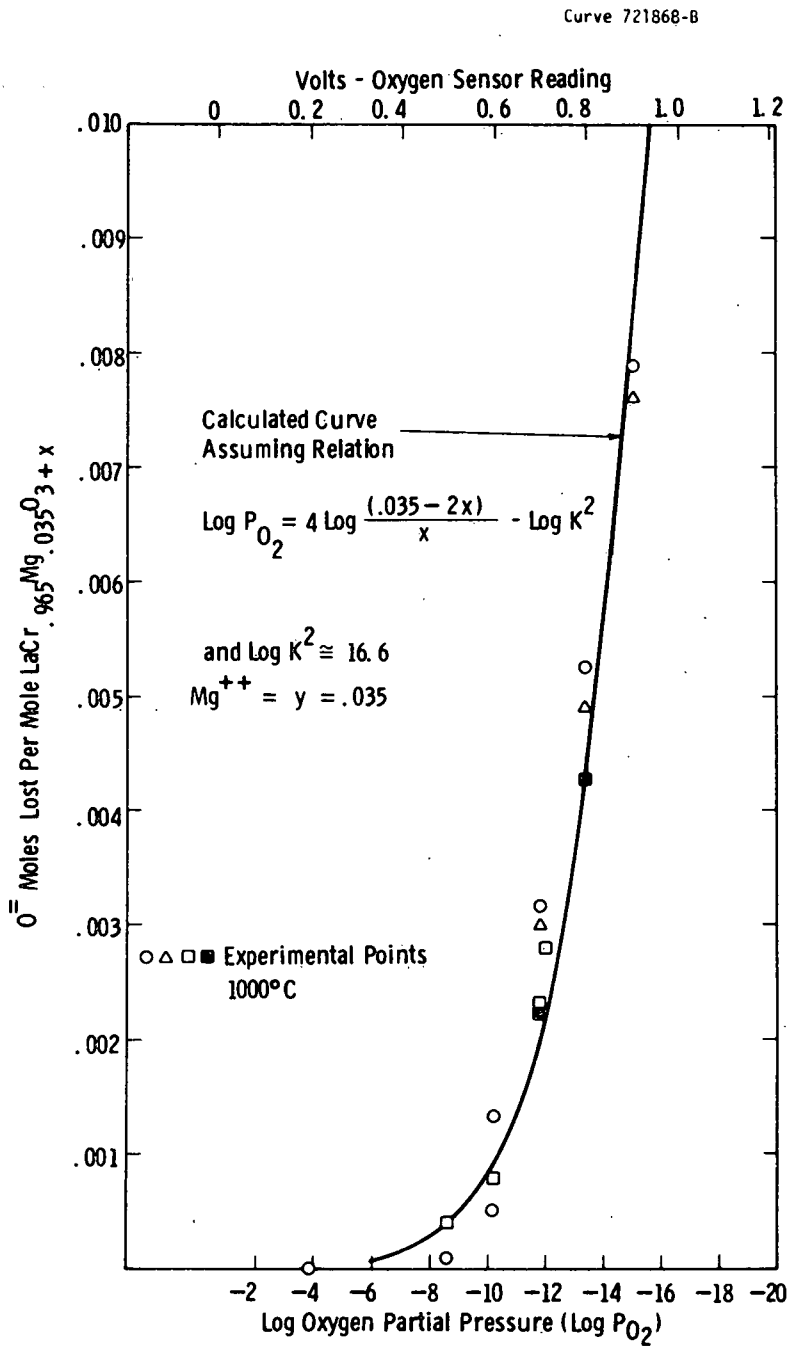

Fig. 5.36—Oxygen loss from $LaCr_{.965}Mg_{.035}O_3$ interconnection layer, stripped from nickel cermet electrode, vs. P_{O_2}

The relationship between the oxygen loss from lanthanum chromite doped with either Mg^{++} or Sr^{++} is not explained by a simple model. For specimens annealed in air for a few hours at 1650 C to 1700 C, the oxygen loss behavior is approximated by the relationship:

$$\log P_{O_2} = 4 \log \frac{(Y-2x)}{x} - \log K^2 \qquad (1)$$

Comparisons of experimental data on $LaCr_{.75}Al_{.23}Mg_{.02}O_{3-x}$ (Y = .02) and $La_{.84}Sr_{.16}CrO_{3-x}$ (Y = .16), with curves calculated from this relationship are illustrated in Figures 5.33 and 5.37. One hypothetical model, consistent with this relationship, assumes that: (1) the alkaline earth dopant is, essentially, randomly distributed in the oxide; (2) an oxygen vacancy is trapped next to an alkaline earth ion; (3) for each $O^{=}$ vacancy, one electron is associated with an alkaline earth ion plus a nearest neighbor oxygen ion vacancy, and another electron is associated with an alkaline earth ion, without a vacancy, thereby eliminating two positive hole charge carriers which are normally associated with the presence of two Mg^{++} or Sr^{++} doping ions. We might indicate this by the following equation, involving localized charge complexes:

$$(Mg^{++} \cdot Cr^{+++} \cdot 2\ O^{=} \cdot \square_{O^{=}})^{+1} + (Mg^{++} \cdot Cr^{+++} \cdot 3\ O^{=})^{-1}$$

$$+ 1/2\ O_2 \rightleftarrows 2\ (Mg^{++} \cdot Cr^{+++} \cdot h^{+} \cdot 3\ O^{=}) \qquad (2)$$

where there is a net charge change in two localized regions of the oxide crystal for each oxygen vacancy $\square_{O^{=}}$ and where h^{+} represents a positive hole charge carrier. Writing this in terms of an equilibrium constant:

$$K = \frac{(Mg^{++} \cdot Cr^{+++} \cdot h^{+} \cdot 3\ O^{=})^2}{(Mg^{++} \cdot Cr^{+++} \cdot\ 2\ O^{=} \cdot \square_{O^{=}})(Mg^{++} \cdot Cr^{+++} \cdot 3\ O^{=})\ P_{O_2}^{1/2}} \qquad (3)$$

Writing this in terms of a logarithmic relation for graphing purposes and setting $Mg^{++} = Y$ and $\square_{O^{=}} = x$ we obtain Eq. 1 which we have used to

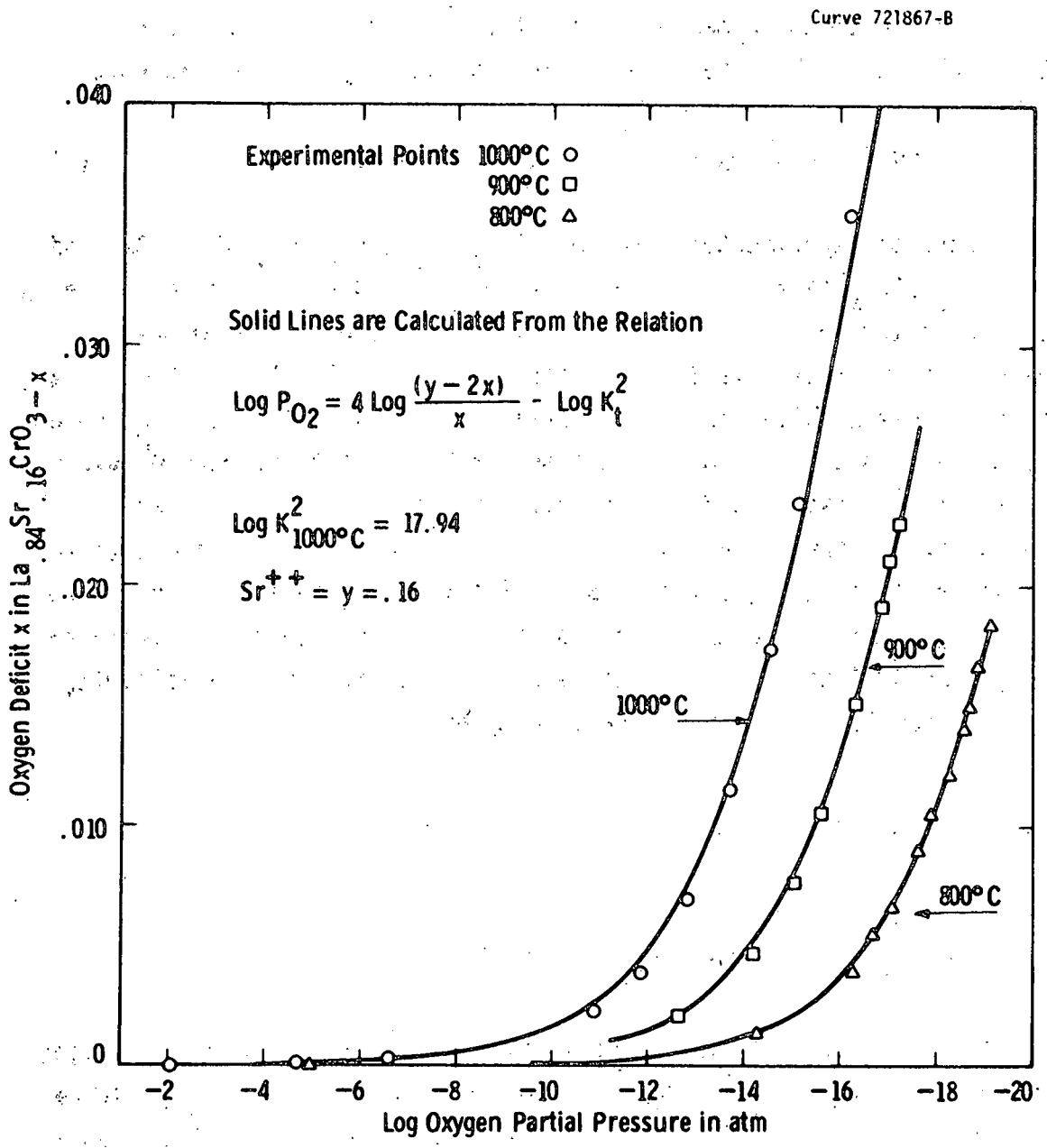

Fig. 5.37—Oxygen deficit x of $La_{.84}Sr_{.16}CrO_{3-x}$ vs. oxygen partial pressure

calculate curves to approximately represent the data in Figures 5.33, 5.36, and 5.37. Log K^2 for each of these curves was chosen arbitrarily to provide approximate agreement with experiment. We note that Log K^2 is smaller in Figures 5.33 and 5.36, representing two different Mg^{++} contents, than for the Sr^{++} case. However the strontium doping level is higher and this could perhaps account for at least part of the difference. Since higher log K^2 values (at similar doping levels) result in lower oxygen loss, this could indicate an advantage of strontium, over magnesium doping. However, as yet, low Sr^{2+} doping levels, comparable with that of the magnesium-doped samples, have not been experimentally examined. If a true difference between the Mg^{++} and Sr^{++} dopings does exist, it could be related either to the different alkaline earth ion involved or to the different crystal positions occupied by the small Mg^{++} and the large Sr^{++} ions.

In summary, these oxygen loss data, along with those based on direct chemical analysis and pycnometric density techniques, indicate that films can be produced by the EVD technique which are thermodynamically stable, stoichiometric and very dense. Electrical conductivity measurements of the films show values within the useful range of the fuel cell stack. The only troublesome feature is related to the small oxygen deficit and accompanying small permeability for oxygen in fuel atmospheres. In earlier stacks this caused indium oxide to flake off those areas of the interconnection where air (oxygen) access is poor.

5.2.4.5 High Temperature Resistivity of $In_{1.96}Sn_{0.04}O_{3\pm X}$ as a Function of Oxygen Partial Pressure

Due to the finite oxygen diffusivity within the lanthanum chromite interconnection material there is the real possibility that a low oxygen partial pressure condition may exist at the air electrode-interconnection interface. It was, therefore, deemed important to obtain information on the high temperature resistivity of air electrode material (tin-doped indium oxide) as a function of oxygen partial pressure.

5.2.4.5.1 Specimen Preparation and Measurement

Homogenized powder, corresponding to the composition $In_{1.96}Sn_{0.04}O_3$, was ground, reacted at 1500°C, reground, and finally sintered into disks at 1500°C for 6 hours. From this material a bar specimen was cut (27 mm x 4 mm x 3 mm). Four electrode bands (platinum, 4 μm thickness) were sputtered onto its surface and suitable platinum wire leads were attached to these bands, completing a four-terminal specimen. This test sample was mounted in the measurement furnace where the desired oxygen partial pressures were achieved by the use of flowing mixtures of oxygen-inert gas or hydrogen-water-inert gas. The specimen resistance was determined by a standard four-terminal method.

5.2.4.5.2 Results and Discussion

Times for equilibration of the specimen with the atmospheres varied from minutes (1000°C, $P_{O_2} \geq 10^{-2}$ atm) to hours (900°C, $P_{O_2} \leq 10^{-2}$ atm),

as judged by the time required for the specimen resistance to become constant. Reversibility, indicated by the repeatability in resistance when the sequence of atmospheres employed was reversed, was very good at 1000°C. The results are presented in Figure 5.38. Due to the porous character of the specimen, the resistivity was about one order of magnitude higher than that of a dense vapor deposited film (see previous contract Final Report).[1]

The resistivity decreased with decreasing oxygen partial pressure, as would be expected for an n-type oxide semiconductor. It was found that the data for specimen resistivity, ρ, could be fitted by an equation of the form

$$\rho = \rho_1 P_{O_2}^{1/n} + \rho_2 \qquad (1)$$

where ρ_1, ρ_2, and n were constants. The values found for n were 7.0 at 900°C and 6.7 at 1000°C. The form of Eq. (1) is in agreement with theoretical work by DeWit[9] for undoped In_2O_3. He predicts the first term with n = 6 as a consequence of the non-stoichiometric decomposition reaction

$$O^{=} \rightleftharpoons \square^{o} + 2e + \tfrac{1}{2} O_2 \qquad (2)$$

where $O^{=}$ is an oxygen ion, $\square^{o}$ is an oxygen ion vacancy, and e is an electron. In addition he suggests that a significant grain boundary resistance is present in polycrystalline specimens; this would lead to the second term, ρ_2, in Eq. (1).

This approximate agreement with Eq. (2) for the decomposition reaction is surprising. As discussed elsewhere in this report, one would expect to find the SnO_2 incorporated into the In_2O_3 lattice, either via

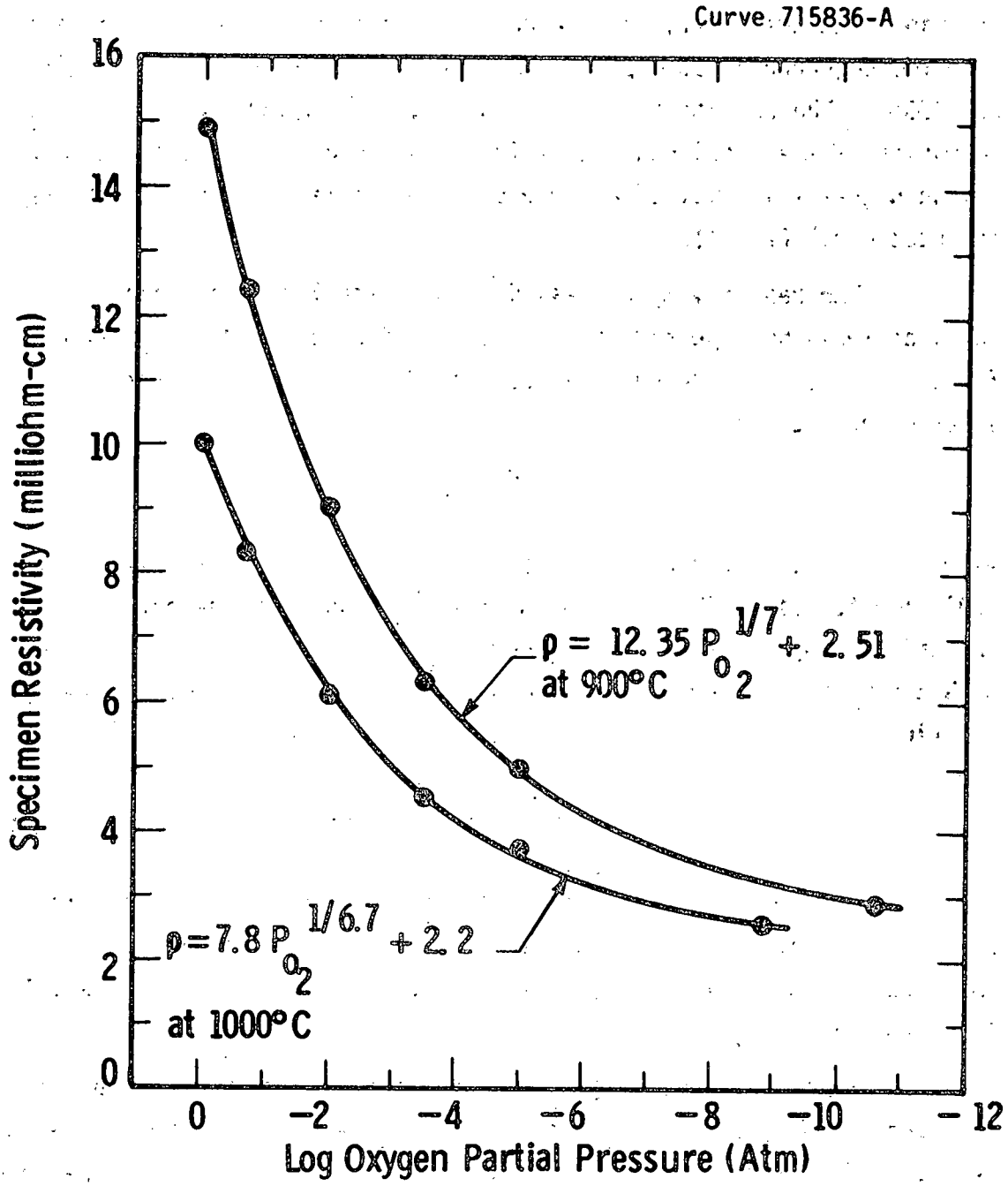

Fig. 5.38 — High temperature resistivity of a bulk specimen of $In_{1.96}Sn_{0.04}O_{3\pm X}$ vs. oxygen partial pressure. A semi-empirical equation having the form $\rho = \rho_1 P_{O_2}^{1/n} + \rho_2$ has been fitted to the data

interstitial oxygen ions or via cation vacancies. In the former case the decomposition reaction would be

$$O_I^{=} \rightleftharpoons \frac{1}{2} O_2 + 2e \qquad (3)$$

where $O_I^{=}$ is an oxygen ion interstitial, while in the latter case the reaction would be

$$O^{=} + \frac{2}{3} \square^{\text{cat.}} \rightleftharpoons \frac{1}{2} O_2 + 2e \qquad (4)$$

where $\square^{\text{cat.}}$ is a cation-site vacancy. In either case, application of the mass action law leads to $\rho \propto P_{O_2}^{1/4}$ at the higher oxygen partial pressures, in strong disagreement with the data; however, the expressions for ρ do give an asymptotic value, ρ_2, at low oxygen pressure without the necessity of assuming a grain boundary resistance. Further work would obviously be required before one could specify the precise decomposition mechanism.

5.2.5 Subtask D. Single Cell Life Test

The testing of single cells (including one interconnection) was considered inappropriate, in view of the considerable problems that had to be overcome in component fabrication for long stacks, which became apparent during the course of our work. Thus, the achievement of major life and performance goals of three, or more, interconnected cells made this single cell task superfluous (milestone ▽2).

5.2.6 Subtask E. Small Stack Life Test

Life testing is underway on stack #8, which represented the first thin film stack that delivered more than 10 watts of power. The stack life history is shown in Figure 5.39. During the first 45 days of operation, the stack was cooled down several times for inspection, since some erratic terminal voltage had been observed. Complete temperature cycles are indicated by a double-arrow, while a cooling and heating cycle is indicated by a downward or an upward arrow, respectively. It was found that this voltage fluctuation was caused by leaking gold seals in the test fixture, which allowed some fuel and air to mix. Gold seals were used only as an expedient for test purposes. Some alloying may have lowered the melting point of the gold (which is re-used several times). During testing, three re-sealing procedures were required, after which the stack performance had stabilized, but at a lower terminal voltage. During the re-sealing operation, the stack had to be shortened, which resulted in the loss of several end cells. This accounts for the fact that only 10, out of 20 cells, remain in the test fixture. This is the reason for plotting the voltage curve, normalized for 15 cells in Figure 5.39. For day 60 in 1980 (February 29) and later, the performance is plotted for the actual 7 cells on test.

For 2000 hours of operation the stack was tested by using hydrogen as the fuel and operating at 400 mA/cm^2. During this period the average cell voltage exceeded, considerably, the target of 0.66 V (0.72 V after 2000 h). Then the fuel, delivered to the stack, was

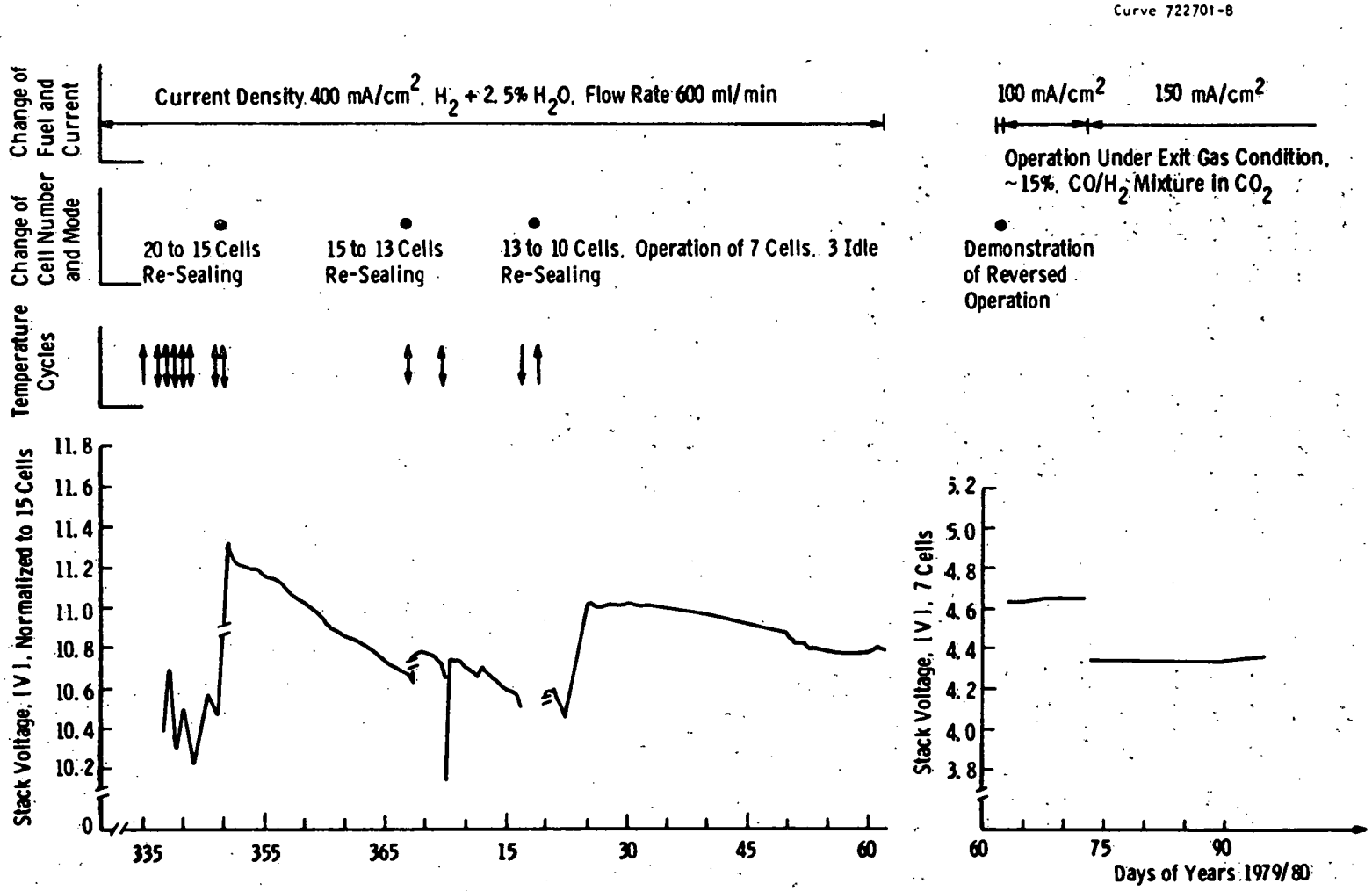

Fig. 5.39—Life event chart of first 10 watt HTSOE thin film fuel cell stack. Active cell area 1.85 cm^2. 1000°C ± 5° operating temperature (stack #8)

changed to a lean-condition "coal gas," a mixture of hydrogen and carbon monoxide, diluted with CO_2. If one assumes the peak performance of the stack at day 351 (Dec. 17, 1979) as 100%, then the stack performance deteriorated by, approximately, 5% during the 2000 hour test. It can be concluded, however, that this deterioration was not directly attributable to stack component deterioration, since voltage fluctuations seemed to be associated both with deteriorating seals, as well as with improved sealing conditions. Further evidence that cell stack components are stable in performance is shown by the steady voltage achieved under lean fuel conditions, starting day 63 (March 3, 1980) and continuing throughout day 95 on the plot of the life test (which is still continuing at this writing). This first "serious" life test of any thin film stack and test equipment indicated only one major problem, namely, the need for a reliable seal design for the test fixture. This problem has now been solved.

During the life test, the test station had to respond to intermittent losses of housepower and air supply. The fail-safe features designed into the test equipment performed properly and protected both the stack and the test apparatus. Housepower and air losses did not adversely effect the stack performance.

5.3 TASK 3. STACK PERFORMANCE EVALUATION

During the course of the two year continuation program we have prepared, or attempted to prepare, a large number of fuel cell stacks. Most of these attempts, however, were directed toward improvement of processing parameters, rather than to produce stacks for test evaluation, per se. Once a certain processing method proved to be advantageous or promising, we fabricated a test stack, to investigate the influence of a change in a component or a change in a processing parameter, upon stack performance. Nine such test stacks have been prepared, of which eight have been tested (#7 stack was not tested when it was determined that the plasma sprayed porous zirconia layer of the air electrode was too dense).

5.3.1 Five and Seven Cell Stack Performance (Stack #2)

A 7-cell stack (stack #2) was prepared from the downstream end section of a 25-cell stack, with respect to its location in the EVD reactor, during the electrolyte and IC deposition. The performance of stack #2 was compared with that of the first stack, tested under the previous contract in February 1978.* The first and last cell of the stack were equipped with current and potential leads and the stack was heated slowly to the operating temperature of 990°C with forming gas (to protect the fuel electrode from oxidation, until the gold-washer seals were tight). Hydrogen/3% water was used as the fuel and air was the oxidant. Figure 5.40 shows the initial stack performance.

The stack was cooled slowly to room temperature for instrumentation of individual cells. This was done after end sealing, in order to avoid damaging the mechanically-unstable compression seal. This seal becomes stronger after the gold washers are compressed and conform to the tube circumference. In Figure 5.40 stack #2 performance of five cells is compared with that of stack #1. Cells 1 and 7 in stack #2 were used as potential-monitoring cells, to determine inlet and outlet fuel potential.

---

*The first stack was produced from a .15 m long section, which represented the front portion of a stack having both an interconnection and electrolyte deposited by the EVD process.

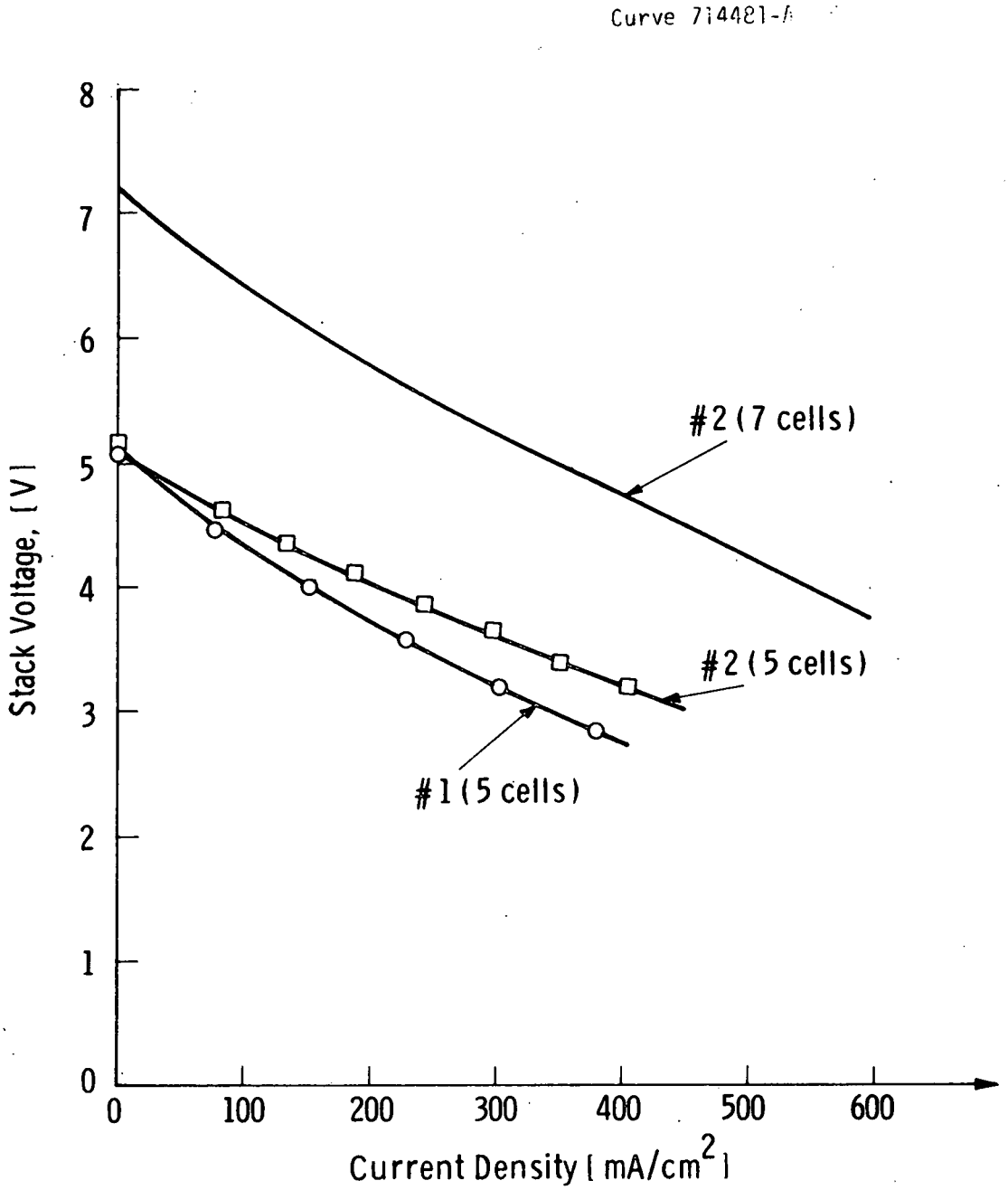

Fig. 5.40 – Performance of cell stacks at 990°C in air using H_2/3% H_2O as fuel (less than 5% fuel consumption)

Overpotential losses during stack operation were investigated, using the current interruption technique. The results are plotted in Figure 5.41 and, again, compared with results obtained from stack #1. The comparison shows that both stacks behave similarly with respect to slow (concentration) polarization. Stack #2 shows some improvement (5 to 10%) over stack #1.

However, considerable improvement is seen with respect to the reduction of ohmic resistance of stack #2, which is only 50 percent of the internal resistance of stack #1. The calculated IR characteristic shows that a further reduction by 50 percent should be achieved with present materials. This IR curve was calculated for the following conditions:

- Temperature - 1000°C
- Stack circumference - 4.15 cm
- IC active band width - 0.25 cm
- IC thickness - 40 μm
- IC resistivity - 31 Ω-cm
- Active cell band width - 0.43 cm
- Electrolyte thickness - 20 μm
- Electrolyte resistivity - 10 Ω-cm
- Fuel electrode ρ/δ - 0.1 Ω
- Air electrode ρ/δ - 0.4 Ω
- Equalized conductor length for fuel and air electrode (center of electrode to center of interconnection) - 0.55 cm

Using these data one calculates average resistances for five interconnected cell components as follows:

Fuel electrodes	0.066 Ω
Air electrodes	0.265 Ω
Electrolyte	0.056 Ω
Interconnections	0.598 Ω
TOTAL	0.985 Ω

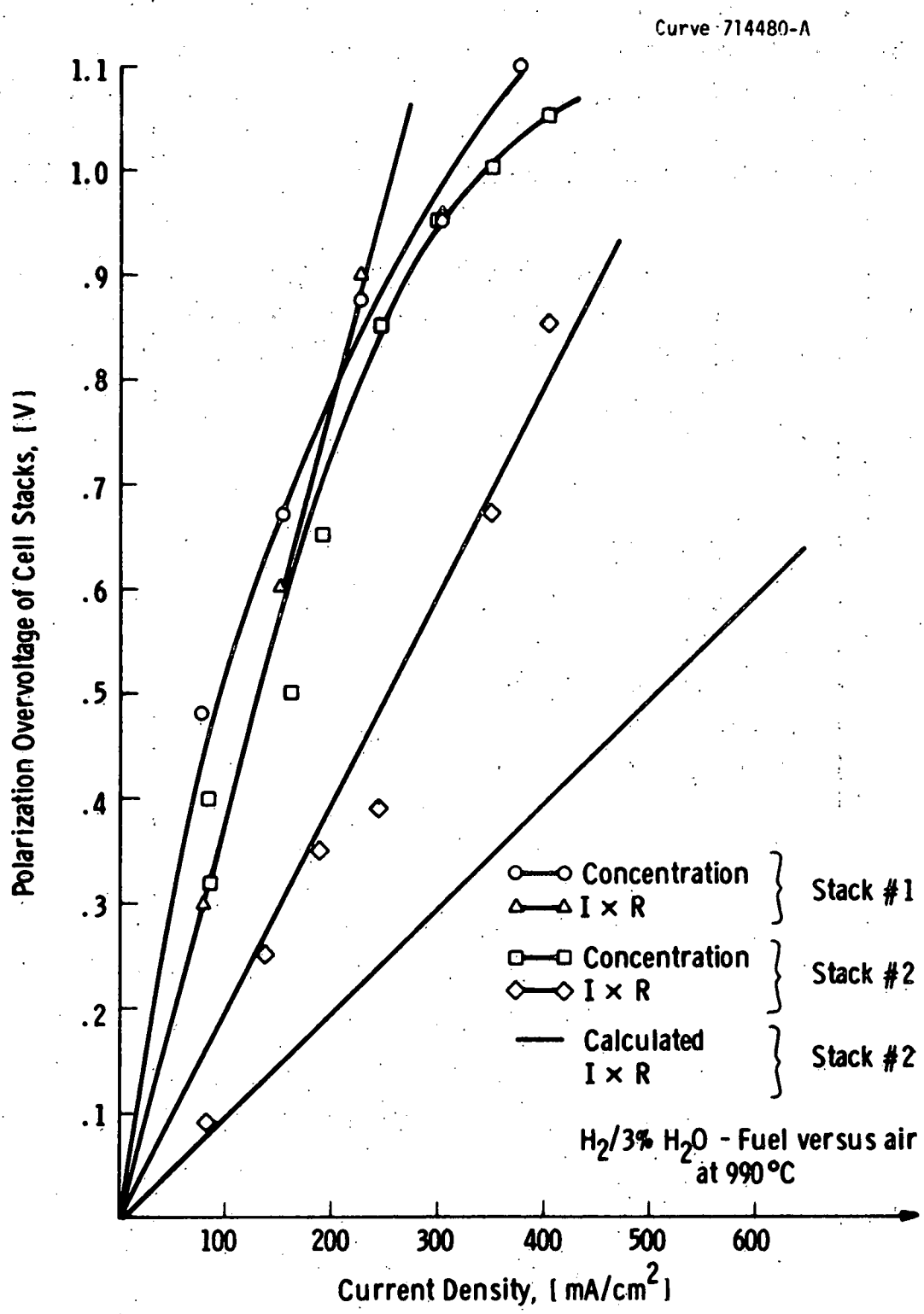

Fig. 5.41 – Polarization losses in #1 and #2 stacks of 5 cells each

The reduction of internal resistance of stack #2 was due to improvements in deposition conditions for IC materials. Also, better-conducting air and fuel electrodes had been fabricated. The approximate calculation showed, also, that resistance-related improvements in performance could best be achieved by reducing air electrode and IC resistance. While air electrode conductance could be improved moderately, it was believed that of the interconnection could be improved by almost one order of magnitude, after proper doping levels had been obtained.

The calculations did not take into consideration the resistance that was introduced by the porous layer between electrolyte and air electrode collector, due to the absence of measured data. It was assumed, however, that this resistance could add as much as 0.1 Ω to the total stack resistance.

Slow, but steady, deterioration of stack performance was observed from the beginning of the test. The deterioration was not caused by leaks, as open stack voltage was near 99 percent of the theoretical value. It had been observed that, during the first temperature cycle, indium oxide flakes had fallen off the interconnection region, as seen in the photo of stack #2 if Figure 5.42. This effect had been noted also in stack #1, yet not to the degree as in stack #2. Stack #2 had a thicker In_2O_3 layer than stack #1 and, when it lifted off the IC, it flaked in much larger patches. During testing it became obvious that the stack would not meet the life performance goal after 1000 hours of operation and therefore, it was removed from the life test apparatus. The stack was disassembled for analysis. The flaking of In_2O_3 - current collector over the IC leads to additional lateral resistance losses in the collector and introduces contact resistance between the air electrode collector and the IC. None of these losses had been considered in the cell resistance calculations, because of the inability of making valid assumptions. These facts could explain the considerable discrepancy between measured and calculated ohmic resistance of the cell stack. After removal from the life test apparatus, the cell stack was leak tested. It exhibited similar gas tightness, as before mounting and elevated temperature operation.

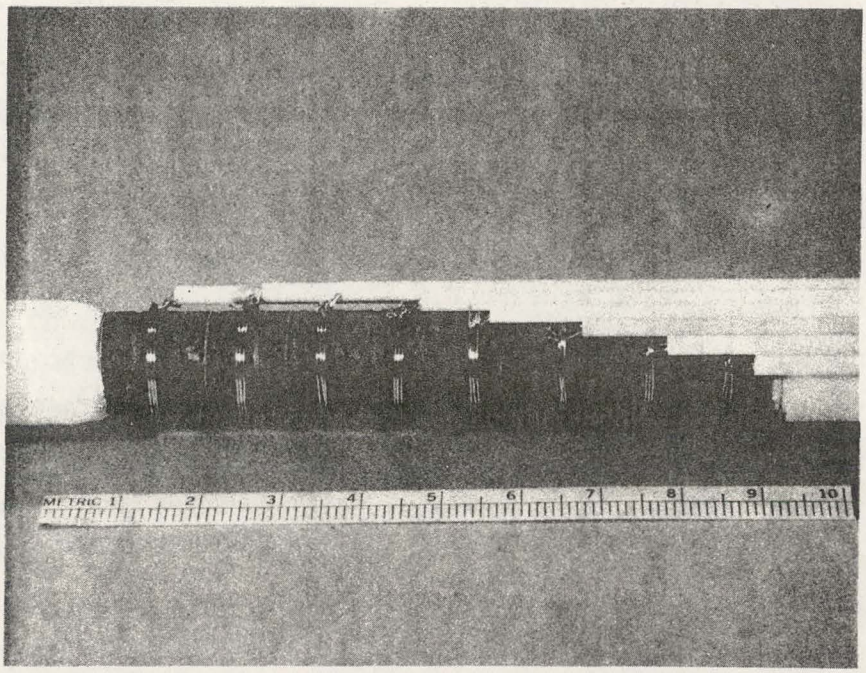

Fig. 5.42. Five-cell stack test of seven-cell module (stack #2), (showing flaking in the dark crystalline IC bands).

5.3.2 Five-Cell Stack Performance (Stack #3)

Stack #3 was prepared with the specific goal of reducing the IC resistance losses, using the latest improved deposition techniques for lanthanum chromite. The air and fuel electrode performance of stack #3 can be assumed to be similar to that of stack #2, because of identical materials and fabrication techniques. The improvement in stack performance was, therefore, attributed to the higher conductivity of the IC layer, see Figure 5.43, curve A. The stack, initially, exceeded the performance goal of this program (0.66 V at 400 mA/cm^2), demonstrating the correctness of our assumption that the reduction of internal resistance, especially that of the IC layer, will improve stack performance considerably. Similar to stack #2, the stack performance deteriorated, due to In_2O_3 - flaking from the IC area.

5.3.3 Fourteen-Cell Stack Performance (Stack #4)

Durable air electrode-IC contact should lead to steady stack performance. In order to test materials, that can be applied to IC's, we chose strontium-doped lanthanum manganite sintered powder layers. Since the resistivity of this material is close to 5×10^{-3} Ω cm (when dense), we used it also as air electrode current collector. Curve B in Figure 5.43 represents the stack characteristic. The stack performance was steady (for seven days; four thermal cycles) and demonstrated the possibility of using other oxides in contact with the IC. However, performance goals could not be achieved, due to the higher resistance in the air electrode current collector (porous $La_{0.9}Sr_{0.1}MnO_3$) of the stack.

5.3.4 Conclusions of Performance for Stack #2 to Stack #4

It has been shown that performance goals of 0.66 V at 400 mA/cm^2 can be obtained, yet IC contacting problems to In_2O_3 prevented steady stack performance. Steady, yet insufficient performance was obtained with doped lanthanum manganite IC contacts. The goal of our work, therefore, was directed to combining both materials to meet stack target performance.

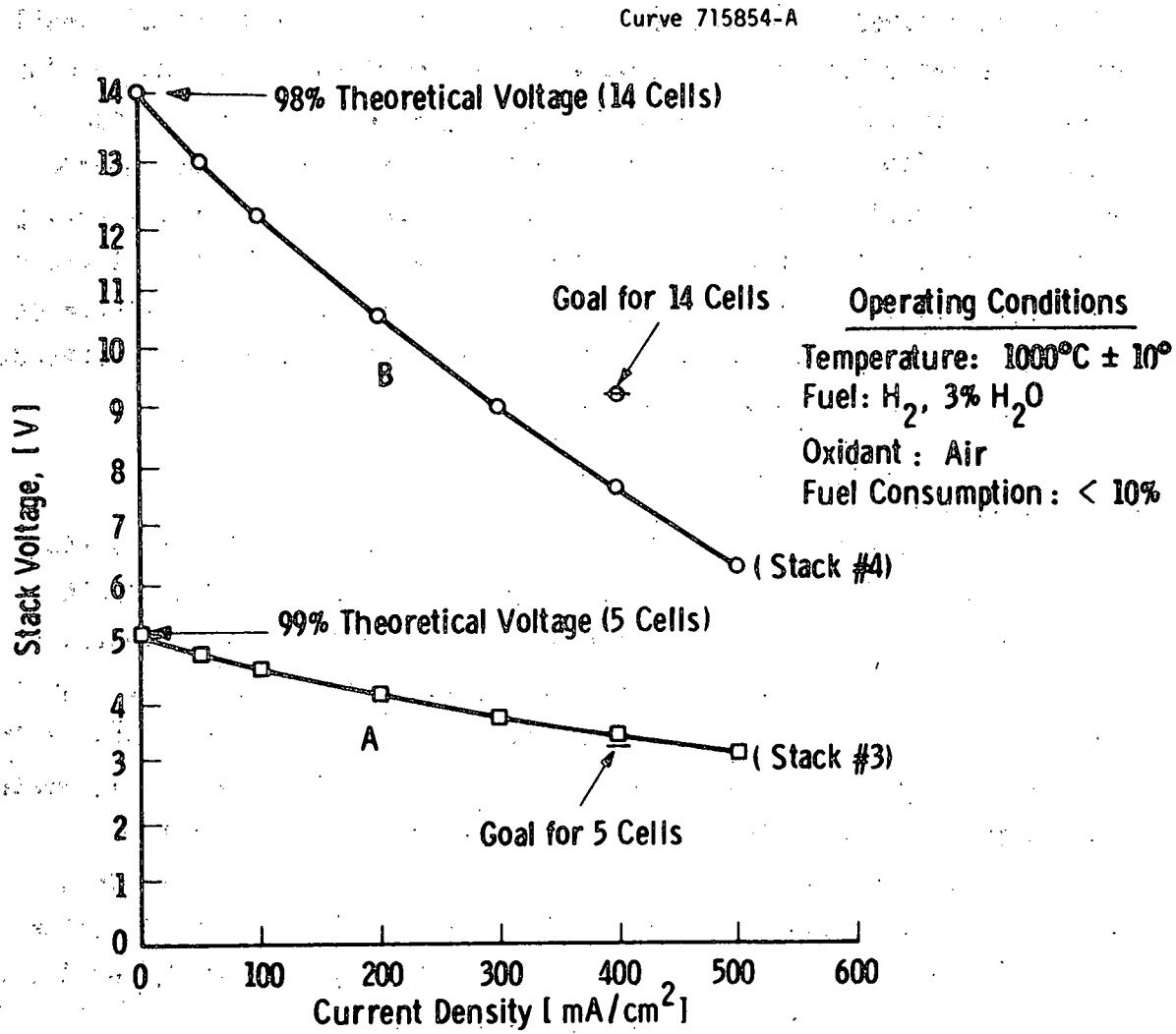

Fig. 5.43 – State-of-the-art performance of cell stacks
A - In_2O_3 - air electrode B - La MnO_3 - air electrode

Stacks were to be fabricated, that would connect the IC material with the In_2O_3 air electrode current collector, via a porous layer of lanthanum manganite, sandwiched between these two layers. The short excursion into testing doped La MnO_3 as air electrode current collector, suggests future work in trying to replace In_2O_3 altogether, by less expensive and less attack-susceptible oxides.

5.3.5 Eighteen-Cell Performance (Stack #5)

Interconnection-air electrode contact deterioration can be prevented through the use of lanthanum manganite as the primary contact to the modified lanthanum chromite IC*, based on test results obtained in 14-cell stack #4. The introduction of this new cell component necessitated immediate life testing, before a recommendation could be made for incorporating it into a stack that could achieve a 1000 hour life goal.

An eighteen-cell stack was fabricated, using the interconnection over the electrolyte overlap technique.* A strontium-doped lanthanum manganite layer was used as the air electrode, contacting the IC. The layer was sinter bonded to the electrolyte and the IC material, using sintering aids. The porous structure was impregnated with cobalt-praseodymium oxide, which served as the active air electrode material. The finished stack was leak tested and leaks were detected in overlap areas, due to layer delamination. Nevertheless, the stack was tested, because some leaks can be tolerated in the absence of indium oxide current collector, since lanthanum manganite is relatively forgiving with respect to reduction attack. Hydrogen-3% water vapor was used as the fuel (with less than 10% consumption) and air as the oxidant. The stack failed to achieve full theoretical voltage (actually, 94% of theoretical), yet the performance was relatively stable, increasing slightly over the first one hundred hours

---

* Right side of Figure 5.7, Annual Report, April 1979, p. 29.

and slightly decreasing for the remaining 900 hours. The ohmic stack resistance was high, due to poor air electrode conductance and polarization, so that the stack was operated at only 200 mA/cm^2 (50% of design goal) at 0.63 V average cell voltage (0.66 $\overline{V}$, design goal). Figure 5.44 shows the performance variation during the 1000 hour life test. The performance stability in the presence of obvious leaks is impressive.

After test completion, the stack was disassembled and inspected. Figures 5.45 and 5.46 show the total stack and Figure 5.47 is a close-up view, indicating no change in appearance due to test. Leaking areas, however, were evidently eroded due to hot spot action, as seen in Figure 5.46. The visual inspection did not reveal any real problem, with respect to using lanthanum manganite as the contact to the air electrode stack component. Confirmation of that impression was obtained through microscopic analysis of polished stack cross sections. Figures 5.48, 5.49, 5.50, and 5.51 show views of three critical stack areas. None reveal any solid state component interaction during the 1000 hour life test at 1010°C. The stable nature of the components and their interfaces are very important, with respect to potential stack-life-prediction. From these results, it was concluded that these component combinations would probably be stable for a much longer time than 1000 hours, with an order of magnitude improvement in life to be expected within the next two years.

5.3.6 Twenty-Cell Stack Performance (Stack #6)

The encouraging life test data of stack #5 (sintered lanthanum manganite air electrode) led to the fabrication of cell stack #6, using plasma sprayed lanthanum manganite air electrodes. It was hoped that the plasma sprayed lanthanum manganite layer would be more conducting than the sintered layer, applied in stack #5, and thus raise the power output to the targeted, 10 watt level for 20-cell stacks.

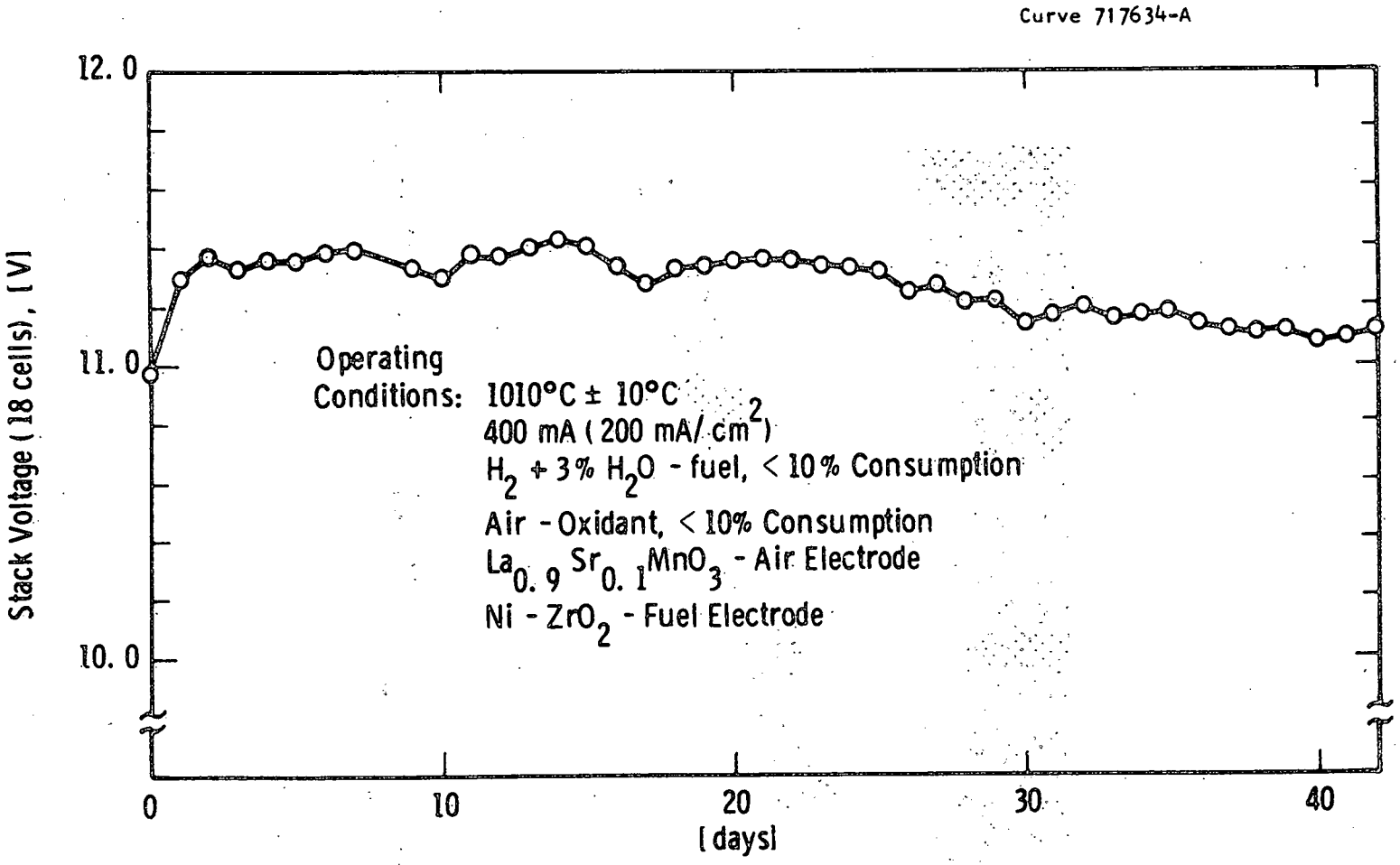

Fig. 5.44 — 18 Cell stack (Stack #5) life test characteristic

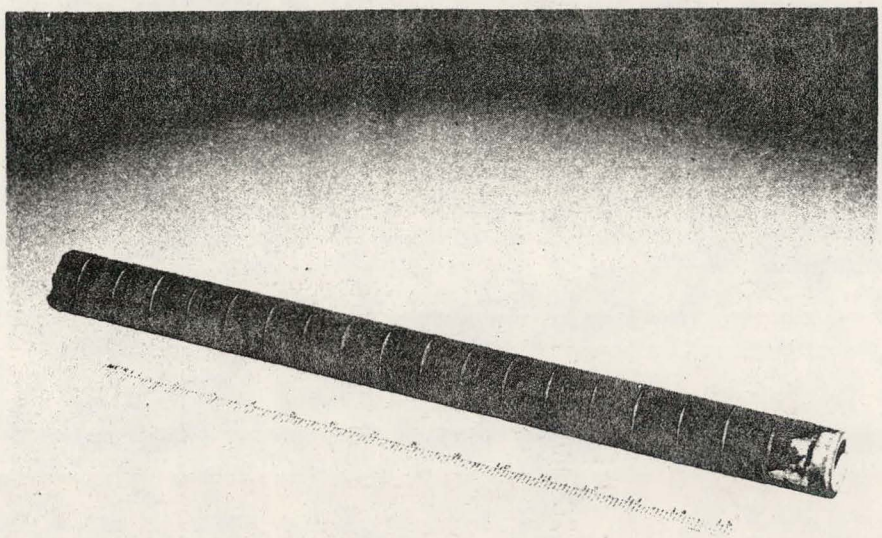

Fig. 5.45. 18-cell stack (#5) appearance after 1000 hour test at 1010°C (good side).

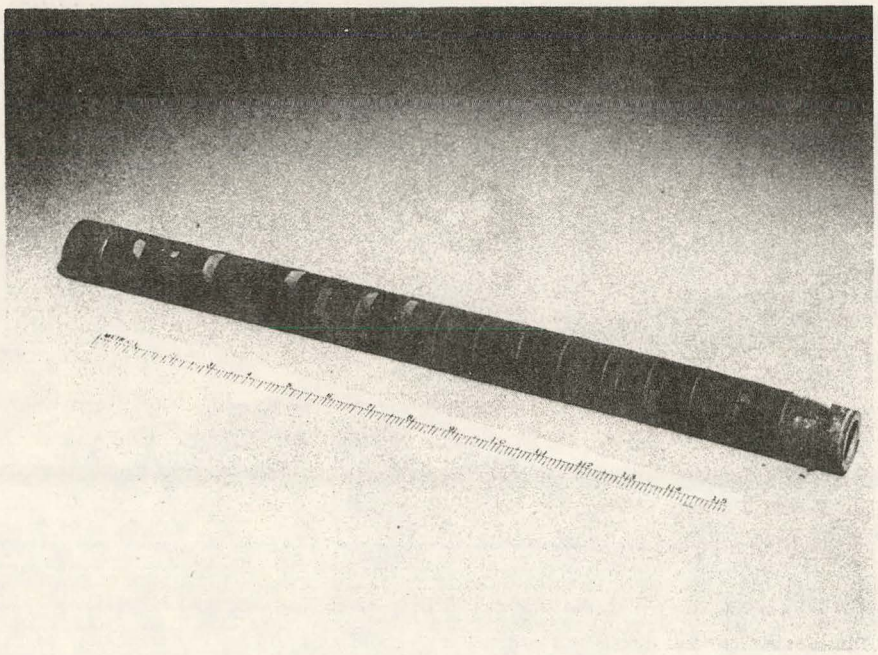

Fig. 5.46. 18-cell stack (#5) appearance after 1000 hour test at 1010°C, showing damaged areas resulting from butt joint leaks in interconnection-electrolyte interfaces.

RM-80913

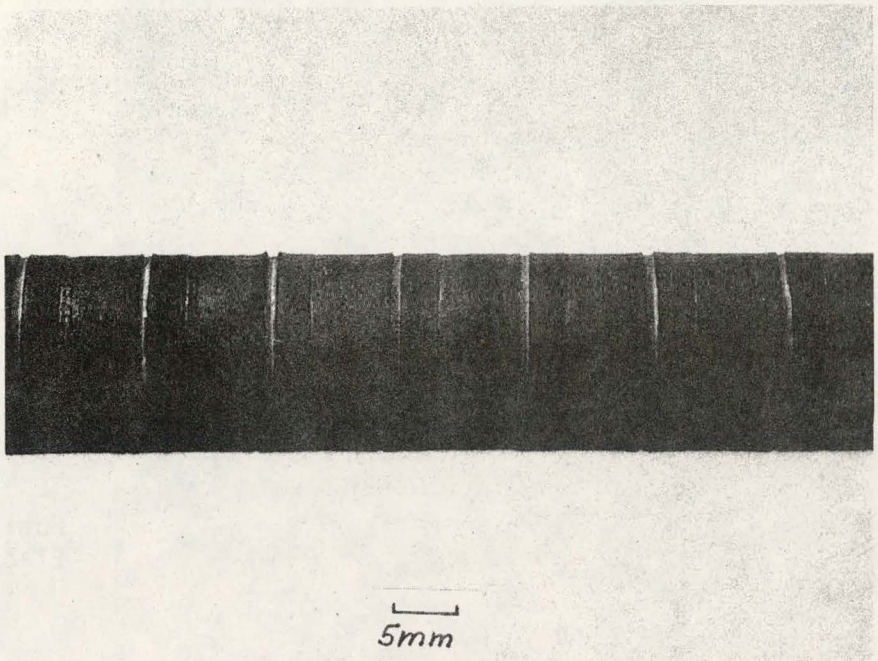

Fig. 5.47. 18-cell stack (#5) close-up, showing unchanged appearance after 1000 hours continuous operation at 1010°C.

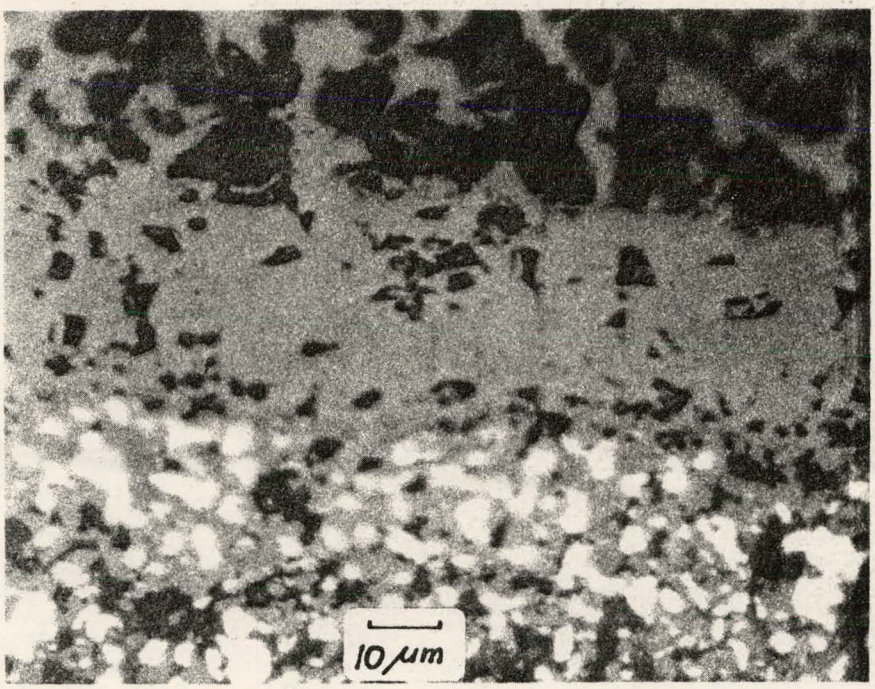

Fig. 5.48. Lanthanum manganite - lanthanum chromite - fuel electrode sandwich after 1000 hours of operation at 1010°C.

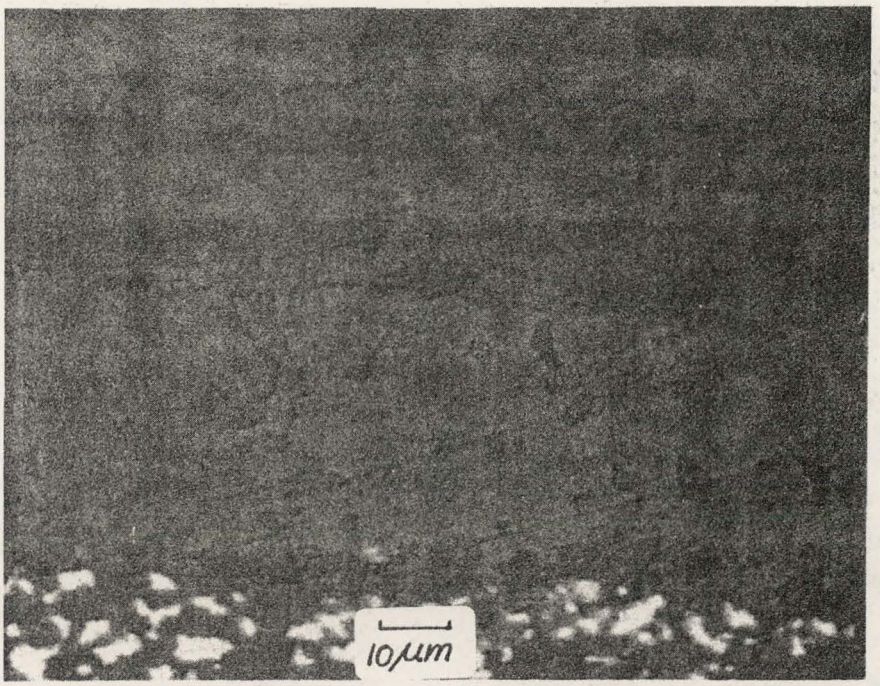

Fig. 5.49. Electrolyte - lanthanum chromite - fuel electrode sandwich in overlap region, after 1000 hours of operations at 1010°C.

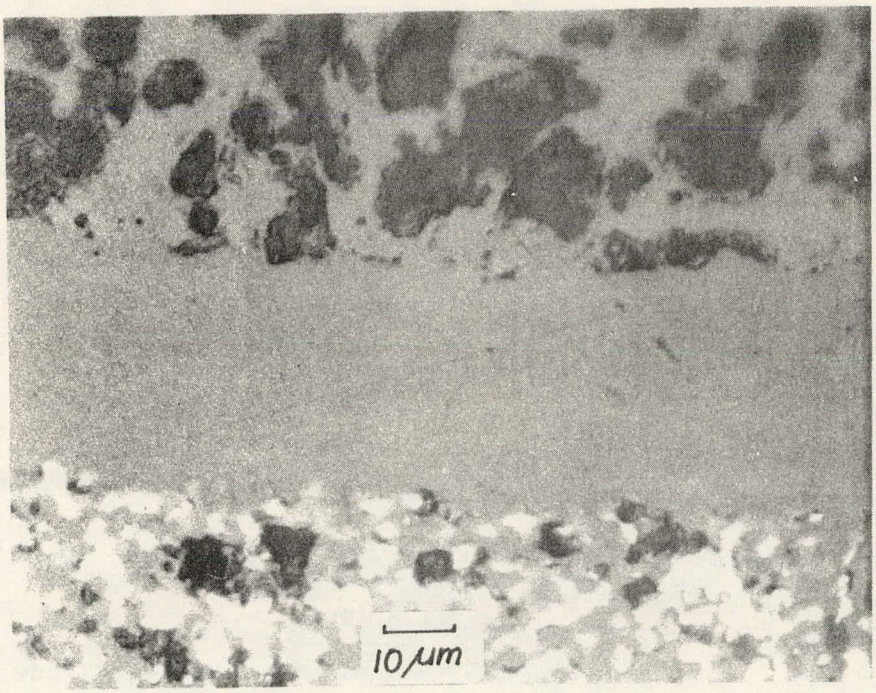

Fig. 5.50. Lanthanum manganite - electrolyte - fuel electrode sandwich after 1000 hours of operation at 1010°C.

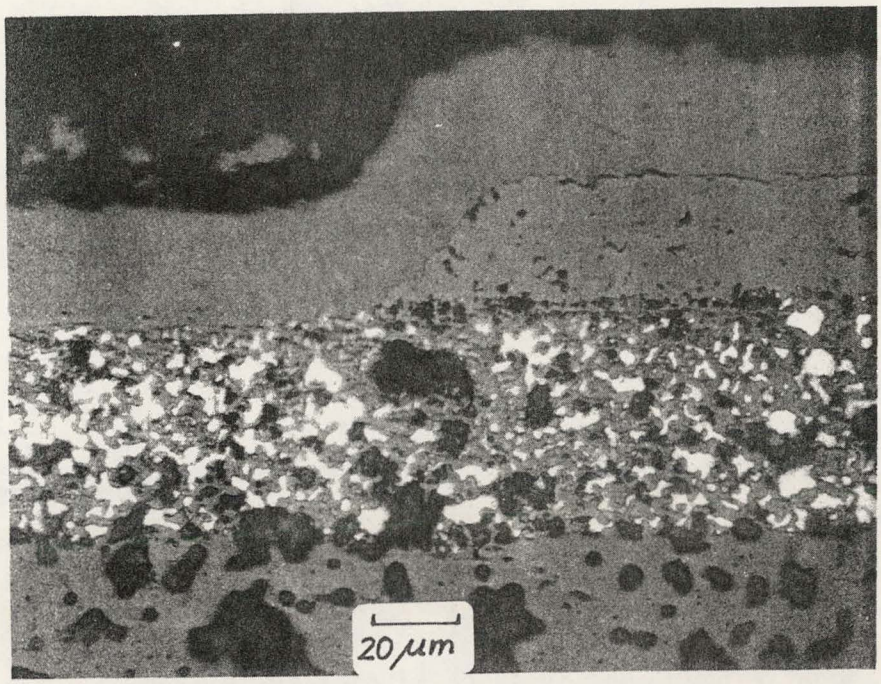

Fig. 5.51. Critical seal area of stack (electrolyte overlapping interconnection). Appearance after 1000 hours of operation at 1010°C.

Stack #6 was tested and the performance characteristic is shown in Figure 5.52. The poor performance of the stack #6, as compared to #5, was due to the interface between the air electrode and the electrolyte being masked by large areas by dense plasma-sprayed electrode material. This structure is explained by the sudden quenching of the molten, sprayed droplets that exit the plasma jet and impinge on the much colder substrate. The sintered air electrode layer of stack #5 did not block the vital air electrode/electrolyte interface and showed much reduced polarization, even though its lateral electrode resistance was higher than that of the plasma-sprayed electrode. Figure 5.53 is a cross section through the active cell areas of a) a sintered lanthanum manganite electrode and b) a plasma sprayed electrode in contact with electrolyte. Figure 5.53 shows that the air electrode porosity is also reduced by plasma spray coating, which may contribute further to stack overvoltage.

The fact that both stacks did not achieve full stack voltage can be explained by misalignment of air electrode coatings and electronic shorting across insulating gaps between cells by the cobalt praseodymium oxide impregnation. This caused short currents in both stacks. The shorts, however, have no significant effect on the slope of the stack characteristic, yet they do reduce stack voltage considerably.

In subsequent experiments on stack fabrication, plasma sprayed layers of this material helped to improve cell resistances downward, to $\sim$0.13 Ω/cell.

5.3.7 Subtask A. Power Output

The purpose of this subtask was to fabricate a fuel cell stack that can deliver, at least, 10 watts of peak power, using H_2-3% H_2O fuel inlet fuel and air as the oxidant source, at 1000°C.

Curve 721090-A

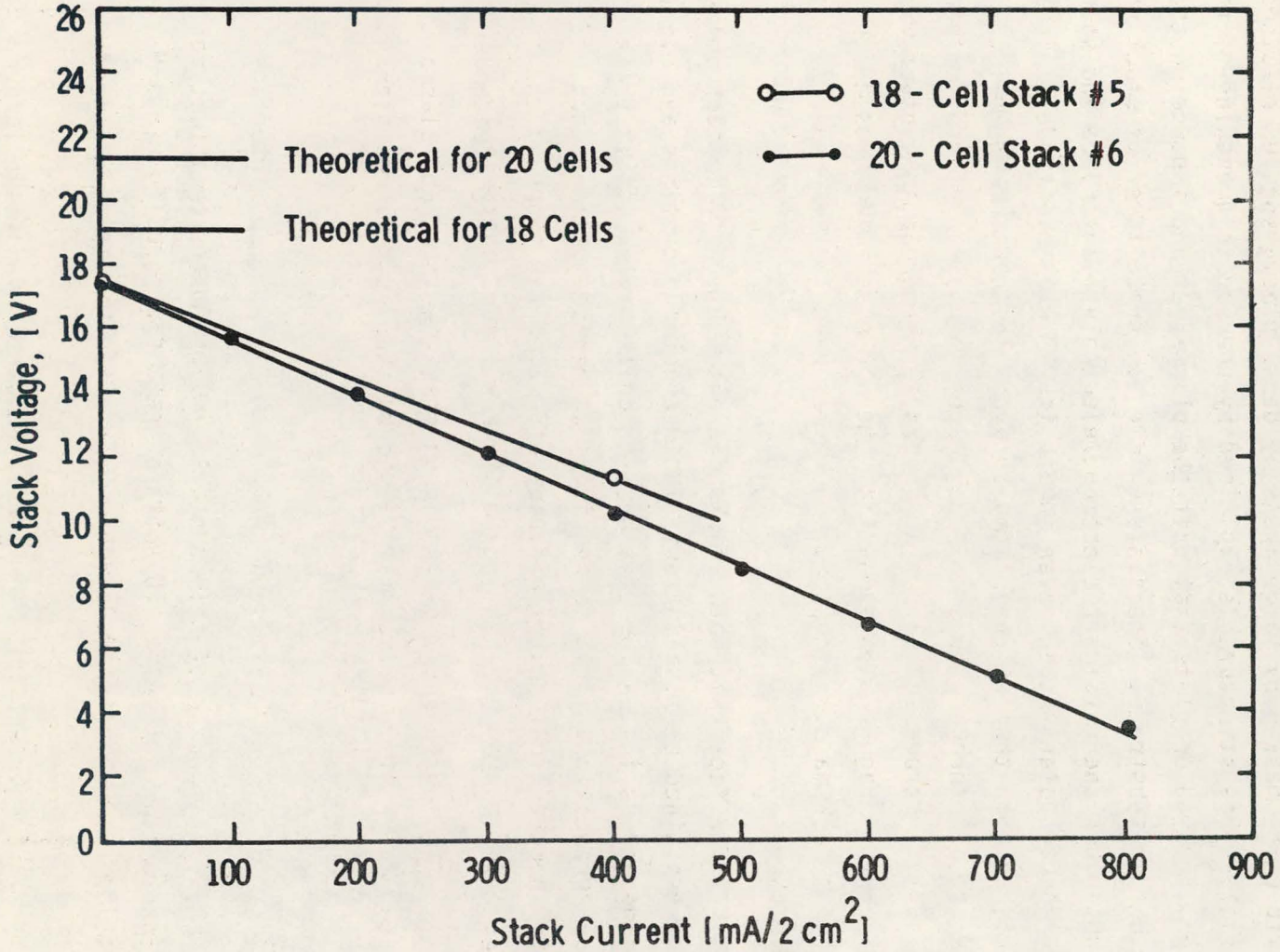

Fig. 5. 52 – Performance of cell stacks 5 and 6 at 1010°C ± 10°C

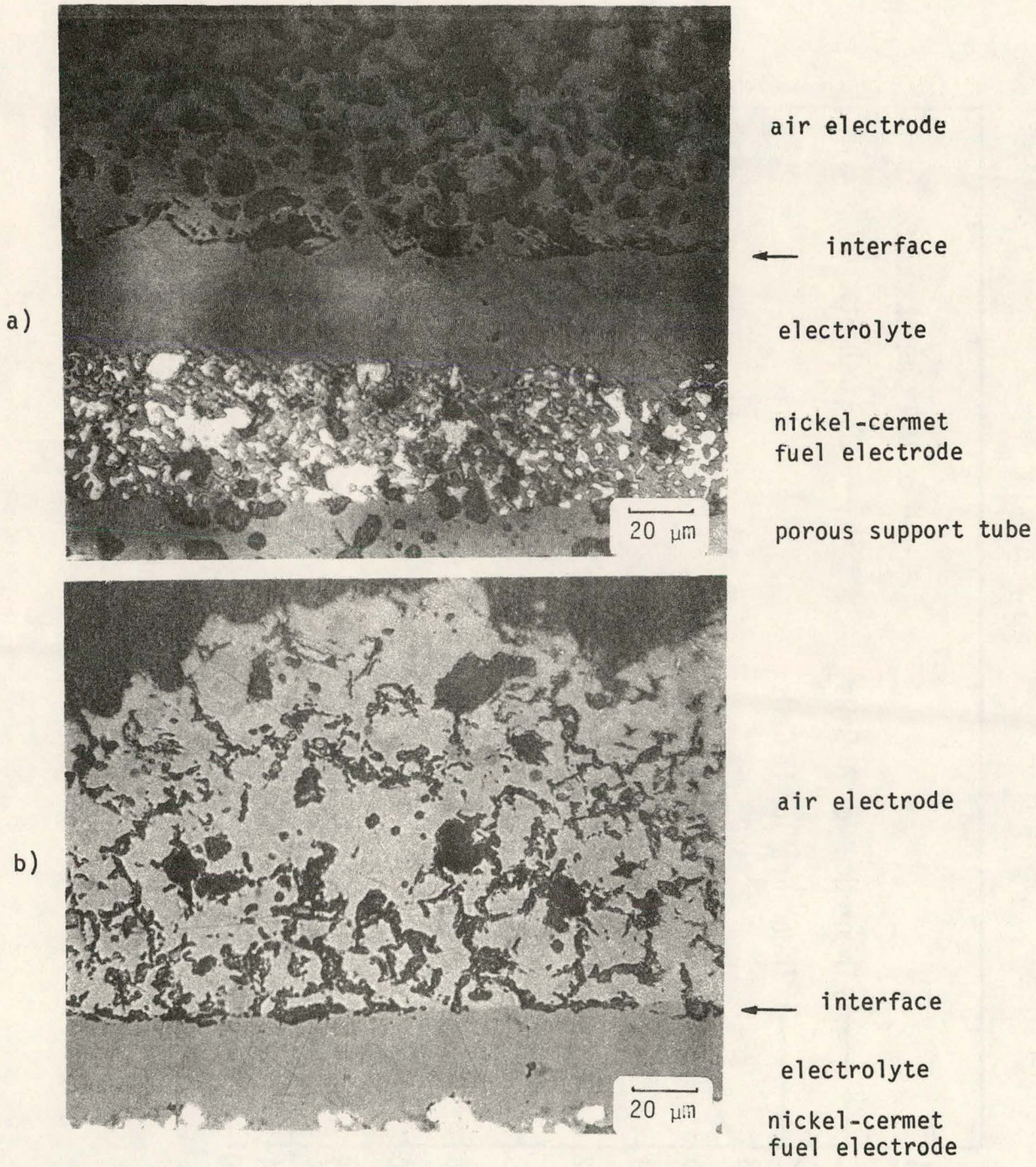

Fig. 5.53. Cross section through a) sintered, b) plasma sprayed lanthanum manganite air electrode, interfacing solid oxide electrolyte.

5.3.7.1 First Thin-Film 10 Watt Stack (Stack #8)

Stack #8 incorporated all the improvements we had made with respect to processing parameters. especially through elimination of pre-deposition contamination in EVD runs. Also this stack was constructed with a porous interface at the air electrode current collector-IC interface.

The 20-cell arrangement (stack #8) delivered more than 13 watts at half the open stack voltage; the 15-cell stack arrangement delivered 11 watts, under similar conditions (H_2-3% H_2O fuel inlet condition, air oxidant). Both exceeded the 10 watts, minimum, stack power requirement for a 20-cell stack.

As can be seen from the performance characteristics (Figures 5.54 and 5.55), we tested the stack under fuel-rich, as well as modified exit-gas compositions (with N_2 as the diluant instead of CO_2). During these tests we established maximum-allowable current densities, as determined by the point at which the fuel electrode is anodically oxidized. This point is easily found by current interruption techniques and by the general "unforgiving" behavior of the cell stack. These crucial tests were performed during the 8th day of stack operation. It was concluded that a certain amount of stack deterioration was due to these stringent tests. Also, volume expansion of the nickel fuel electrode, during anodic oxidation, could lead to undue mechanical stresses in the solid state structure and could lead to separation from, or cracking of, the solid electrolyte, while life testing was progressing.

Due to the development of leaky seals in the test-assembly, the stack was temperature-cycled eleven times for inspection and resealing attempts. After the last sealing procedure, the stack arrived at a stable performance plateau, having completed nearly 1800 hours of operation at 400 mA/cm^2 with hydrogen as the fuel. During this time period, the stack showed a decline in performance of only 5%, if its peak performance during the ninth day of operation is assumed as 100%. As explained in Section 5.2.6 we had to eliminate end cells for resealing purposes, so that the 10 watt (plus) power output was achieved with 15-20 interconnected cells for 650 hours. In conclusion, the observed performance deterioration was caused by the leaky stack seals in the test fixture and not by component interaction.

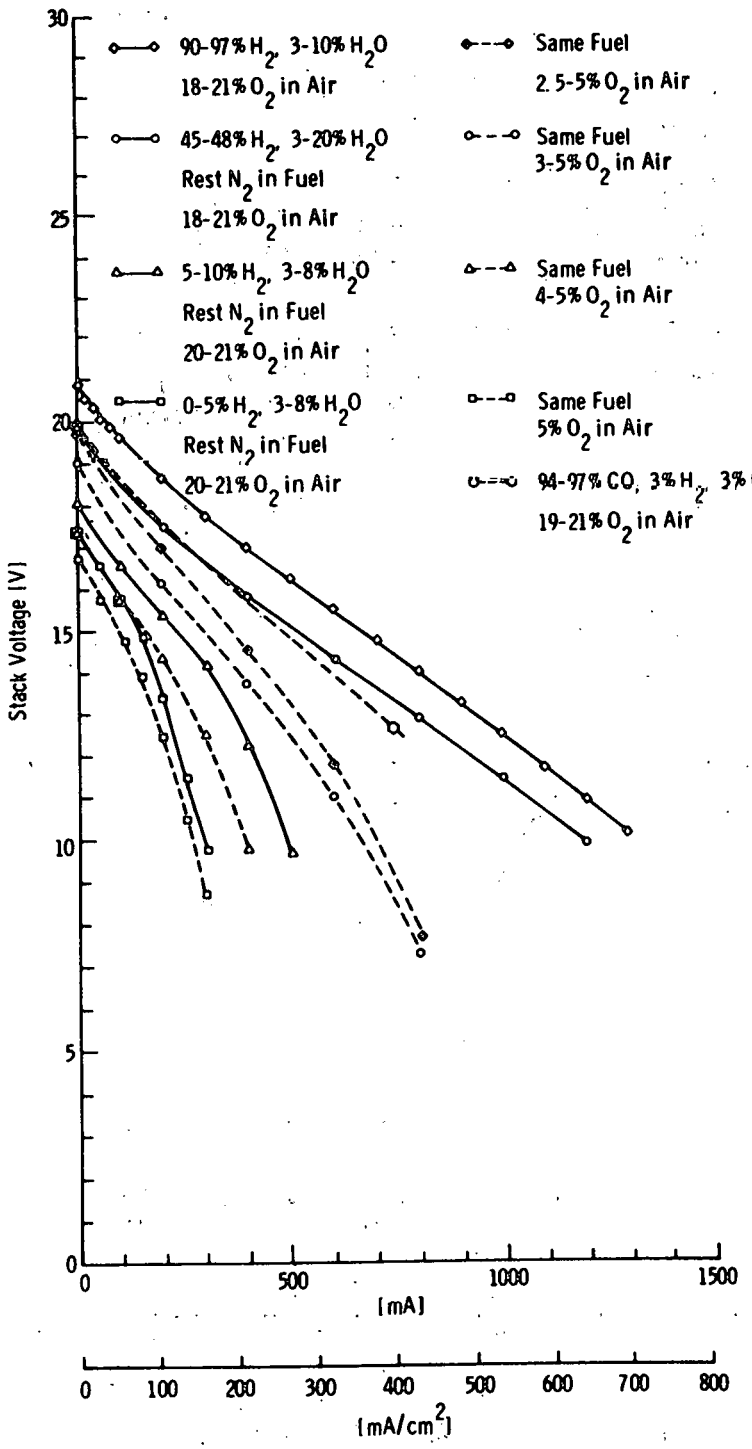

Fig. 5. 54 – Performance of 20-cell stack #8 at 1000°C under various fuel and oxidant conditions

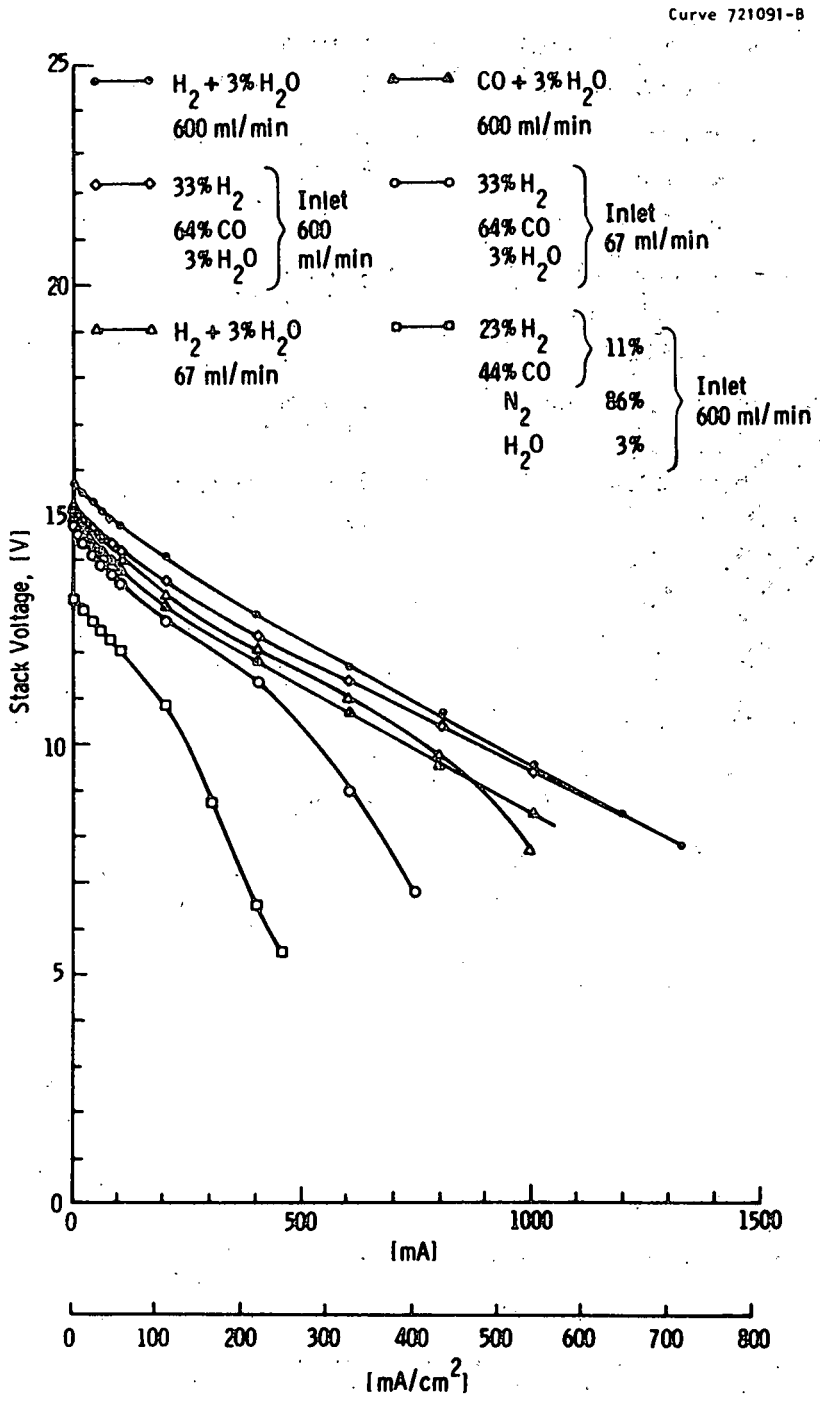

Fig. 5. 55 — Performance of 15-cell stack (Stack #8) at 1000°C, under various fuel conditions (21% minus O_2 in air, ~600 ml/min)

After 2000 hours of operation, we converted from rich fuel (H_2 + 3% H_2O) to a gas containing only 15% fuel (40% H_2 + 60% CO) mixed with 85% carbon dioxide. Such a fuel compares, favorably, with near-exit gas conditions that are anticipated in a practical fuel cell generator. The performance of a 7-cell section of the stack #8 is shown in Figure 5.39 at a current density of 100 mA/cm^2 and 150 mA/cm^2. The inlet fuel gas potential is close to 755 ± 5 mV versus air. The stack assumed a stable, voltage performance plateau immediately and life testing is continuing.

5.3.7.2 Second Thin Film 10 Watt Stack (Stack #9)

Another stack was fabricated, using the same processing sequence, as for stack #8, which had 18 interconnected cells. The stack performance is shown in Figure 5.56. The stack performed for two days, using hydrogen as the fuel, at 400 mA/cm^2. The two end cells were then separately instrumented, to determine inlet and outlet fuel potential. The stack has been cooled and has been reserved for electrical testing, using complex admittance measurements. This will be the first attempt to employ this technique for electrical-stack analysis. The successful completion of this stack shows the ability of reproducing processing and performance parameters.

5.3.8 Stack Performance Evaluation in Electrolysis Mode

After having achieved the life- and performance-target goals on the program with cell stack #8, we conducted an additional test, to demonstrate the reversibility of the mode of operation. This short-time test was done in order to obtain further information on the basic capability of an HTSOE fuel cell, that could be part of an energy storage system, which would require the stack to operate as an electrolyzer. Also, due to the fact that the cell is driven by a DC power source, one can increase the current density, considerably, and thereby, test stack resistive behavior. The test results, using CO/CO_2 mixtures and H_2/H_2O mixtures, respectively, are summarized in Figure 5.57 and Figure 5.58.

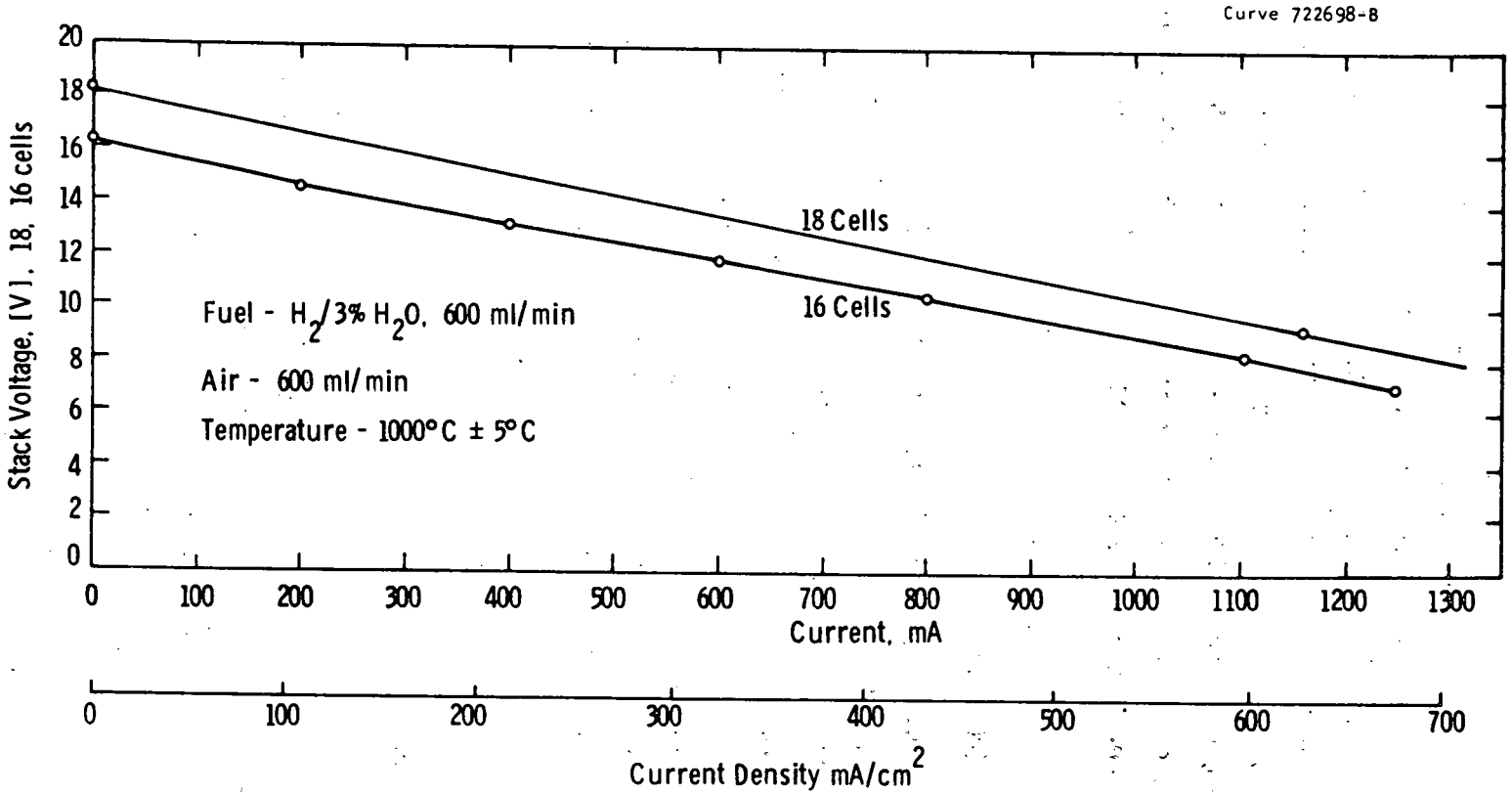

Fig. 5.56 – Performance of second 10 watt HTSOE thin film fuel cell stack (stack #9)

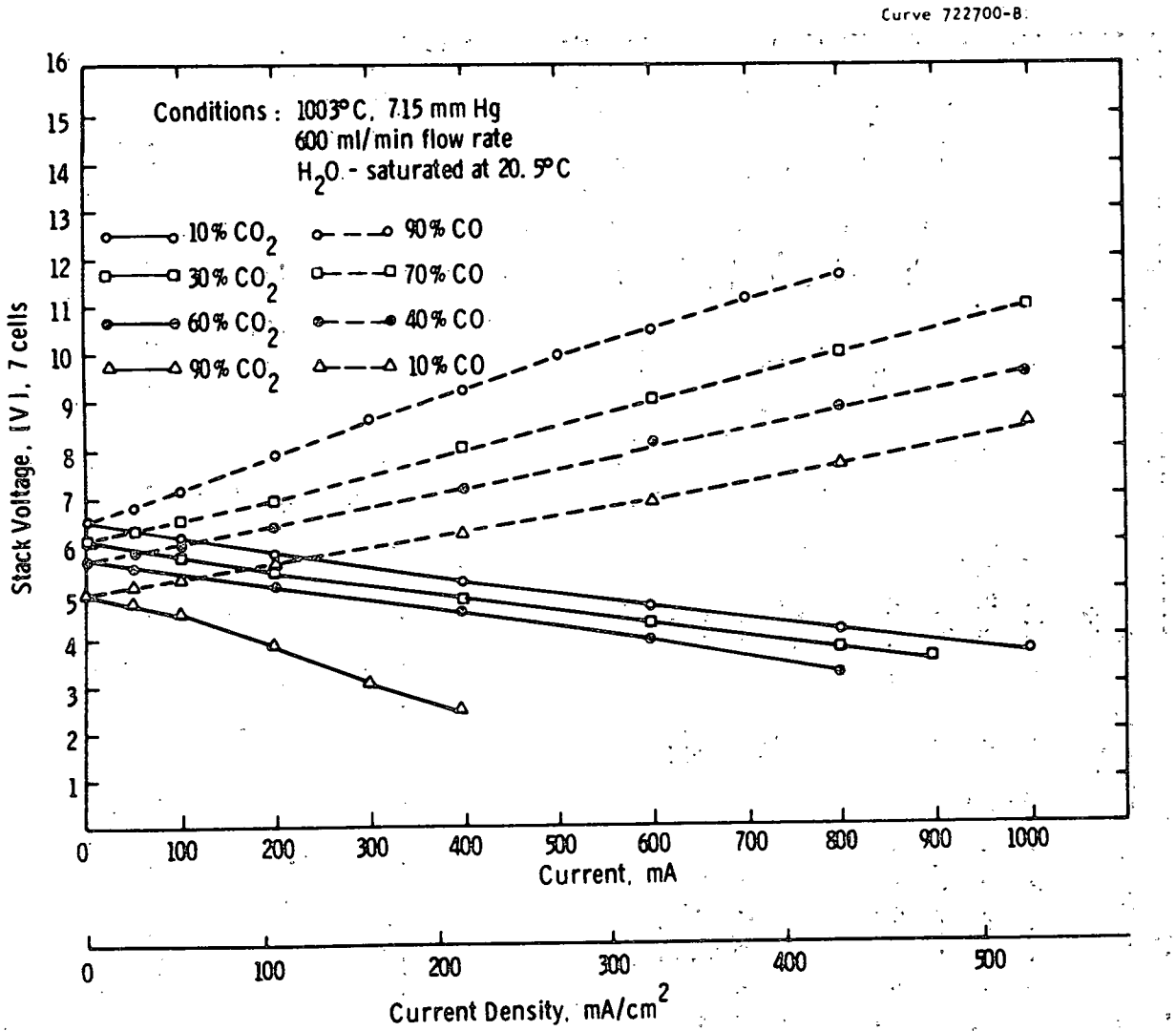

Fig. 5.57—Demonstration of reversibility of 7-cell stack, using CO/CO_2 gas mixtures

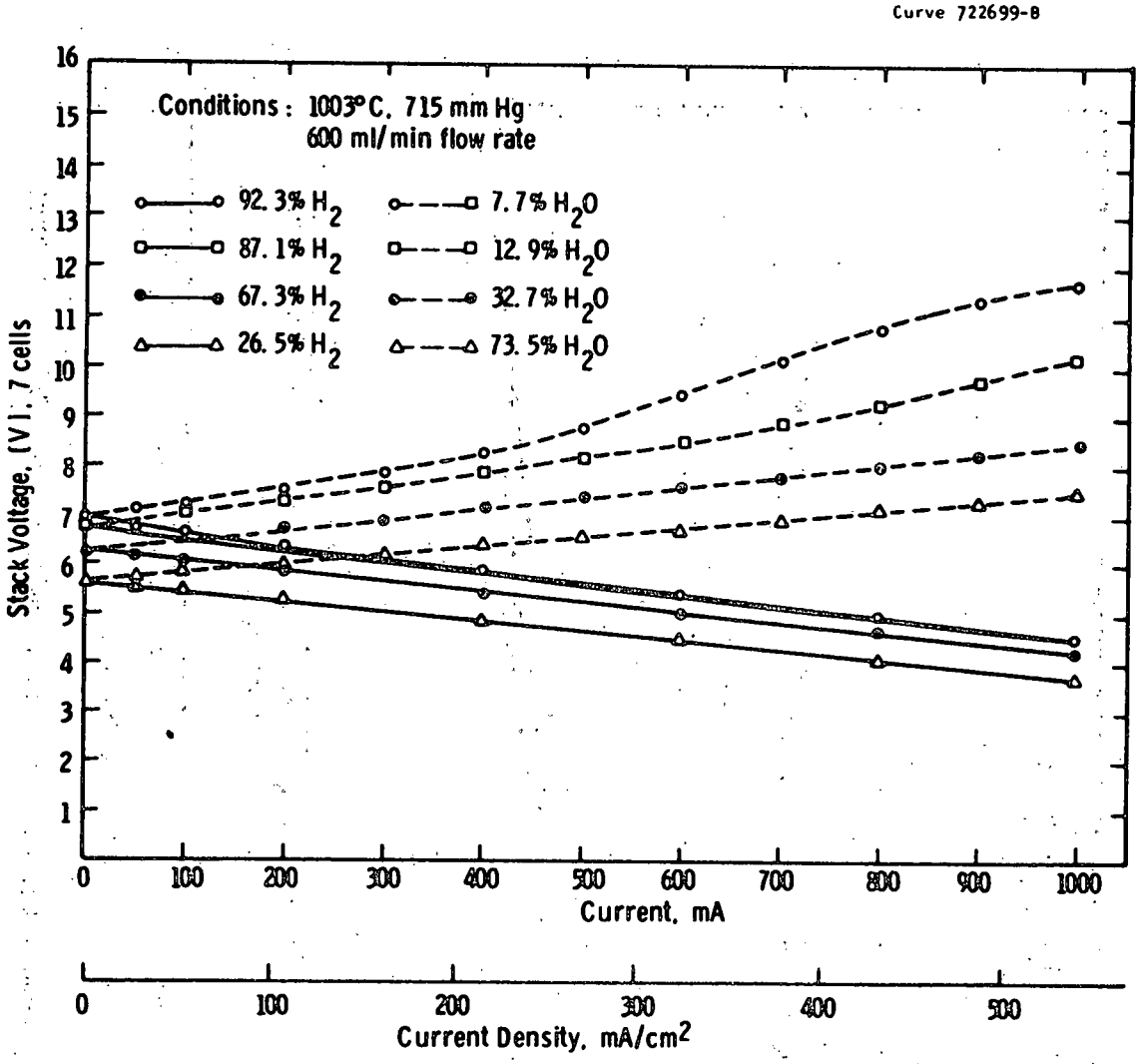

Fig. 5.58—Demonstration of reversibility of 7-cell stack, using H_2/H_2O gas mixtures

The open stack potential in these tests is equal for the fuel cell and electrolyzer mode of operation, because a flow of air was used even during the electrolyzer mode of operation. A simple potential adjustment must be made to arrive at the electrolysis cell voltage with pure oxygen on the oxide electrode.

5.3.9 Effect of Inter-Cell Electrical Leakage on the Cell Open Circuit Potential

It has been observed that, during the preparation of the fuel electrode, nickel oxide can diffuse into the stabilized zirconia of the porous support tube and increase its electronic conductivity. This would provide a current leakage path between adjacent cells and, consequently, reduce the cell open circuit potential below the theoretical value.

To determine whether these effects actually occurred, a section of porous support tube containing only fuel electrodes was tested. The specimen was placed in a hydrogen-water atmosphere and the leakage resistances (through the support tube) between two sets of adjacent fuel electrodes were measured over a temperature range of 400 to 1000°C. A wide range of applied potentials were employed (20 to 1000 mV) but the resistances measured were independent of the potential, and were nearly identical for the two sets of electrodes. A plot of this resistance as a function of temperature is presented in Figure 5.59. Activation energies for the conduction process were high, about 1.2 to 1.8 eV, and of the magnitude expected for electronic conduction in these oxides. At 1000°C the leakage resistance was about 45 ohms.

The effect of a leakage resistance of this magnitude on a cell comparable to those of the experimental five cell stack can be estimated. One would expect the open circuit potential, V_o, to be approximately 27 mV lower than the theoretical value, E_o. From the actual stack data one finds that V_o was about 38 mV lower than E_o. Considering the uncertainties in the electrode gap spacings and the diffusion of the nickel oxide which produced the leakage resistance, it is felt that this was reasonable agreement.

One concludes that: (1) the fuel electrode preparation treatment introduces a moderate amount of electronic conductivity into the zirconia of the porous support tube and (2) this provides a current leakage path between adjacent cells which results in a 3 to 4% reduction of the open circuit potential below the theoretical value.

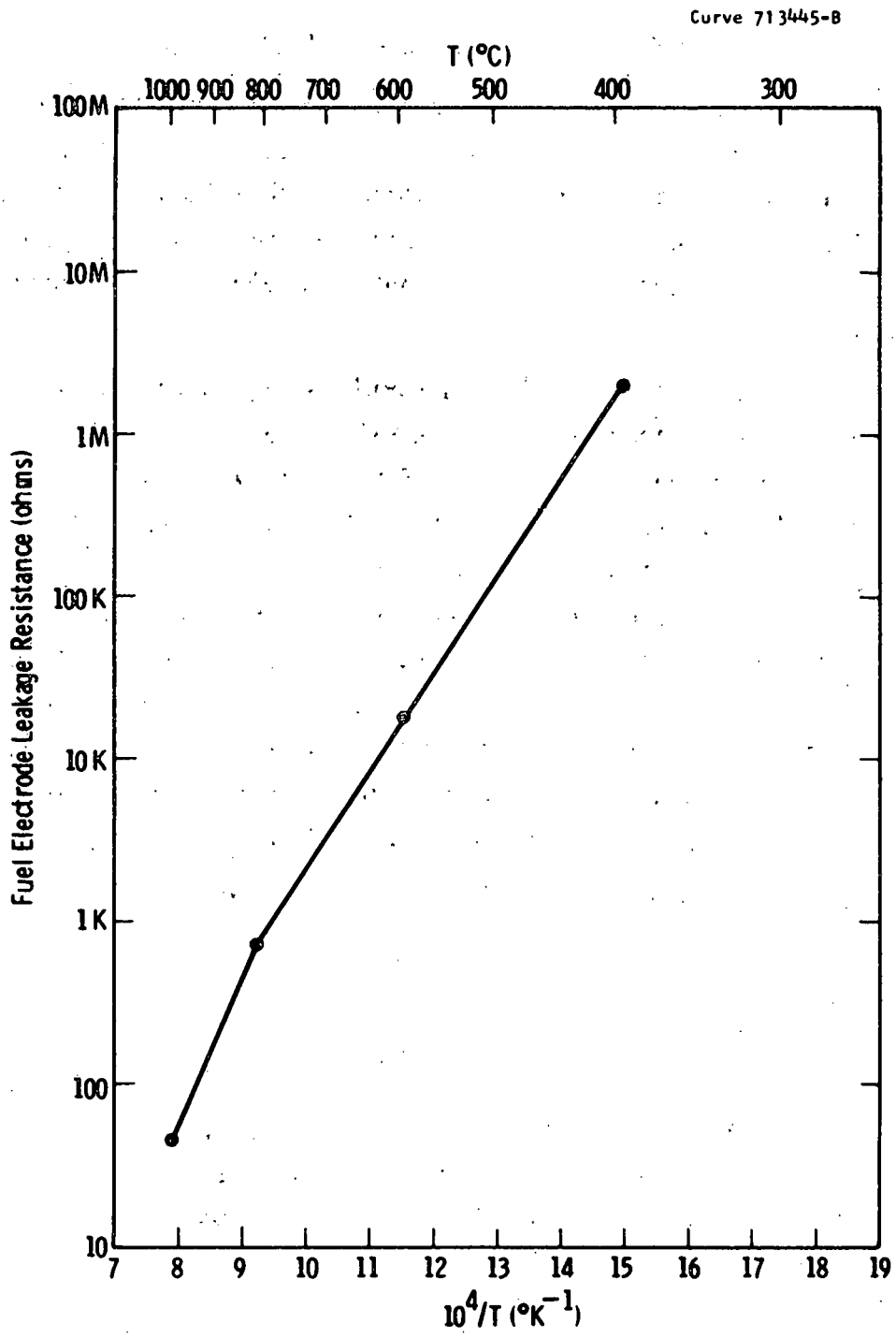

Fig. 5.59 — Leakage resistance between adjacent nickel fuel electrodes vs temperature in a hydrogen-water atmosphere

5.3.10 Concentration Polarization at the Fuel Electrode

An understanding of the concentration polarizations in our thin film fuel cell electrodes (and porous support tube) is important for two reasons: (1) it will enable us to minimize stack voltage losses due to concentration polarizations and (2) it will aid in choosing an optimum support tube, having both adequate strength and good gas diffusion characteristics.

In a previous report,[10] a simple analysis was presented for the current-voltage characteristic of a HTSOE fuel cell stack, operating with hydrogen-water fuel. A good fit of the theory to the experimental data for a fuel cell stack was obtained. The results led to the interesting conclusion that a significant amount of water concentration polarization was occurring in the fuel electrode-porous support tube structure. In the analysis, the parameter, S_{H_2O}, appeared, which was, essentially, a diffusion conductance coefficient for water vapor in the porous electrode-support tube structure. It was found that a good fit between the theory and data was obtained by assuming S_{H_2O} = 2,015 mA/atm.

S_{H_2O} for water-hydrogen was then calculated, directly, from the pore geometry of the support tube and the gas interdiffusion coefficient. By definition

$$S_{H_2O} = \frac{I}{\Delta P_{H_2O}} \tag{1}$$

where I is the stack current and ΔP_{H_2O} is the corresponding partial pressure difference of water vapor across the fuel electrode-support tube structure. It can be shown that for a simple pore diffusion mechanism, Equation (1) leads to

$$S_{H_2O} = A \frac{D_{eff}}{\delta} \cdot \frac{2F}{Q_o} \tag{2}$$

where A is the surface area of one cell, D_{eff} is the effective interdiffusion coefficient for water vapor-hydrogen in the porous structure, δ is the thickness of the porous structure, F is the Faraday constant, and Q_o is the quantity of gas ($cm^3 \cdot atm$) corresponding to one mole at 1000°C. The effective diffusion coefficient, D_{eff}, can be related* to the true interdiffusion coefficient for water vapor-hydrogen by

$$D_{eff} = \frac{\varepsilon}{\tau} D_{H_2O-H_2} \qquad (3)$$

where ε is the porosity (approximately 0.3 for our support tubes), τ is the tortuosity (approximately 3), and $D_{H_2O-H_2}$ is the binary diffusion coefficient for water vapor and hydrogen at 1000°C, extrapolated from literature values[12] to be approximately 12 cm^2/sec. One then obtains $D_{eff} \simeq 1.2$ cm^2/sec. Using this value, plus the appropriate values for A and δ for the first five-cell stack tested, one obtains a calculated value of S_{H_2O} = 58,500 mA/atm. This is a factor of ~30 higher than that derived from early stack tests, mentioned above.

*Estimation of the effective diffusion coefficient is greatly simplified here by the fact that the hydrogen and water vapor are counterdiffusing in equimolar quantities; thus no bulk viscous flow is involved. See reference (11).

One possible explanation for the above discrepancy would be incorrect assumptions about the pore structure on which D_{eff} depends. For example if a very large number of closed pores were present in the bulk of the nickel cermet fuel electrode or porous support tube, or at the interfaces, this would require one to revise D_{eff} to a much lower value, thereby reducing the discrepancy.

A simple way to resolve the matter would be to measure D_{eff} in the porous support tube. This could be done at room temperature, using a convenient pair of gases, such as N_2 and O_2, since what one actually wishes to estimate is D_{eff}/D_{12} where D_{12} is the true interdiffusion coefficient for gases 1 and 2. One possible way this might be done is shown schematically in Figure 5.60. Pure nitrogen is flowed through a section of porous tube plus fuel electrode. Oxygen from the air diffuses through the tube into the nitrogen stream where it can then be detected by an oxygen gas analyzer at the exit of the porous tube. The differential pressure across the porous tube must, of course, be kept small, to avoid bulk viscous gas flow through the tube wall. A very instructive set of experiments would start with the composite porous support tube-porous fuel electrode, as it actually is used in the fuel cell. Sequentially, various layers would then be removed by sandblasting or etching (fuel electrode surface, entire fuel electrode, porous support tube outer and inner surfaces) to reveal their contribution to D_{eff}.

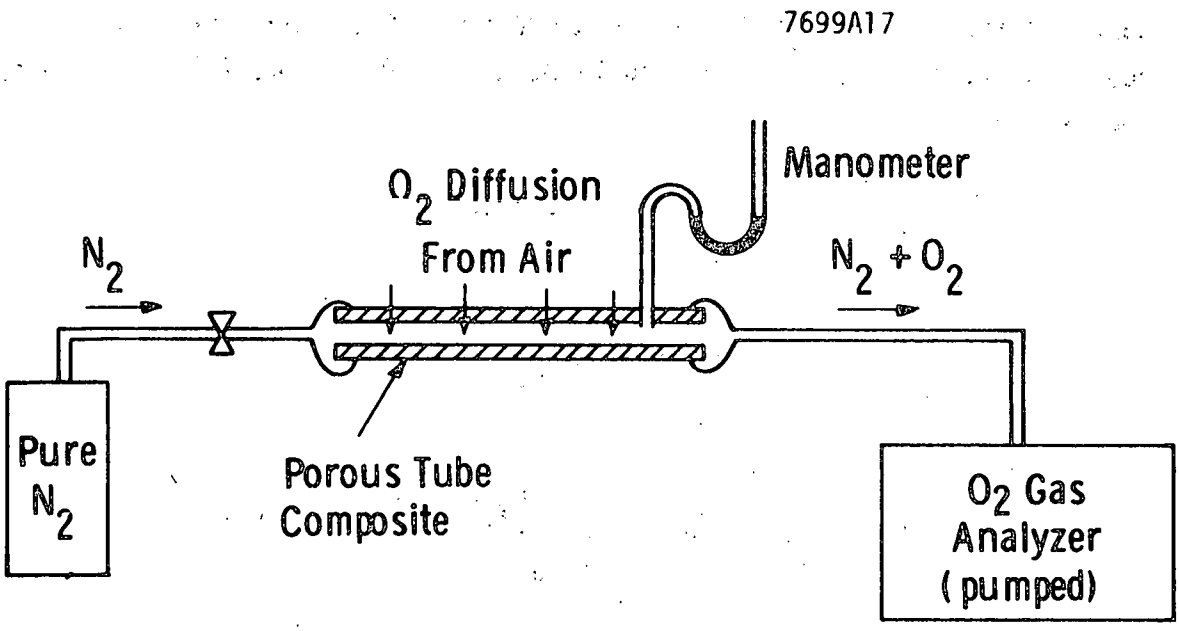

Fig. 5.60— Schematic of experiment for measuring effective diffusion coefficient for gases through the fuel cell support composites (porous support tube plus nickel cermet fuel electrode, for example).

5.3.11 Analysis of the Electrical Performance of an HTSOE Fuel Cell Stack with H_2-H_2O Fuel

To interpret experimental data for thin film, fuel cell stacks, under test with hydrogen-water fuel mixtures, a simple theory for the stack current-voltage characteristic (V-I curve) was devised. Only ohmic and concentration polarization voltage losses were considered; charge transfer polarization was assumed negligible for hydrogen-water operation at 1000 C.[13] The equations obtained for the V-I characteristic were as follows:

$$V = V_o - IR_o - \eta_{air} - \eta_{hydrogen} - \eta_{water} \tag{1}$$

$$\eta_{air} = \left(\frac{RT}{4F}\right) \ln\left(\frac{S_{O_2} P_{O_2}}{S_{O_2} P_{O_2} - I}\right) \tag{2}$$

$$\eta_{hydrogen} = \left(\frac{RT}{2F}\right) \ln\left(\frac{S_{H_2} P_{H_2}}{S_{H_2} P_{H_2} - I}\right) \tag{3}$$

$$\eta_{water} = \left(\frac{RT}{2F}\right) \ln\left(\frac{S_{H_2O} P_{H_2O} + I}{S_{H_2O} P_{H_2O}}\right) \tag{4}$$

where V is the stack voltage, V_o is the open circuit potential, I is the stack current, R_o is the ohmic resistance, the η's are concentration overpotentials, R is the gas constant, T is the absolute temperature of the stack, the S's are gas diffusion conductances for the electrodes, and the P's are partial pressures.

5.3.11.1 Air and Hydrogen Concentration Overpotentials

- They produce curvature in the V-I characteristic which is concave downward.
- They have limiting currents which correspond to O_2 or H_2 starvation at the electrode-electrolyte interfaces.
- For typical fuel cell parameters they are nearly linear at low to moderate currents and become rapidly non-linear (and large) at high currents.

5.3.11.2 Water Concentration Overpotential

- It produces a curvature in the V-I characteristic which is concave upward.
- No limiting current occurs; H_2O pressure at the electrode-electrolyte interface can become large.
- For typical fuel cell test parameters, this overvoltage is significantly large and non-linear at low currents. It increases relatively slowly at high currents.

An example of the V-I characteristic and the contributions of the various overpotentials are shown in Figure 5.61. These curves were calculated from Equations (1) through (4) for a hypothetical fuel cell having the parameters listed. Since the usual range for operation and/or life testing with this cell would be below a maximum current of approximately 1000-1200 mA, the relative importance of the water concentration polarization compared to that of air or hydrogen is evident.

5.3.11.2.1 A Comparison of the Theory with Stack Data

An important simplification in the equations can be made for the case where the cell current is well below (< one half) the limiting air or hydrogen polarization currents. This is often the situation in normal stack tests. Within this range, Equations (2) and (3) for the

Curve 713443-8

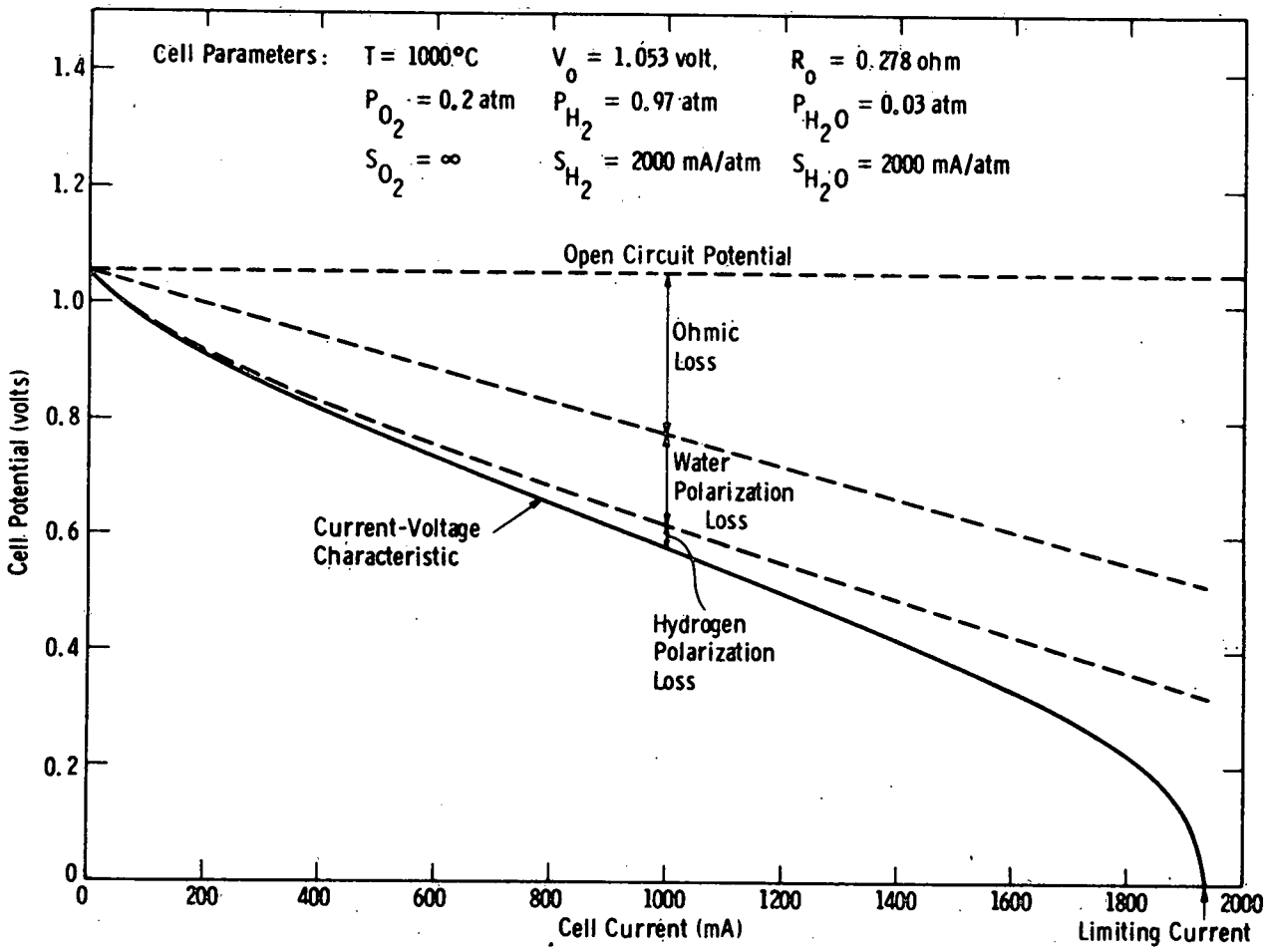

Fig. 5.61 – Theoretical behavior of the current-voltage characteristic for a cell, showing the ohmic and concentration polarization voltage losses. For this example the air electrode concentration polarization is assumed negligible; when present, it is very similar to the hydrogen concentration polarization in behavior

air and hydrogen overpotentials are then almost linear with current. This permits one to write the V-I characteristic equation for low-to-moderate current as

$$V = V_o - IR_1 - \left(\frac{RT}{2F}\right) \ln \left(\frac{S_{H_2O} P_{H_2O} + I}{S_{H_2O} P_{H_2O}} \right) \tag{5}$$

where

$$R_1 = R_o + R_{air} + R_{hydrogen} \tag{6}$$

so that there is only one non-linear term, the water overpotential.

A least squares fit of Equation (5) to the data for a five-cell stack[14] was carried out with the results shown in Figure 5.62. By proper choice of parameters V_o, R_1, and S_{H2O}, a good fit of the V-I characteristic was obtained. The value of R_1 required, 1.55 ohms, was just slightly larger than the experimentally determined value of ohmic resistance, R_o, which was 1.46 ohms. This is consistent with relatively small air and hydrogen overpotentials (small values for R_{air} and $R_{hydrogen}$) which was postulated earlier.

5.3.11.3 Diagnostic Technique Suggested by the Theory

A standard diagnostic technique employed in fuel cell work is the current interruption method[15] which enables one to determine the total concentration overpotential, η, from both electrodes. To determine the separate fuel and air electrode contributions, η_{fuel} and η_{air}, requires a suitable reference electrode. For a single thin film fuel cell this is difficult; for a multi-cell stack it becomes experimentally impractical.

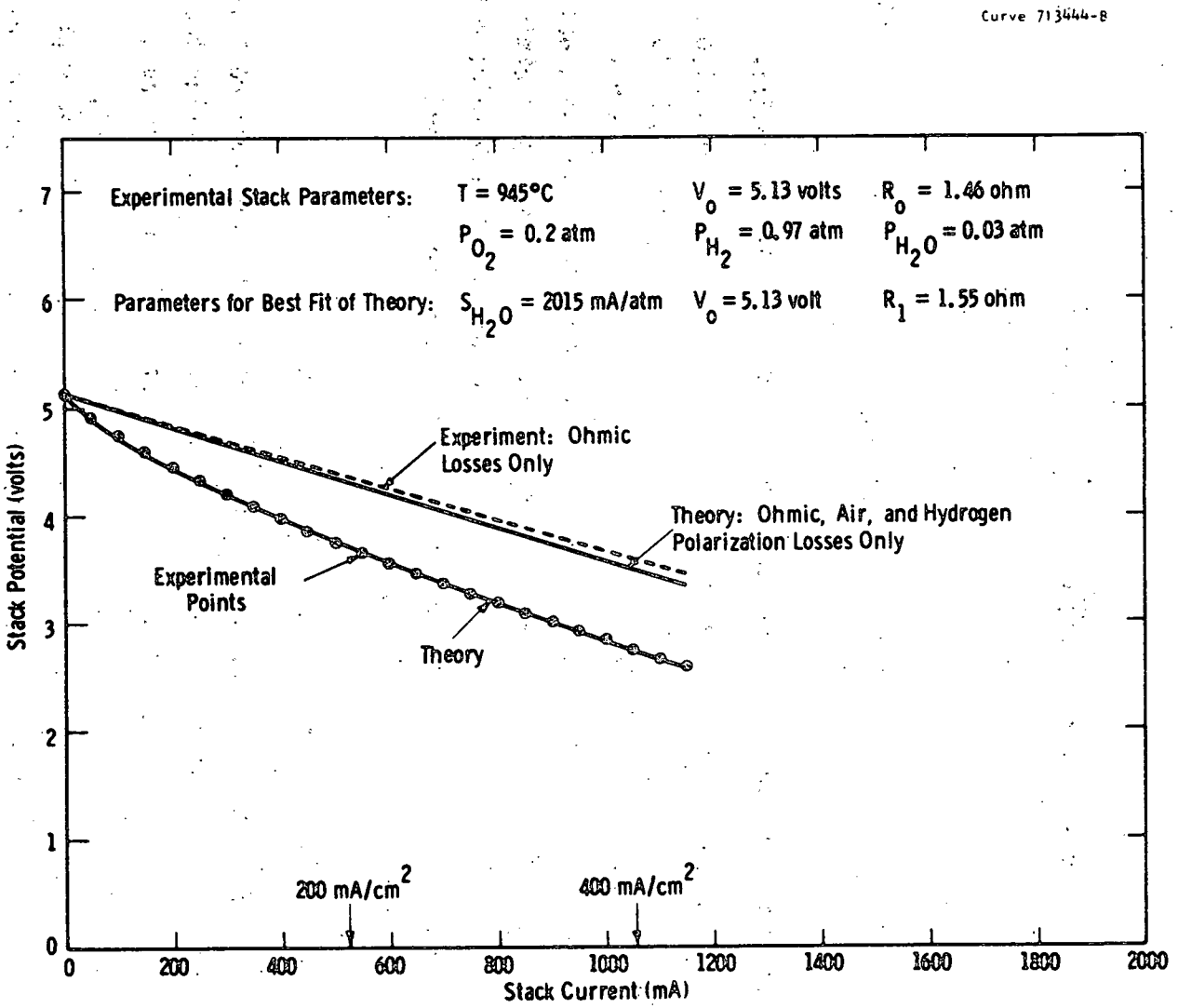

Fig. 5.62 — Comparison of experiment (points, dashed line) and theory (solid lines) for the current-voltage characteristic of a stack with hydrogen-water fuel. The lower theoretical curve includes the water polarization loss discussed in the text.

One promising application of the theory is in a technique for determining the overpotential components η_{air}, $\eta_{hydrogen}$, and η_{water} for single or multi-cell units with no additional electrodes. According to Equations (2), (3), and (4), each overpotential component depends on a different fuel or air component partial pressure, provided the current is held constant. Therefore, measurement of the total overpotential at constant current for two (or more) values of a fuel or air component partial pressure should enable one to determine the corresponding overpotential and its diffusion conductance coefficient, S.

5.3.12 Subtask B. Effect of Fuel and Air Conditions

This task is concerned with the testing of cell stacks and/or stack components and/or their interfaces, under a variety of conditions, to which they might be exposed in the operation of an envisioned fuel cell generator.

The principal techniques available for this task are: (1) DC current-voltage characteristics measured under normal, rich, and lean fuel and air conditions; (2) interrupted DC current-voltage measurements for separating slow and fast cell polarizations and (3) AC complex impedance measurements for obtaining detailed information on the nature of the polarizations.

Our first application of the complex impedance technique to thin film fuel cells is described below. A major objective in the work has been to experimentally determine the resistance of the fuel cell electrolyte layer, independent of whatever complexities might be present in the electrode processes.

5.3.12.1 Electrical Characterization of Electrolyte Layer-Fuel Electrode Combination Specimens by Complex Impedance Measurements

A detailed description of the complex impedance method may be found elsewhere.[16,17] Basically it consists of three steps: (1) measurement of the specimen complex impedance over a wide range of frequencies; (2) deduction, from the data, of an equivalent AC electrical circuit for the specimen and (3) identification of the AC circuit elements with specific ionic or electronic processes occurring in the specimen and its electrodes.

5.3.12.1.1 Specimen Preparation and Measurement

Each specimen tested was a segment of a partially completed fuel cell, consisting of porous support tube, nickel-cermet fuel electrode and EVD-deposited solid electrolyte, onto which was sputtered a small platinum counter-electrode (5 μm thick, ~0.08 cm^2 area). Platinum

wire leads, attached to the nickel fuel electrode and platinum counter-electrode, completed the two-terminal specimen whose effective area was that of the small counter-electrode. A hydrogen water atmosphere at 1000°C was employed. The electrolyte layer for specimen #13 was deposited by using the Grafoil protective sleeve technique (discussed in Section 5.1.1, Subtask A) as a protection against predeposition contamination; the electrolyte layer for specimen #15 was deposited without this precaution.

The complex impedance measurements were made using the scheme shown in Figure 5.63. As indicated, three measurements, taken directly from the scope trace (which is a stationary ellipse), plus the value of the standard resistor employed, are sufficient to yield the unknown resistive component, R_u, and the reactive component, X_u, at a given frequency. While this technique is not one of high precision, it is fairly rapid, does not require the large capacitances of bridge methods, and allows one to detect current-voltage non-linearity in the specimen, if present. For good results the oscilloscope employed should have amplifiers which are well-balanced at all frequencies and which have low common-mode error. The resistance and inductance of leads to the specimen must, of course, be kept small. In our apparatus a duplicate set of leads, shorted at the far end, was used for determining the lead impedance corrections. Measurements were made over a frequency range of 1 Hz to 50kHz, with a maximum rms voltage of 28 mV applied to the specimen.

5.3.12.1.2 Analysis of the Data

The data consist of pairs R_u, X_u (AC resistance, AC reactance), measured at a number of different frequencies. These are then plotted as points, R_u, X_u, in a rectangular coordinate system (the complex impedance plane) as shown in Figures 5.64, 5.65, and 5.66. The locus of points in this type of plot generally shows distinctive features which are very helpful in choosing an equivalent circuit for the specimen and estimating the values for the circuit elements.

Dwg. 7715A74

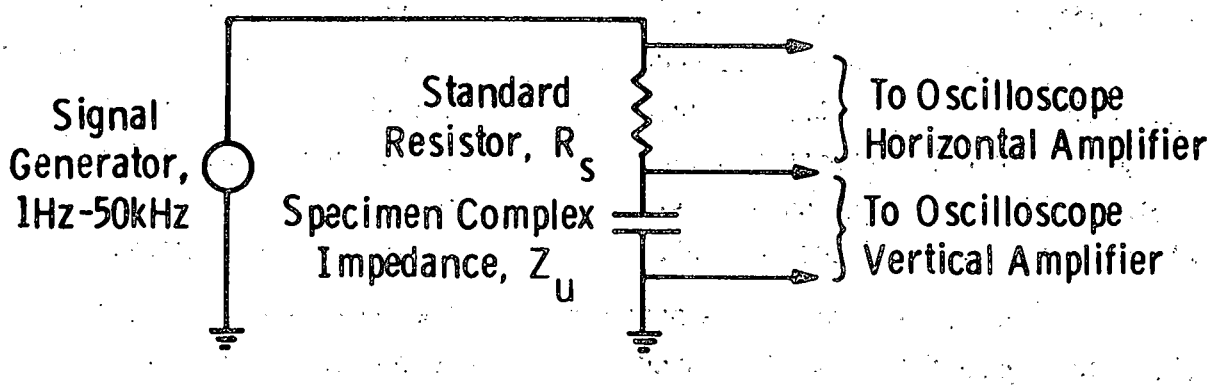

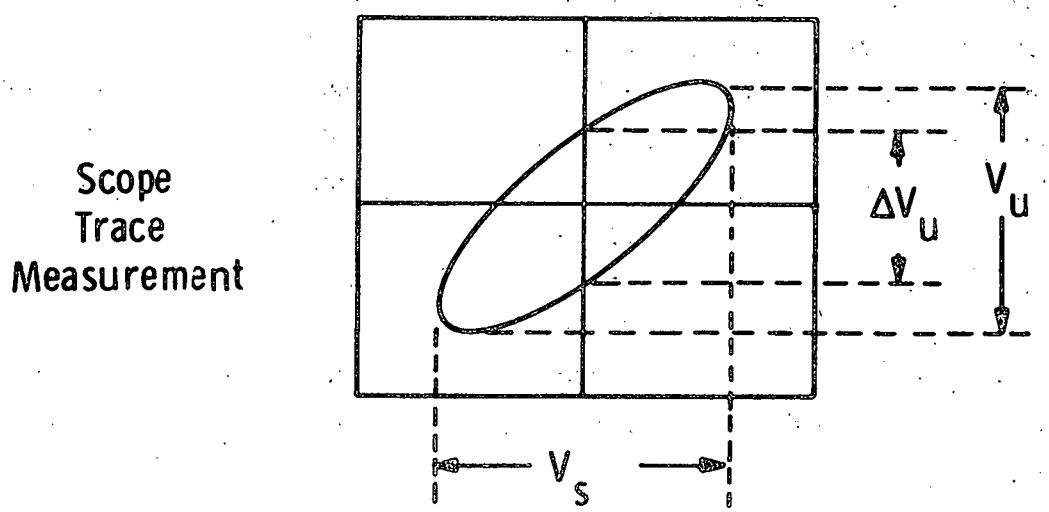

Specimen (unknown) Complex Impedance $Z_u = R_u + jX_u$

Specimen Resistance $R_u = R_s \left(\sqrt{V_u^2 - \Delta V_u^2} / V_s \right)$

Specimen Reactance $X_u = R_s (\Delta V_u / V_s)$

Fig.5.63 – Method for determining the specimen complex impedance

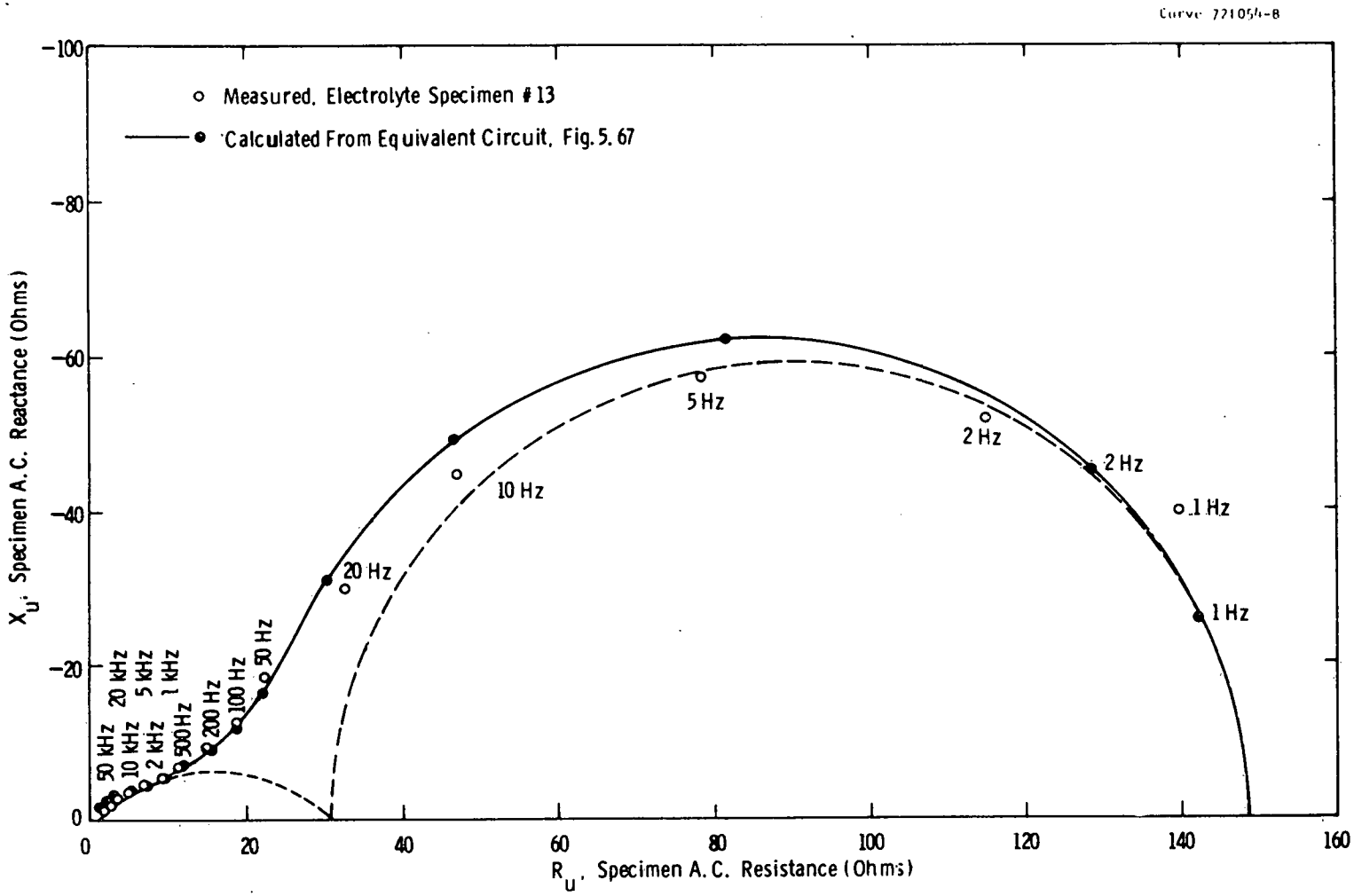

Fig. 5.64—Plot of measured (●) and calculated (○) values for the complex impedance of Specimen #13 (fuel electrode, solid electrolyte, platinum electrode) at frequencies from 1 Hz to 50 kHz. A hydrogen-water atmosphere at 1000°C was employed. (Dashed lines show the asymptotic behavior for each dispersion, taken by itself)

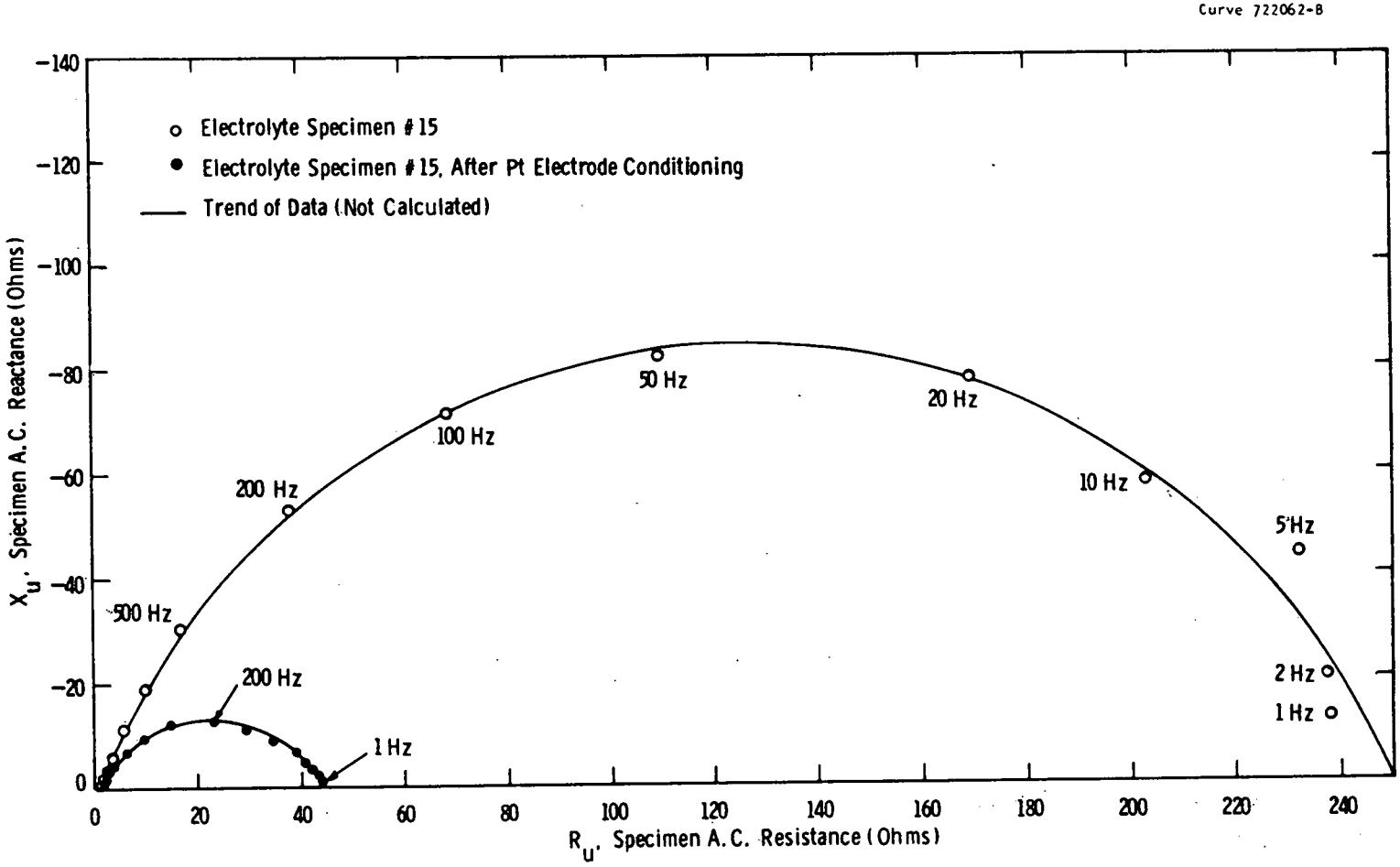

Fig. 5.65 — Plot of complex impedance data for Specimen #15 (fuel electrode, solid electrolyte, platinum electrode) before and after conditioning the platinum electrode (see text). Measurement frequencies ranged from 1 Hz to 50 kHz in a 1, 2, 5 sequence. A hydrogen-water atmosphere at 1000°C was employed

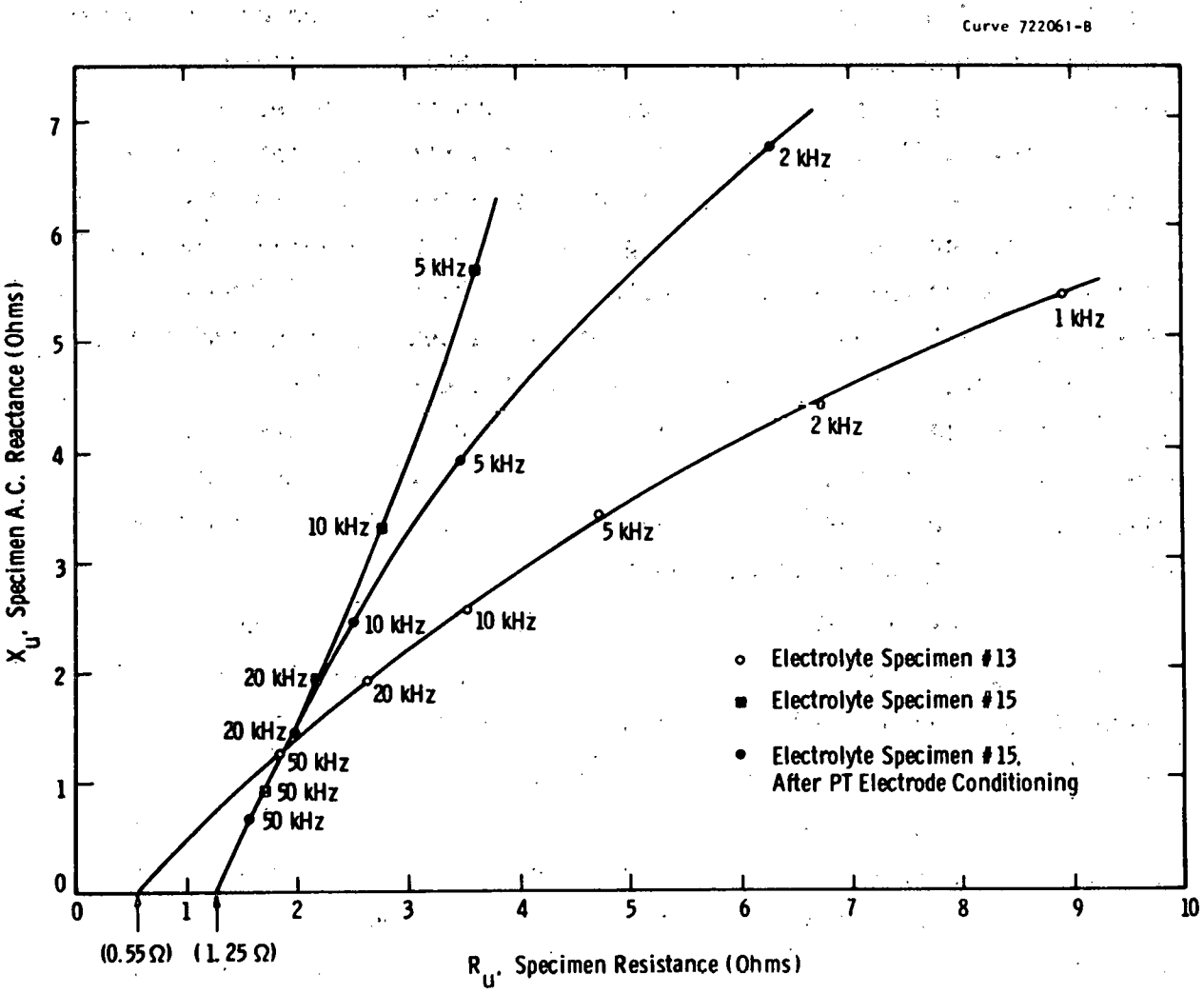

Fig. 5.66 – Plot of complex impedance data at the higher frequencies for Specimens #13 and #15. Arrows indicate specimen electrolyte layer resistances obtained by extrapolation

In Figure 5.64 (specimen #13) the points from 1 Hz to 20 Hz followed approximately a semi-circular arc which is characteristic of a resistance and capacitance in parallel. From the diameter of the circle and the frequency at the apex of the circular arc one estimates, approximately, the values of the resistance and capacitance. A second region, showing distinctive behavior, occurred for the points between 1 kHz and 50 kHz. The low circular arc, which intercepts the R_u-axis at ~45 , is characteristic of a Warburg impedance* and resistance in parallel. In this instance the circuit parameters could be estimated from the chord of the arc and the apex frequency. The points between 50 Hz and 500 Hz represent a transition between the two regions described previously, which overlap in the frequency domain. Extrapolation of the high frequency data to its intercept with the R_u-axis yielded a resistance value which was primarily that of the electrolyte film. This procedure was carried out on an expanded plot as shown in Figure 5.66.

The final result for the equivalent circuit of specimen #13 is shown in Figure 5.67. Initially-estimated circuit parameters were adjusted to give an optimal fit between the experimental points and the calculated points as shown in Figure 5.64.

In Figure 5.66, the data are shown for specimen #15, before and after a "conditioning" of the platinum counter-electrode, by passing a moderate DC current (125 mA/cm^2) through the specimen. In terms of the equivalent circuit, Figure 5.68, the DC electrode resistance was drastically altered by this treatment. The electrolyte layer resistance, determined by the extrapolation of high frequency data in Figure 5.66, was unchanged. The impedance Z_e could not be represented by any simple circuit element but showed behavior intermediate to that of a capacitor and a Warburg impedance.

*The Warburg impedance is a special AC circuit element which often appears in the equivalent circuits for diffusion-limited electrode reactions. For further details see References (16) and (17).

Dwg. 7715A75

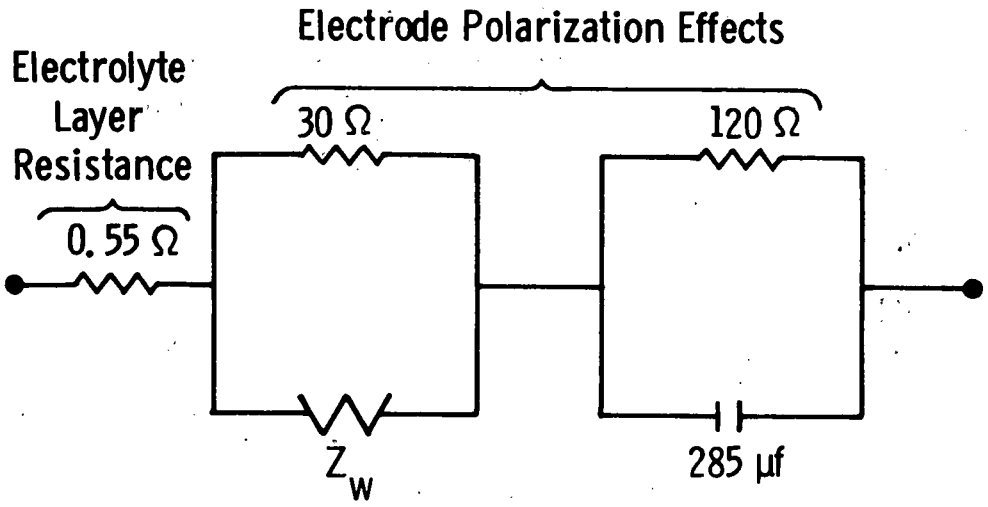

Fig. 5.67 — Equivalent circuit for the specimen #13. Z_w is a Warburg impedance (see text), given here by

$$Z_w = \frac{285\ \Omega}{\sqrt{f\,(Hz)}} - j\frac{285\ \Omega}{\sqrt{f\,(Hz)}}$$

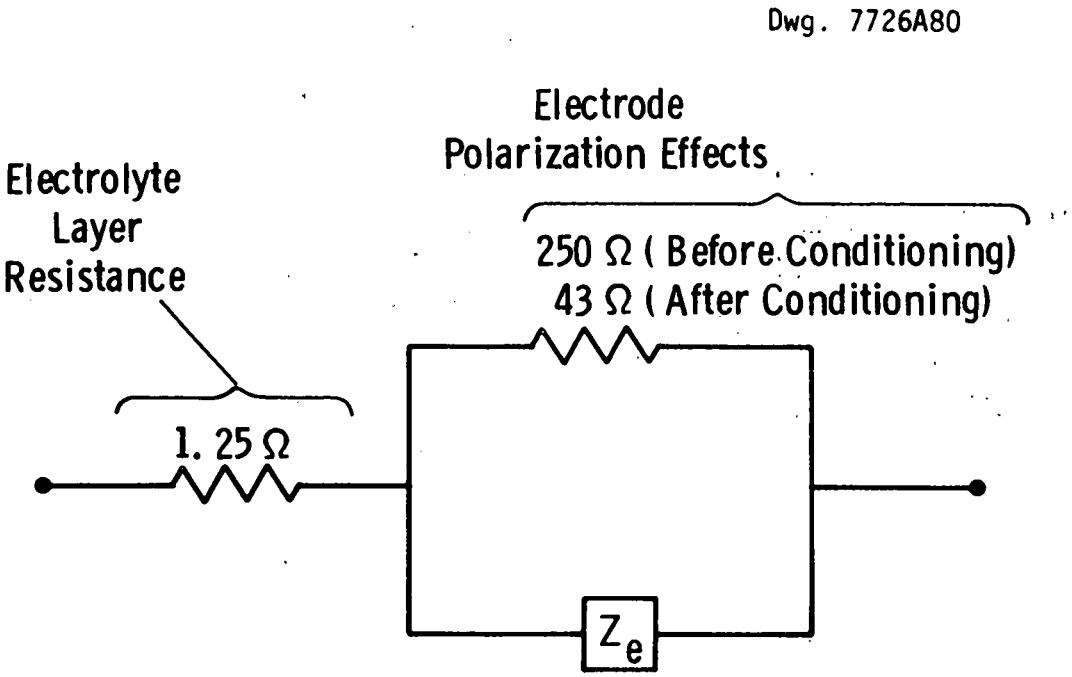

Fig. 5. 68 – Equivalent circuit for Specimen #15. The impedance Z_e and the conditioning referred to above are discussed in the text.

5.3.12.1.3 Interpretation of Results

As shown in the equivalent circuits of Figures 5.67 and 5.68, the measurements yielded electrolyte layer resistances of 0.55 and 1.25 ohms for specimens #13 and #15, respectively. Combined with the thickness and area of the electrolyte measured, these values gave electrolyte layer resistivities of 7 ohm-cm for specimen #13 and 17 ohm-cm for specimen #15. The 7 ohm-cm resistivity is comparable to the lowest literature values reported for ZrO_2-Y_2O_2 solid solutions and is indicative of a high quality electrolyte layer. The 17 ohm-cm resistivity value is still adequate for thin film fuel cells, but suggests that predeposition contamination might have influenced the quality of this film.

Some limited conclusions, regarding the electrode polarization processes, may be drawn from this present data. The choice of dense, sputtered-platinum counter-electrodes for the specimens was unfortunate since they obviously were blocking to oxygen flow, as indicated by the high DC specimen resistance. The large reduction in the DC resistance of specimen #15, produced by "conditioning" with a moderate DC current, confirmed this. Such treatment has been shown to reduce blocking by creating pores in an otherwise dense platinum film.[16] It was reassuring to note that this treatment did not affect the high-frequency extrapolation used to estimate the specimen electrolyte layer resistance. We were not successful in finding a combination of circuit elements for Z_e which would yield satisfactory predictions for individual data points, as was done for specimen #13. Again, it is possible that the predeposition contamination in specimen #15 was a factor in this case.

The Warburg impedance behavior observed in specimen #13 at the higher frequencies indicates a diffusion-limited process, involving one of the electrode reactant species. From our present data it is not clear whether this too was associated with the platinum counter-electrode or, rather, the nickel-cermet fuel electrode.

Additional measurements, employing non-blocking counter-electrodes in tests in which the temperature and hydrogen-water atmosphere are varied, should make it possible both to observe fuel electrode polarization processes in our specimens and to identify them. The application of a DC bias current to the specimen during measurement will also be investigated.

5.3.12.2 Effect of Fuel and Air Concentrations on Stack Performance and Life

Stack #8 was tested under a variety of rich and lean fuel (H_2 or CO) conditions as well as normal and lean O_2 conditions. These results were presented in Section 5.3.7.1 and the data have been presented in Figures 5.54 and 5.55. During the past 1800 h of life testing of stack #8 (seven cells), a lean fuel condition (15% CO/H_2 in CO_2) has been employed. Here the average cell voltage has been stable at $\sim$ 0.62 V, at 150 mA/cm^2 (Figure 5.39).

5.4 REPRODUCIBILITY OF 10 WATT STACKS

Originally, the program required that, at least, 10 stacks of about 20 cells each would be fabricated and tested, to demonstrate reproducibility of 10 watt stacks.

5.4.1 Stack Comparison Testing

Due to the emphasis needed in the program to refine the fabrication procedures, particularly, in the interconnection, in the air electrode and in the interconnection/air electrode interface areas, these stacks were not constructed and tested. However a second stack (Stack #9) was built, during the program, which, when tested, did demonstrate 10 watts of power capability, showing that the performance obtained in stack #8 was repeatable in other stacks (see Section 5.3.7.2).

5.5 Task 5: The Design, Cost and Benefit of an Industrial Cogeneration System, Using an HTSOE Fuel Cell

In September 1979, two additional tasks were established for the program. Task 5 relates to a Design, Cost and Benefit Analysis of the HTSOE fuel cell in an industrial cogeneration application. Task 6 evaluates the effect of impurities in the fuel gas on the HTSOE fuel cell performance and life, and sets minimum tolerance levels for these impurities.

In Task 5, a study is being conducted to identify an appropriate industrial cogeneration application and determine its potential economic value. In Task 6 the effects of impurities, particularly, sulfur-bearing species, will be determined, as well as tolerance levels of these species.

Work on Task 5 is scheduled for completion in September 1980 and a separate report will be prepared which summarizes all the findings of that study.

Task 6 will be completed in June 1980 with respect to results of testing a stack, using a simulated coal gas fuel that has sulfur species impurities.

The objective of Task 5 is to select a promising industrial application for "commercial-size" HTSOE fuel cell modules, so that a conceptual design can be envisaged, to the extent necessary to estimate the economic viability of the system. Three major efforts involved are:

1) selection of a specific cogeneration application
2) preparation of a preliminary system design that identifies all components and performance capability
3) use of the above design to estimate cost, environment, and conservation benefits.

5.5.1 Selection of a Promising Industrial Cogeneration Application

This subtask is completed. After a literature search, examination of pertinent reports dealing with similar cogeneration applications, it seemed appropriate to select the integrated aluminum facility at Corpus Christi, Texas, as covered in the TRW report to DOE -- "Feasibility Study for Industrial Cogeneration Fuel Cell Application," Contract DE-AC-03-78-C5-40227. This selection not only encompasses the thermal/electric output of the HTSOE system, but will enable direct comparison with another fuel cell type to be made. Also, the temperature-thermal/electric requirement for this application is among the best for a variety of applications considered in other application studies, e.g., Institute of Gas Technology for the Gas Research Institute.

5.5.2 Preparation of a Conceptual Design of the Selected System and Its Mode of Operation

A conceptual systems design, see Figure 5.69, has been prepared to provide the most effective means of preheating air and fuel for the HTSOE fuel cell system, and for producing electric power and process steam from the hot exhaust gases from the cell. The design requires a cell construction that would permit partitioning of spent fuel, add spent air, and utilization of those two gas streams, separately, in the production of electric power and steam.

The design was reviewed to assess the type of HTSOE cell construction that would apply to the separate production of spent fuel and spent air. It was concluded that a more reliable, potentially more economical, cell module could be constructed if the spent fuel did not have to be isolated from the spent air. Thus, only a combined spent fuel/air combustion product stream should be utilized for fuel preheat and for steam/power production.

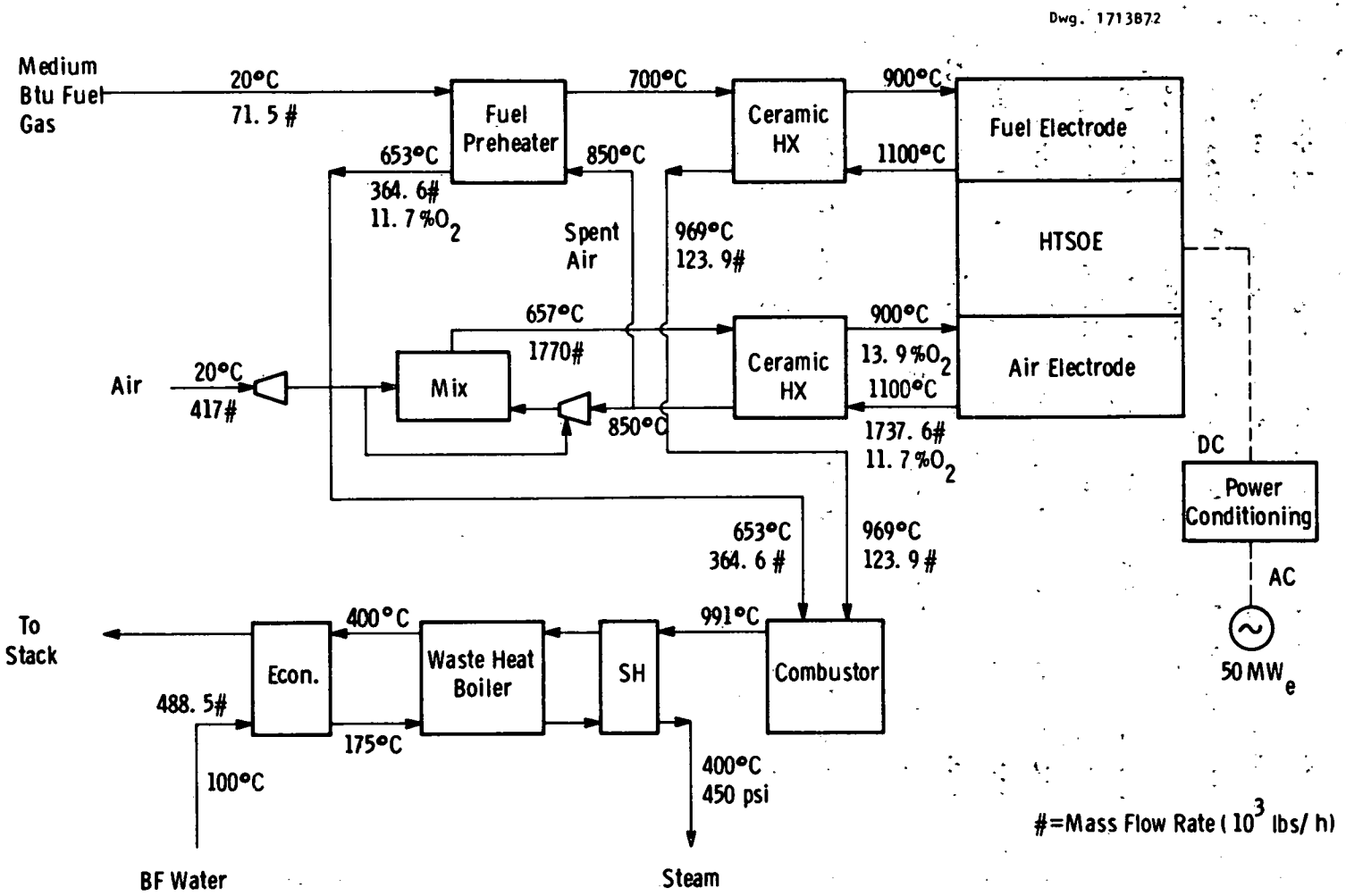

Fig. 5.69 — HTSOE fuel cell system flowsheet (100% steam option)

The system in Figure 5.69 is presently being modified to provide the most effective means of utilizing such a combined HTSOE cell off gas. A parametric study of waste heat steam and power production is underway. The limiting cases, 100% waste heat to process steam and 100% waste heat to electric power, will be assessed. A third case will be included, to produce steam and power both, in proportions appropriate for an integrated aluminum production plant. All of the system design conditions are being keyed to the requirements of the integrated aluminum facility at Corpus Christi, Texas, as studied by TRW in their report to DOE, previously mentioned. The systems diagram and performance characteristics study is scheduled for completion in June 1980.

5.5.3 Estimate the Cost, Environmental and Conservation Benefits

Work on this task will start as soon as the above task nears completion.

5.6 Task 6. HTSOE Fuel Cell Stack Tolerance to Fuel Impurities

The purpose of this subtask is to examine the effect of sulfur, and other possible impurities, in fuel gas, as might be present in fuel derived from coal gasification, on the performance of the solid state fuel cell.

5.6.1 Subtask A. Evaluate Effects of Candidate Fuel Gas Impurities on Cell and Stack Performance and Life

Prior to testing an HTSOE fuel cell stack, with an inlet fuel gas having a sulfur-specie as an added impurity, a preliminary investigation was conducted to evaluate stack component susceptibility to sulfidation -- in particular, the fuel electrode and the interconnection. Here the IC was tested because no known data exists to predict its behavior at 1000°C in the presence of sulfur-species. The fuel electrode was studied since it is the most vulnerable of the HTSOE fuel cell components to sulfur attack.

This subtask consists of three general studies: (1) calculations from available thermodynamic data of the possible reactions of sulfur-containing species in the fuel gas with nickel, cobalt, lanthanum chromite and other constituents of the fuel cell stack which contact the fuel stream; (2) microweighing measurements* near 1000°C (i.e., the operating fuel cell temperature), to determine the threshold conditions for sulfidation of individual or combined stack components exposed to the fuel stream and (3) experimental examination of the performance (open circuit voltage and operating current and voltage of the fuel cell) of solid state fuel cell stacks, as a function of sulfur content of the fuel gas, temperature and $(H_2 + H_2O)/(CO + CO_2)$ ratios in the fuel gas.

---

*Measurements made as a function of fuel composition, temperature and partial pressures of the sulfur species in the fuel.

5.6.1.1 Tolerance of Stack Components to Sulfur Species in the Fuel Gas

Data from thermodynamic calculations is presented graphically in Figures 5.70 through 5.76. They illustrate the general magnitude of sulfur-containing gas concentrations in the coal-gas fuel, which could cause sulfidation of a fuel electrode and of lanthanum chromite, for varying operating parameters of the fuel cell stack. Seven significant results have been derived from this study.

1) Nickel or cobalt fuel electrodes should show a minimum tolerance for sulfur-containing gases at a fuel cell no load voltage between 0.70-0.75 volt, depending on the temperature. (Figures 5.70 and 5.71).

2) Fuel gases higher in H_2/H_2), as compared to CO/CO_2, show a higher sulfur gas tolerance. (Figure 5.72)

3) Fuel electrodes show a much higher sulfur gas tolerance at 1000 C, as compared with 700 C. (Figure 5.73).

4) Cobalt electrodes show a considerably higher sulfur gas tolerance than nickel electrodes. (Figure 5.71).

5) The major sulfur gas species in a fuel gas of the fuel cell are expected, thermodynamically to be SO_2 at voltages below 0.7 volt, and H_2S and to a lesser extent COS, at voltages above 0.8 volt (no load voltage). (Figure 5.75).

Curve 712838-A

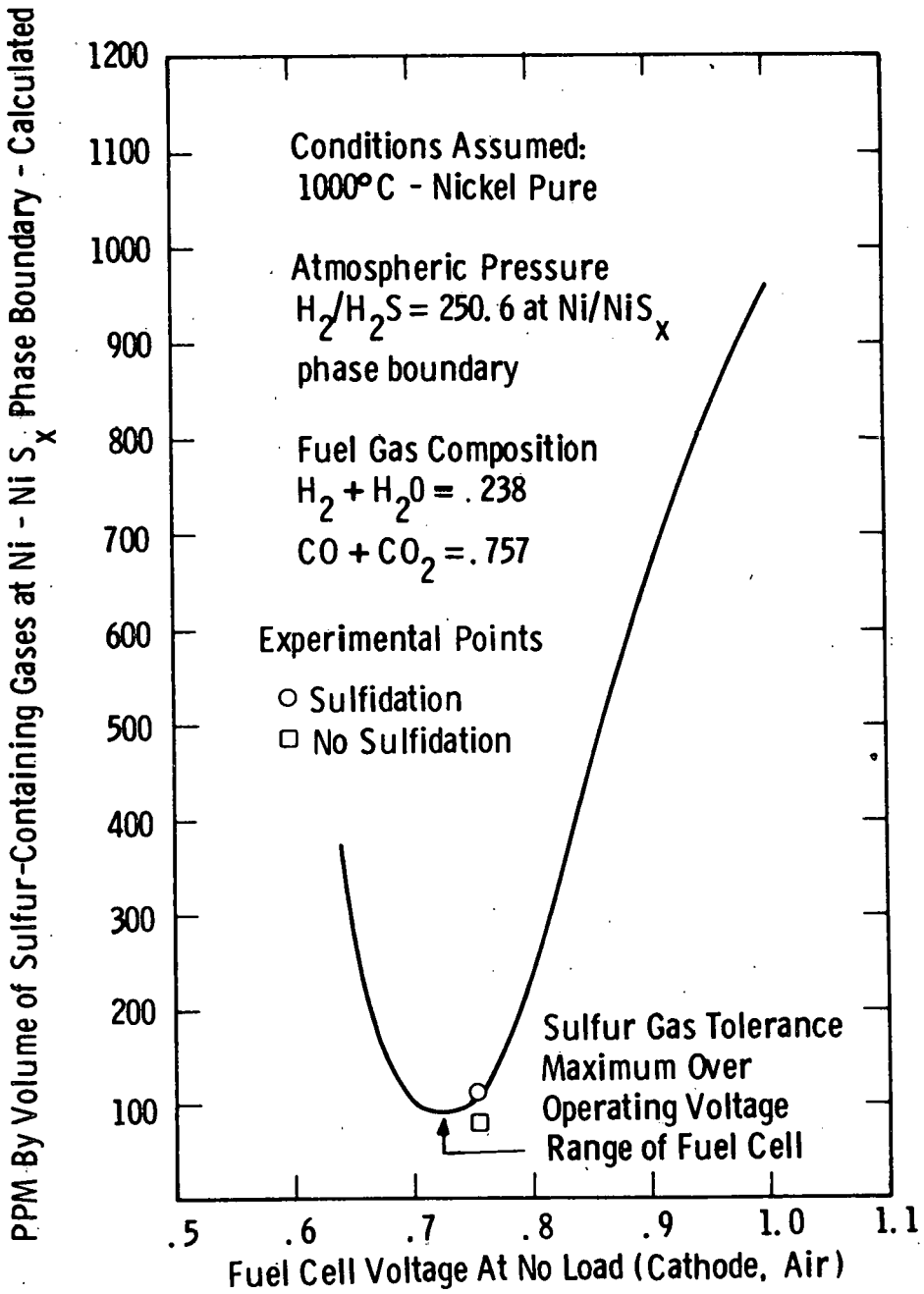

Fig. 5.70 – Concentration of sulfur-containing gases at which a nickel fuel electrode begins to form Ni S_x vs fuel cell voltage at 1000°C

Curve 712835-A

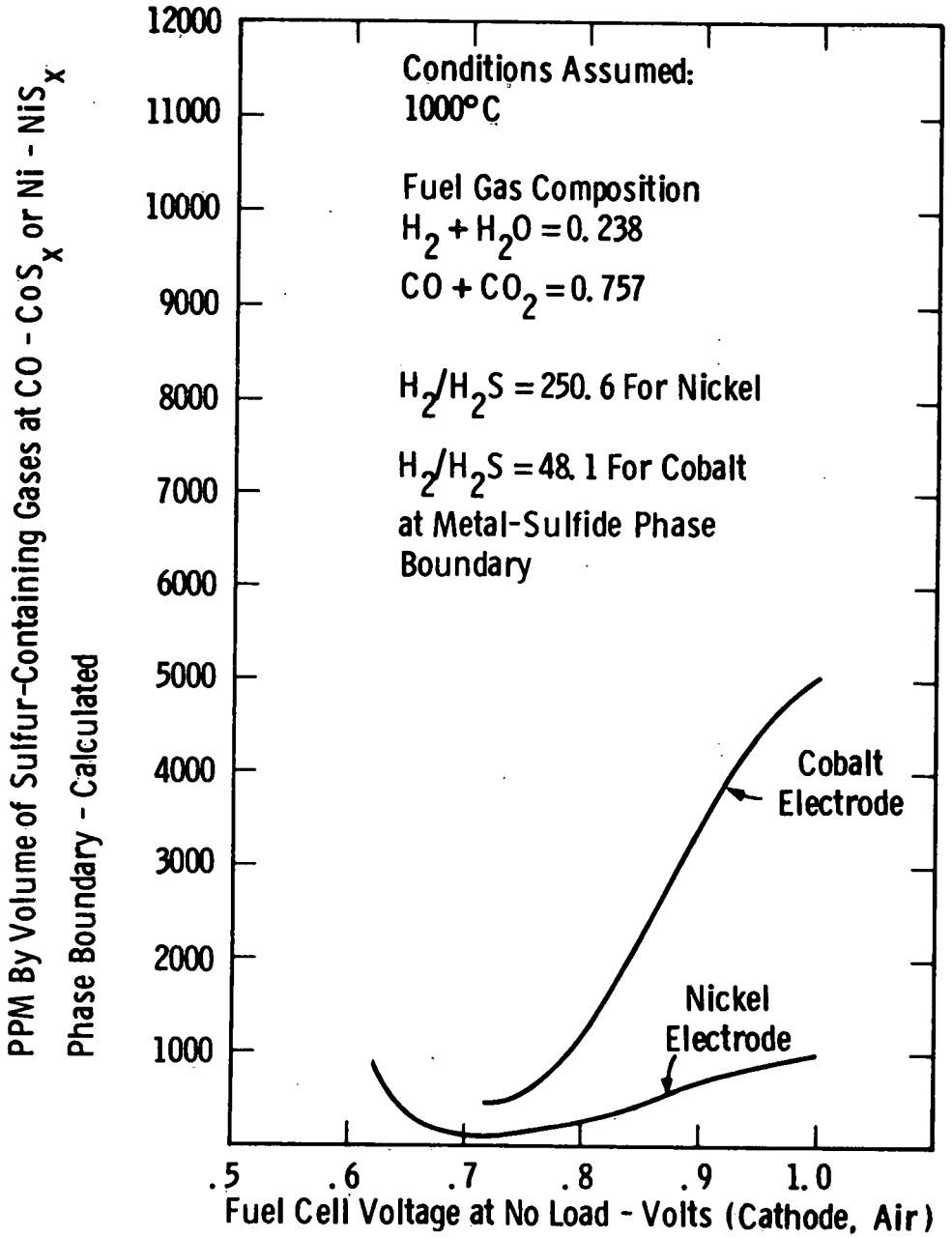

Fig. 5, 71 – Concentration of sulfur-containing gases at which nickel and cobalt fuel electrodes will begin to sulfide vs the fuel cell voltage

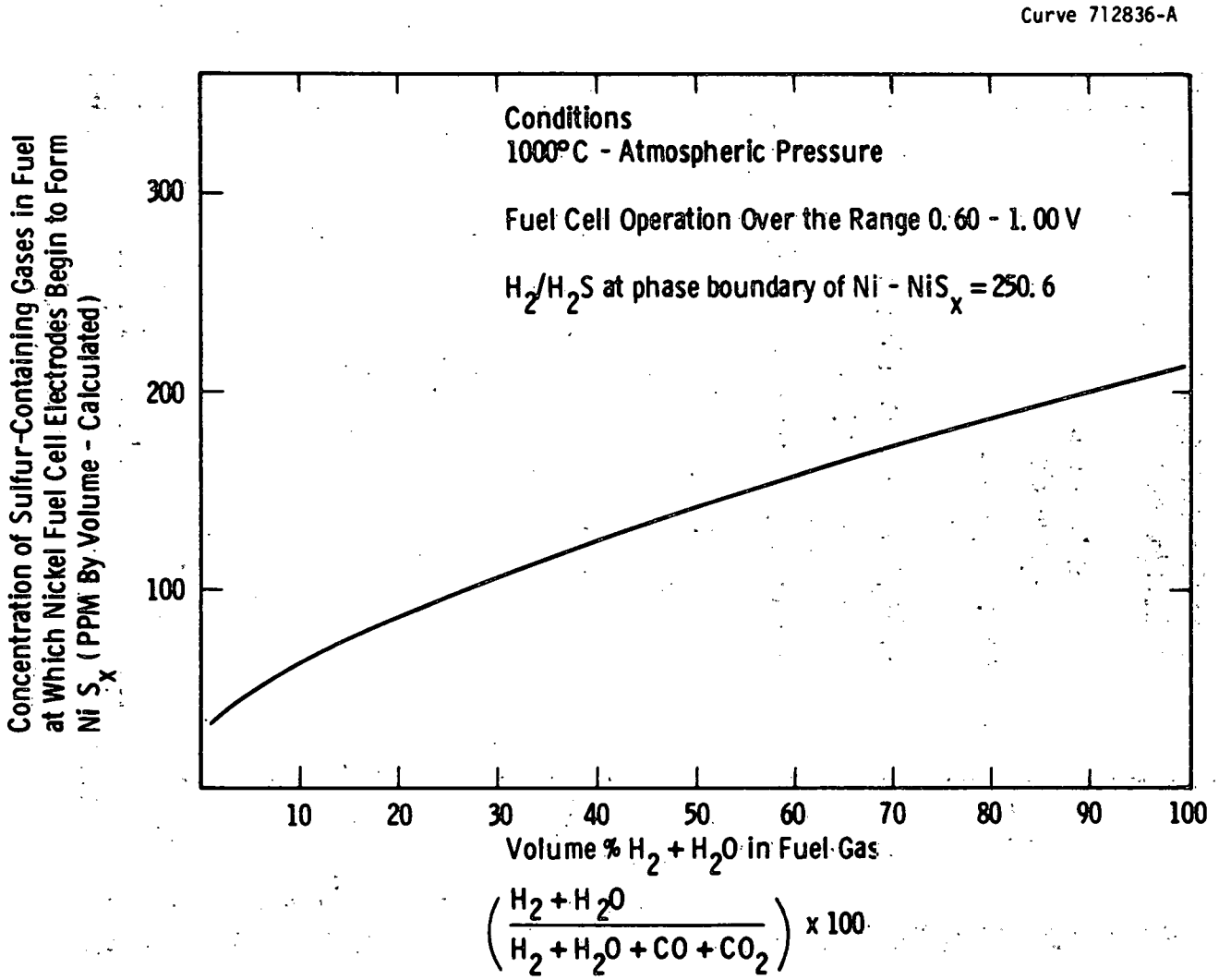

Fig. 5.72—Tolerance of nickel electrodes to sulfidation as a function of fuel gas composition

Curve 712834-A

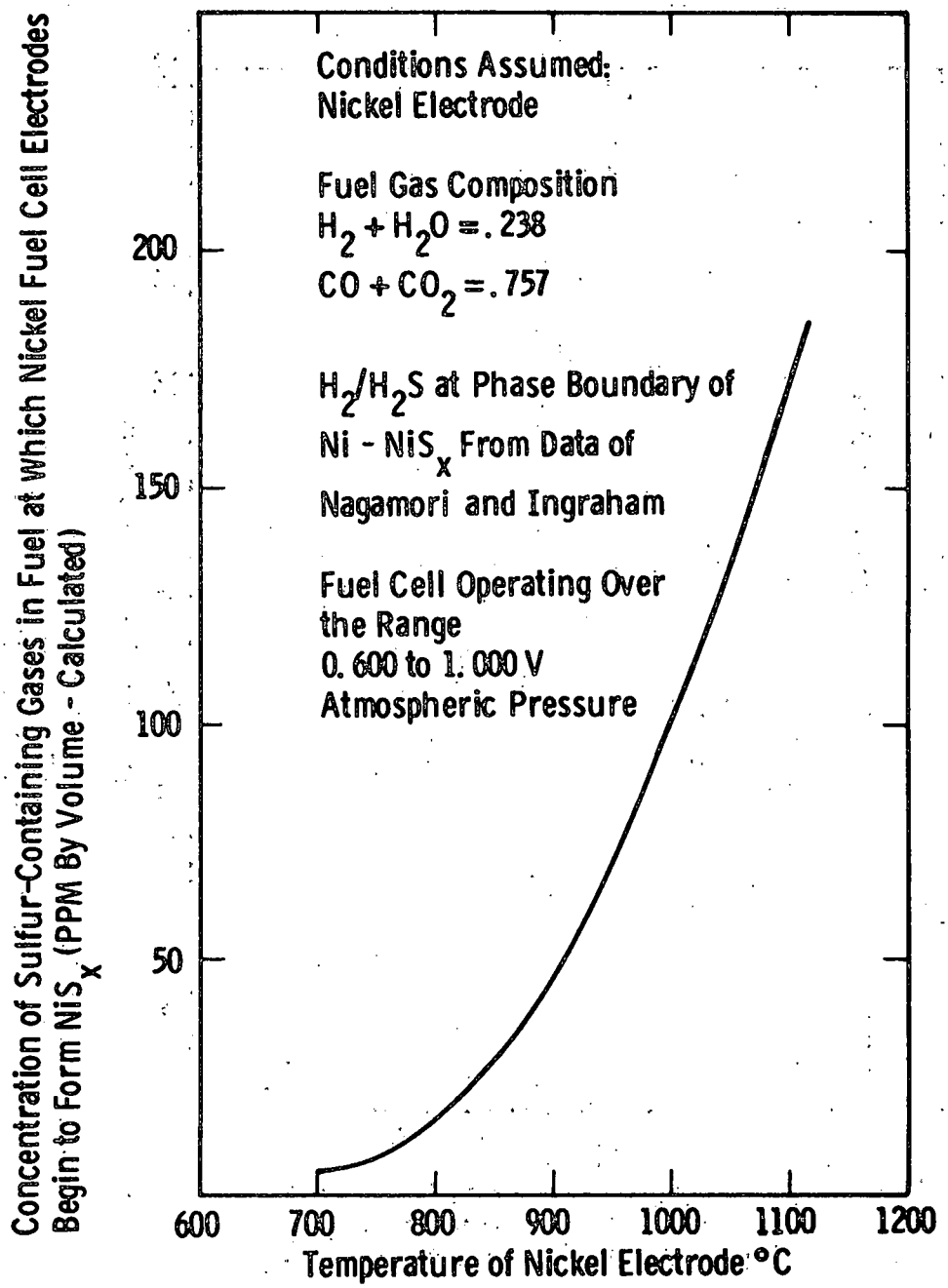

Fig. 5.73—Tolerance of nickel electrodes to sulfidation as a function of temperature

Curve 712837-A

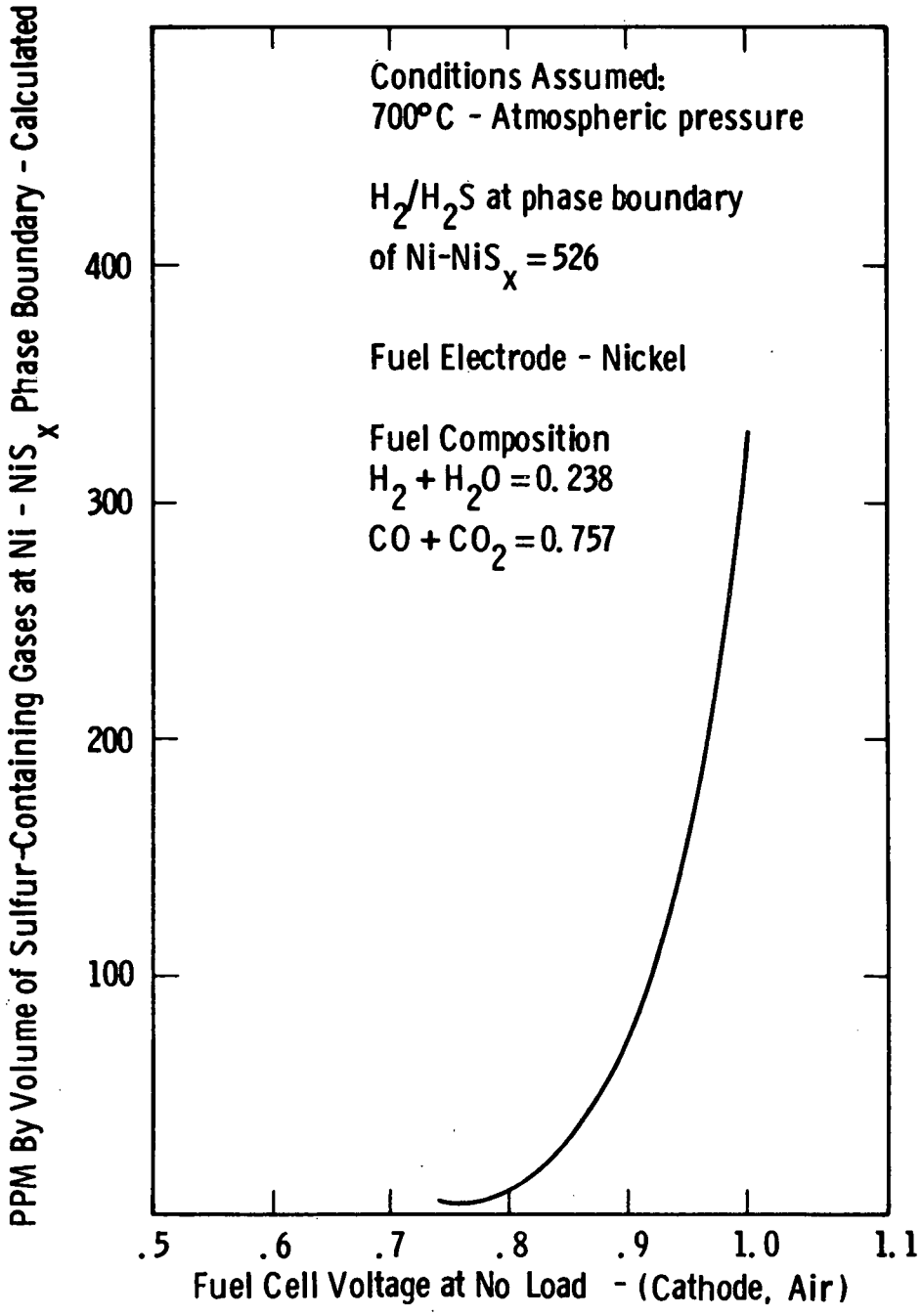

Fig. 5.74—Concentration of sulfur-containing gases at which a nickel fuel electrode begins to form NiS_x vs fuel cell voltage at 700°C

Curve 712833-A

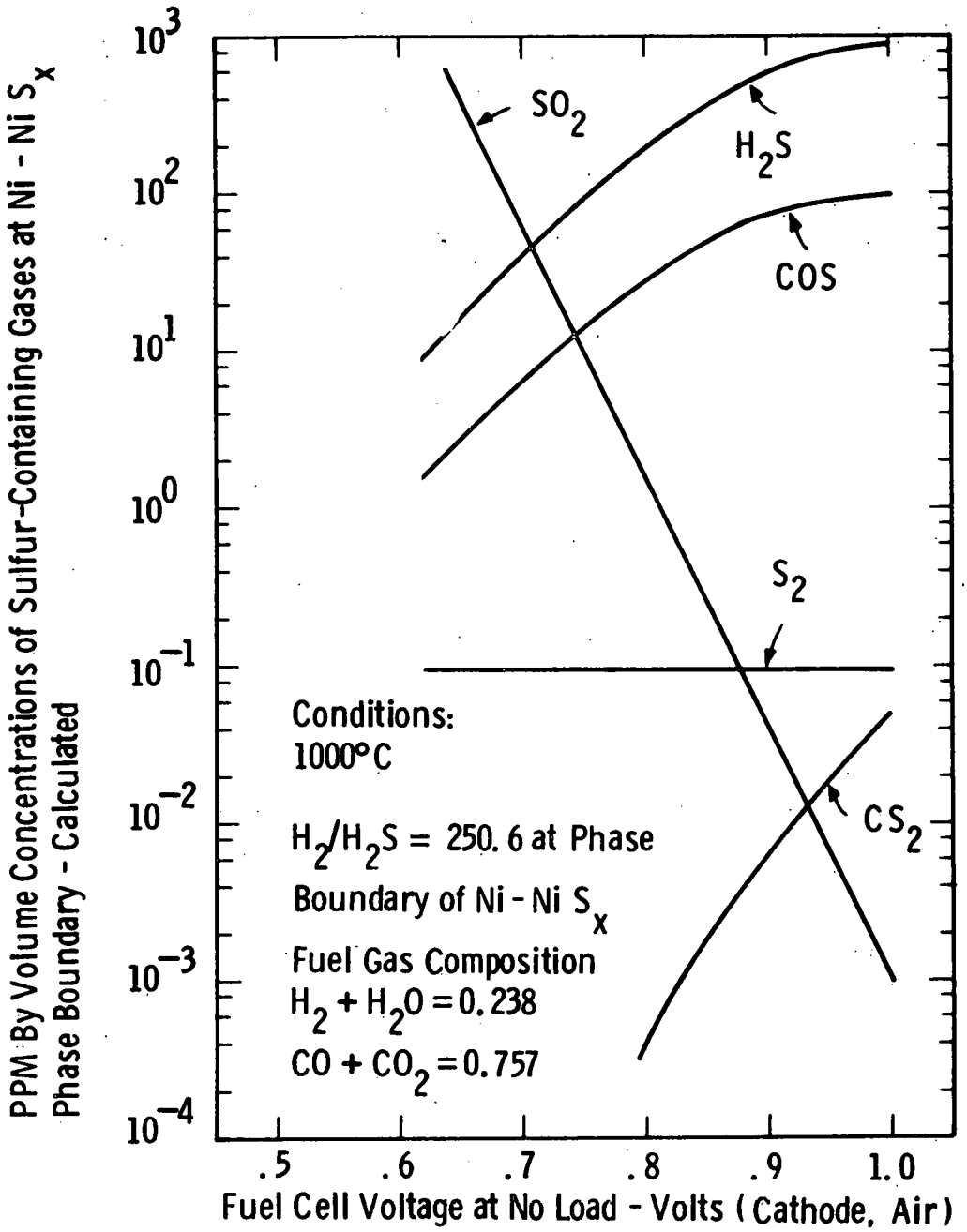

Fig. 5.75—Concentrations of sulfur-containing gases at Ni - Ni S_x phase boundary vs fuel cell voltage - calculated

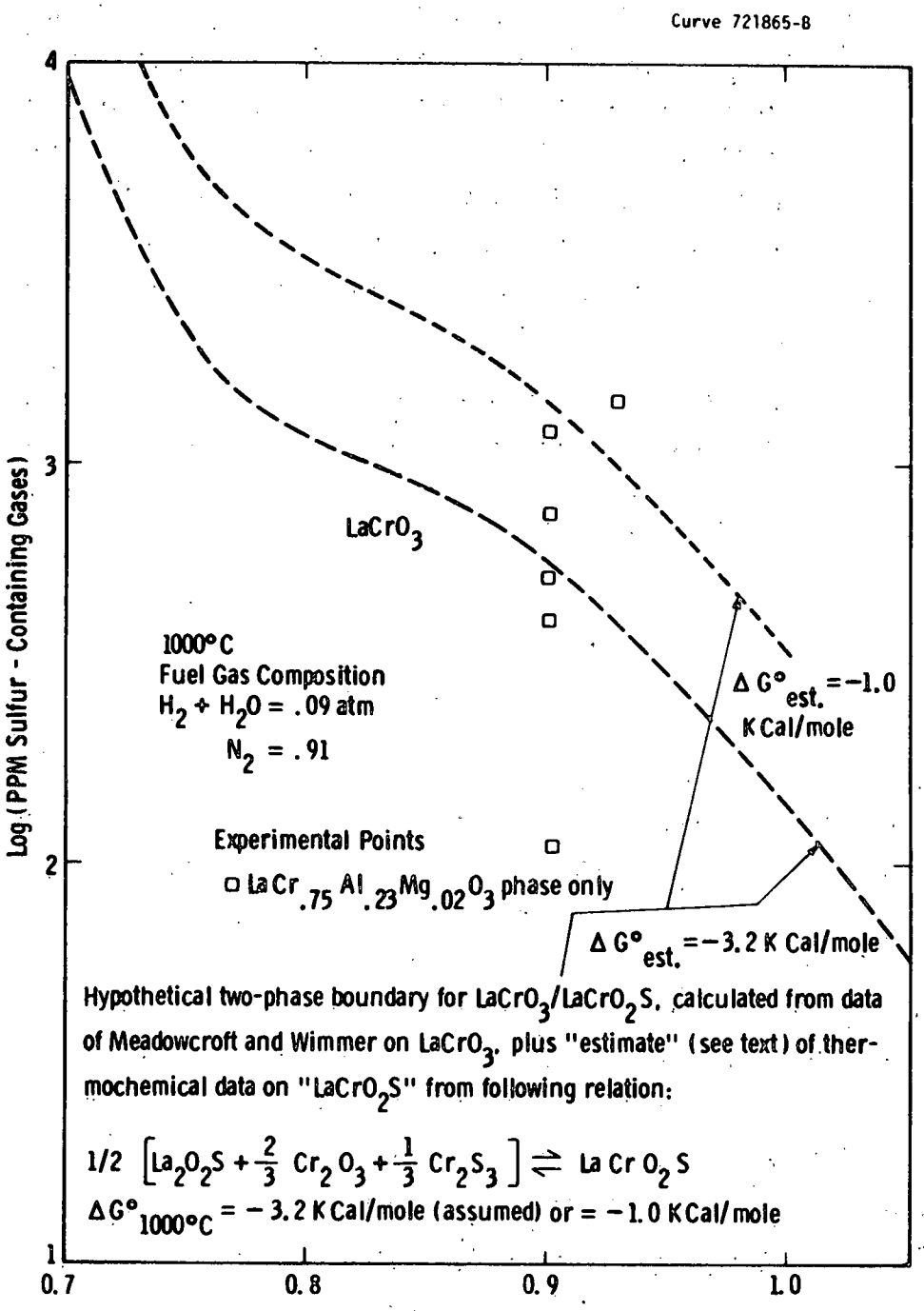

Fig.5.76—Exposure of lanthanum chromite to fuel gas ($H_2 + H_2O$) containing sulfur

6) As a typical example, for a fuel cell composition of $H_2 + H_2O \simeq 24$ mole % and $CO + CO_2 \simeq 76$ mole %, sulfidation of nickel should occur at about 90 ppm by volume of sulfur containing gases at atmospheric pressure and 1000 C, and at about 5 ppm at 700 C in the minimum tolerance region which occurs in the no load fuel cell voltage range of about 0.7 to 0.8 volt.

7) The minimum sulfur gas concentration level required to sulfidize lanthanum chromite, over the fuel cell voltage range of 0.7-1.0 volt, is greater than that of nickel (Figure 5.76).

The high-temperature microweighing apparatus was altered to measure threshold sulfur contents in a hydrogen or carbon monoxide containing fuel gas, required to just cause the onset of sulfidation of nickel, lanthanum chromite and other stack components. Figure 5.77 is a schematic drawing of this apparatus. As indicated, the fuel gas passes through a thermostated tube for controlled addition of water vapor, to provide a fuel with a fixed H_2/H_2O ratio, which can be blended with a CO/CO_2 mixture. The nickel, or other specimen, is suspended from the microbalance within a heated alumina tube, in contact with a flowing fuel gas stream. The start of reaction with sulfur containing gases is detected by an increase in weight of the sample with time, as the sulfur content of the fuel gas is increased.

The entire microweighing system is heated to 40-50°C, to permit use of higher vapor pressures of water than was possible in our earlier apparatus, which operated at room temperature.

Where data requiring water vapor pressures of more than $\sim 5 \times 10^{-2}$ atmosphere are needed, the lower pressure data are related to the higher pressure region by thermodynamic calculations.

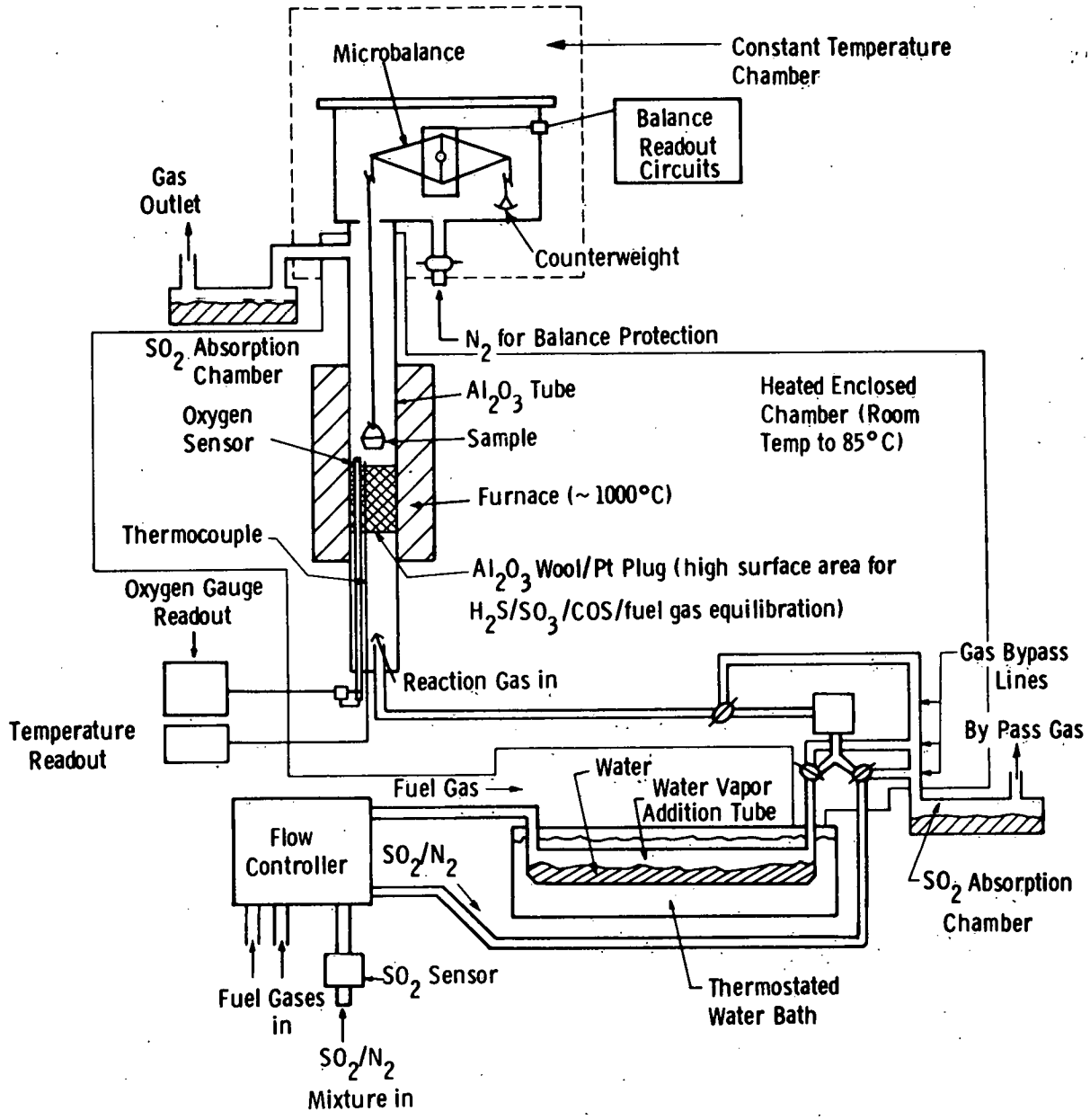

Fig. 5.77 — System for measuring weight changes of anode chamber materials in fuel gases containing water vapor and gaseous sulfur species

In our first experiments using the modified microweighting system, we examined the reactions of sulfur-containing water/hydrogen fuel gas mixtures with nickel and lanthanum chromite near 1000°C. The results are compared with thermochemical calculations for critical oxygen pressure regions in Figures 5.70 and 5.76 for nickel and lanthanum chromite, respectively. The available thermodynamic data for the NiS/NiS_x phase boundary appear suitable for such a comparison, but corresponding data for the lanthanum chromite system are incomplete. For the latter system the free energy of formation of $LaCrO_3$ is of uncertain accuracy and the sulfur-containing phase at the boundary between $LaCrO_3$ and the first related sulfur-containing phase is not known. However, using an analogy to the formation of La_2O_2S, we might anticipate formation of the oxysulfide of lanthanum chromite, namely $LaCrO_2S$, and that its Gibbs free energy of formation from known species, i.e.,

$$1/2\ La_2O_2S + 1/3\ Cr_2O_3 + 1/6\ Cr_2O_3 \rightarrow LaCrO_2S \qquad \text{(Reaction 1)}$$

might be of the same magnitude to that for the somewhat similar reaction,

$$1/2\ La_2O_3 + 1/2\ Cr_2O_3 \rightarrow LaCrO_3 \qquad \text{(Reaction 2)}$$

for which data of Meadowcroft and Wimmer[18] suggest a value of about -5.09 kcal/mole at 1000°C. However, no sulfidation of lanthanum chromite was detected in our experiments (see Figure 5.76) at "equivalent fuel cell voltages," up to 0.925 V in $(H_2 + H_2O)$ mixtures and up to 1500 ppm by volume of $(H_2 + H_2S)$ in the fuel gas, at 1000°C.

By comparison, thermochemical calculations (see Figure 5.76), even using as small a negative value of the Gibbs free energy of formation as -3.2 kcal/mole for the hypothetical Reaction 1, would predict (assuming the data of Meadowcroft and Wimmer for Reaction 2 is correct), that "$LaCrO_2S$" should form above about 600 ppm by volume of sulfur-containing gases in $(H_2 + H_2O)$ at 0.9 V and 1000°C.

Therefore, the experiments lead us to conclude that existence of a "$LaCrO_2S$" phase is doubtful, and more importantly, over the probable operating voltage range of the fuel cell (0.7-1.0 V) at 1000°C, the nickel fuel electrode, rather than the lanthanum chromite interconnection, will determine the maximum allowable sulfur content of the fuel gas. For the future, extended data will be obtained for both the nickel and lanthanum chromite systems, for the zirconia support tube and for actual sections of the fuel cell stack. Operational data of the effect of sulfur gas levels in the fuel on operating stack performance will then be interpreted by using this information.

6.0 Future Work

Work will continue into June 1980 on determining the effect(s) of sulfur impurities in the fuel gas on the performance and life of the HTSOE fuel cell stack.

The Design, Cost and Benefit Study, related to the application of the HTSOE fuel cell to an industrial cogeneration plant, will continue and will be completed and reported in September 1980.

A new proposal has been submitted to DOE/ANL and DOE/ Washington, D.C., and is nearing final negotiation, to continue work in the HTSOE fuel cell. This program of 3 years duration, comprises 7 major tasks: cell component advancement, stack testing under simulated service conditions, alternate fuel cell stack designs, initial design of a heat exchanger bundle, fuel cell bundle bench test evaluation, a materials availability study and a further refined plant system design, cost and benefit study.

THIS PAGE

WAS INTENTIONALLY

LEFT BLANK

7.0 References

1. Final Report, Task E4, "Thin Film Battery/Fuel Cell Power Generating System," Westinghouse Electric Corporation, DOE Contract No. EY-76-C-03-1197, March 31, 1978.
2. Mordfin, L. and Kerper, M. J., "Strength Testing of Ceramics -- A Survey of Mechanical and Thermal Properties of Ceramics," Proceedings of Symposium, 1968 National Bureau of Standards, U.S. Department of Commerce, Special Publication 303, pp. 243-262.
3. O'Keefe, M. and Morse, W. J., J. Phys. Chem., 65, 1438 (1961).
4. Kellogg, H. H., Trans. Met. Soc., AIME, 236, 602-15 (1966).
5. Dewit, J. H. W., J. Solid State Chem., 8, 142 (1973); 13, 192 (1975).
6. Groth, R., Phys. Stat. Sol., 14, 69 (1966).
7. Andersen, H., personal communication.
8. Andersen, H., Murphy, R., and Humphrey, K.,"The Rare Earths in Modern Science and Technology," Edited by Gregory J. McCarthy and J. J. Rhyne, Plenum Press, New York (1978).
9. DeWit, J. H. W., J. Solid State Chem., 8, 142 (1973); 13, 192 (1975).
10. Annual Report, C-1197-13, "Thin Film Fuel Cell/Battery Power Generating System," DOE Contract No. DE-AC-0379ET11305, April 30, 1979.
11. Berger, Carl, "Handbook of Fuel Cell Technology," Prentice-Hall, Inc., Englewood Cliffs, NJ, 1968, pp. 157-171.
12. Vargaftik, "Tables in the Thermophysical Properties of Liquids and Gases," John Wiley and Sons, New York, 1975, p. 634.
13. Etsell, T. H. and Flengas, S. N.,"Overpotential Behavior of Stabilized Zirconia Solid Electrolyte Fuel Cells," J. Electrochem. Soc., 118, 1890 (1971).

14. Isenberg, A. O., "Technology Advances in Solid State High Temperature Fuel Cells," National Fuel Cell Seminar, July 11-13, 1978, San Francisco.

15. Sverdrup, E. F., Archer, D. H., Alles, J. J., and Glasser, A. D., "Hydrocarbon Fuel Cell Technology," Academic Press, Inc., New York, 1965, p. 311.

16. Sluyters, J. H., "The Impedance of Galvanic Cells," Rec. Tran. Chim., 79, 1092, 1101 (1960).

17. Bauerle, J. E., "Study of Solid Electrolyte Polarization by a Complex Admittance Method," J. Phys. Chem. Solids, 30, 2657 (1969).

18. Meadowcroft, D. B. and Wimmer, J. M.,"Volatile Oxidation of Lanthanum Chromites," Paper 87-B-73, 75th Annual Meeting of the American Ceramic Society, Cincinnati, Ohio, April 29 - May 3, 1973.

8.0 APPENDIX A

PAST PROGRAM SUMMARY

Highlights of progress on the past contract program (DOE EY-76-C-03-1197), conducted during April 1, 1976 - March 31, 1978, are presented for the various tasks and subtasks, as specified in detail in the Design Plan of that program.

A.1 TASK 1. MATERIALS IDENTIFICATION AND SELECTION

A.1.1 Subtasks A and B. Interconnection Search and Identification

Work on the interconnection material identified a modified rare earth chromite as a very promising interconnection material. Specifically, modified lanthanum chromite, exemplified by the composition $La_{.95}Mg_{.05}Cr_{.75}Al_{.25}O_3$, was selected from among several systems studied, as having the most suitable properties for a cell interconnection material. No other oxide system investigated with comparable conductivity could be modified to produce the good thermal expansion match, low volatility, and negligible chemical interaction with other cell components that are available with this material.

As a result, this system received special effort in the second year of the program, to optimize its properties and to establish fabrication procedures for obtaining thin layer interconnection films. Films were successfully produced by electrochemical vapor deposition, initially onto fuel electrode substrates, and then as part of the fuel cell stack fabrication.

Additional work in this area was aimed at minimizing ionic transfer of oxygen ions through the interconnection layer, during cell operation.

A.1.2 Subtask C. Development of Other Stack Components

Selection of the other stack components was fixed during the first year of effort and further work on them was primarily aimed at refining their fabrication into useful thin films. These materials are:

- support tube -- porous, calcia-stabilized zirconia (15 mol % calcia)
- fuel electrode -- nickel cermet (nickel deposited in a porous, stabilized zirconia skeleton)
- solid electrolyte -- yttria-stabilized zirconia (from 8 to 12 mole % yttria)
- composite oxide air electrode -- tin-doped indium oxide (1 to 5 wt % SnO_2) current collector, with praesodymium oxide impregnation of the zirconia skeleton.

A.2 TASK 2. FABRICATION TECHNIQUES

Techniques for producing films of the various active components proceeded to the level where they were used to produce fuel cells and fuel cell stacks. Concurrently, an extrusion process was developed to produce, in-house, the porous support tubes.

4.2.1 Subtask A. Interconnection

RF sputtering was used to produce films for basic property evaluations, whereas an electrochemical vapor deposition (EVD) technique was developed that produced modified rare earth chromite compositions that are both leak-tight and conducting, as thin films ($\sim$40 μm). This EVD technique was subsequently used in fabricating the fuel cell stack that was tested on the program.

A.2.2 Subtask B. Electrolyte

The solid electrolyte, yttria-stabilized zirconia, was readily-prepared as a thin film by the EVD process. This process was reconfirmed on this program and was used to produce solid electrolyte films for the combination testing of components and fuel cell stacks.

A.2.3 Subtask C. Air and Fuel Electrode

Coating of zirconia support tubes with fuel electrode slurry compositions, along with firing and subsequent nickel reduction in hydrogen, was reconfirmed as a viable process for producing the nickel-cermet, porous fuel electrode. This process was used in the preparation of the fuel cell stacks.

The CVD process was developed to a sufficient level to enable preparation of uniform films of tin-doped indium oxide, air electrode current collector. This process was used in the preparation of the fuel cell stack that was tested in this program.

A.2.4 Subtask D. Porous Support Tube

Extrudable mixtures, prepared by combining selective size fractions of refractory starting powders and calcining at 1780°C, produced tubes that met the specifications of open porosity (>25 volume percent), tensile strength (>5000 psi) and thermal expansion ($\sim$10 x 10^{-6} m/m°C at 1000°C). Surface pores of the tubes were 10-11 μm in diameter with some variation in pore sizes, caused by agglomerates of water swelling starch plasticizers, used in the batch material preparation for extrusion.

A.3 TASK 3. COMPONENT TESTING

Equipment was built and used to test the fuel cell components and the fuel cell stack evaluated in this program.

A.3.1 Subtask A. Interconnection

Testing of interconnection films for composition and properties was ongoing throughout the program for gas tightness, resistivity, thermal expansion, doping level and oxygen vacancy concentration.

A.3.2 Subtask B. Combinations

A crossed-electrode testing concept and specimen was evolved and equipment was assembled, to enable combinations of fuel cell components to be tested in various atmospheres.

A.3.3 Subtask C. Useful Life Testing

A 5-cell fuel cell stack was fabricated and evaluated on the program. Three series connected cells of this stack met the program goals -- displaying 80% voltage efficiency at 200 mA/cm^2 for 700 hours with less than 10 percent voltage degradation at 950° to 980°C in a hydrogen - 3% water vapor fuel atmosphere.

A.4 TASK 4. ALTERNATE ELECTROLYTES AND BATTERY DESIGNS

Work scheduled in this area involved:

1) keeping abreast of developments in the field, with regard to alternate electrolytes, and evaluating, in an initial manner, any that show promise to the Westinghouse thin film fuel cell.
2) modifying cell and cell stack design, if the test results indicated problems, particularly, with respect to mechanical over-stressing of cell or cell stack component(s).

No alternate useful electrolytes were developed in the solid electrolyte field during the 2 years of the completed program. Test data on the fuel cell stack was so favorable that no major design changes have been contemplated.

9.0 APPENDIX B

OPERATION, DESIGN CONCEPT AND APPLICATION OF THE HIGH TEMPERATURE, SOLID OXIDE ELECTROLYTE FUEL CELL

B.1 INTRODUCTION

Fuel cells are electrochemical generators of direct current electricity. Unlike conventional generators, based on heat cycles, they have no Carnot efficiency limitations, and can, theoretically, yield high energy efficiencies. Of all fuel-cell power systems, that system, based on a stabilized-zirconia solid electrolyte, offers the highest achievable efficiency. A battery design study, conducted prior to this program, indicated that power densities of 7 kW/ft^3 of fuel cell module could be achievable with the state-of-the-art materials and fabrication processes defined at that time, when the stacks would be operated at 80% electrical efficiency. The high-temperature solid oxide electrolyte (HTSOE) fuel cell would operate at 1000°C, without the need of expensive catalysts, on a carbon monoxide-hydrogen gas mixture, provided by the gasification of coal. The fuel generator would operate at 1000°C for several reasons: a) the resistivity of the solid electrolyte is sufficiently low at this temperature to permit high levels of electrical efficiency at high current densities, and b) the high-grade heat released can be used for steam generation, which can be used for steam bottoming or for direct sale.

In one concept, clean pipeline coal gas could be supplied to the high-temperature, solid oxide electrolyte fuel cell and the by product, hot exhaust gas (CO_2) from the fuel cell generator would be used to produce steam in an off-gas, waste heat boiler. This steam would then be used to support either an industrial process, adjoining the fuel cell site, or for additional power generation, via a steam turbine, or both, to enhance the overall system efficiency.

Apart from the efficiency advantage and the use of a non-critical fuel, the HTSOE fuel cell is attractive from other standpoints.

- Air pollution from the fuel cell power system would be minimal. (Carbon dioxide and water vapor are the only species emitted.)
- Since the heat rejected by the fuel cell could be employed to gasify coal or produce steam, thermal pollution of the environment, due to waste heat, would be minimized.
- The fuel cell generating process would not require cooling water, consequently, siting of plants would not be dependent on plentiful water supplies.

The commercial feasibility of this new power system greatly depends on the useful life of the generator. At the onset of this continuation program, the useful life of the thin-film fuel cell stack

had achieved ∿700 hours at temperature, but with the promise of much longer life indicated by the stable nature and makeup the individual component layers of the fuel cell itself. The ERDA-directed, NASA-managed, Energy Conversion Alternatives Study, conducted in 1975-76 at the Westinghouse Research Laboratories, indicated that, for fuel-cell power systems to be competitive from an electricity-cost standpoint, the useful life of the fuel cell module must exceed 30,000 hours.

B.2 TECHNICAL BACKGROUND

Solid electrolyte fuel cells generate electrical energy from fuel and air. In this section a fuel cell power system is described, including: (1) how solid-electrolyte cells produce electrical energy, (2) how individual cells can be combined to form high-performance batteries, and (3) how batteries can be combined with auxiliary equipment into plant concept . Also reviewed are the major technical problems that must be resolved to allow demonstration of a long-lived, high-performance fuel-cell battery.

B.2.1 How Solid Electrolyte Fuel Cells Generate Electricity

As shown in Fig. B.1, a solid electrolyte fuel cell consists of four basic components: an air electrode, a solid electrolyte, a fuel electrode, and a porous support tube. A fifth component, the interconnection between adjacent cells, is not shown.

The porous tube of stabilized zirconia, which serves as a mechanical support for the fuel cell, has an approximate wall thickness of 1000 μm. In contrast, the individual component layers lie in the thickness range of 20 to 50 μm.

Exposed to the air flow is the air electrode. One kind is a composition of oxides, such as $(In_2O_3)_{0.98}(SnO_2)_{0.02}$ current collector, fabricated in a porous structure that is readily permeated by oxygen from air which flows over it. Here, praesodymium oxide is discontinuously deposited onto a porous zirconia matrix that underlies the current

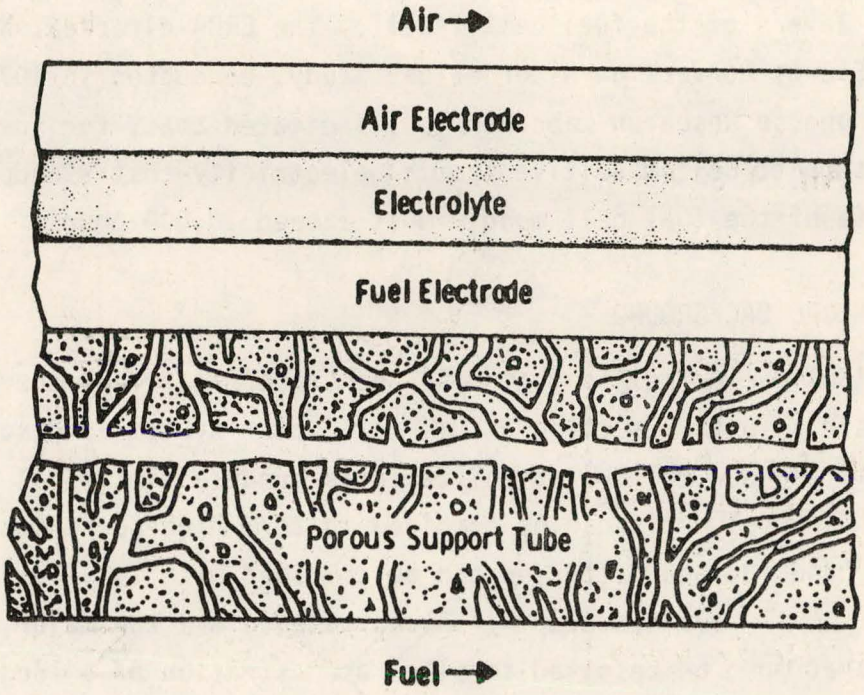

Fig. B.1 Schematic Cross-Section of a Thin-Film Fuel Cell

collector and represents the active part of the air electrode. This active PrO_2 effects the necessary $O_{2(g)}$ to $2O^{=}$ transition. Oxygen molecules from the air accept electrons through an external electronic circuit, leaving the electrode positively charged, and forming oxygen ions, $O^{=}$, as shown in Fig. B.2.

If the external circuit is closed, the oxygen ions enter the second component of the cell, a dense zirconia ceramic, such as yttria-stabilized zirconia (solid electrolyte) and pass through this layer at elevated temperature, due to the oxygen concentration gradient across the ceramic.* If an $O^{=}$ enters at the air electrode-electrolyte interface, an $O^{=}$ emerges at the electrolyte-fuel electrode interface, thus preserving the electrical neutrality of the material. The gases on either side of the cell will not penetrate through this impervious

*This gradient is established with air on one side and fuel gas on the other side.

Dwg. 6442A93

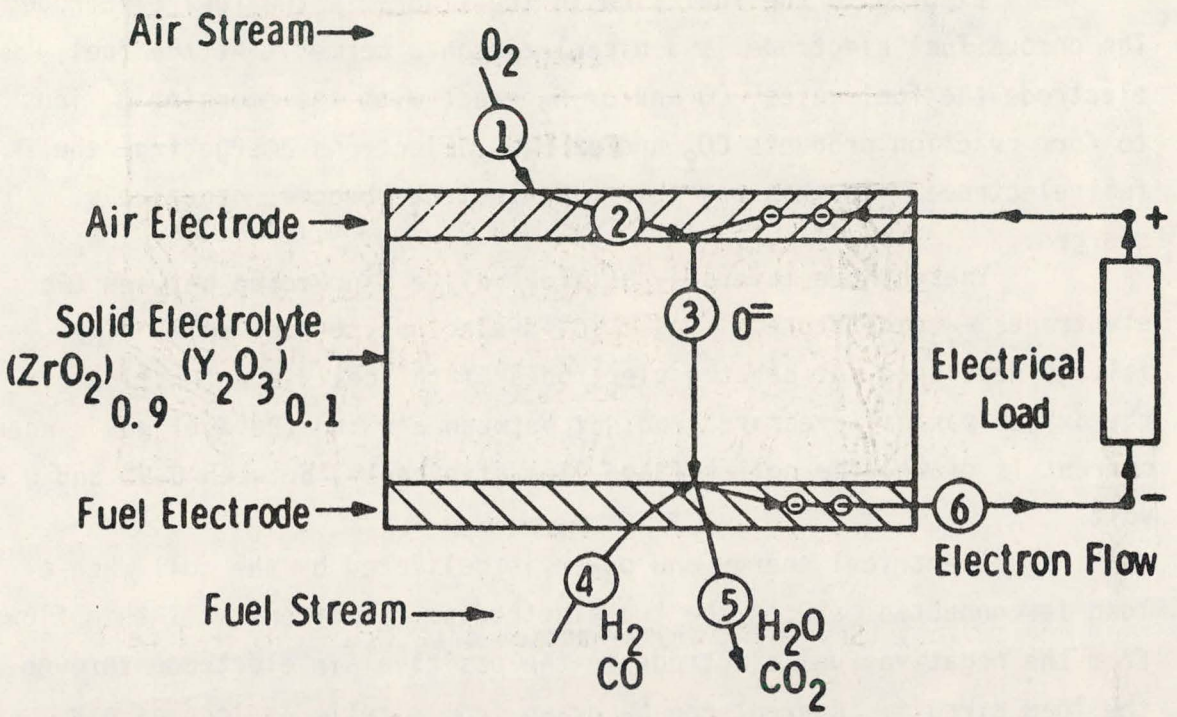

1 Oxygen molecule diffuses through air to electrode
2 Oxygen atom picks up two electrons from air electrode to form oxygen ion in electrolyte
3 $O^=$ oxygen ion transport through electrolyte
4 Fuel diffuses to reaction site and reacts with $O^=$ ion releasing electrons to fuel electrode
5 Reaction product leaves reaction site
6 Electrons from fuel electrode flow through external load to air electrode

Fig. B.2 Schematic Diagram of a Solid Electrolyte Fuel Cell, Indicating How Oxidation of the Fuel Generates Electric Current to the External Load

electrolyte layer, so that the reaction can only take place when current is drawn from the cell stack. Since the ceramic electrolyte has no electronic conductivity, no electrical short circuit can occur in the cell.

Exposed to the fuel flow in the figure is the fuel electrode. The porous fuel electrode is a nickel-zirconia cermet. At the fuel electrode the fuel gases, CO and/or H_2 react with the emerging $O^=$ ions to form reaction products CO_2 and/or H_2O. Electrons emerge from the fuel electrode. In this way the fuel electrode becomes negatively charged.

These three layers -- an electrolyte sandwiched between two electrodes -- constitute a single solid-electrolyte fuel cell. The voltage developed between the electrodes of the cell is a function of the oxygen partial pressure gradient between air and the fuel gas. When current is drawn, the cell voltage lies, typically, between 0.95 and 0.65 volt.

Electrical energy and power is delivered by the cell when a load is connected between the two electrodes. Electrons will then flow from the negative fuel electrode to the positive air electrode through the load circuit. Current can be drawn from a cell, as long as air and fuel gases are supplied and the combustion products removed. Current densities of 300 mA/cm^2 have been obtained from solid-electrolyte cells, while still maintaining cell efficiency at 80 percent. The output voltage produced at such currents is a function of the ohmic losses and concentration polarization losses in the electrodes.

B.2.2 Fabrication of Fuel-Cell Stacks

To obtain the voltages required for a practical system, cells must be connected in series. The technique, illustrated in Fig. B.3, provides a potentially low-cost method of making a series-connected stack of cells. This modular stack design is aimed at minimizing ohmic losses at relatively high current densities. It is necessary to provide an electrolyte surface area of approximately 5 ft^2/Kw, based upon state-of-the-art single cell performance.

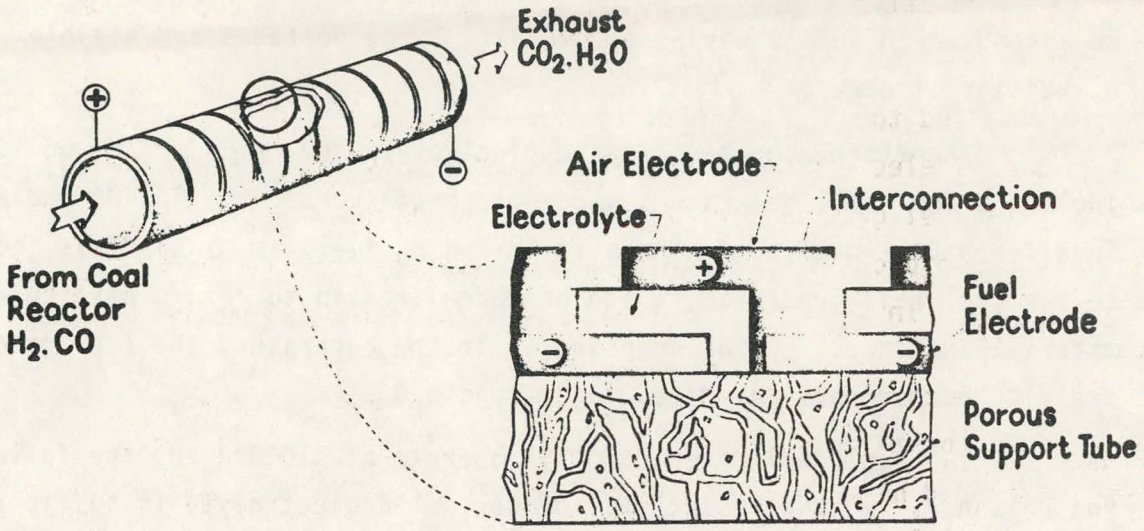

Fig. B.3 Cross-Section of the Westinghouse Thin Film, High-Temperature, Solid Electrolyte Fuel-Cell Stack

A group of cells, each about 0.5 cm wide around a porous tube of about 1.3 cm O.D., are series-connected to form a stack. As schematically shown in the cross-section of Fig. B.3, all cells on the tube are series-connected by joining the air electrode of one cell to the fuel electrode of an adjoining cell, through an electronically conducting interconnection. The interconnection must be fabricated as a gas-tight film, just as in the case of the electrolyte. Particular attention must be paid to the junction between the electrolyte and interconnection films to ensure gas impermeability in this region as well.

As indicated in the figure, a solid-electrolyte fuel cell stack consists of five components: an air electrode, a solid-electrolyte, a fuel electrode, and a cell interconnection, all approximately 50 μm, and a porous support tube with an approximate wall thickness of 1000 μm.

B.2.3 Operation of the High-Temperature Fuel Cell

To produce a practical energy system, individual cells must be assembled in such a way as to generate large voltages and sizable quantities of power.

Therefore, the basic solid-electrolyte fuel cell system would include a fuel cell generator, a ceramic heat exchanger and a DC and AC inverter. Coal-derived fuel gas (a CO and H_2 fuel gas mixture) is fed to the fuel cell generator, which has been treated to remove particulate material and excess sulfur compounds. In the generator, the fuel gases are electrochemically oxidized to CO_2 and H_2O.

The fuel cell generator will operate at ~1000°C for the following reasons: (a) the resistivity of the solid electrolyte is sufficiently low (~20 Ω cm) to permit high levels of electrical efficiency at high current densities, (b) the heat released in the fuel oxidation can be efficiently used elsewhere.

A battery design study has indicated that power densities of 7 kW/ft^3 of fuel cell module are achievable with state-of-the-art materials and fabrication processes, when the stacks are operated at 80 percent electrical efficiency.

The air necessary for the operation of the generator is brought in separately. The N_2 of the air and the unreacted O_2 emerge from the generator, exchange heat with the incoming air, and exhaust to the surroundings. AC power is available at the DC converter network.

B.2.3.1 The Fuel Cell-Heat Exchanger System

Figure B.4 indicates the components of a possible HTSOE fuel cell generator-heat exchanger system. Here the fuel cell generator would be composed of a high-temperature, heat exchanger component that is integrated with the cell stacks. The system would allow the final

Dwg. 7690A02

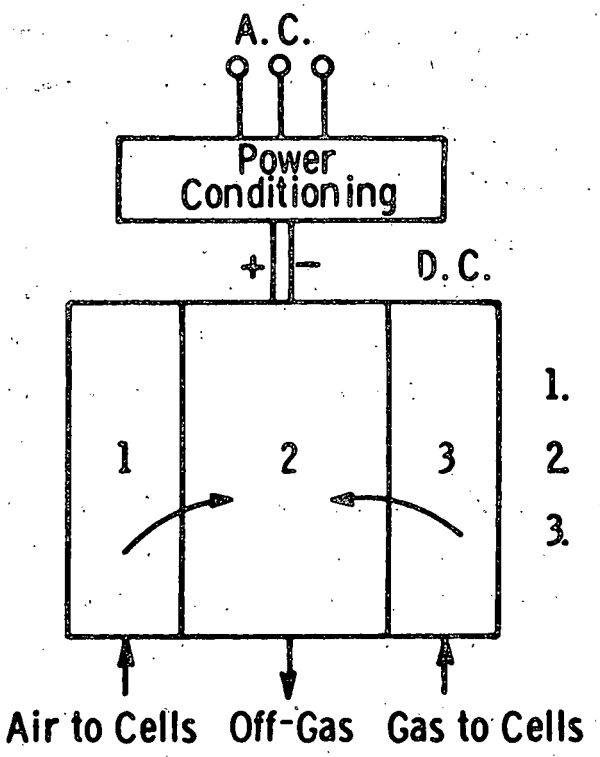

1. Air Heat Exchange
2. Generator Core
3. Fuel Heat Exchange

Fig. B-4 — Heat exchange — generator — power conditioning scheme

heating of fuel and air in a ceramic heat exchanger to the operating temperature of the cell stacks. A ceramic heat exchange is necessary because of the unavailability of metallic alloys that are stable at 1000°C for extended periods of time.

B.2.4 High-Temperature, Industrial Co-Generation Systems

A potential application for the HTSOE fuel cell would be in an industrial cogeneration plant. Such a plant would have an output of ∿50 MWe and would be capable of delivering steam from an off-gas, waste heat boiler to an industrial process, or for power generation (by a steam turbine), or both.

B.2.5 Fuel Cell Industrial Cogeneration

For the cogeneration scheme the fuel cell auxiliary systems components and their flow diagram interrelationships are given in Fig. B.5. The coal gas supply system (not shown) would deliver clean, pipeline coal gas to the cogeneration system. Salient features of this system would include the following:

1. Coal gas would arrive from some central gasification facility, would be distributed to the industrial site at an intermediate Btu value, and would be delivered at 1 bar, with no more than 100 ppmv H_2S, with provision for additional desulfurization, if needed.
2. Products of combustion from this gas would contain less than 0.1 lb. $SO_2 10^6$ Btu to meet any SO_2 control level now in existence, or proposed.

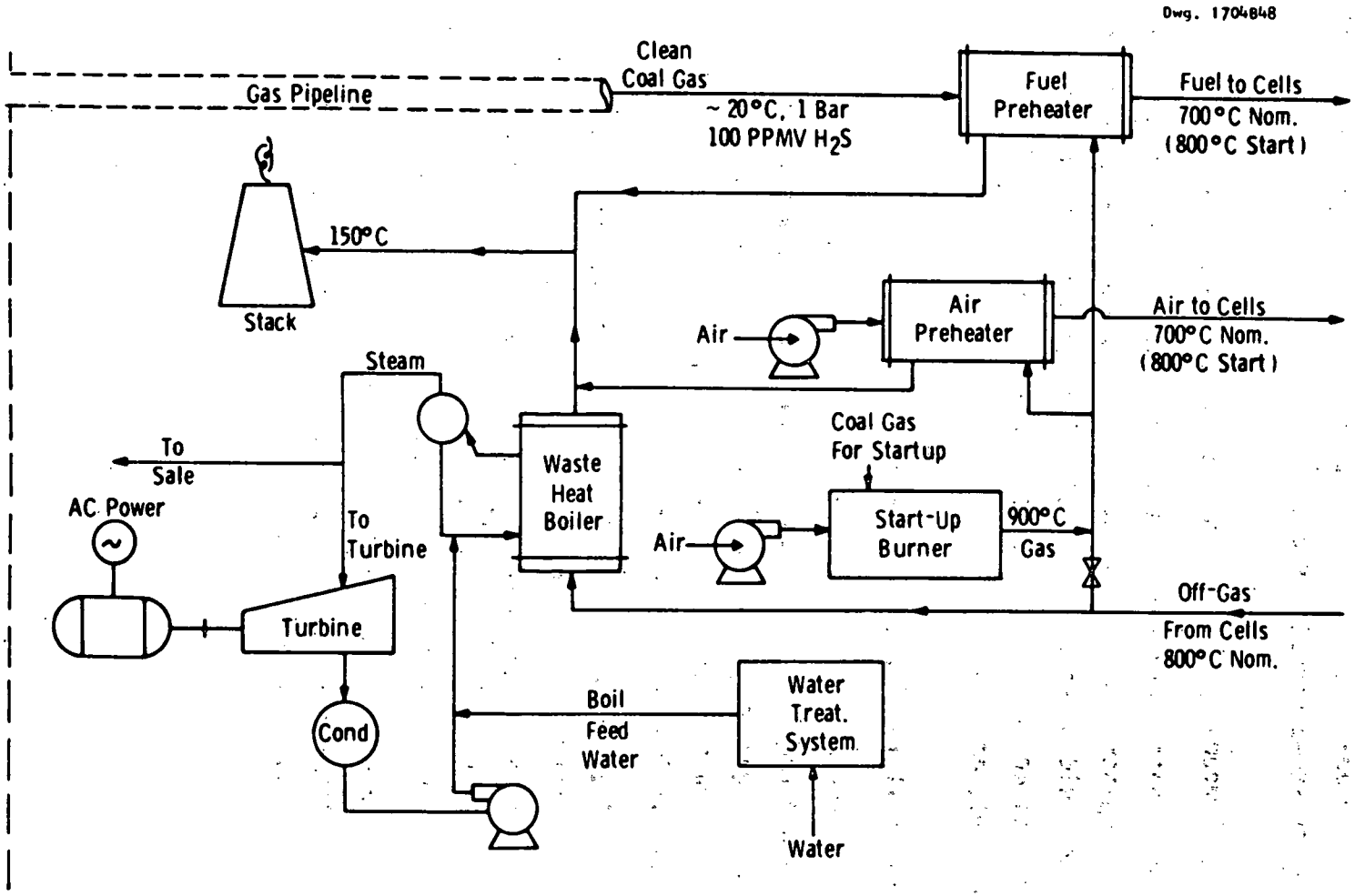

Fig. B-5 – Proposed HTSOE fuel cell auxiliary systems

3. Fuel and air preheaters would use 800°C gas from the fuel cell outlet combustors.
4. Start-up heat would be supplied at 900°C for a limited period of time, to provide start-up fuel and air at 800°C to the fuel cells. These conditions represent the maximum temperatures that would be achieved in the heat exchanger (only during the last few hours of cell start-up heating).
5. Preheater materials and design would consider the presence of H_2S in the fuel gas to avoid carbon deposition from a reverse Boudouard reaction.
6. Steam from the off-gas waste heat boiler would be used by an industrial process, adjacent to the fuel cell site, or for power generation, or both.

☆U.S. GOVERNMENT PRINTING OFFICE: 1981-740-145/2023